

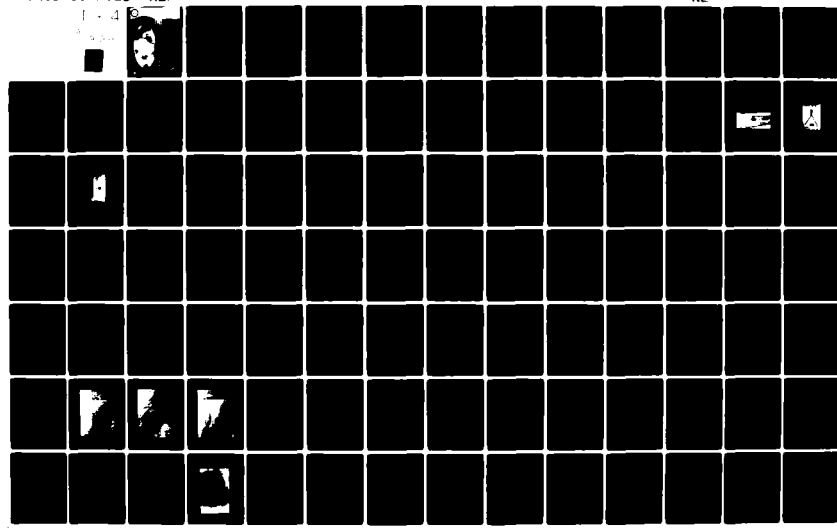
AD-A091 046 WASHINGTON UNIV SEATTLE DEPT OF OCEANOGRAPHY
FORCED INTERNAL WAVES IN THE ARCTIC OCEAN. (U)
MAY 80 J H MORISON
REF-M80-10

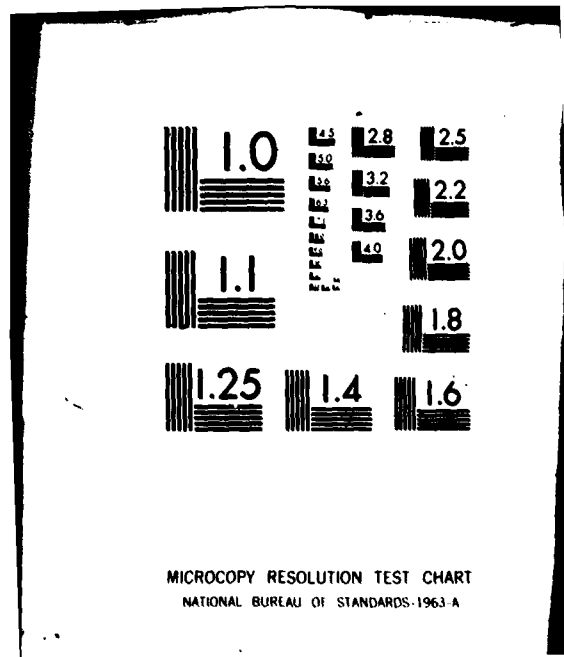
F/G 8/3

N00014-75-C-0186
NL

UNCLASSIFIED

1 - 4







the department of

OCEANOGRAPHY

AD A091046



LEY

12th

L REPORT

FORCING INTERNAL WAVES
IN THE ATLANTIC OCEAN

by

Howe Morris

This document has been approved
for release, distribution, and sale; its
use is unlimited.

Office of

0024

OCT 29 1980

Reference M80-10
MAY 1980

A

80 10 27

DR

UNIVERSITY OF WASHINGTON
DEPARTMENT OF OCEANOGRAPHY
Seattle, Washington 98195

(12) 307

(9) Final report

(6)

Technical Report

FORCED INTERNAL WAVES IN THE ARCTIC OCEAN

by

(10) James Howe Morison

(11) M. 78

This report consists of a dissertation presented by the author
in partial fulfillment of the requirements for the degree of
Doctor of Philosophy.

(15) N00014-75-C-0186

N00014-77-C-0024

Office of Naval Research
Contract N-00014-75-C-0186

This document has been approved
for public release and sale; its
distribution is unlimited.

(14) REF-M80-10

Contract N-00014-79-C-0024

J. Dungan Smith

J. Dungan Smith
PRINCIPAL INVESTIGATOR

Jan Van W.

James Howe Morison
PRINCIPAL INVESTIGATOR

G.C. Anderson

George C. Anderson
ASSOCIATE CHAIRMAN FOR RESEARCH

Reference M80-10
May 1980

Reproduction in whole or in part is permitted
for any purpose of the United States Government

340810 set

University of Washington

Abstract

FORCED INTERNAL WAVES IN THE ARCTIC OCEAN

By James Howe Morison

A

Chairperson of the Supervisory Committee: J. Dungan Smith
Geophysics

When the surface of an ocean is disturbed by the effects of a storm, motions may be excited in the pycnocline by the action of forced internal waves. This dissertation deals with experimental and theoretical studies of such motions.

During the Arctic Mixed Layer Experiment in the Spring of 1976, manifestations of forced internal waves were observed with a new profiling current meter - CTD system. The device is unique in that it is capable of producing simultaneous, accurate profiles of density and horizontal velocity, repeatedly and at high frequency. Of particular interest are measurements made with the instrument in the upper 80 m of the ocean during a small storm which occurred April 8, 1976. During the storm the isopycnals deflected downward about 2 m and then rebounded and oscillated with periods on the order of 5 to 10 hours. Horizontal velocity perturbations at about the inertial frequency were also excited by the storm.

In an effort to explain the observed motions, new theories were developed which deal with the forcing of internal waves by surface stress, atmospheric pressure and buoyancy flux. Solutions are derived

for the forced motions as sums of internal wave normal modes. Arbitrary stratification is allowed below the surface mixed layer and the kinematic surface boundary condition is used.

The solution for forcing by surface stress is unique in that it combines the use of arbitrary stratification with a body force approximation for surface stress. Two different integral expressions are derived for the response and they give identical results. Using estimates of surface stress based on ice velocity measurements from a large array of AIDJEX navigation buoys, the response of the first 49 modes are combined to predict the response as a function of depth and time at the experimental location. The resultant vertical displacement response resembles qualitatively the observed motions in phase and form but is smaller than the observed response by a factor of three. The predicted velocities display inertial oscillations extending across the top pycnocline just as observed but are also three times smaller than the observed motions.

The response to surface pressure is determined using normal mode decomposition. This produces a result identical to that of A. Leonov and Y. Miropolskiy. The response to atmospheric pressure is found to be negligible but the pressure response is used in the model of internal waves driven by buoyancy flux in leads.

The model of buoyancy flux forced waves is an extension of a model by L. Magaard. It employs a vertical diffusion coefficient which is large in mixed layer and zero below. Using a buoyancy flux geometry and magnitude representative of conditions during the storm yields predictions of vertical displacement on the order of 1.2 m, nearly twice as large as those predicted for surface stress forcing. This contrasts

with Magaard's finding that, for a temperate ocean, the buoyancy flux response should be less than the stress response. The difference is that the buoyancy flux response increases with wave number and the forcing is at shorter wavelengths (lead spacing \sim 10-20 km) in the Arctic than in temperate oceans. Horizontal velocities predicted by the model display shears at the inertial frequency with an amplitude of about 2 cm sec^{-1} which are quite similar to the observed oscillations. Due to the simplifying assumption of no horizontal salt advection, the displacement and velocity predictions became unreasonably large at high wavenumbers. This has required the forcing for wavelengths shorter than 5.5 km be neglected and suggests a better model would account for the effects of horizontal spreading.

The conclusion of the dissertation is that internal waves forced by surface stress and buoyancy flux probably accounted for much of the observed response on April 8, 1976 and that, in general, forced motions create vertical displacements on the order of 1 meter at wavelengths down to a few kilometers. The remnants of such motions, which persist after forcing stops, may also appear as significant events when the ice moves over them, thus adding further complexity to observations of the responses of subsequent storms.

CONTENTS

	Page
LIST OF FIGURES	iv
LIST OF TABLES	ix
ACKNOWLEDGMENTS	x
 Chapter	
1. INTRODUCTION	1
2. THE ARCTIC MIXED LAYER EXPERIMENT	5
2.1 Experimental Goals and Plan	5
2.2 Camp History and General Results of the Experiment	7
2.3 The Arctic Profiling System	10
3. EXPERIMENTAL RESULTS	28
3.1 General Features	28
3.2 The Event of April 3	48
3.3 The Event of April 8	51
3.4 Lead Convection Observed During the AMLE	71
4. FORCED INTERNAL WAVES AND THE APRIL 8 STORM RESPONSE	83
4.1 Theoretical Models of Internal Wave Generation by Surface Forces	83
4.2 Derivation of Response Functions for Internal Waves Driven by Surface Pressure and Stress	91
4.3 Forcing of Internal Waves by Buoyancy Flux at the Surface	122

Chapter	Page
4.4 Calculation Techniques and General Results for N^2 , Eigenfunctions and Response Integrals	132
4.5 The Wave Number Frequency Response	164
4.6 Internal Waves Forced by Surface Stress During the April 8 Storm	173
4.7 Response to Buoyancy Flux	200
4.8 A Combined Stress and Buoyancy Flux Response	218
5. SUMMARY AND CONCLUSIONS	223
REFERENCES	237
APPENDICES	
A. APS SENSOR CALIBRATION AND DATA PROCESSING	242
B. EQUATIONS OF MOTION	282
C. LIST OF PHYSICAL VARIABLES IN CHAPTERS 4 AND 5	285

LIST OF FIGURES

Figure	Page
2.1 Sketch of AMLE camp layout showing the key instruments used	6
2.2 Maps showing position of AMLE camp at Big Bear (BB) in the Beaufort Sea and the layout of the AMLE camp on a refrozen lead	8
2.3 The APS	11
2.4 The APS current meter triplet	12
2.5.The sensors in the IRU	14
2.6 Data from a single downcast of the APS made at 1333 AST, April 8, 1976	18
2.7 Data averaged from 12 APS profiles taken between 1322 and 1422 AST, April 8, 1976	20
2.8 Average of 16 APS profiles made between 0712 and 0812 AST, April 5, 1976	24
2.9 Data from a single downcast of the APS made at 1504 AST, April 8	26
3.1 Average of 12 temperature and salinity plots made between 1322 and 1422 AST, April 8, 1976	29
3.2 Isopycnal depths versus time and 2 m winds for the AMLE	30
3.3 Fifteen minute averages of horizontal velocity relative to the pack ice as measured with the APS	33
3.4 Northward ice velocity from three AIDJEX camps Caribou (CA), Snowbird (SB) and Blue Fox (BF)	52
3.5 Eastward ice velocity from three AIDJEX camps Caribou (CA), Snowbird (SB) and Blue Fox (BF)	53

Figure	Page
3.6 NOAA-4 satellite image of the Beaufort Sea, 1000 AST, April 7, 1976	56
3.7 NOAA-4 satellite image of the Beaufort Sea, 1000 AST, April 8, 1976	57
3.8 NOAA-4 satellite image of the Beaufort Sea, 1000 AST, April 9, 1976	58
3.9 The u velocity contours relative to the average velocity between 10 m and 20 m, along with 2 m winds	62
3.10 The v velocity contours relative to the average velocity between 10 m and 20 m, along with 2 m winds	63
3.11 σ_t profiles before, during and after the April 8 storm	67
3.12 A simple two layer model of deepening of the seasonal pycnocline due to convergence in the mixed layer	69
3.13 The AMLE camp as seen from the air during evacuation on April 11, 1976	72
3.14 Velocity and σ_t as measured with the APS from 1430 to 1530, after the lead opened at the end of the experiment	73
3.15 Salinity versus time at 20.5 m, 45.5 m, and 75.5 m	74
3.16 Salt flux = $\bar{q} = \bar{u} (S_{dn} - S_{up})$ at 1500, April 10	77
4.1 Contour of integration in the complex σ plane for solving the stress forced problem	111
4.2 The Brunt Väisälä frequency, N , as a function of depth for the Beaufort Sea	135
4.3 Interpolated values of N on a logarithmic depth scale	139
4.4 Interpolated values of N on an arithmetic depth scale	140

Figure	Page
4.5 Eigenvalues for Beaufort Sea, $k = 14.8$ and $k = .92$	150
4.6 Eigenfunctions and eigenfunction derivatives for $k = .92$, modes one through four	152
4.7 Eigenfunctions and eigenfunction derivatives for $k = 14.8$, modes one through four	154
4.8 The modal responses to surface stress, $R_n / \lambda_n \omega_n$	158
4.9 The modal response to surface pressure, $R_n / \lambda_n \omega_n$	159
4.10 Three-dimensional perspective plot of the wave number frequency response for displace- ment at the pycnocline, $k = .92$, mode one	166
4.11 Three-dimensional perspective plot of the wave- number frequency response for velocity, u_p , in the mixed layer $k = .92$, mode one	168
4.12 Three-dimensional perspective plot of the wave-number frequency response for velocity, v_p , in the mixed layer $k = .92$, mode one	170
4.13 Three-dimensional perspective plot of the wave-number frequency response for displacement at the pycnocline, $k = .92$, mode three	171
4.14 The internal wave forcing at Big Bear	177
4.15 The AIDJEX buoy array at the time of the AMLE	180
4.16 Sketch illustrating the model of lead distribu- tion near the AMLE camp at Big Bear on April 8, 1976 and the assumed small scale distribu- tion of forcing	184
4.17 The predicted isopycnal response to surface stress and observations at Big Bear in the upper 90 m of the water column	187
4.18 The predicted response to surface stress at Big Bear over the whole ocean depth	193

Figure	Page
4.19 Contour plots of absolute and relative u velocity due to stress response	196
4.20 Contour plots of absolute and relative v velocity due to stress response	197
4.21 Predicted isopycnal responses in the upper 90 m of the water column to buoyancy flux in leads open on April 8	206
4.22 Predicted isopycnal response over the full ocean depth to buoyancy flux conditions identical to those of Figure 4.21	207
4.23 Predicted isopycnal responses in the upper 90 m of the water column for conditions identical to those of Figure 4.21 except the initial position of the observation point is -8.25 km	208
4.24 Predicted isopycnal responses over the full ocean depth for conditions identical to those of Figure 4.21 except the initial position of the observation point is -8.25 km	209
4.25 Contour plots of absolute and relative u velocity due to buoyancy flux response	214
4.26 Contour plots of absolute and relative v velocity due to buoyancy flux response	215
4.27 Combination of the stress forced isopycnal response of Figure 4.17 and the buoyancy flux forced isopycnal response of Figure 4.21	219
A.1 Current meter angles of attack	243
A.2 Current meter calibration facility	248
A.3 A three-dimensional perspective sketch of $G(\alpha, \theta)$ vs. $\tan \alpha$, $\tan \theta$	252
A.4 Head on calibration for mechanical current meters	254
A.5 Yaw correction coefficients	258
A.6 Pitch correction coefficients	259

Figure	Page
A.7 Sketch of the APS triplet showing the numbering convention used to identify the current meters	263
A.8 $G_1(C_o, h_o)$ for APS triplet	267
A.9 $G_2(C_o, h_o)$ for APS triplet	268
A.10 Block diagram of data reduction scheme used for analyzing APS data	271
A.11 Raw frequency data from the three APS current meters for 1059-1102 AST 4/8/76	273
A.12 Data from rate gyro #1 (Positive pitch forward) and accelerometer #1 (positive forward) showing oscillations with 1.26 sec period	275

LIST OF TABLES

Table	Page
3.1 Salt Flux and Required Lead Widths	80
4.1 Wave Numbers for Maximum Velocity Response	172
4.2 $S_a(n)$ for $n = 1 + 5$	185
4.3 Contributions to the Stress Response at Different Wavelengths	190
A.1 Instruments in Arctic Profiling System	245
A.2 Angle of Attack Correction Polynomial Coefficients	261
A.3 Coefficients for APS Triplet Angle of Attack Corrections	269

ACKNOWLEDGEMENTS

**This work was supported financially by Office of Naval Research
Contracts Number N-00014-75-C-0186 and Number N-00014-79-C-0024.
Logistical support was provided by the Naval Arctic Research Labora-
tory and the AIDJEX Office.**

Chapter 1

INTRODUCTION

The Arctic mixed layer is a shallow surface zone of nearly homogeneous density, bounded below by a strong pycnocline. It is important in the dynamics of the Arctic Ocean because it is the region through which the vertical exchange of momentum, heat and mass between the interior ocean and the ice cover or atmosphere occurs. The most commonly discussed mechanism for such exchange is the generation of turbulence at the ocean surface by the effects of wind and ice motion and the consequent mixing of mass and momentum across the pycnocline. These processes are irreversible, deepening the mixed layer and increasing the surface density. However, momentum may also be transferred across the pycnocline by conservative processes, that is by processes which do not require turbulent transport at the pycnocline and which are reversible. An important example of the latter type is the generation of forced internal waves by various mechanisms. For example, horizontal variation in wind stress at the surface often causes convergence in the mixed layer which in turn deepens the pycnocline and forces readjustment of the mass field at depth. In this way the mixed layer structure is changed and motions are excited below the seasonal pycnocline with no increase in mixed layer density and no turbulence at the pycnocline.

Forced internal waves can also be driven by a surface buoyancy flux. In temperate oceans this may be due to surface heating, cooling or evaporation but in an ice covered ocean the most important buoyancy

flux is that due to haline convection, caused by the freezing of sea water in open leads. The circulation patterns that result from lead convection are unique in that they produce significant changes in density and velocity in the mixed layer over relatively short horizontal length scales. These changes involve convergence and divergence in the mixed layer and thus drive internal motions in the main pycnocline.

Forced internal motions are important for several reasons. First, no matter what the magnitude of a storm may be, some forced internal motion will result; even if the storm is too weak to cause changes at the pycnocline through mixing there, a change in pycnocline depth can be expected. The mechanism thus provides a virtually continuous input of energy to the main pycnocline. This energy is dispersed through internal wave processes. Second, the forced motions persist after a storm ends, leaving the density and velocity field disturbed over a wide range of length scales. Finally, interpretation of the behavior of the mixed layer requires an ability to separate the relative effects of turbulent mixing and forced internal motions during storms. This is only possible if one has a complete understanding of at least one of the processes and that associated with the inviscid response appears to be more readily characterized quantitatively.

In this dissertation the processes of internal wave generation by surface stress and by buoyancy flux in leads will be discussed in light of observations and theoretical considerations. It will be shown that both of these processes make significant contributions to changes in the velocity and density structure of the upper Arctic Ocean. The internal wave responses forced by surface stress and buoyancy flux

non-uniformity are examined and each one is shown to produce rapid displacements of the pycnocline with a magnitude on the order of one meter and to induce horizontal velocities from one to ten centimeters per second under typical conditions.

The motivation for this work comes from data gathered during the Arctic Mixed Layer Experiment which was conducted from an ice camp in the Beaufort Sea during March and April 1976. The experiment provided a unique opportunity to study forced internal motions. Meteorological and oceanographic conditions were quite calm until one short storm occurred. The structure of the storm was documented fairly well with ice navigation data and satellite photographs and the ocean response was measured quite well during the entire period with a profiling current meter - CTD. Thus, the data gives a good picture of the ocean responses to an isolated event and can be compared with theoretical predictions in a meaningful way.

In what follows, Chapter 2 deals with the motivation for and history of the Arctic Mixed Layer Experiment. The profiling current meter - CTD will also be described there. Chapter 3 deals with all the observations made during the experiment and in so doing, a broad range of topics is discussed. Aside from the storm response, data pertaining to the lead convection process will be presented. This chapter also highlights the usefulness of the profiling current meter - CTD system. In Chapter 4 emphasis is focused on the forced internal wave response. Theories for the forced response to surface stress, pressure, and buoyancy flux are developed and simulations are compared to the experimental

data. The work discussed in Chapter 4 comprises the core of the dissertation.

Chapter 2

THE ARCTIC MIXED LAYER EXPERIMENT

2.1 Experimental Goals and Plan

The goals of the Arctic Mixed Layer Experiment (AMLE) were to investigate the turbulent boundary layer under smooth ice and to study the response of the Arctic mixed layer to various types of forcing. A previous near surface experiment performed by McPhee and Smith (1976) produced boundary layer measurements generally showing good agreement with existing theories but which were degraded by the effects of a small pressure ridge. It was hoped that performing the boundary layer experiment under a large refrozen lead, rather than from multi-year ice, would avoid this problem. A site on smooth ice also would provide an excellent location at which to measure changes in the mixed layer structure in response to boundary layer processes.

The experimental plan called for setting up a camp comprised of three buildings. A sketch of the proposed configuration is given in Figure 2.1. Under one building a profiling current meter - CTD was to be cycled continuously through the upper 100 m or so of the water column. Among other things this instrument was intended to provide data showing changes in the velocity and density fields due to turbulence in the mixed layer. Under the second building, 25 current meter triplets were to be mounted on three tubular masts extending to a maximum depth of 55 m. This arrangement, which has been discussed in detail by Smith

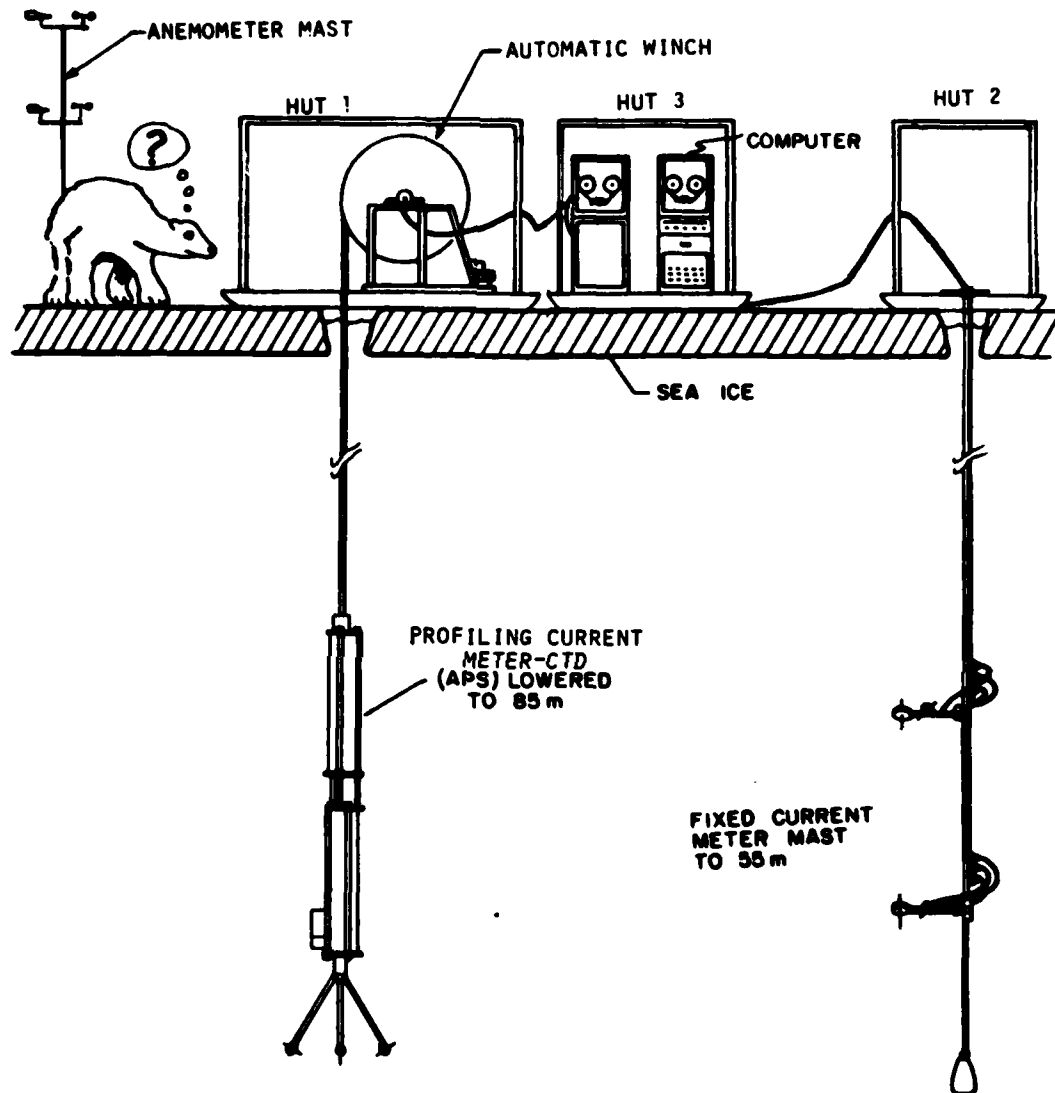


Figure 2.1. Sketch of AMLE camp layout showing the key instruments used: the Arctic Profiling System, the mast of fixed current meters (actually three separate masts were installed with a total of 25 current meter triplets), and the anemometer mast with sensors at 2 m and 4 m.

(1974a), McPhee (1974) and Smith (1978), was to be used to measure turbulent flow in the boundary layer and to detect any velocity fluctuations that might occur in the upper pycnocline. Data from all sensors was to be fed to a NOVA 1200 computer system, housed in the third and smallest building. This light-weight hut was designed to be evacuated on a sling by helicopter in case the relatively thin ice on which the camp was to be situated began to break up. Also included in the plan was an anemometer mast supporting two Aanderaa cup anemometers at heights of 2 m and 4 m.

2.2 Camp History and General Results of the Experiment

In practice the camp arrangement was much as planned. The experiment was conducted in March and April of 1976 with the help of the AIDJEX staff. The author spent a week at the AIDJEX ice camp, Caribou, examining potential sites from various types of aircraft. Eventually a suitable location on a 1 m thick refrozen lead, approximately 3 km south of the abandoned AIDJEX camp, Big Bear, was deemed acceptable and was occupied on March 13, 1976. With one exception, the surface relief of this six-month old feature was less than 20 cm, the exception being a small ridged area with a maximum elevation of 1 m. The area of smooth ice was about 1.5 km long in the east-west direction and about 1 km wide in the north-south direction.

Figure 2.2 is a sketch of the general camp layout indicating the salient local features. It also includes a larger scale map showing the camp position relative to the AIDJEX camps. The huts were placed 1 km from the west end of the smooth ice in anticipation of

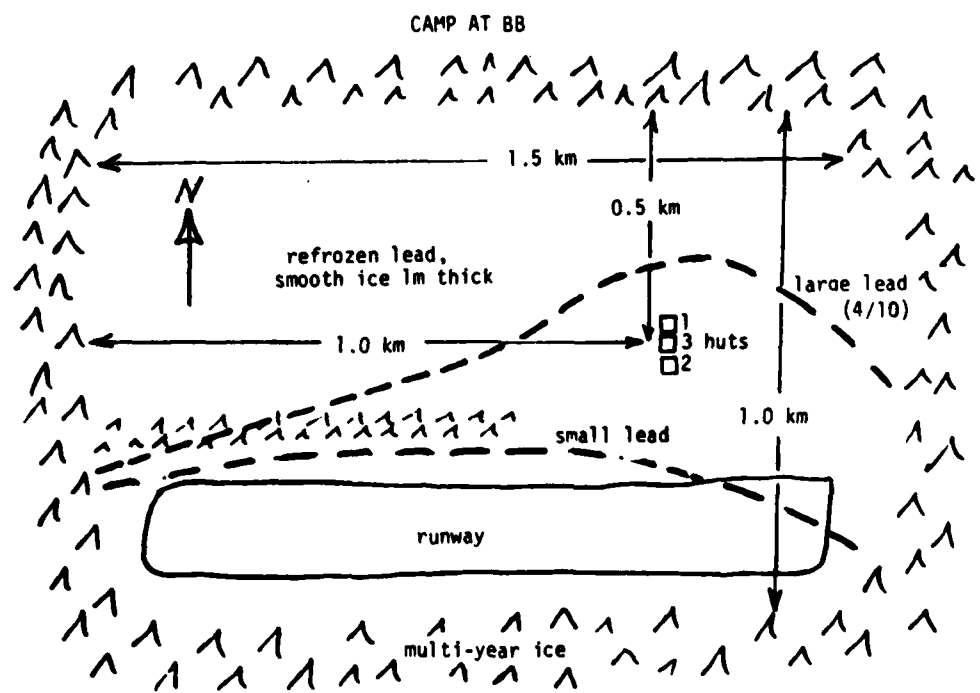
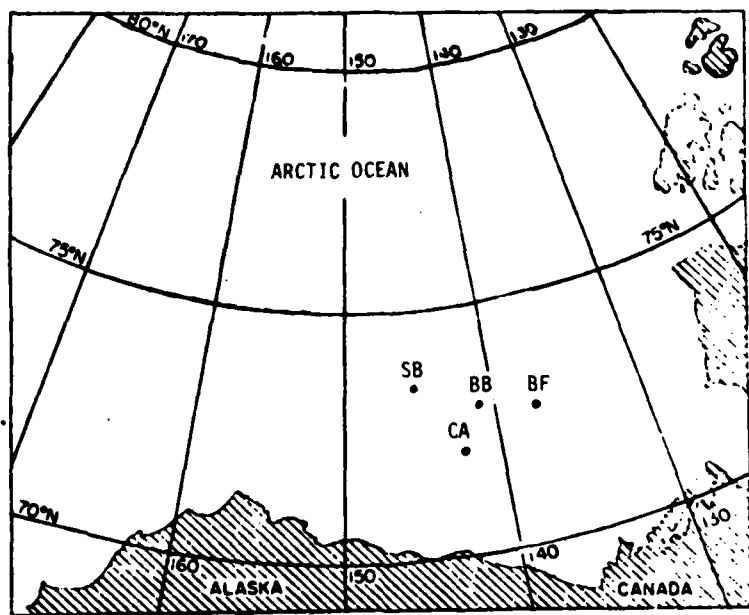


Figure 2.2. Maps showing position of AMLE camp at Big Bear (BB) in the Beaufort Sea and the layout of the AMLE camp on a refrozen lead. Also shown are the relative positions of the AIDJEX camps Caribou (CA), Blue Fox (BF) and Snowbird (SB).

predominantly westward ice motion due to occasional storms.

During the first two weeks the main effort was devoted to building the runway, moving 3 huts for the old Big Bear camp and setting up the scientific gear (e.g., computer, current meter masts, winch and profiling system). Numerous technical problems delayed full operation until April 1. By that time the camp was arranged according to the experimental plan.

From March 13, when the camp was first occupied, until April 8, atmospheric conditions were generally quiet. The only operational problems during this period were caused by a small lead which opened to .6 m for a few hours on March 17 and again to a width of 3 m on April 6 (see Figure 2.2 for the lead location). Currents during this period were found to be very small.

On April 8 a storm occurred which lasted the whole day. This storm caused significant relative motion of the ice and the measured water velocities reached 15 cm sec^{-1} . It is this small storm and the response it produced which provides the data for most of this dissertation.

Calm conditions prevailed again on April 9 and 10 but a large lead opened through the camp on April 10 at 1200 AST. By 1200 AST on April 11 it had reached a width of over 1 km. Due to the precarious position of the camp it was struck rapidly after the lead opened and was abandoned by 1800 on April 11.

Owing to the calm conditions that prevailed during most of the experiment, the turbulent boundary layer flow measurement program was not very successful. Currents were below the threshold of the fixed

current meters most of the time and the one storm which did occur was too short to set up a steady state Ekman layer. However, the profiling current meter has a zero threshold velocity and produced a continuous record of the changes in the mean properties of the mixed layer which occurred throughout the experimental period. Thus, although the intended boundary layer study was not successful, it was possible to observe what was effectively the impulse response of the upper ocean starting from a quiescent initial condition. Because the bulk of the useful data was gathered with the profiling device and because the instrument is new and unique, the next section is devoted to a brief discussion of it.

2.3 The Arctic Profiling System

The Arctic Profiling System (APS) is a wire lowered device used for making continuous vertical profiles of density and velocity. A discussion of it is given by Morison (1978) and very complete descriptions of the instrument, the techniques used to process data from it, and current meter calibration procedures are given in Appendix A. Figure 2.3 is a photograph of the APS lying on its side. The three main sub-components are illustrated. They are: the current meter triplet, the inertial reference unit (IRU) and the CTD (conductivity, temperature, depth). The APS is lowered in the orientation shown in Figure 2.1.

The current meter triplet is used to measure the complete velocity vector relative to the descending APS. A closeup of it is shown in Figure 2.4. The current sensors are 3.5 cm diameter, partially

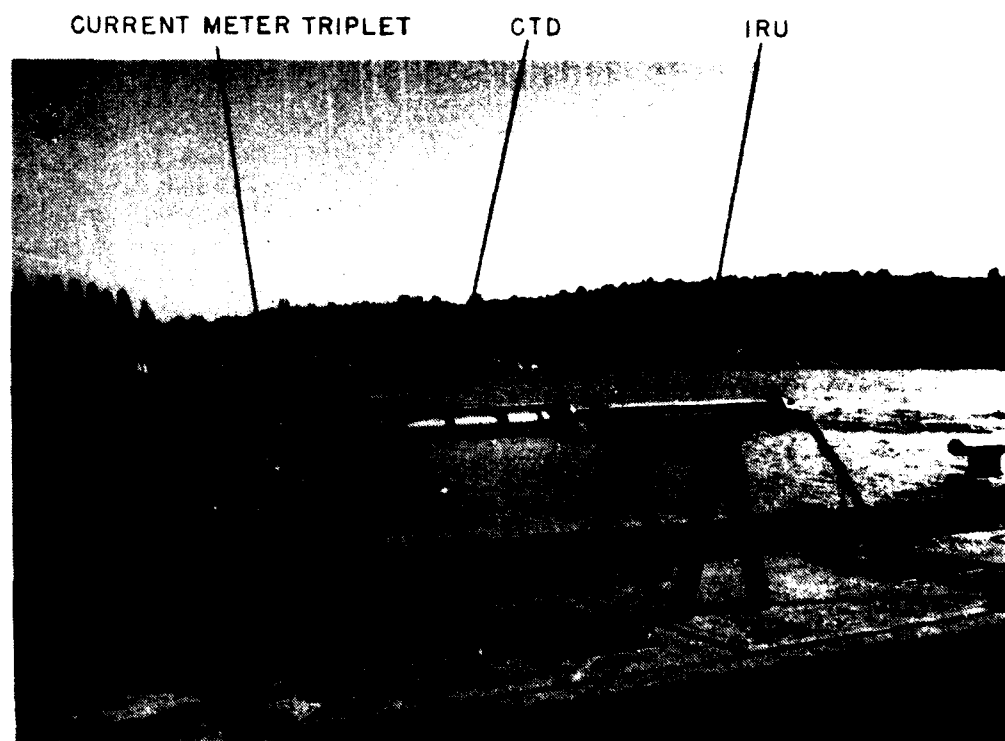


Figure 2.3. The APS. The three main components are shown: Current meter triplet, CTD, and the inertial reference unit (IRU).

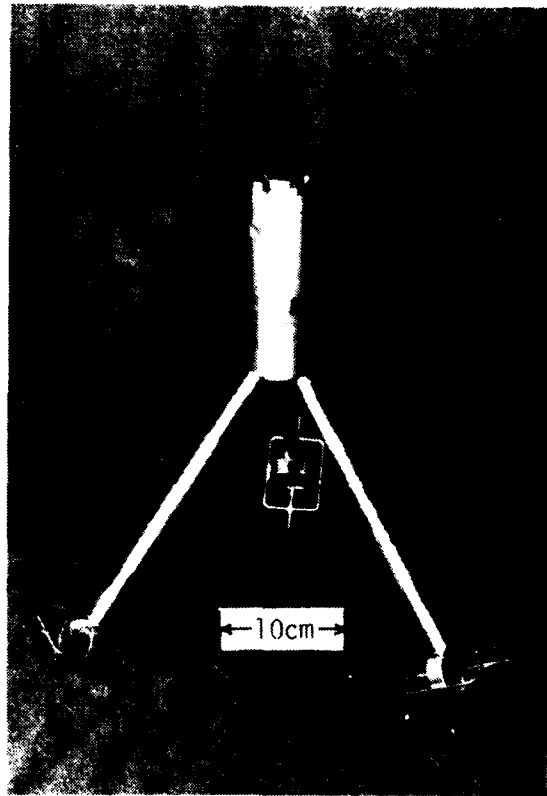


Figure 2.4. The APS current meter triplet.

ducted, four bladed rotors of the type discussed by Smith (1974a), McPhee and Smith (1976), and Smith (1978). To a close approximation the rotation rates of the propellers are proportional to the component of water velocity parallel to their axes. The rotor heads are mounted with the axis pointed toward the triplet centerline at an angle of 54.7 degrees to the vertical, placing them on orthogonal axes with each current meter sensing an equal component of the lowering velocity. The rotation rate of each propeller is determined by means of a Hall effect device in the end of the current meter support tube which detects the field produced by magnets in the tips of two of the rotor's four blades. The output of the Hall effect device is amplified to form a square wave, the frequency of which is proportional to rotation rate. Three such frequency signals comprise the output from the current meter triplet.

The IRU is used to measure the orientation of the APS. A photograph of the disassembled unit is shown in Figure 2.5. It consists of three basic sensor packages: a Humphrey D604-0115-1 north seeking gyro compass, a group of three Sundstrand QA 1100 accelerometers in a triaxial mount, and a Hamilton standard three axis rate gyro. The compass produces a voltage signal proportional to the azimuthal orientation of the APS. The accelerometers sense both tilt and acceleration but their low frequency output is dominated by tilt while their high frequency output is dominated by acceleration. Therefore, an averaging scheme is used to filter out the acceleration component and yield a tilt measurement. The rate gyros measure the rate of change of angular position. Conceivably their output could be integrated to yield angular position but the units used were not of sufficient accuracy to

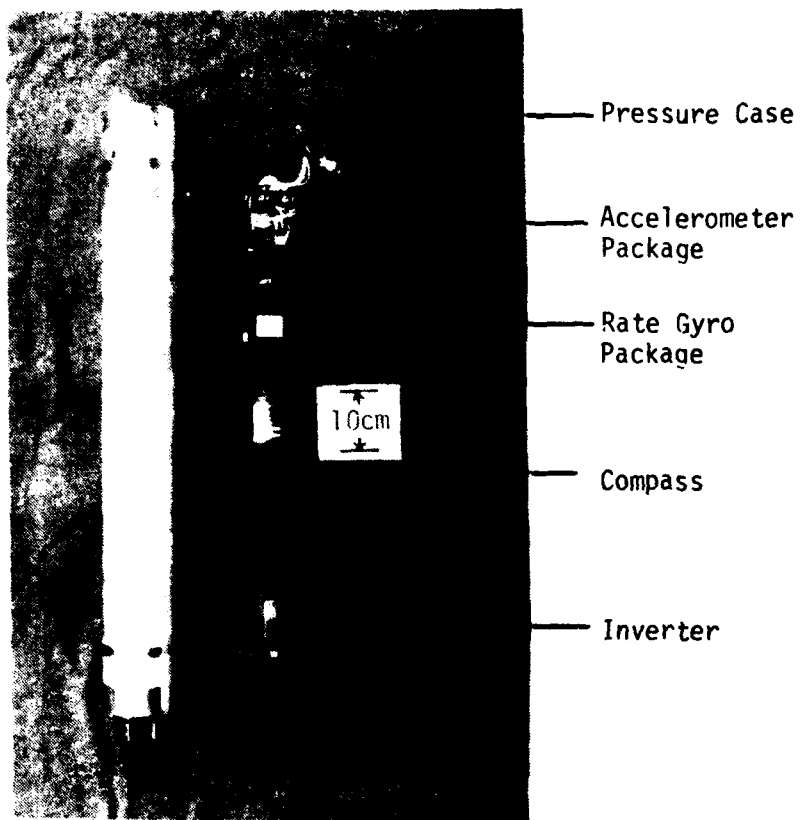


Figure 2.5. The sensors in the IRU. The accelerometer package, rate gyros, and north-seeking gyrocompass are shown.

permit this integration to be carried very far in time. However, the units were used to determine the maximum frequency at which the accelerometers could be used as tiltmeters.

The CTD is used for measuring water conductivity, temperature, and depth. It is a standard Guildine 8101A. Specifications for it and the other individual sensors in the APS can be found in Appendix A.

The APS is held together by an arrangement of stainless steel bars. It is 2 m long and weighs 61 kgm in air and 48 kgm in water. It was lowered through a 36 cm hole in the ice on a 32 conductor electro-mechanical cable by an automatic winch. The winch was hydraulically powered, had a drum diameter of 1.5 m, and was constructed of plywood to facilitate air transport and field assembly. The hydraulic system incorporated a device to regulate the rotation rate of the drum and this, along with the large drum diameter, assured a constant lowering speed. The automatic control of the winch was effected with a two way solenoid valve actuated by a two pole microswitch. Balls of foam rubber at each end of the cable tripped the microswitch in such a way that the cable was reeled in and out between the two balls. During the experiment the APS was cycled automatically between 0 m and 85 m continuously, each up/down cycle requiring 5 minutes.

Data from all sensors in the APS were recorded using a Data General NOVA 1200 minicomputer system. The system included two Ampex digital tape drives for recording data, a Preston 12 channel, 14 bit A/D converter for processing the analog signals from the CTD and IRU sensors, and current meter interface circuitry. The outputs of all the other sensors except the anemometers were also recorded with this system.

The processing of APS data since the Mixed Layer Experiment has proceeded along the following lines. First current meter output frequencies are averaged over a 1.2 sec window every .4 sec. This averaging period has been chosen in order to eliminate the effects of a natural 1.2 sec oscillation of the instrument. From the frequencies, initial estimates, v_1 , v_2 , v_3 , of the current meter velocities are calculated using calibration coefficients determined from zero angle of attack. Here

$$v_j = af_j + b \quad j = 1, 2, 3 \quad (2.3.1)$$

$$a = 3.601 \text{ cm/pulse}$$

$$b = 1.809 \text{ cm/sec}$$

$$f_j = \text{frequency in pulses/sec}$$

If the angular response of the current meters were a perfect cosine, no further corrections would be required. However, the actual calibrations, as determined by tests described in Appendix A, deviate slightly from a perfect cosine response and the initial estimates must be modified by the current meter angle of attack corrections G_1 , G_2 , and G_3 . These corrections are given by a polynomial in v_2/v_1 and v_3/v_1 . The polynomial has been derived as a curve fit to the result of iterative determinations of angle of attack corrections over a large range of velocities (see Appendix A for details). Once G_1 , G_2 and G_3 are determined, the true current meter velocities, $U_j = G_j v_j$, are calculated.

These velocities are in the triplet coordinate system and must be transformed to a reference frame carried with the profiling device and oriented north, east, and down. They are first transferred to a coordinate system carried with the APS and oriented forward, to the

right and down the vertical axis using a transformation dependent only on triplet geometry. The rotation into the body carried, earth centered coordinate system is achieved using tilt information from the accelerometers and the bearing measured by the compass. The actual transformations used are given in Appendix A.

Horizontal velocities calculated in the manner described above for data from a single downcast are shown in Figure 2.6 along with σ_t as calculated from the CTD data. The data for the plot was gathered at 1333 on April 8 during the one storm which occurred during the AMLE. The profile is made over 2.5 minutes real time. The noise on the σ_t plot is generated by the gyrocompass. Comparison with σ_t profiles made when the compass was off indicate that although the noise looks objectionable, if averaged over 1 m, the noisy profiles yield comparable results to the noise-free profiles.

The plus signs indicate 10 minute averages of velocity as measured by the mast mounted current meters at 1333. In general the mast mounted meters were below threshold but during the storm they produced usable data. Information from the fixed meters has been analyzed in much the same way as that from the APS current meter. In particular the same method of determining frequency is used; however averages are taken over 10 current meter records (4.096 sec) instead of three records.

Agreement between the fixed current meter data and the APS velocity data is good, the fixed meter values generally falling within the ± 0.5 cm/sec scatter in the profile data. While the APS profile reproduces the average velocity shown by the fixed meters, it also

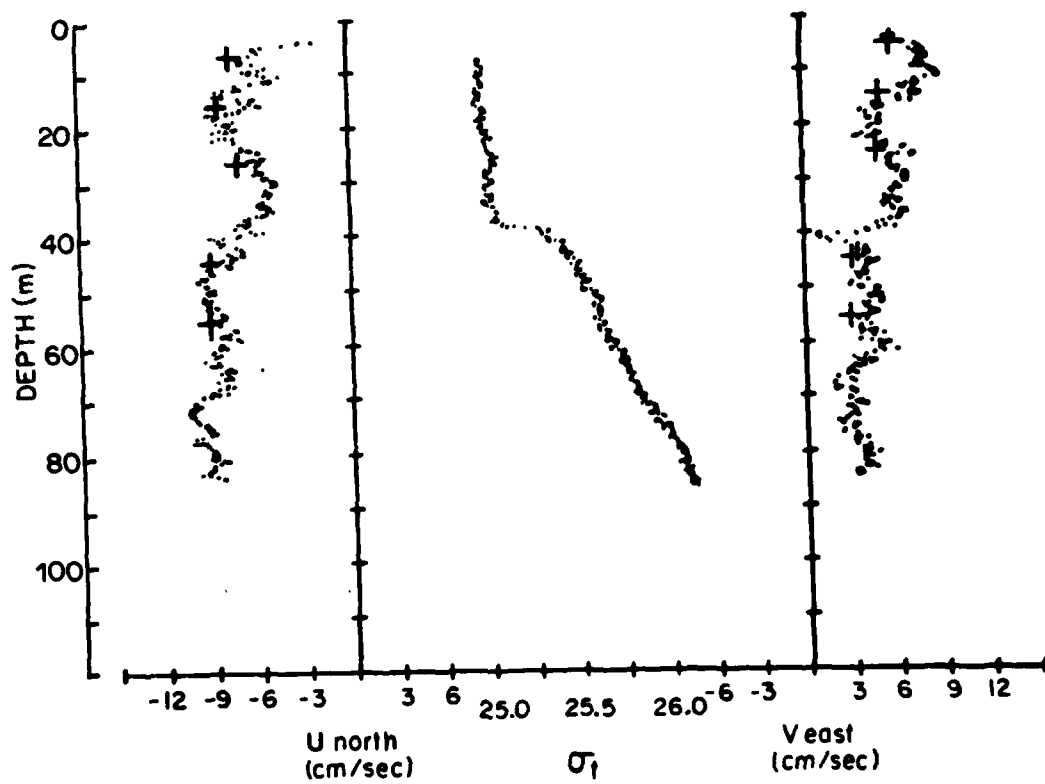


Figure 2.6. Data from a single downcast of the APS made at 1333 AST, April 8, 1976. The + signs are velocity values from fixed current meters.

provides much more detail in the vertical structure of the velocity field. For example, the jet-like feature in v at the pycnocline is completely unresolved by the fixed meters.

Profiles were originally made every five minutes but it is useful to smooth the data by combining several profiles. This is done by averaging all the points from successive profiles in 1 m depth bands. Results from this averaging scheme also yield estimates for the noise in the data and permit further comparison of velocity data from the APS and fixed meters. Figure 2.7 shows velocity and σ_t profiles obtained from one data tape; it includes average results from 12 profiles made over one hour. Also shown as plus signs are the fixed meter velocities averaged over the whole tape. The profiles of Figure 2.6 were from the tape averaged to obtain Figure 2.7 and much of the structure observed in the single profile of Figure 2.6, such as the jet in v at 40 m, is preserved in the average profile. This consistency indicates such features are real rather than manifestations of noise in the measurements.

The consistency of the results can also be illustrated with statistical data from the tape averages. The variances of the velocity measurements in the 1 m bands over 1 hour are computed when the profile averages are made. The resulting standard deviations for u and for v in each of the bands range from a minimum of 0.3 cm/sec (σ_v at 29.5 m) to a maximum of 1.7 cm/sec (σ_u at 3.5 m) but exceed 1 cm/sec in only 11 instances out of 160 (u and v in 80 bands). The standard deviation corresponding to the average variance over all depths is ± 0.654 cm/sec and values for individual 1 m bands typically are close to this. The variations include not only instrumental errors but also natural

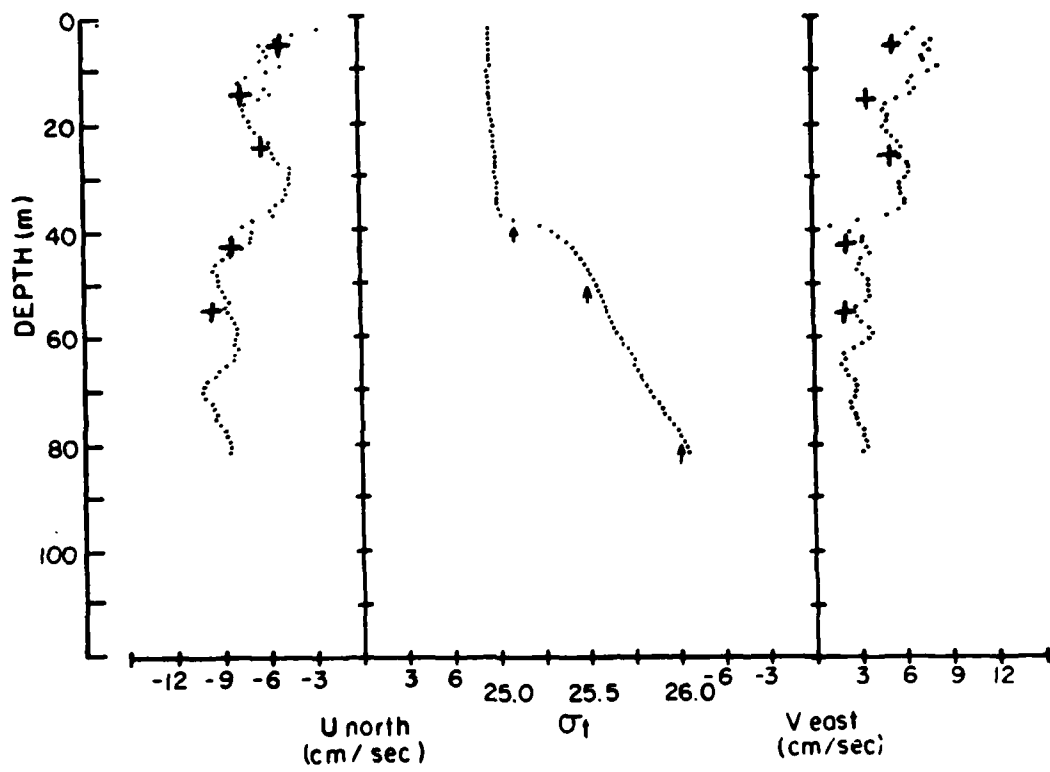


Figure 2.7. Data averaged from 12 APS profiles taken between 1322 and 1422 AST, April 8, 1976. The + signs are average velocity values from fixed current meters.

variations in the flow velocity. However, during the period being discussed here, the currents were fairly constant and the individual profiles are burdened with $\pm 0.5 \text{ cm sec}^{-1}$ noise so the standard deviations over one hour probably are due in large to the noise in individual profiles.

The average velocities from the fixed current meter data agree quite well with the profile averages. However, the tape average does reveal a slight systematic difference between the two data sets. This is especially apparent in the v values from the fixed meters which are slightly less than those from the profiles. The difference is due almost entirely to a difference in current direction; the directions (expressed as bearings) from the fixed meters average 8 degrees greater than those from the profile data at the same levels. In contrast, the average difference in speed (speed from fixed meters minus speed from the APS) is only -0.1 cm/sec .

Comparisons of fixed current meter data and velocity profiles from the four other tapes made while the APS gyrocompass was operating and the fixed meters were above threshold yield results comparable to those of Figure 2.7. The difference in direction between the fixed meters and the profiles for all five tapes is $+10 \text{ degrees} \pm 7 \text{ degrees}$ and the difference in speed is $+0.55 \pm .5 \text{ cm/sec}$. The consistency of the average difference in direction indicates it is due to an error in the north reference alignment of the masts or the compass in the APS or a combination of the two. Such a difference is not important for the purpose to which the profile data is being used in this dissertation but if the mast data and profiles were being used together to study

boundary layer phenomena the mast data (or profile data) would have to be rotated 10 degrees to bring the two data sets into alignment.

The slight difference in speed measurements between the two systems indicate that on the average, speeds from the fixed meters are a little higher than those from the APS. This is probably due to the APS moving slightly in the direction of the flow as it is lowered. Such lateral motion is to be expected from an instrument lowered on a cable, but the APS is heavy enough so that, given the weak current conditions in the Arctic, the horizontal motion is very small (.55 cm/sec). For this reason the measured velocities will be considered relative to the ice even though in principle they are relative to the APS.

Overall the performance of the APS as a velocity sensor is quite good. The variance of an individual profile such as that of Figure 2.6 indicates the resolution of the instrument is 0.5 cm/sec. Using comparisons of the profile data with the fixed meter data as an indication of the accuracy of the APS is pessimistic because errors in the values from the fixed masts are also involved and these may be considerable in view of the near threshold (for a whole triplet) velocity conditions. Nevertheless, such a comparison indicates the accuracy in speed is better than 1 cm/sec and, neglecting the systematic difference in direction, the current direction is accurate to better than 7 degrees.

Of course, one big advantage of the profile measurements is that they resolve the complete velocity structure down to fairly small scales. In this case, lowering at 60 cm/sec and using a 1.2 sec

averaging time, features with depth scales on the order of 2 m can be resolved.

The tape averaged density data of Figure 2.7 is much smoother than that of Figure 2.6. Averaging over a 1 m depth interval and 12 profiles eliminates most of the noise induced by the gyrocompass. The standard deviation for the 1 m bands ranges from $.003 \sigma_t$ units to $.074 \sigma_t$ units; the maximum occurring at the pycnocline where vertical motion of the water has the greatest effect on local σ_t . The standard deviation corresponding to the average variances in all the 1 m bands is $0.055 \sigma_t$ units. This is comparable to the $\pm .034$ scatter in the individual σ_t profile of Figure 2.6 and thus is probably largely due to the noise on the individual profiles comprising the average. Typically a total of 49 values go into each tape average so the uncertainty in each average σ_t value is $\pm .008 \sigma_t$ units.

The tape average profiles of Figure 2.8 were computed from data gathered on April 15 when conditions were quite calm. The figure illustrates another advantage of the APS over other current measurement techniques. That is the ability to resolve very low velocities. The components are less than 4 cm sec^{-1} at all depths and the total speed at 24 m is less than 1 cm sec^{-1} . It is possible to resolve such low flows with the APS because the lowering speed keeps all the current meters turning at well above threshold. As a result, the threshold for horizontal velocity is zero. This feature is particularly advantageous in the Arctic where currents are often quite weak.

Because the gyrocompass introduced noise in the CTD signals it was shut off during the recording of every other data tape. It has

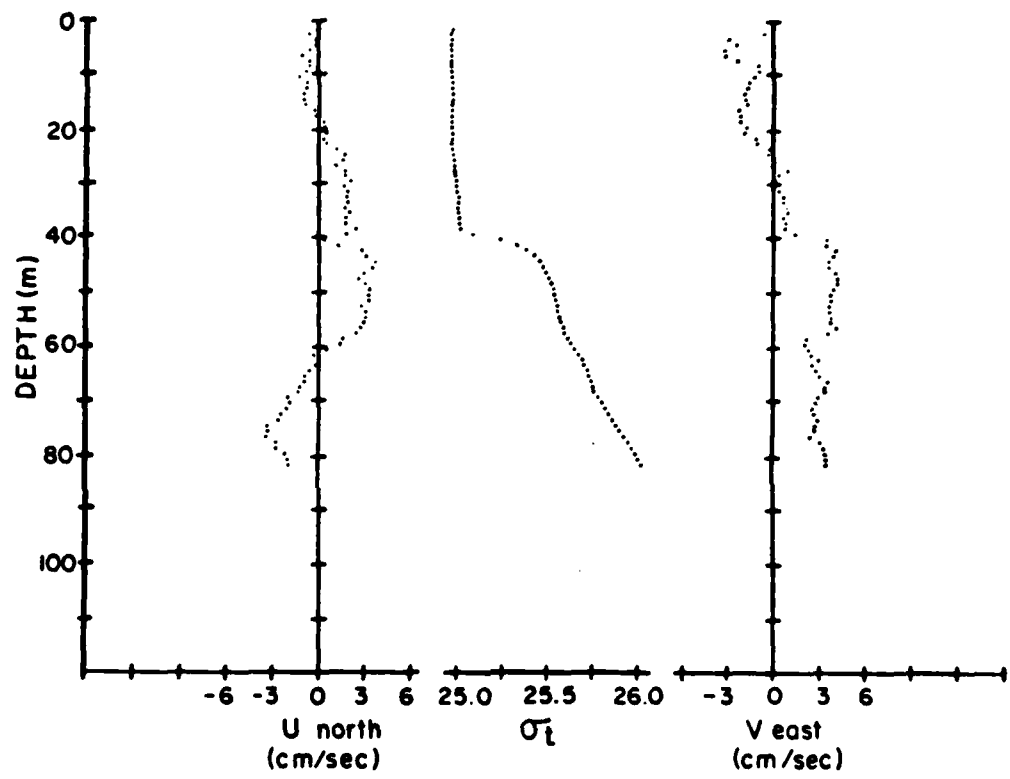


Figure 2.8. Average of 16 APS profiles made between 0712 and 0812 AST, April 5, 1976. The velocity profiles demonstrate the ability of the APS to measure weak currents.

been possible to reconstruct most of the profiles for which no compass data exists. In comparing outputs of the gyrocompass produced during profiles several hours apart, it has been found that the bearing versus depth is remarkably consistent profile to profile. The large torque balanced cable and large diameter winch drum produced almost the same rotation pattern on every lowering. For this reason it has been possible to interpolate the bearings for a profile without a compass signal from adjacent profiles with a compass signal. First 1 m averages of the velocities are calculated assuming a compass bearing of zero. Then, the bearing for each 1 m block is interpolated from bearing profiles from previous and subsequent tapes and the velocities are rotated with the interpolated bearing to obtain individual profiles.

For the one hour period following that represented in Figure 2.7, the profiling system was used with the gyrocompass shut off. The resulting nine profiles were processed in the above manner and averaged to obtain the plot of Figure 2.9 (only 9 profiles were completed during the hour due to technical problems).

These velocity component profiles compare well with the corresponding one hour average velocity components from the fixed current meters (indicated by +), and comparisons of current meter mast data with velocity profiles from three other tape averages made with interpolated bearings show results comparable to those displayed by Figure 2.9. The differences between the mast and profile data for all four tapes are also similar to those in tapes made with the gyrocompass turned on. As with the complete APS data, the profiles with interpolated bearing indicate directions averaging 10 degrees less than those

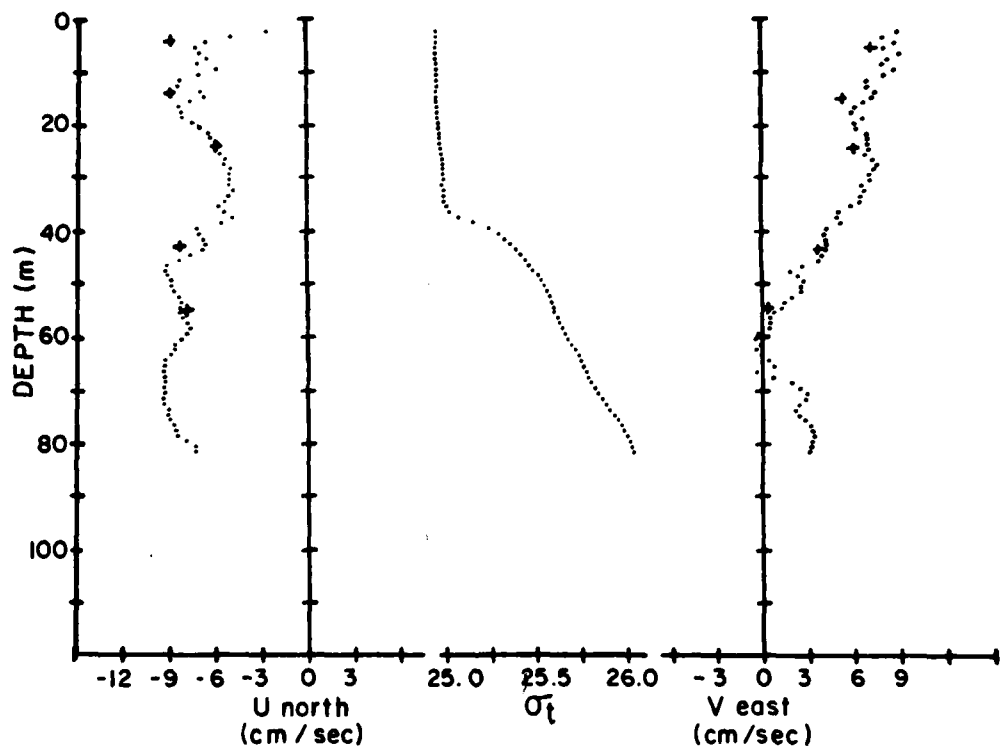


Figure 2.9. Data from a single downcast of the APS made at 1504 AST, April 8. Velocities were computed using interpolated bearings. The + indicates data from fixed current meters.

from the fixed meters with a variation in the differences of ± 7 degrees. The speed difference is slightly greater for the interpolated bearing profiles, averaging $+0.93$ cm/sec with a variation of ± 0.8 cm/sec. In general it appears interpolation of bearing works well. The validity of the bearing interpolation scheme is also indicated by the smooth transition from one velocity profile to another which it produces.

The σ_t profile of Figure 2.7 is comparable to that of Figure 2.9, supporting the opinion that the noise caused by the gyrocompass can be successfully filtered out by profile averaging.

Tape averages of the type shown in Figures 2.7 and 2.9 were made for every data tape. These profiles are useful in that they are averages over 18 (only the APS triplet being recorded) or 12 (APS and mast triplets being recorded) profiles which were gathered consecutively as a group. Basically, every bit of data is used. However, during data collection, there were often gaps between tapes when no recording was done. Also no attempt was made to start each data tape at a particular time. As a result the tape averages are not evenly spaced in time. In order to present the data at even time increments and in order to resolve rapid changes in the velocity field, another averaging scheme was used. The method basically involves averaging individual profiles in 15 minutes blocks and it will be described further in the next chapter. Examples of both types of averaging schemes will be used in subsequent chapters.

Chapter 3

EXPERIMENTAL RESULTS

3.1 General Features

Figures 2.7, 2.8, and 2.9 show σ_t profiles representative of those encountered during the AMLE. A mixed layer of weak stratification extends to about 40 m. At the base of the mixed layer is a sharp top pycnocline. The density increases there by more than 0.5 σ_t units between 40 m and 50 m. Below 50 m the stratification is representative of upper part of the main pycnocline.

Profiles of salinity and temperature corresponding to the σ_t plot of Figure 2.7 are given in Figure 3.1. Because the temperatures are uniformly low, the stratification is controlled by salinity and the profiles of salinity and σ_t are quite similar in shape. The water in the upper 80 m is of the type termed Arctic (surface) Water by Coachman (1963). It is water of relatively low salinity (31°/oo to 33°/oo) with temperature at or near the freezing point. The slight temperature maximum at 40 m may be due to an interfingering of Bering Sea water with the surface water. AIDJEX temperature profiles from the same period indicate the major temperature maximum representing the core of the Bering Sea water is just below 80 m.

The chronology of events as far as the oceanographic observations during the AMLE is concerned is represented in Figure 3.2. It shows isopycnal depths plotted versus time along with the 2 m wind data. The isopycnal depths were calculated from tape average density profiles.

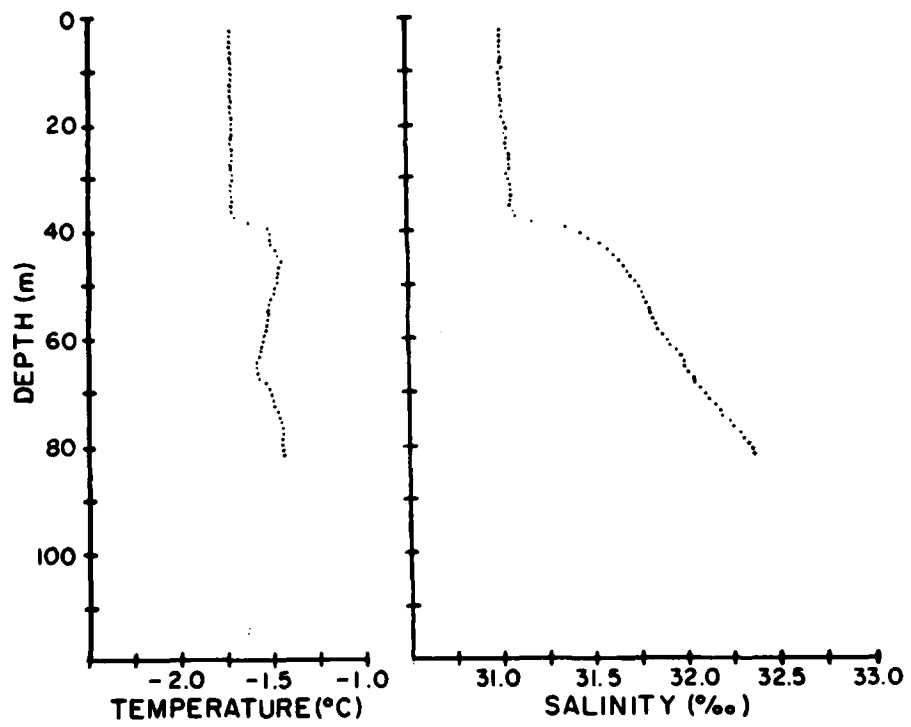


Figure 3.1. Average of 12 temperature and salinity plots made between 1322 and 1422 AST, April 8, 1976.

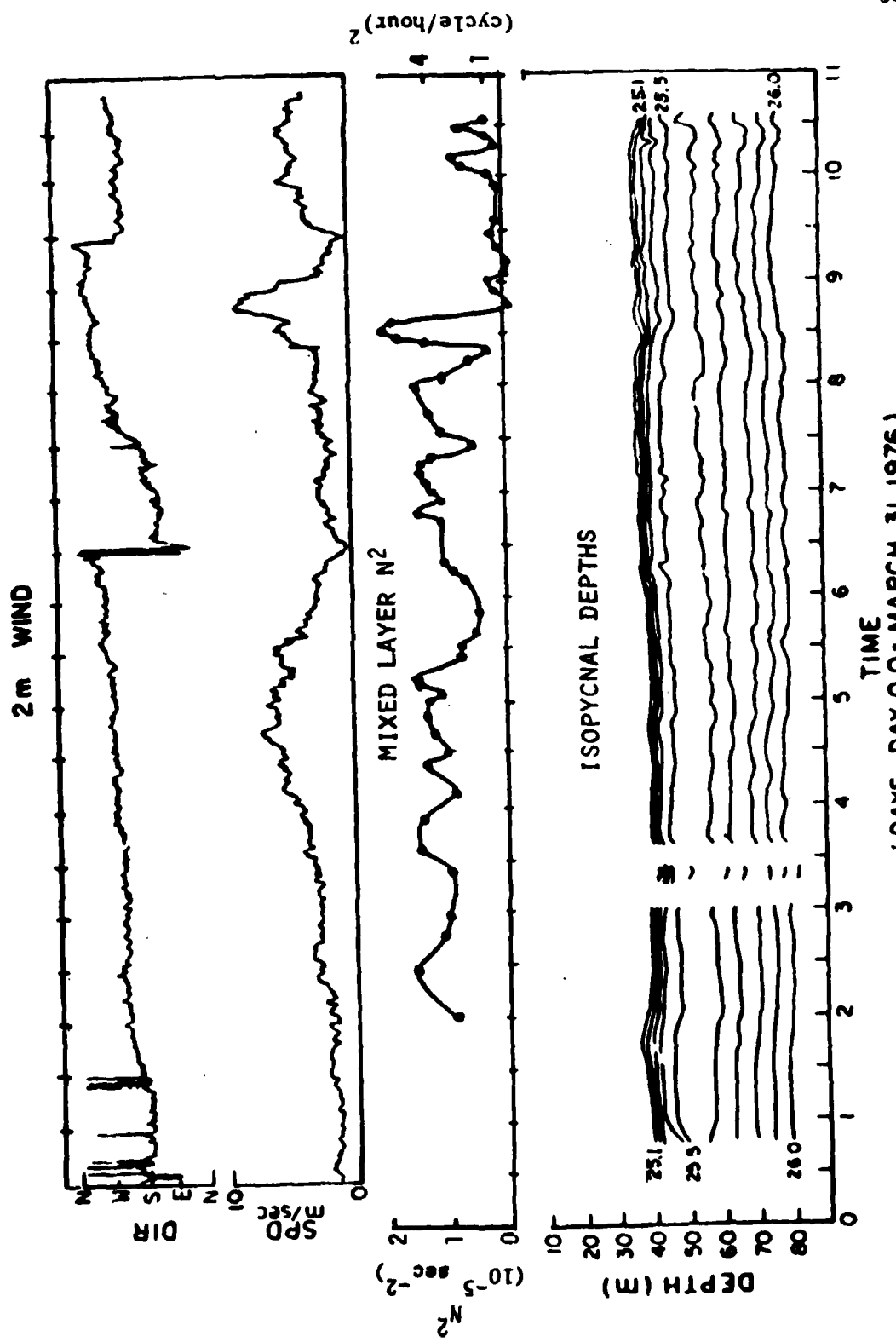


Figure 3.2. Isopycnal depths versus time and 2 m winds for the AMLE. Also shown is the Brunt Väisälä frequency between 10 m and 30 m.

Comparison of plots made over short periods with individual density profiles indicated the changes in density structure were well resolved with tape averaged data. The locations of the isopycnals corresponding to σ_t equals 25.1, 25.5, and 26.0 are shown by arrows, \uparrow , in Figure 2.7. The top of the region of maximum stratification or mixed layer depth is represented best by the 25.1 isopycnal. The 25.5 isopycnal is at the knee of the upper pycnocline and the 26.0 isopycnal is at the bottom of the APS profiles.

Conditions were quite calm throughout most of the AMLE and for the most part the isopycnals shown in Figure 3.2 are at constant depth. The first significant activity occurred on April 3. As Figure 3.2 shows, the isopycnals increased in depth about 4 m during the morning of April 3 but returned to their original positions by mid-afternoon. This event is not well resolved by the data set but is real and appears to be due to the presence of a front or eddy. Possible explanations for it will be discussed in Section 3.2.

After April 3 the isopycnal depths are quite constant for four days. The wind record also shows low wind speeds except on April 4 when the wind speed reached about 6 m sec^{-1} . The wind direction at that time was to the west-southwest. As will be explained in Section 3.3 a northward wind component is necessary to break the ice pack free from the Alaska-Canada coast; so, the winds of April 4, though significant, did not produce ice motion. As shown by the isopycnal plots oceanographic conditions remained calm.

On April 8 the isopycnals were displaced again, showing a general pattern of depression, rebound, and oscillation. The typical

magnitude of the depression below 38 m was 2 m. This event coincided with a small storm. The wind record indicates wind speeds began to rise about 1030 and reached a maximum of about 9 m sec^{-1} at 1941. The wind direction was to the west-northwest. Apparently the wind speed was high enough and had a large enough northward component to break the pack ice away from the coast because significant ice motion occurred. The storm ended by April 9 and the wind and isopycnal plots indicate relatively calm conditions prevailed until about mid-day on April 10.

On April 10 a lead broke through the camp. The response shown in the isopycnal plots consists of rapid changes in the isopycnal depths in the pycnocline. Associated with these changes was an increase in mixed layer salinity.

The events of April 3, April 8, and April 10 will be discussed at length but first the general features of the velocity records must be examined. Figures 3.3a through 3.3l show velocity profiles relative to the ice as measured with the APS throughout the experiment. Before these were constructed, individual profiles were averaged in 15 minute blocks over 1 m depth intervals. The results were stored on tape. In order to make Figures 3.3 a-l, the 15 minute average profiles were smoothed over 3 m depth and a one hour time interval. If there were less than two 15 minute average profiles in a one hour block, no profile was constructed. In the figures the average relative velocity is centered over the time for which the profile applies and the average is plotted above the profiles as \bar{U} and \bar{V} . Also shown are velocities (indicated by X) averaged over the depth range 10 m to 20 m and over one raw data tape.

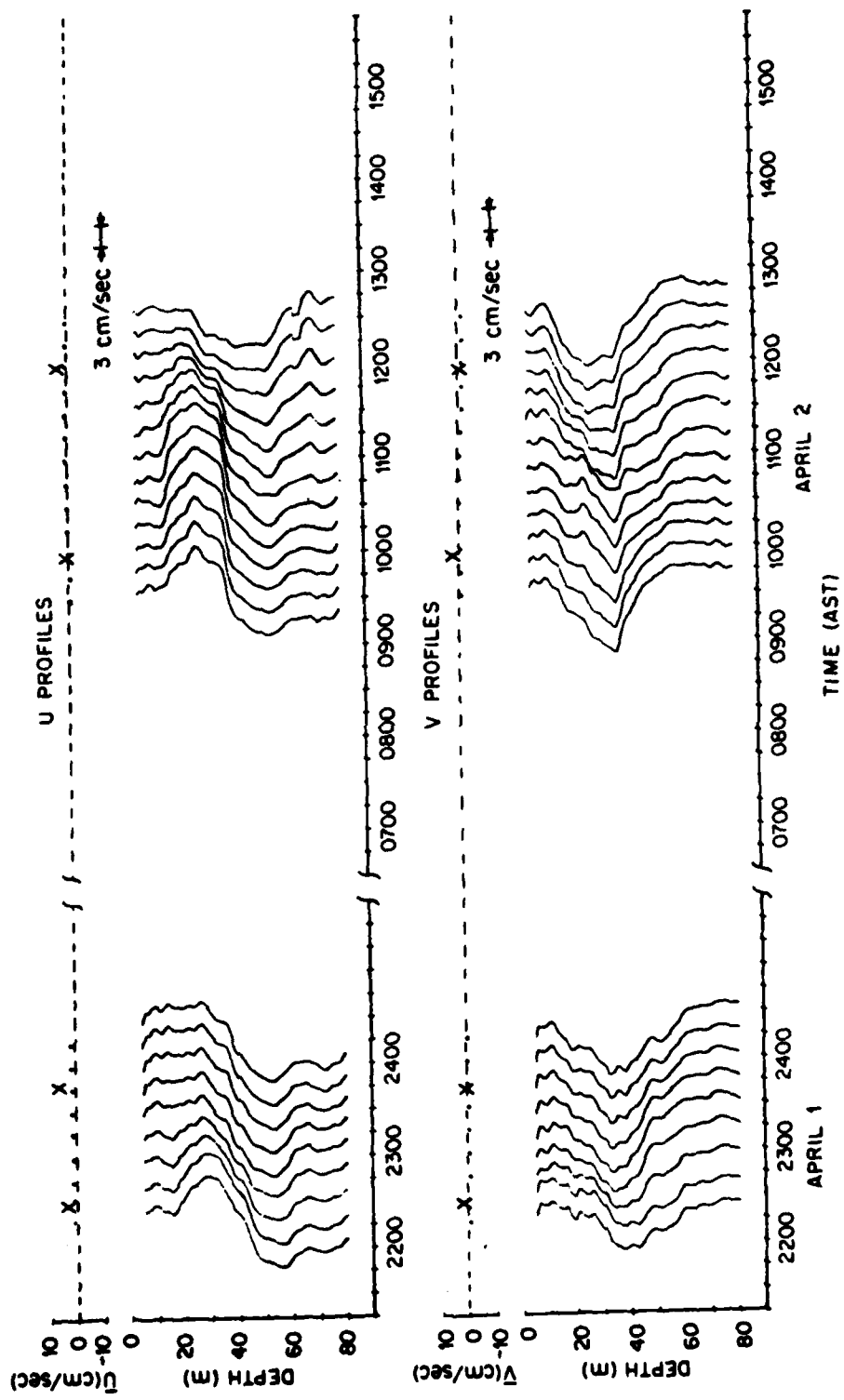


Figure 3.3. Fifteen minute averages of horizontal velocity relative to the pack ice as measured with the APS. The average velocity over depth is centered at the applicable time tic and the average velocity is plotted at the top of the graph.

3.3a. 2130 AST, April 2 to 1515 AST, April 2.

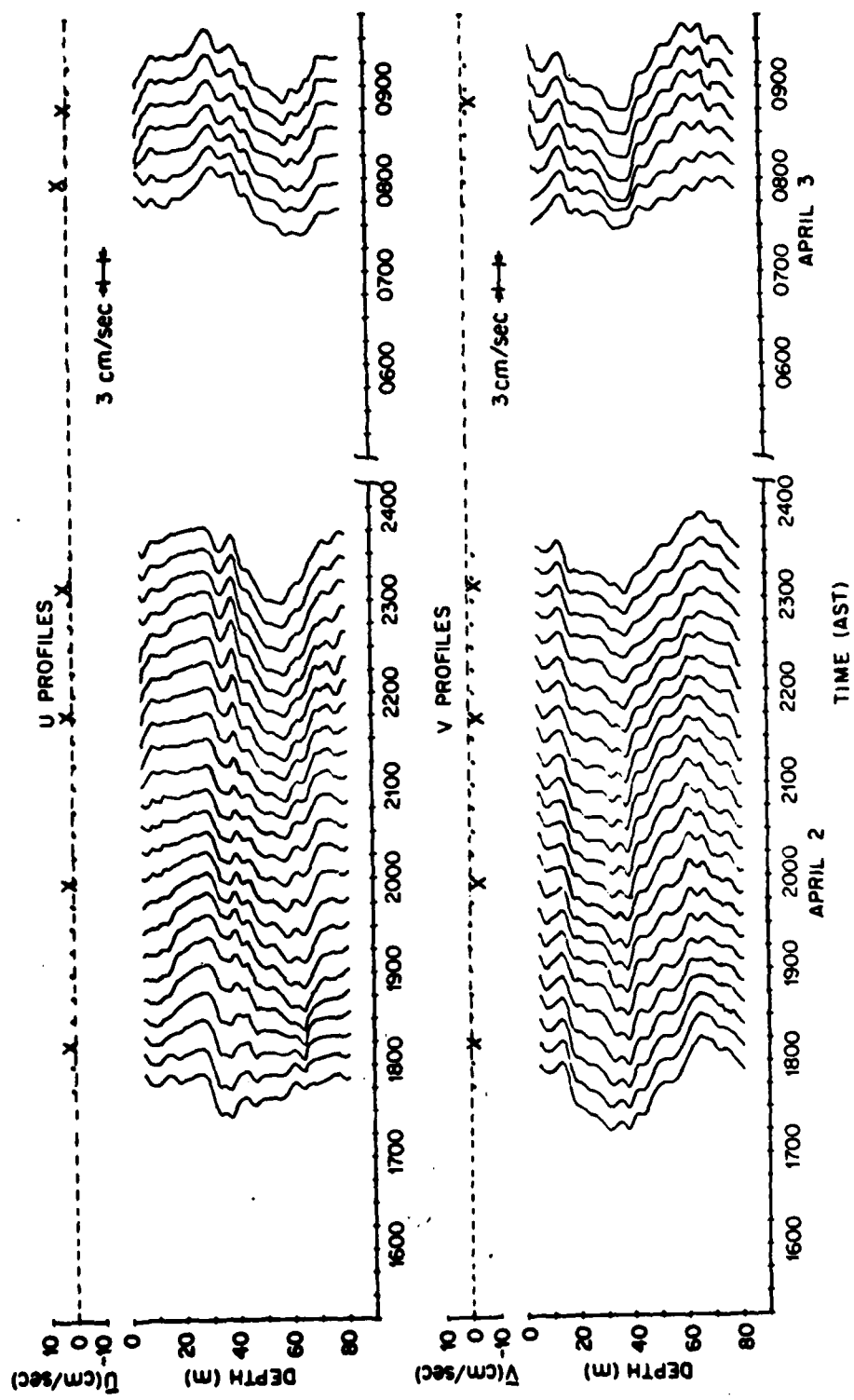


Figure 3.3. Continued

3.3b. 1530 AST, April 2 to 0915 AST, April 3.

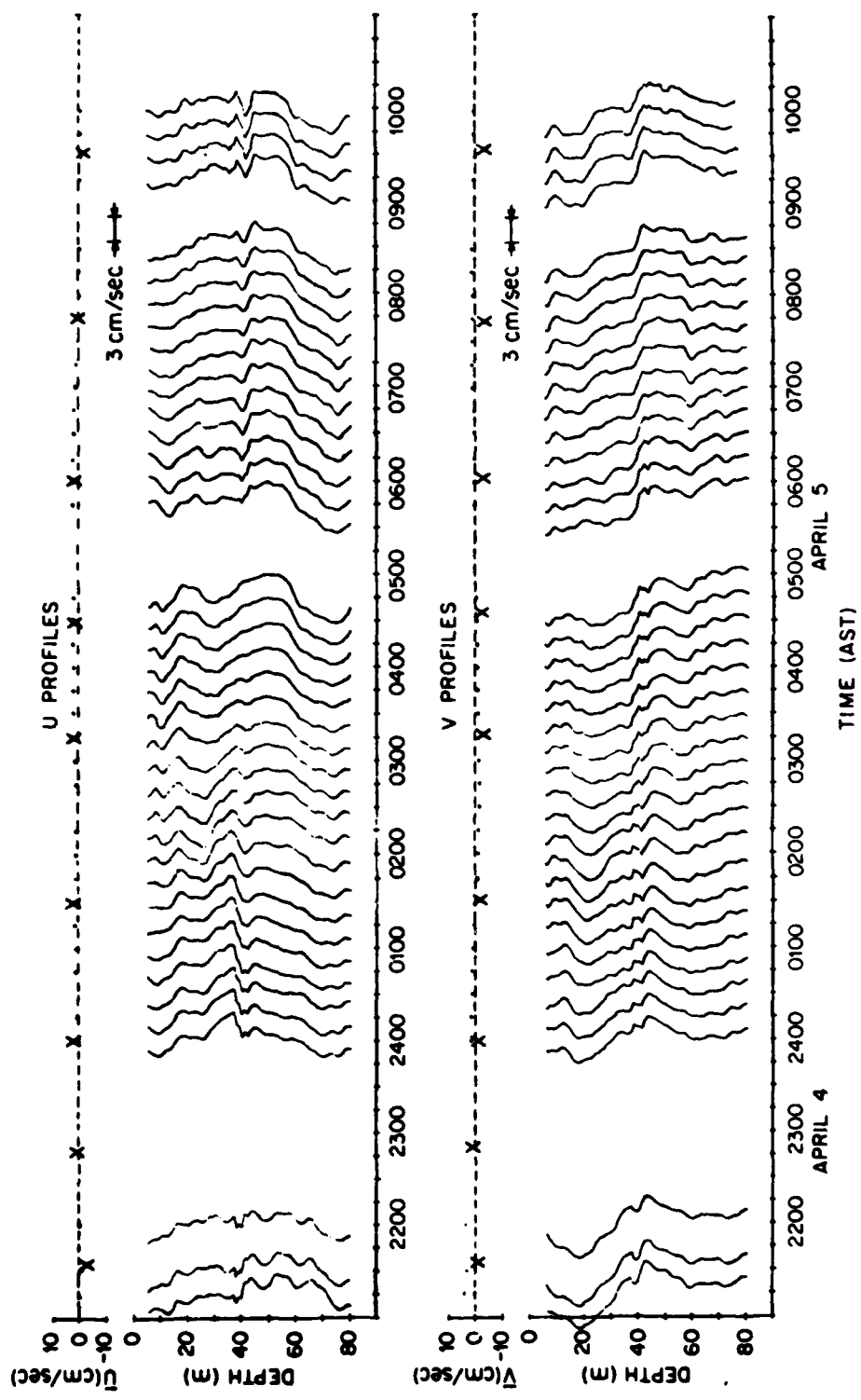


Figure 3.3. Continued

3.3c. 2115 AST, April 4 to 1030 AST, April 5.

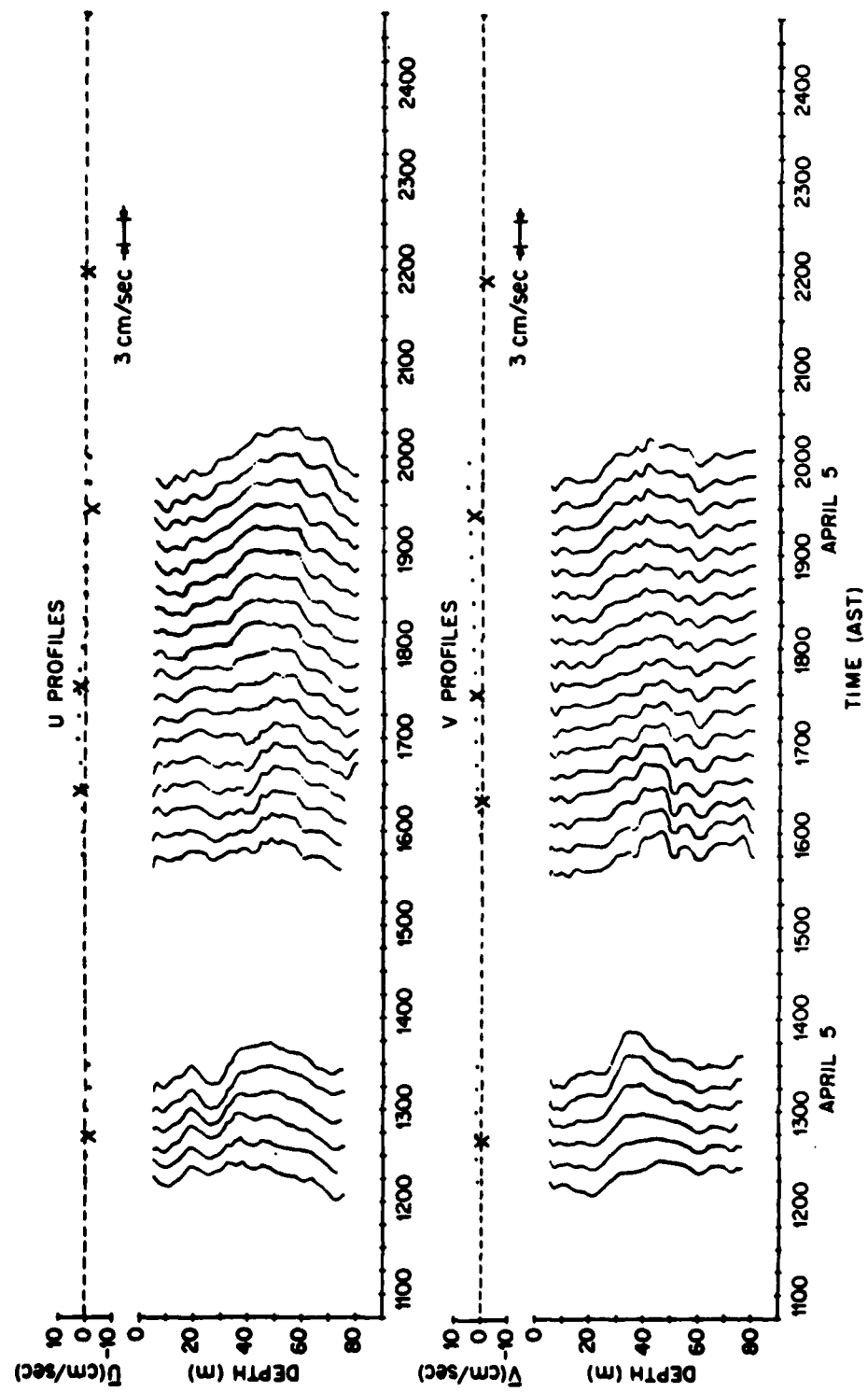


Figure 3.3. Continued

3.3d. 1100 AST, April 5 to 2400 AST, April 5.

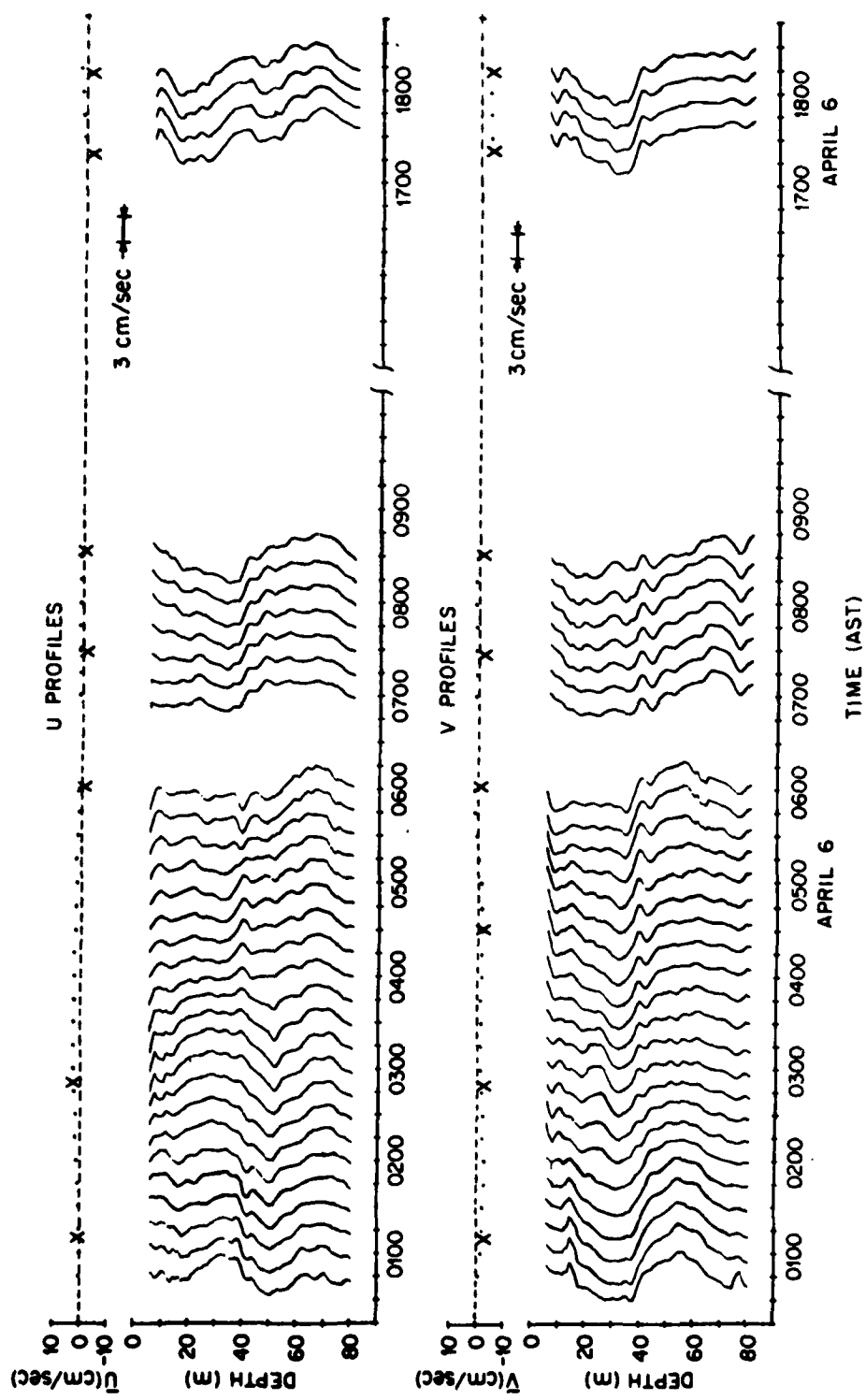


Figure 3.3. Continued

3.3e. 0030 AST, April 6 to 1815 AST, April 6.

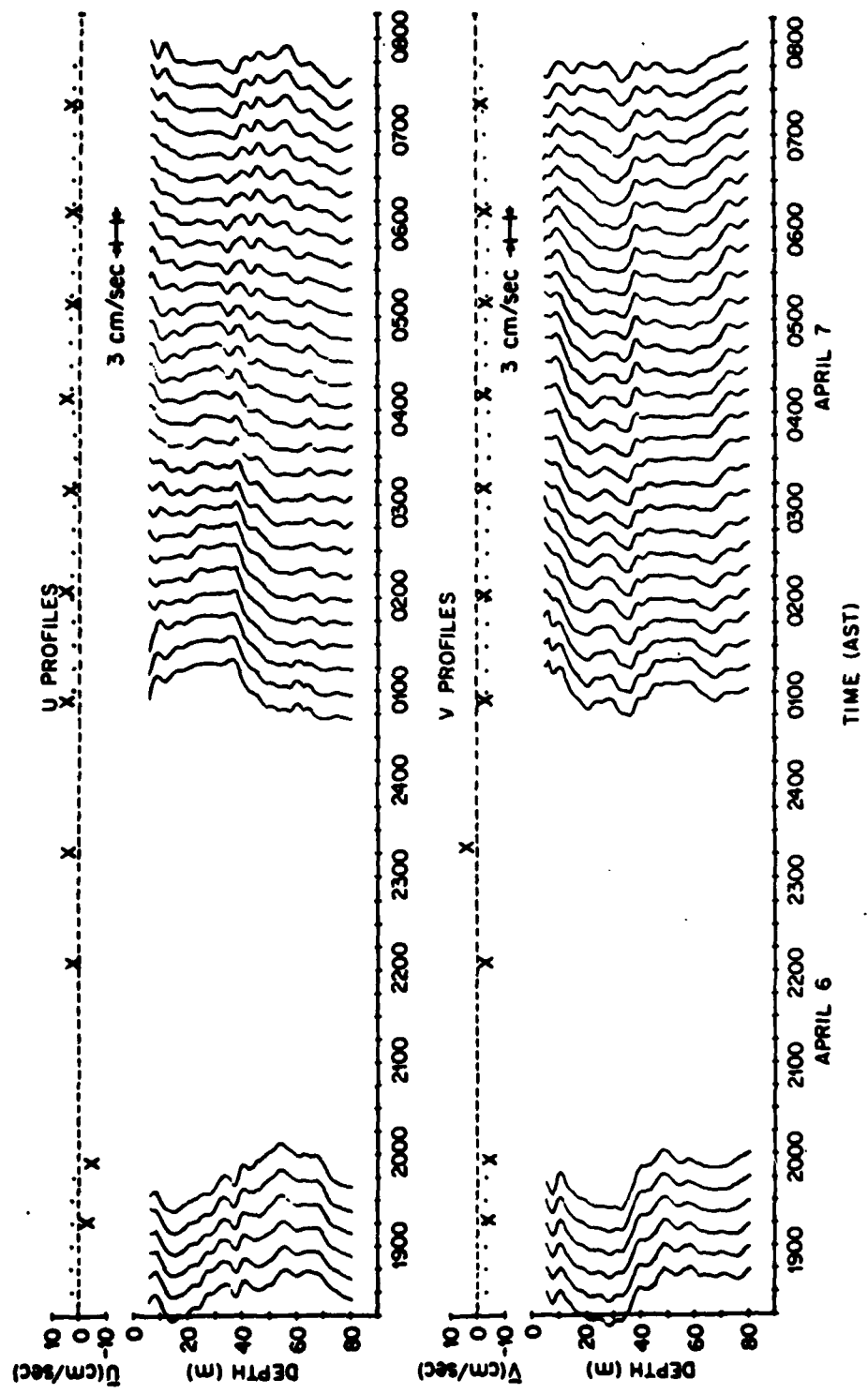


Figure 3.3. Continued

3.3f. 1830 AST, April 6 to 0745 AST, April 7.

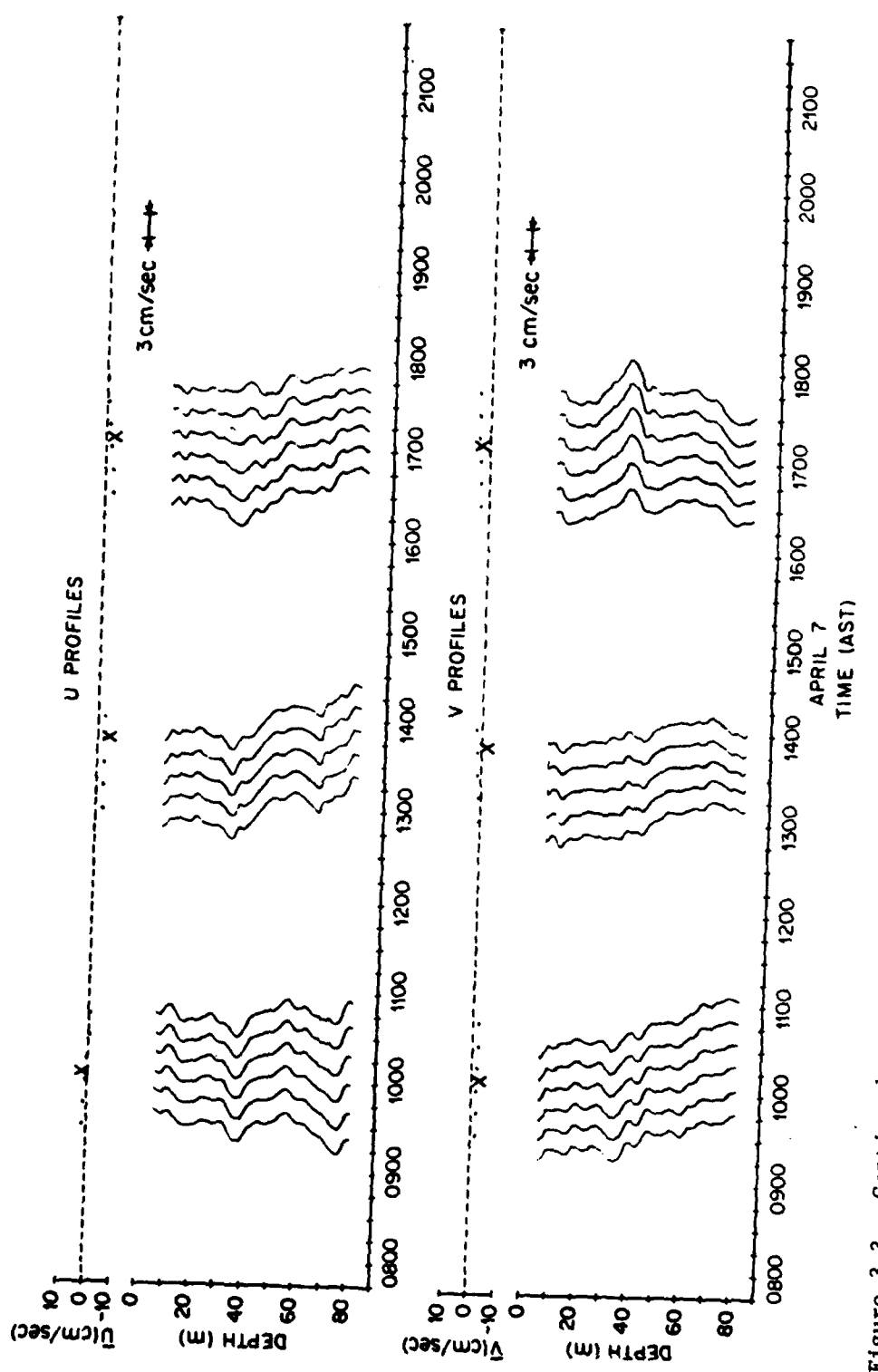


Figure 3.3. Continued

3.3g. 0800 AST, April 7 to 2115 AST, April 7.

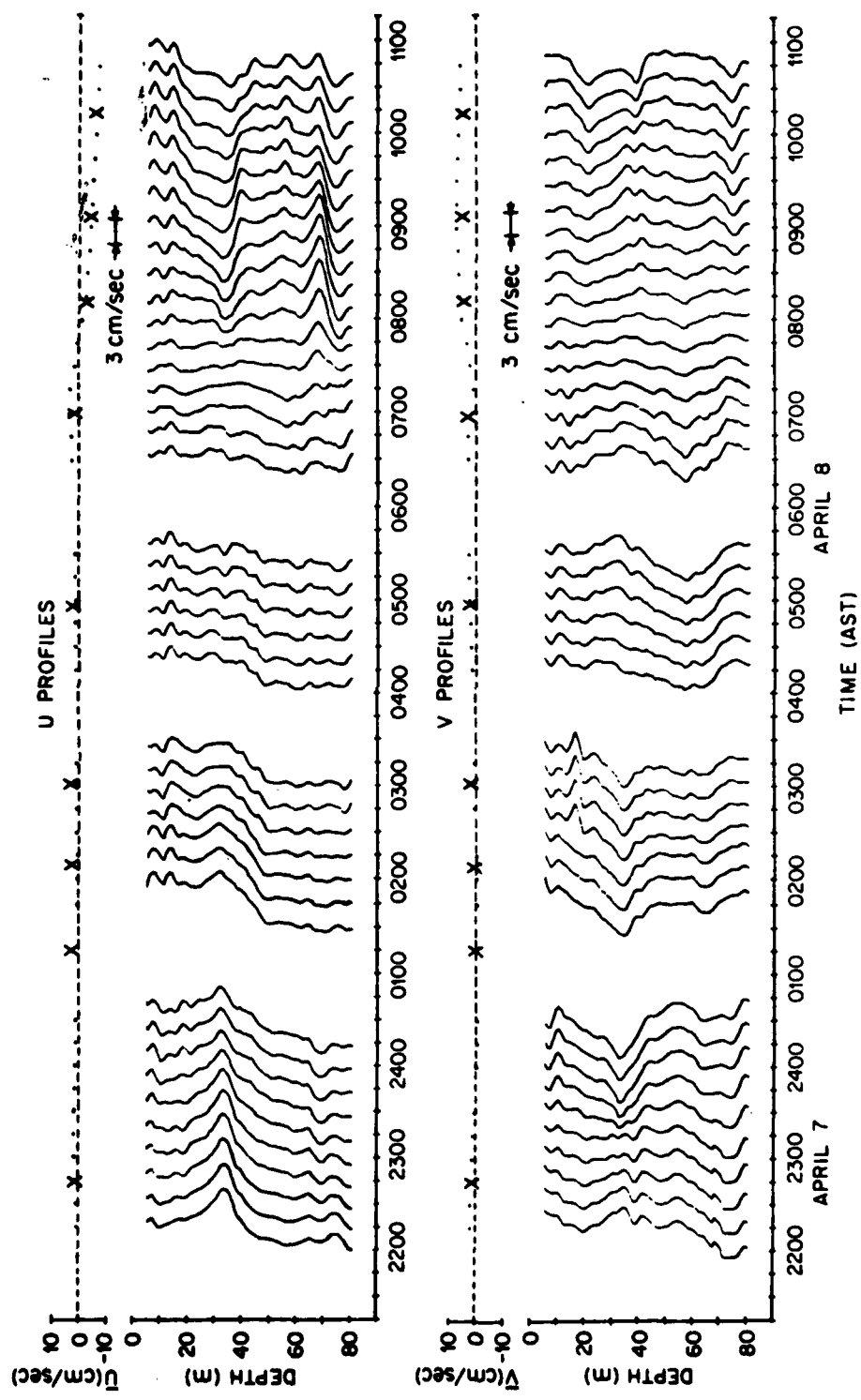


Figure 3.3. Continued

3.3h. 2130 AST, April 8 to 1045 AST, April 8.

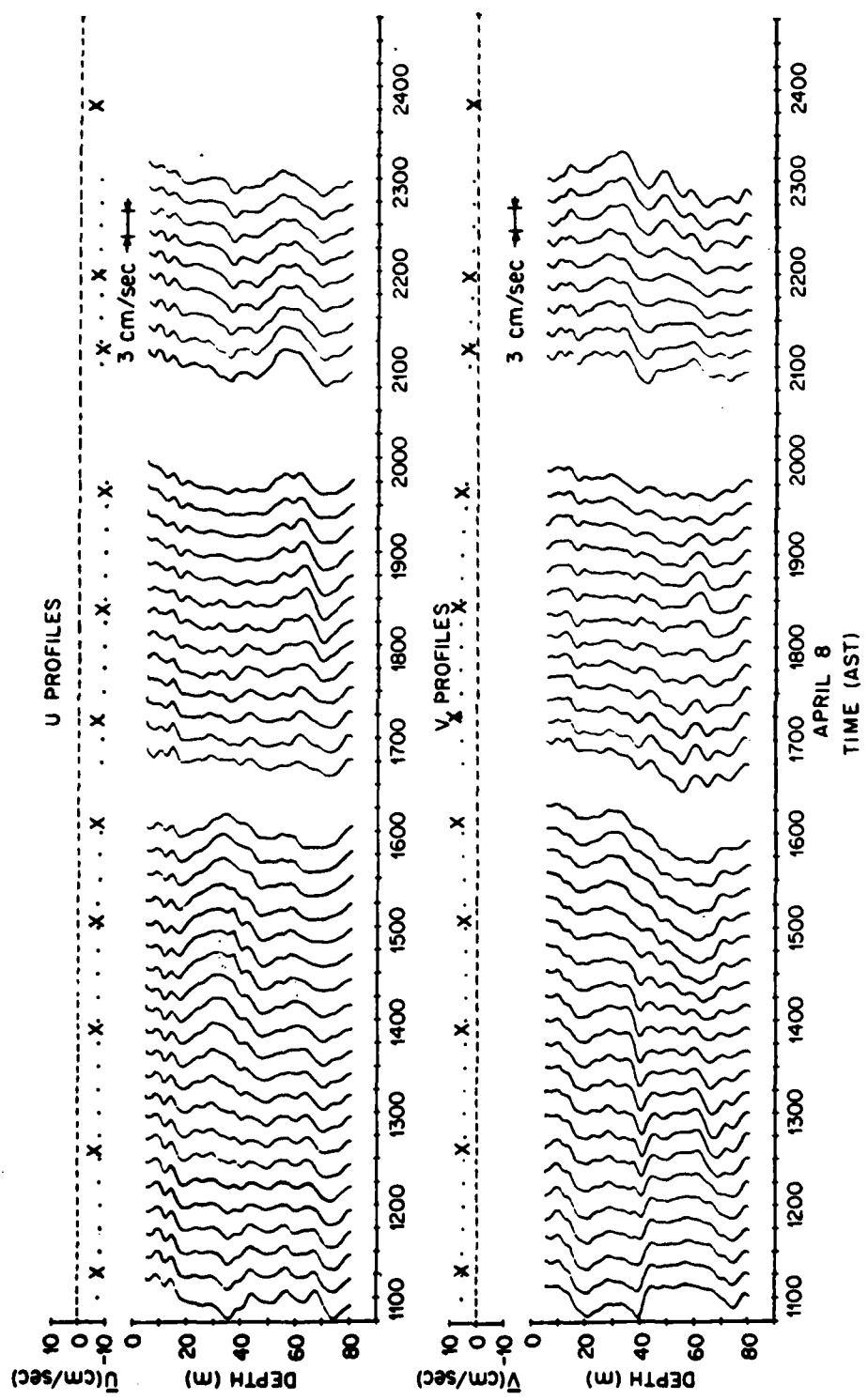


Figure 3.3. Continued

3.3i. 1100 AST, April 8 to 2400 AST, April 8.

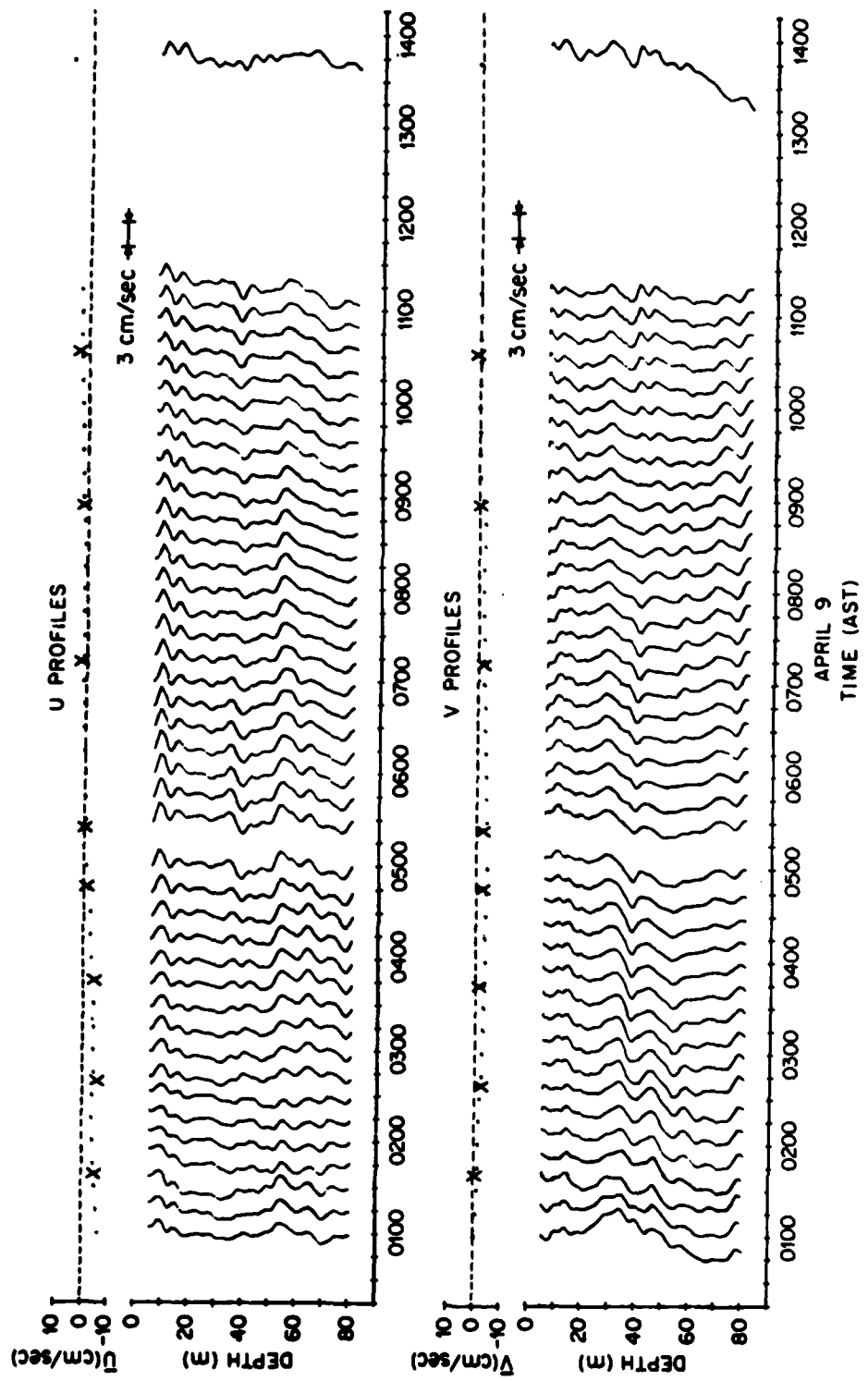


Figure 3.3. Continued

3.3j. 0030 AST, April 9 to 1345 AST, April 9.

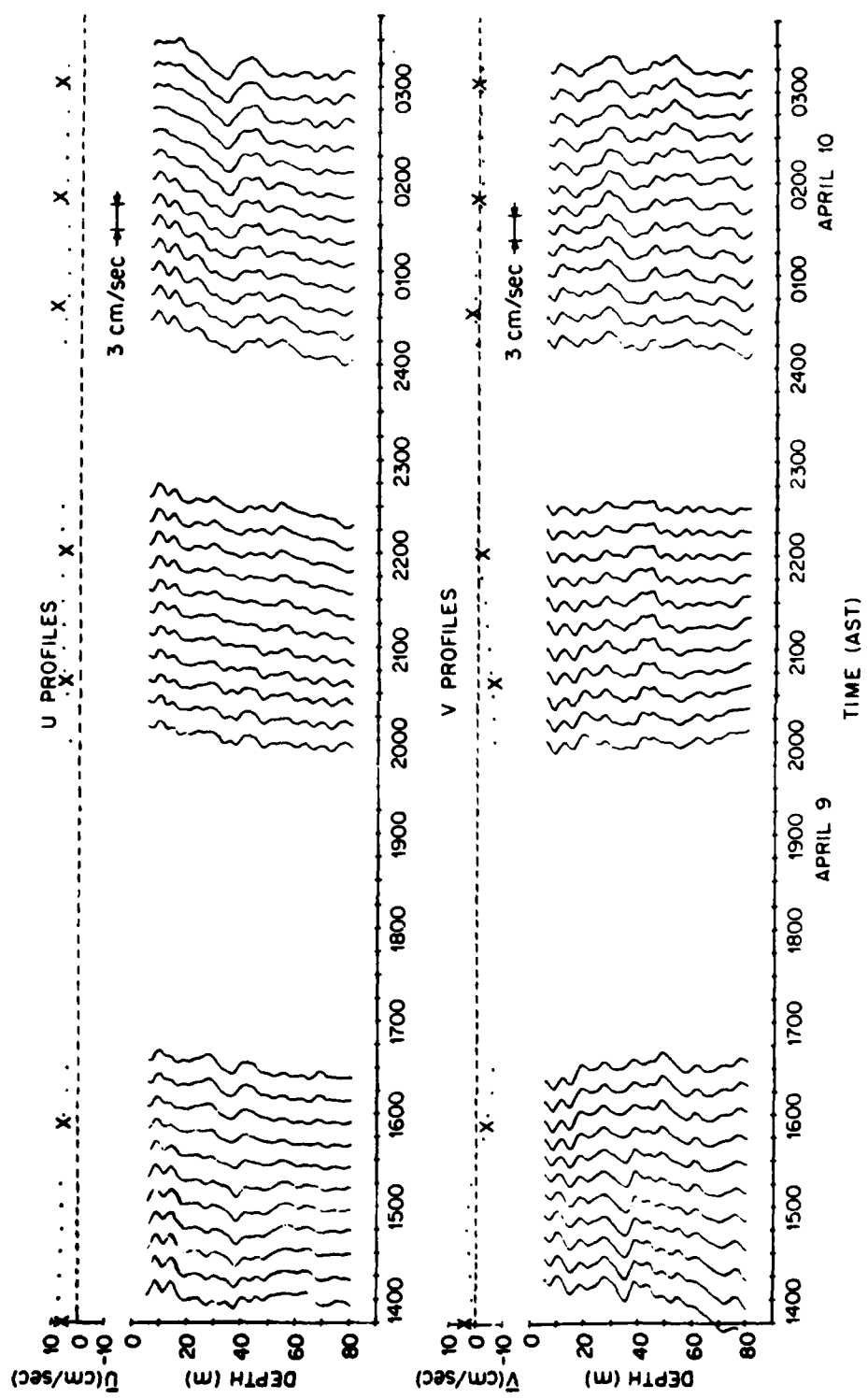


Figure 3.3. Continued

3.3k. 1400 AST, April 9 to 0315 AST, April 10.

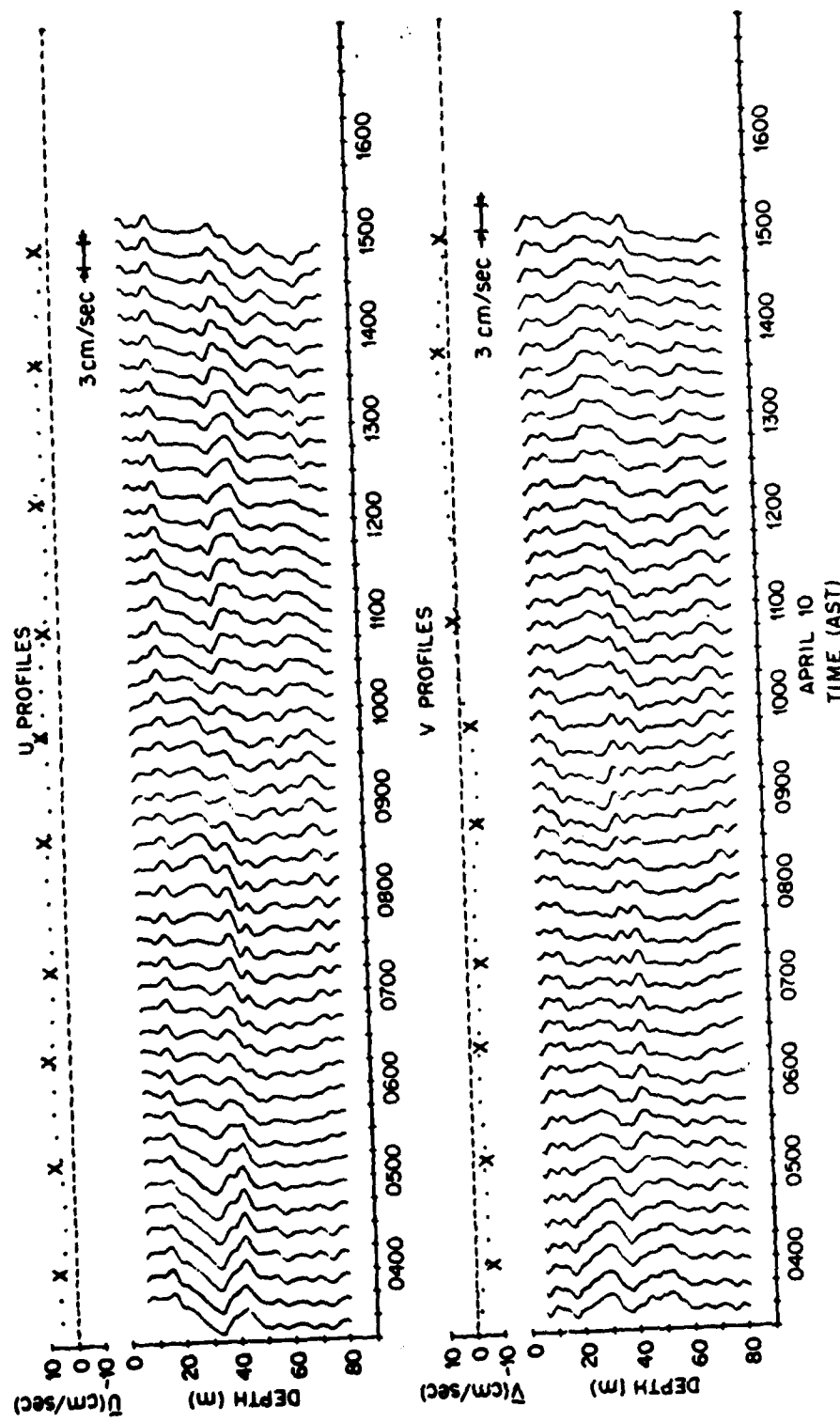


Figure 3.3. Continued

3.30. 0330 AST, April 10 to 1645 AST, April 10.

These graphs are unique in the sense that the profiles are made at such high frequency. Perkins and VanLeer (1976) describe an ingenious self-contained profiling system but their device moves slowly through the water column (10 cm/sec) and is not capable of the high frequency sampling shown here. Sanford (1975) has developed a dropped velocity profiler, as have Evans and Rossby (1976). These units are capable of profiling over large depth ranges in the open ocean but retrieving and rearming the instruments requires a couple of hours and the cycle times are correspondingly long.

Examination of the profiles reveals several interesting features. The first that stand out are the large shears at the 40 m depth shown on April 1, 2, 3, and 8. The largest occur on April 2 in the u component when the change in velocity across the pycnocline is about 7.5 cm sec^{-1} . This is during a period when the average relative water velocity, and by inference the ice velocity, is negligible. Thus the shears observed April 1, 2, and 3 are not due to surface forces but, as will be discussed in Section 3.2, are associated with a small baroclinic feature to the northeast of camp. On April 8 strong shears were in evidence during the initial stages of ice motion and are part of a general storm response.

The observed shears are not strong enough to cause turbulence at the pycnocline. If turbulence is to be generated by shear production, the local gradient Richardson number,

$$R_i = \frac{g \frac{d\rho}{dz}}{\left[\frac{dv}{dz} \right]^2} = \frac{N^2}{\left[\frac{dv}{dz} \right]^2}$$

must be less than .25. For the v velocity component of April 2 at 1100 in Figure 3.3a the velocity shear is the maximum observed at the pycnocline and the corresponding R_i is 3.184, more than an order of magnitude greater than the critical R_i . The velocity change is about 6 cm/sec over a depth of 3.5 m. In order to achieve the critical R_i the change in velocity over this depth span would have to be 21 cm sec^{-1} . Thus, it is unlikely shear at the pycnocline produced turbulence at this or any other time during the AMLE. Although strong shear layers at the pycnocline may develop as a result of the inertial motion in the mixed layer, Miles McPhee and Roger Colony (personal communication) have pointed out that inertial motions in the Arctic during the winter are suppressed by internal ice stress.

Another striking feature of the velocity profiles is the common appearance of jet-like features throughout the water column. The magnitude of the "jets" ranges up to 3 cm sec^{-1} . They most commonly occur at or slightly above the top pycnocline near 40 m, persist from one to eight hours, and range in vertical extent from 5 m to 20 m. An example of a "jet" at the pycnocline is shown in Figure 3.3b. The u velocity profiles from 2100 to 2400 on April 2 display a "jet" of about $+2 \text{ cm sec}^{-1}$ magnitude superimposed on a shear at the pycnocline. Similar features appear almost every day. The largest "jets" in the pycnocline are shown in the u and v profiles for April 7 in Figures 3.3g and 3.3h. These are of about 3 cm sec^{-1} amplitude and persist for a few hours at a time. Those in v change direction between 1700 and 2400. Figure 3.3e shows "jets" in the top pycnocline on April 6. The "jet" in u builds up to 1 or 2 cm sec^{-1} from 0400 to 0500 then reverses direction

from positive to negative between 0500 and 0600.

Occasionally "jets" appear below the seasonal pycnocline. Examples appear on April 5, 6, 7, 8, 9, and 10 and large scale (>20 m) shears are quite common in the main pycnocline. Such motions are to be expected in the highly stratified regions of the water column. Free internal waves at all wavelengths cause motions with periods between the inertial period (12.55 hours) and the local Brunt Väisälä period (3 to 15 minutes in the seasonal pycnocline and below). Longer period motions can be attributed to forced internal waves and the mean flow field as observed from a moving platform.

"Jets" and shears also occur in the mixed layer. "Jets" appear in the v profiles of April 2 and 3 in Figures 3.3b and 3.3c, the u profiles at 1300 on April 5 shown in Figure 3.3d, and the u profiles between 0900 and 1500 on April 10 shown in Figure 3.3l. Appreciable shear is evident in the mixed layer on April 2 at 1100 in Figure 3.3a, on April 6 and April 7 in Figure 3.3f and on April 10 at 0200 to 0500 in Figures 3.3k and 3.3l. These shears are as large as 6 cm sec^{-1} in 10 m but are not persistent, lasting only for 3 to 7 hours.

If the mixed layer were truly unstratified, "jets" and shears there would be quite difficult to explain. In such a case one would expect most motions to be barotropic. In fact, slight stratification builds up in the mixed layer during calm periods and allows baroclinic motions to exist. The occurrence of a storm breaks down the stratification and the flows in the mixed layer become barotropic. Examination of the mixed layer N^2 plot in Figure 3.2 indicates that this is so. Prior to the April 8 storm, N^2 averaged from 10 m to 30 m is of the

same order as that near the bottom of the main pycnocline. This stratification probably builds up as a result of lead convection which, during calm periods, deposits salt enriched water at depths of density equilibrium between the surface and the top pycnocline. As a result, though the mixed layer appears unstratified compared to the top pycnocline, it can in fact sustain baroclinic motions similar to those found in the main pycnocline plus an additional regime of velocity structures associated with lead convection. Such motions account for the "jets" and other disturbances observed prior to April 8. During the April 8 storm the mixed layer N^2 decreases dramatically. As will be shown in Section 3.3 this is probably due to mixing by boundary layer turbulence. After April 8 the degree of baroclinicity in the mixed layer is greatly reduced in spite of increased mean velocities. "Jets" did appear on April 10 in the mixed layer and were persistent even in view of very weak stratification. However April 10 was a time of vigorous lead activity and they may have been forced by pressure gradients set up by lead convection.

3.2 The Event of April 3

As shown in Figure 3.2, density measurements made between 0736 and 0955 on April 3 display a 4 m downward deflection of all the isopycnals relative to measurements made at 2300 April 2 and at 1500 on April 3. Unfortunately the event is not well documented. The data gaps from 2330 April 2 to 0736 April 3 and from 0956 to 1534 on April 3 are due to operational problems and experiments with an acoustic current meter. Figures 3.3b and 3.3c show an even longer gap in the

velocity record from 0955 AST on April 3 to 2115 AST on the following day.

There are a number of possible explanations for the observed disturbance. One is an instrumentation error but this idea has been abandoned because the density data showed no excessive noise or other sign of instrument malfunction and such a depth shift has never been observed before or since using the Guildline CTD. An event such as this might also be due to internal waves but this is unlikely because the response is too slow to be a free gravity wave and there are no oscillations associated with it. The lack of atmospheric forcing negates the possibility that this is a forced internal wave and the response is too rapid for it to be due to a free internal Rossby wave.

The most likely explanation is that the ice moved over a geostrophically maintained, slow moving, depression such as a front or an eddy similar to those described by Newton et al. (1974) and Hunkins (1974). The velocity data indicates this might be the case. Figure 3.3b shows very strong shears across the pycnocline. Typically the u component decreases a total of about 8 cm sec^{-1} and the v component increases about 8 cm sec^{-1} between 40 m and 60 m. Given that the change in density between these depths is $6 \times 10^{-4} \text{ gm cm}^{-3}$, and assuming the feature was changing very slowly, a geostrophic balance would have required the pycnocline to tilt downward to the northeast with a slope of 2.7×10^{-3} . A 1.5 km northeasterly movement of the ice relative to this depression at 5 cm sec^{-1} would produce the observed pycnocline displacement. At 2300 on April 2 the average relative water velocity between 40 m and 60 m was 3.7 cm sec^{-1} , 218° true. This

corresponds well with the required relative ice velocity and, if the average water velocity in the disturbance is assumed equal to the velocity of the disturbance, the data indicates the required northeasterly displacement did occur. Also, at 0845 on April 3 the relative water velocity averaged between 40 m and 60 m is only 0.9 cm sec^{-1} . Thus, the best explanation for observed response might be that the ice moved northeast relative to a depression in the pycnocline during the early morning of April 3 and stopped around noon on April 3. A knowledge of the velocity profile after 1000 on April 3 would be useful in determining whether the ice continued to move across an eddy. If so, opposite shear patterns would occur during the isopycnal depression and rebound. If the ice moved into and back out of an eddy or back and forth across a front the velocity pattern would be the same during the rise and fall of the isopycnals. It is guessed that the ice moved into and back out of a front or eddy because of the low relative velocity at 0845 on April 3.

In order to say much more about the event of April 3 a more complete data set would be required. In fact the most important point which can be drawn is the importance of high frequency sampling in the mixed layer and upper pycnocline. The event described occurred in less than 18 hours and while the standard sampling scheme used during the AMLE would have resolved it very well, the seven hour gaps in density measurements and even longer gap in the velocity measurements make it very difficult to interpret the response. Even when there is no interest in resolving such events, they will cause aliasing problems when low frequency sampling schemes are used. High frequency sampling is

an absolute necessity for studies of the mixed layer and upper pycnocline.

3.3 The Event of April 8

The storm of April 8 propagated across the Beaufort Sea from west to east and imparted a northwesterly motion to the ice. This can be illustrated with plots of ice motion and satellite photographs of the region. Figure 3.4 shows the ice northerly velocity component u , for the three AIDJEX ice camps, Caribou, Blue Fox and Snowbird, from April 7 to April 10. Figure 3.5 shows the easterly component, v . As illustrated in Figure 2.2 the AMLE camp at Big Bear was bracketed by the AIDJEX camps which were equipped with satellite navigation equipment. The position data from them has been analyzed by the AIDJEX staff using a sophisticated Kalman filtering scheme (Thorndike and Cheung, 1977) and the plots of Figures 3.4 and 3.5 result from that analysis.

Both figures also show the velocities at Big Bear, estimated in two ways: by linear interpolation among the three AIDJEX camps, and by assuming the ice velocity is minus the relative water velocity averaged from 10 m to 20 m. An AIDJEX navigation buoy of the type described by Brown and Kerut (1978) was deployed at the AMLE camp on April 8 and velocity data from this buoy is also shown in Figures 3.4 and 3.5.

As discussed by McPhee (1974), the validity of using relative currents between 10 m and 20 m for estimating ice velocity rests on the assumption that currents below the turbulent boundary layer and above

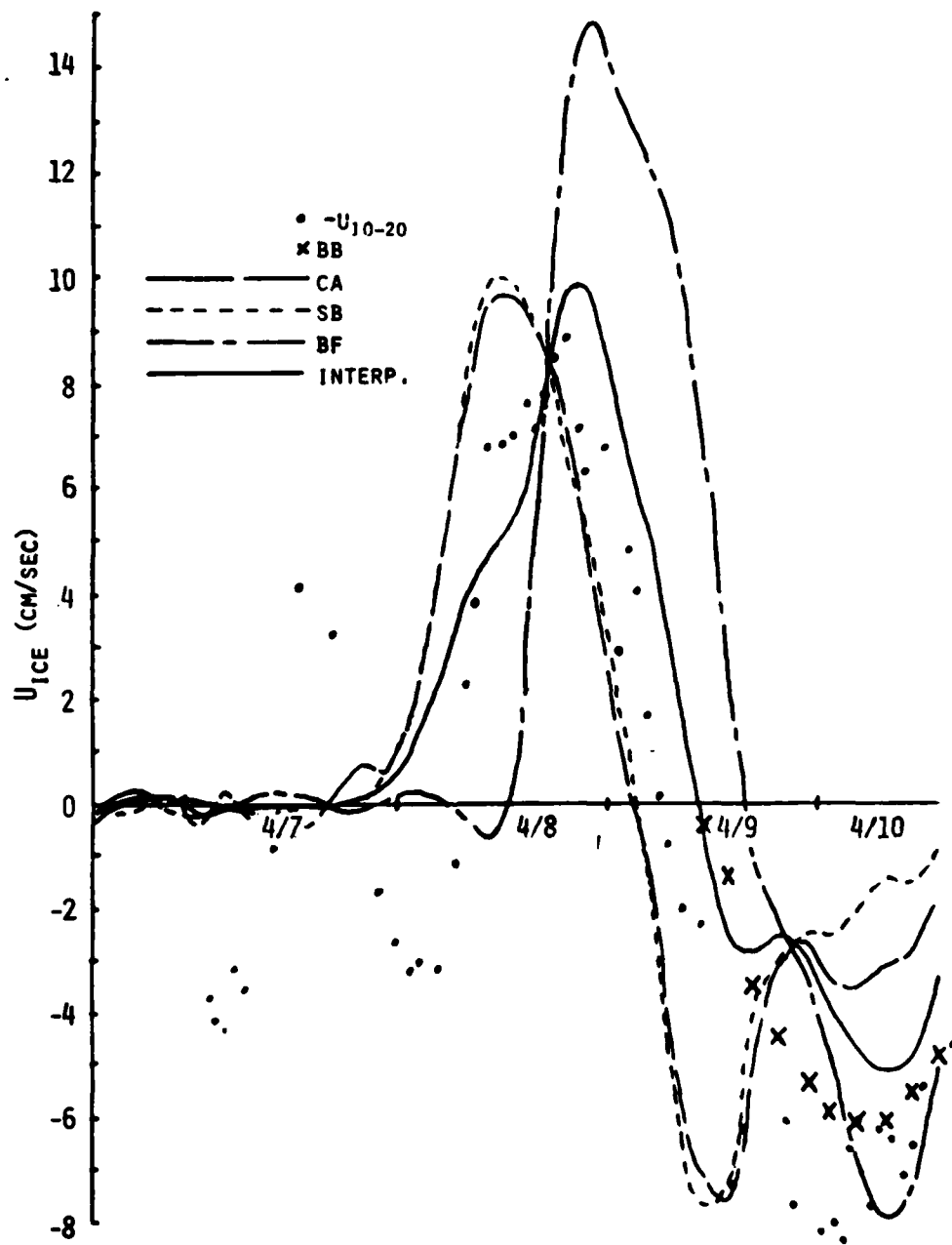


Figure 3.4. Northward ice velocity from three AIDJEX camps Caribou (CA), Snowbird (SB) and Blue Fox (BF). Also shown are the ice velocities estimated for the AMLE camp from interpolation, water velocity averaged from 10 m to 20 m, and from RAMS buoy (BB).

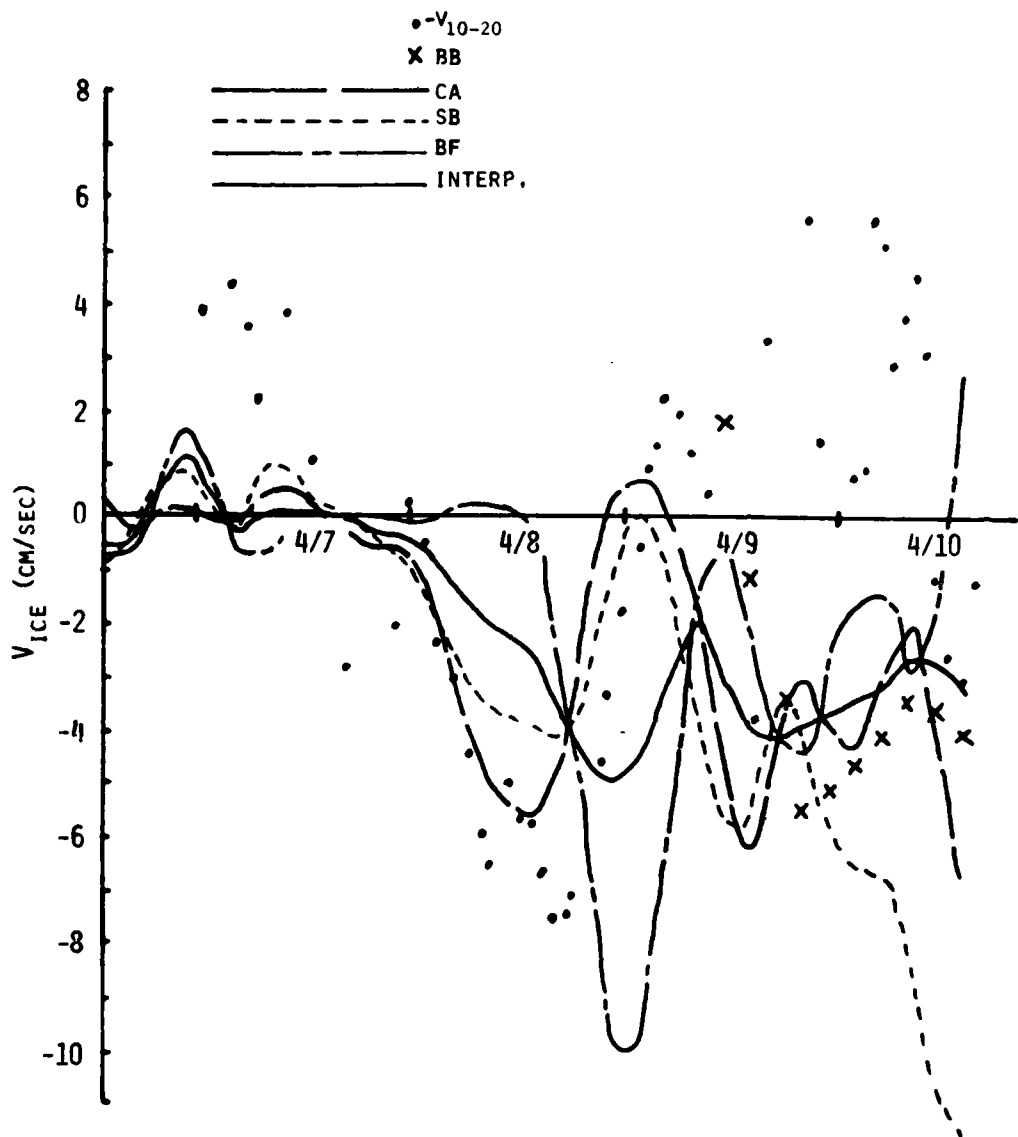


Figure 3.5. Eastward ice velocity from three AIDJEX camps Caribou (CA), Snowbird (SB) and Blue Fox (BF). Also shown are the ice velocities estimated for the AMLE camp from interpolation, water velocity from 1 m to 20 m, and from RAMS buoy (BB).

the region of strong stratification should be due only to rather small ($1 - 2 \text{ cm sec}^{-1}$) barotropic currents. The general agreement between the different ice velocity estimates for Big Bear leads us to believe this idea is reasonable. The differences between the interpolated and current velocity estimates are due to three factors: the existence of baroclinic currents in the mixed layer (especially during calm periods when the mixed layer is partially stratified), deviations of the ice motion from the linear behavior assumed for the interpolation estimate, and high frequency motions not resolved by the camp navigation filtering scheme. In general, agreement is better during periods of rapid ice motion because the magnitude of the baroclinic currents in the mixed layer is decreased relative to the ice velocity. In what follows both interpolated velocity estimates and water velocity estimates will be used to discuss the April 8 storm. This should be acceptable because agreement between the techniques is fairly good during the storm.

According to the AIDJEX camp data, ice velocities were less than 1 cm sec^{-1} through April 7. As can be seen in Figures 3.4 and 3.5 the u components at Caribou and Snowbird began to increase at 2400 on April 7. They peaked at about 10 cm sec^{-1} at 1200 on April 8 and dropped to zero by 0300 on April 9. The v components for these two sites decreased rapidly starting at the time the u components increased. The v component at Caribou reached a minimum value of -5.6 cm sec^{-1} at 1400 on April 8 and returned to zero by 2000 on April 8 while v at Snowbird reached a minimum of -4.2 cm sec^{-1} at 1700, April 8 and went back to zero by 0100 on April 9. The ice velocities at Blue Fox

behaved in a similar way but lagged the motion at Carobou and Snowbird by about 12 hours. The northward motion began at Blue Fox at 1300 on April 8, reached a maximum of 14.8 cm sec^{-1} at 1900, and dropped to zero at 1600 on April 9. The eastward component began to drop at 0100 on April 8, reached a minimum of $-10.0 \text{ cm sec}^{-1}$ at 2400, and went back to -0.6 cm sec^{-1} at 1100 on April 9.

Examination of Figure 3.2 reveals that the increase in ice velocity on April 8 is associated with an increase in wind speed. At that time the wind increased to a peak speed of 8.9 m sec^{-1} and blew in a northwesterly direction. Wind speeds were quite small during the rest of the experiment except on April 4 when the wind blew toward the east at up to 7.1 m sec^{-1} . However, the AIDJEX navigation data and the relative current data of Figure 3.3c both indicate ice motion was negligible on April 4. This is probably because there was no component of wind to the north. When ice in the Beaufort Sea is frozen up after an extended period of calm weather, a wind blowing to the northwest is required to pull the pack ice away from both the Canadian islands and the Canada-Alaska coastline. The NOAA-4 satellite photographs of Figures 3.6, 3.7, and 3.8 along with Figures 3.4 and 3.5 illustrate how this occurred on April 8.

The photograph of Figure 3.6 was taken at 1000 AST on April 7. Alaska and the Chukchi Sea are at the bottom and the Canadian Islands are in the upper right. The AIDJEX ice camps and the AMLE camp at Big Bear are denoted as in Figure 2.2. The ice appears relatively free of leads in this picture. The photograph of Figure 3.7 was taken at 1000 AST on April 8. It shows a pattern of leads running approximately

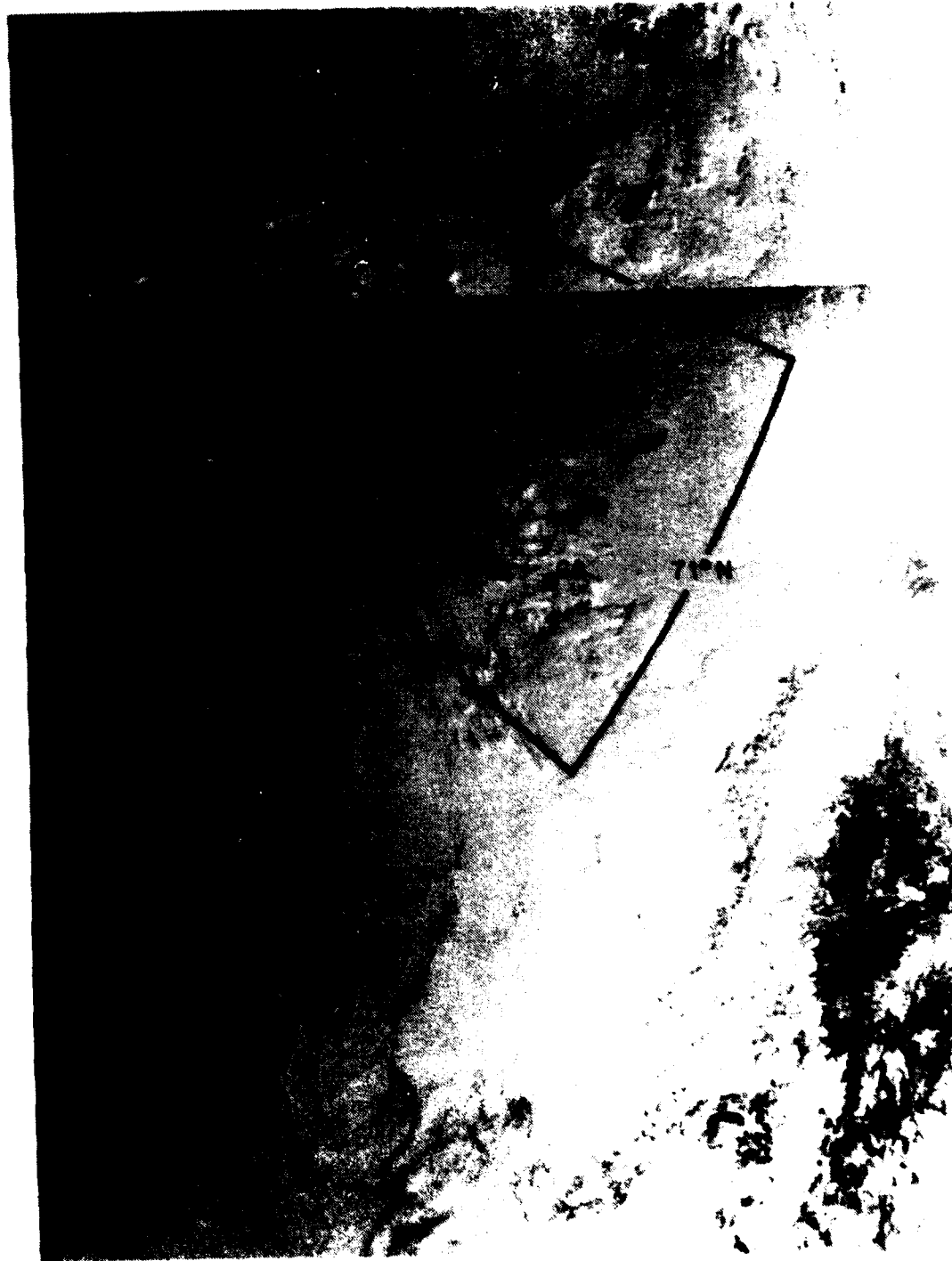


Figure 3.6. NOAA-4 satellite image of the Beaufort Sea, 1000 AST, April 7, 1976. Alaska is at lower right and the Canadian Islands are in the upper right. The ice is relatively free of leads.

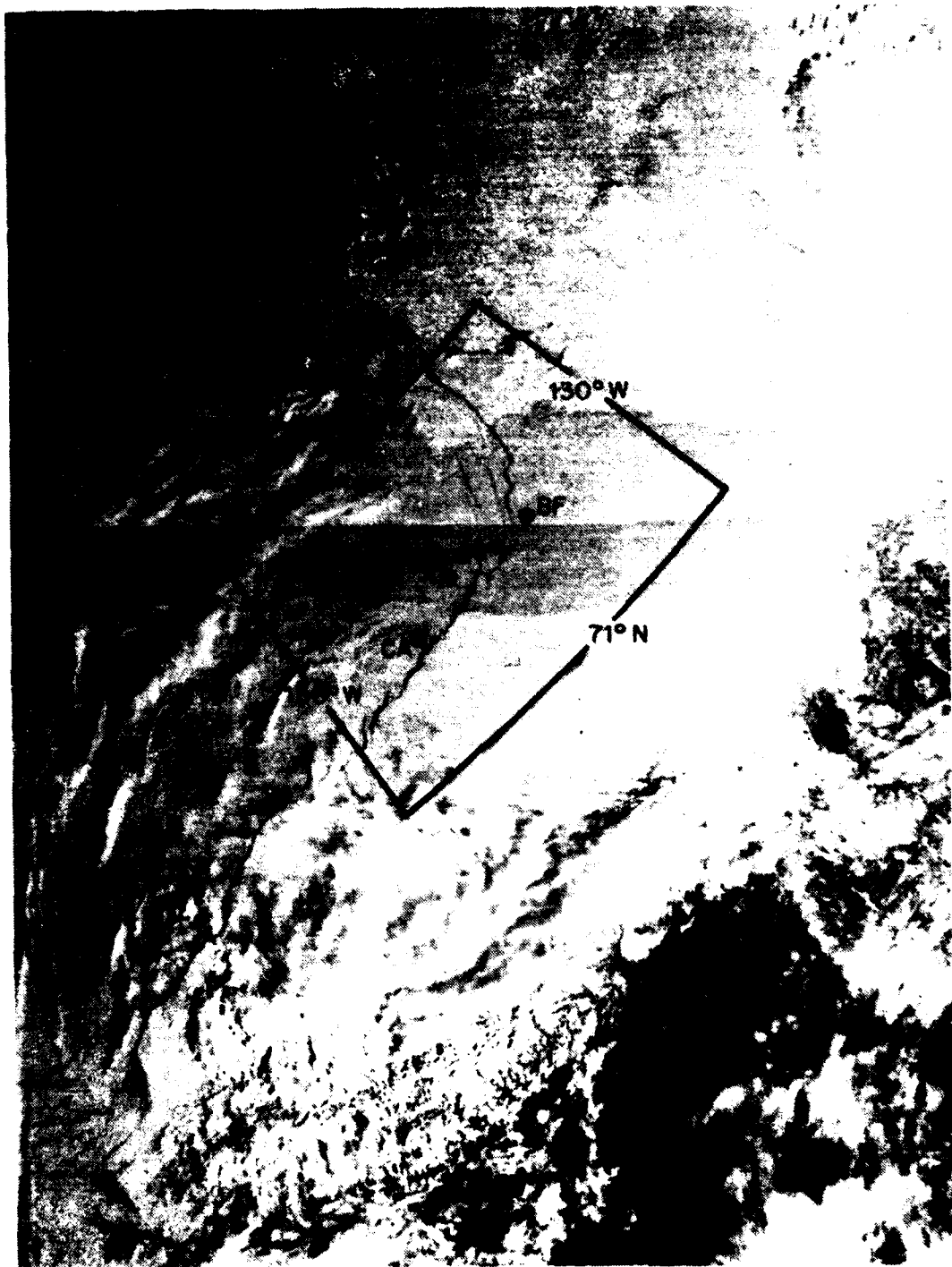


Figure 3.7. NOAA-4 satellite image of the Beaufort Sea, 1000 AST, April 8, 1976. Banks Island is at upper right, Alaska is at the bottom, and the Mackenzie River is at center right. A pattern of leads runs through the AIDJEX camp array.



Figure 3.8. NOAA-4 satellite image of the Beaufort Sea, 1000 AST, April 9, 1976. Alaska is at lower right and the Canadian Islands are in the upper right. The region of numerous leads extends east to the coast of the Canadian Islands.

north-south extending into the AIDJEX camp array from the west. Figures 3.4 and 3.5 show that at 1000 on April 8, the ice was moving rapidly at Caribou and Snowbird and was still stationary at Blue Fox. Figure 3.2 shows the wind at Big Bear had just started to rise and Figures 3.1, 3.3h, 3.4, and 3.5 show the isopycnals and ice were moving. Figure 3.8 was taken at 1000 AST on April 9. The region of numerous leads appears to have moved up to the Canadian islands. By the time the photograph of Figure 3.8 was taken the wind, relative currents and ice velocity had dropped off at Big Bear. The ice velocity at Caribou and Snowbird had also decreased. Only the ice velocity at Blue Fox was still high.

The sequence of events described above indicates a storm with northwestward surface winds moved across the Beaufort Sea from west to east and drove the sea ice in a north-northwestward direction. Judging from Figures 3.4 and 3.5 the time required for the storm to travel from Caribou and Snowbird to Blue Fox was about 12 hours. Alternately, the 10 m wind speed records at the three AIDJEX camps indicate the storm travel time was about 10 hours. Given the average separation distance of 220 km, these times correspond to a storm propagation speed between 18 and 23 kilometers per hour.

A similar pattern of events to that shown in Figures 3.6, 3.7, and 3.8 has been observed in other satellite photographs (P. Martin and R. Hall, personal communication); that is, after a quiet period with little ice motion, leads running north-south first occur off the western edge of Alaska and appear successively as an eastward moving wave. Ice moves south in the Chukchi Sea and a system of east-west shear

leads propagates with the disturbance eastward along the Alaska and Canadian coasts. This pattern of breakup occurs when a weather system with surface winds blowing to the northwest moves from west to east pulling ice offshore and to the west. The lack of ice response on April 4 indicates that without a northward surface wind component the pack does not break away from the coast even if there is a substantial wind component to the west.

The response of the upper ocean to the storm is of particular interest here. Figure 3.2 shows this response in terms of vertical displacement. The isopycnals all display some initial depression followed by varying amounts of rebound and oscillation. An important point is that the ocean began to respond before the wind speed increased at Big Bear. The isopycnals began to move at 0700 on April 8 while the wind speed did not begin to increase until 1030. Figures 3.3h, 3.4, and 3.5 indicate the relative water velocity began to increase by 0700 or before and the isopycnals for σ_t equal to 25.6 and greater began to increase in depth at about 2400 on April 7. The isopycnals at σ_t equal to 25.1 through 25.5 reached maximum depths 2 m to 3 m deeper than the initial values at times between 1000 and 1500, April 8. The wind speed did not reach a maximum of 8.9 m sec^{-1} until 1941. J. D. Smith (personal communication) reports having observed an ocean response prior to the arrival of an Arctic storm on several occasions. The ocean must respond to large scale forcing rather than local conditions. An explanation for this is offered in Chapter 4.

The isopycnal responses to the storm are not the same at all depths. The 25.1 isopycnal drops 2 m by 1030 on April 8 and then

returns to the pre-storm depth and oscillates with a period of about 6 hours. The 25.5 isopycnal dropped a maximum of 4 m by 1500 during the storm and returned to a depth 1 m deeper than that before the storm. The 25.2, 25.3, and 25.4 isopycnals behave in ways intermediate between those of the 25.1 and 25.5 isopycnals. They display a general pattern of initial depression, rebound, and oscillation with periods from 6 to 10 hours. The isopycnals below σ_t equal to 25.5 display a different pattern than those above. They all deepen about 2 m by 0600 on April 8. Then, by 0600 on April 19, they slowly return to depths 1 m to 2 m shallower than their depths prior to the storm.

The velocity field also displays a change in character with the storm passage. As noted in the previous section, the stratification of the mixed layer decreased during the storm and the velocity became more nearly constant over the mixed layer depth. Another aspect of the change in the velocity field is shown in Figures 3.9 and 3.10. These figures are contour plots of velocity in time and depth. The contours are constructed from tape average data and the velocity values are relative to the velocity averages from 10 m to 20 m. The contours thus give an approximate picture of the absolute velocity field. The chief advantage of such plots is that they yield a much more compact view of the velocity field than do velocity profiles of Figures 3.3a-l.

Prior to the storm of April 8, the contours of u and v present a broad amorphous character; at any given depth the same velocity may persist unchanged for a day at a time. After the storm vertical bands of -4 cm sec^{-1} velocity appear and disappear with a period near the inertial period, 12.55 hours. In u these bands show up as -2 cm sec^{-1}

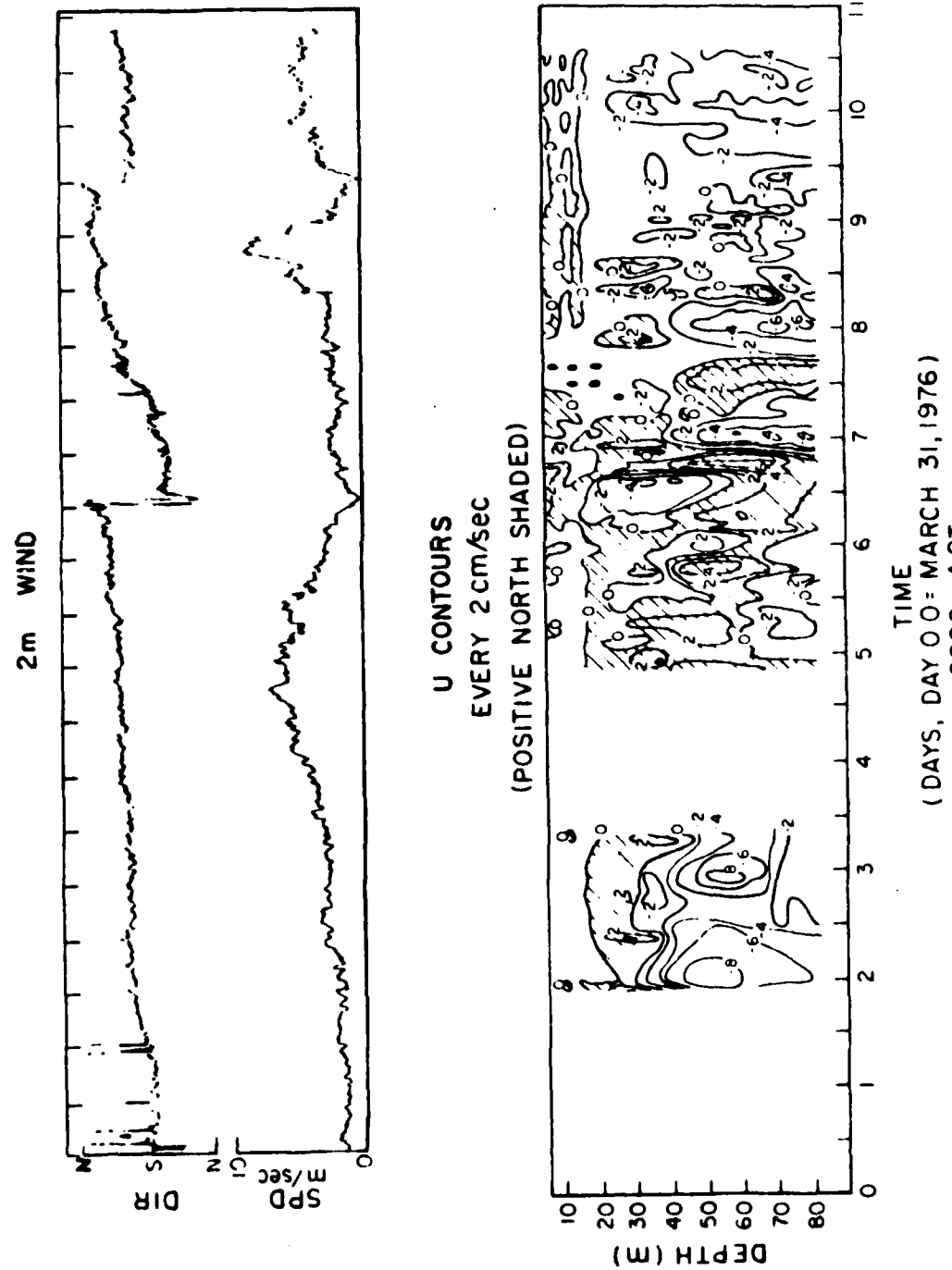


Figure 3.9. The u velocity contours relative to the average velocity between 10 m and 20 m, along with 2 m winds.

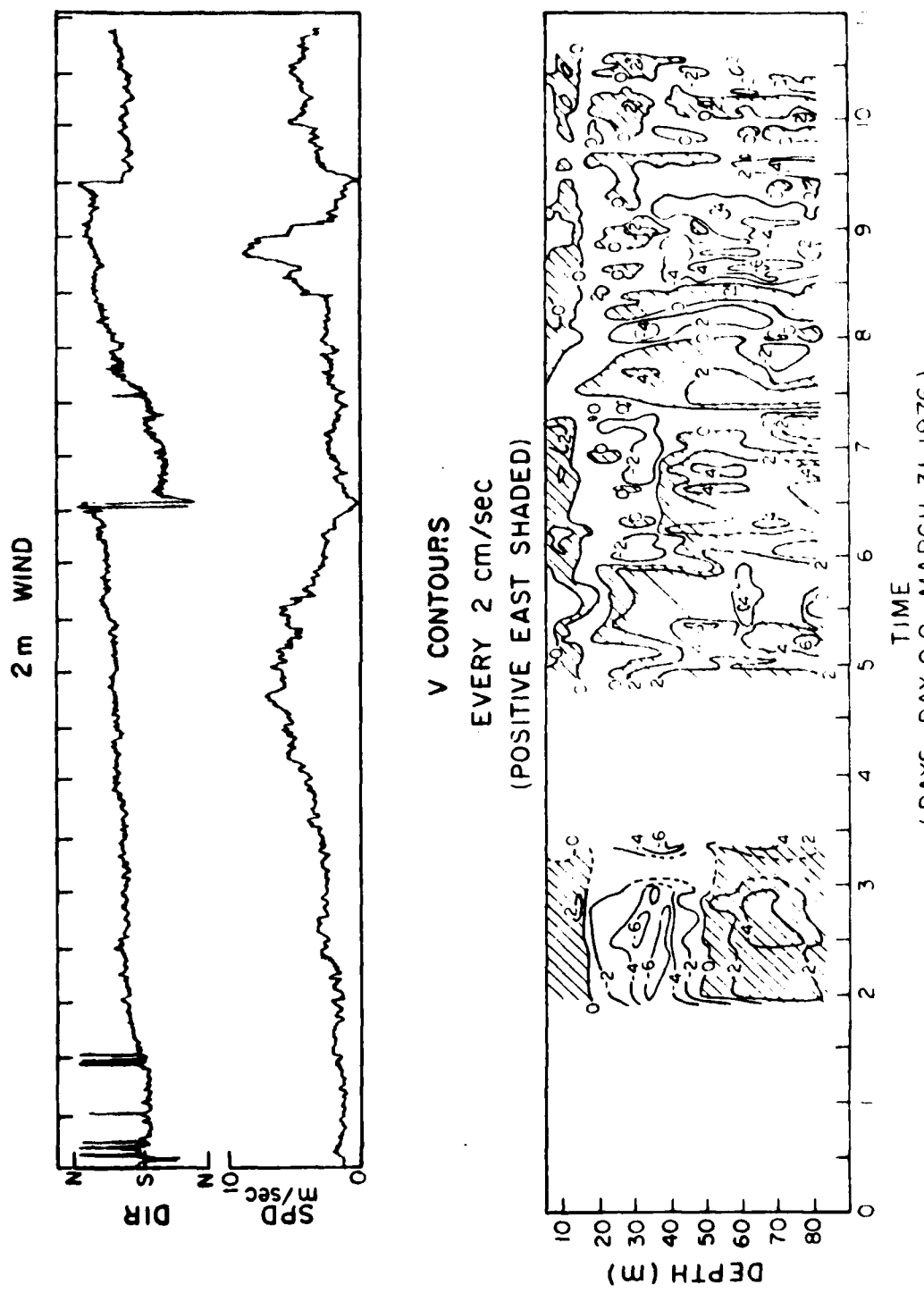


Figure 3.10. The v velocity contours relative to the average velocity between 10 m and 20 m, along with 2 m winds.

and -4 cm sec^{-1} contours below the pycnocline at 0000, 1200 and 2136 on April 8 and at 0936 on April 9. In v the bands show up as -2 cm sec^{-1} contours at 0224, 1424 on April 8 and at 0224 and 1424 on April 9. The v velocity goes negative after u , implying clockwise rotation. The velocity patterns may be due to inertial motions in the ice and mixed layer or they may be due to inertial motions below the pycnocline. In either event, the transition across the top pycnocline is not sharp, indicating some energy at the inertial frequency is transferred across it. Because the shear stress at the pycnocline is negligible, the energy transfer must occur through some means besides turbulent momentum exchange. In Chapter 4 it will be shown that forced internal waves can excite inertial frequency motions which extend from the surface through the pycnocline.

The important question to be answered here is: what are the mechanisms responsible for causing the observed response of the mass and velocity fields to the April 8 storm? Often discussions of the response of the mixed layer to storms involve the idea of deepening the mixed layer by turbulent entrainment at the pycnocline. The turbulence generated during this storm appears to have been sufficient to break down weak mixed layer stratification but too weak to cause entrainment at the pycnocline.

In Section 3.1 it was hypothesized that turbulent mixing was the cause of the decrease in mixed layer stratification on April 8. Two points indicate this is a valid hypothesis; the decrease in stratification resulted in a negligible change in average mixed layer density and the work done by surface stress was sufficient to cause the

observed change in density structure. If the change in stratification were due to mixing, one would expect the average density from 10 m to 30 m to remain the same. In fact σ_t averaged from 10 m to 30 m decreased very slightly, going from 24.98 at 1700 on April 7 to 24.97 at 1500 on April 8. These changes are close to the resolution of the measurements and are no greater than natural variations prior to April 8 when the stratification remained high.

The potential energy change due to the observed reduction in the stratification is $0.82 \times 10 \text{ ergs cm}^{-2}$. If the reduction is due to mixing, the work done by surface stress must be great enough to account for the resulting increase in potential energy. The energy input to the water column is the integral over time of the product of surface stress and ice velocity. A stress estimate for the pack ice can be made using the drag law from the AIDJEX ice model:

$$\bar{\tau}_w = c_w \rho |\bar{v}_i| e^{i\beta} \quad (3.3.1)$$

where \bar{v}_i is the complex ice velocity ($v_{\text{east}} + i u_{\text{north}}$) and $\rho = 1.025 \text{ gm cm}^{-3}$. The drag coefficient, $c_w = 0.0055$, and turning angle, $\beta = 23^\circ$, were determined by McPhee (personal communication, 1977) using a statistical analysis of the ice force balance under summer conditions with ice velocity and wind stress data from the AIDJEX experiment. It should be mentioned that according to Pritchard, et al. (1976) the uncertainty in c_w may be as great as ± 33 percent. Taking \bar{v}_i as minus the 10 m to 20 m average water velocity, the power input $\bar{\tau}_w \cdot \bar{v}_i$, integrated from 0000 to 1200 on April 8 is $5 \times 10^4 \text{ ergs cm}^{-2}$. Thus the energy required to change the potential energy is only 16 percent of

the total energy input. The rest of the energy input must have increased the mean kinetic energy in the boundary layer and gone into dissipation. Because the decrease in mixed layer stratification occurred during the storm and because the surface stress imported enough energy to cause the decrease, it can be concluded that turbulence was the probable cause of the breakdown of mixed layer stratification and the hypothesis of Section 3.1 is most likely correct.

Although storm induced turbulence was a factor in decreasing mixed layer stratification, mixing at the seasonal pycnocline does not appear to have been important. Figure 3.11 shows σ_t profiles before, during and after the storm. In it the base of the mixed layer appears more sharply defined after the storm. This could be due to turbulence at the base of the mixed layer but if so, one would expect the density between 10 m and 30 m to increase when, in fact, it decreased slightly. What is more important, the 25.1 isopycnal only deepened temporarily during the storm, then rebounded and oscillated about its original depth. Thus, even if mixing did cause a breakdown in the mixed layer stratification it did not extend into the highly stratified top pycnocline. It is easy to see why surface layer deepening due to mixing did not occur. Basically, the storm was too weak and short to cause mixing at the depth of the pycnocline. Under conditions of neutral stratification and steady state, the turbulent planetary boundary thickness is about $0.4 u_* / f$ where $u_* = \sqrt{\tau_s / \rho_s}$ is the shear velocity, τ_s is the surface stress, ρ_s the water density and f is the Coriolis parameter ($=1.3906 \times 10^{-4}$ at the AMLE camp). Under stratified conditions the thickness is smaller and time required to increase the boundary layer

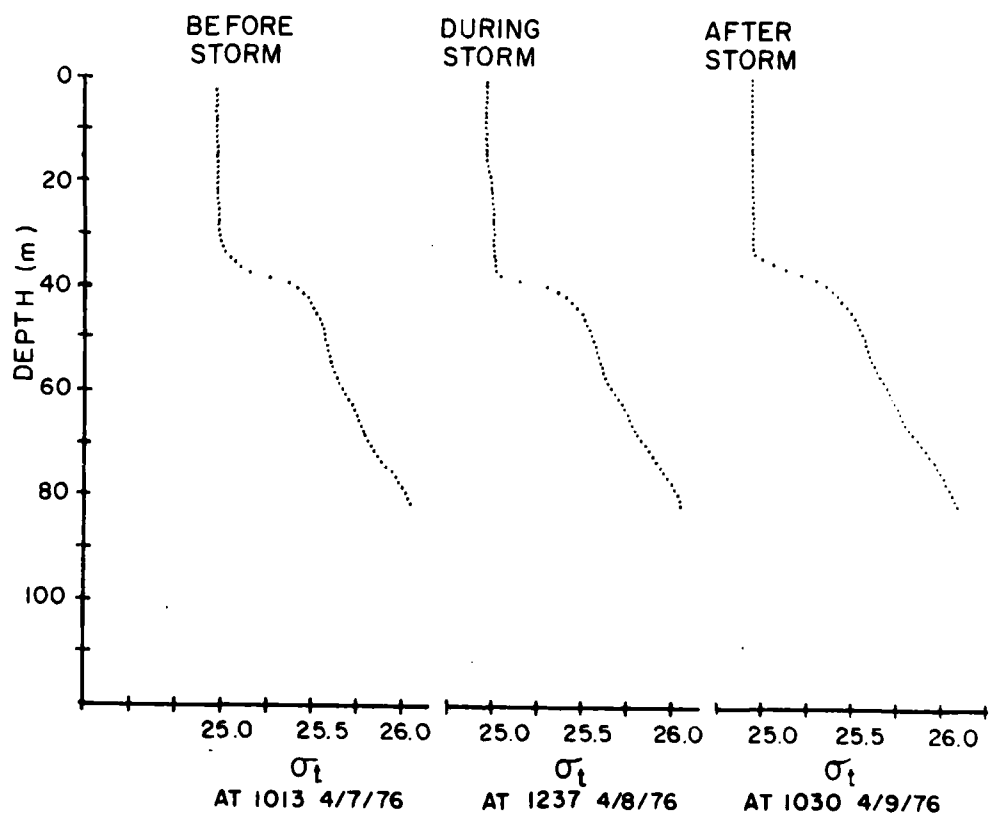


Figure 3.11. σ_t profiles before, during and after the April 8 storm.

thickness to the steady state value after the initiation of surface stress is on the order of an inertial period, $2\pi/f$. Using the average stress on April 8, calculated from (3.3.1), $0.4 u_*/f$ is found to be 16 m. Also the profiles of Figures 3.3h and 3.3i show no shear between 5 m and 20 m in the proper sense to indicate the presence of a turbulent boundary layer. Most of the shear in the boundary layer is above the 5 m minimum depth of the APS profiles. At depths below 16 m turbulence must have been negligible and, though it may have been sufficient to break down the weak stratification in the mixed layer, it was insufficient to cause mixing at the strongly stratified top pycnocline.

If turbulent mixing did not cause the response in the top pycnocline and below, what did? Several facts indicate the response may be an internal wave motion driven in part by forces associated with the storm. The coincidence of the response with the onset of the storm leads one to believe the motion may be forced by the storm. The rebound and oscillations of the isopycnals after the storm are suggestive of internal wave motions. As stated previously, the velocity fluctuations below the pycnocline with periods on the order of the inertial period are similar to what one would observe in the presence of low frequency internal waves.

One manner in which the storm could cause internal wave motion can be shown by examining the effect of horizontal variations in surface stress. The initial depression of the isopycnals can be caused by convergence in the mixed layer due to Ekman pumping. Consider the simple two layer model of the ocean around Big Bear shown in Figure 3.12. At the beginning of the storm the northward ice velocity first

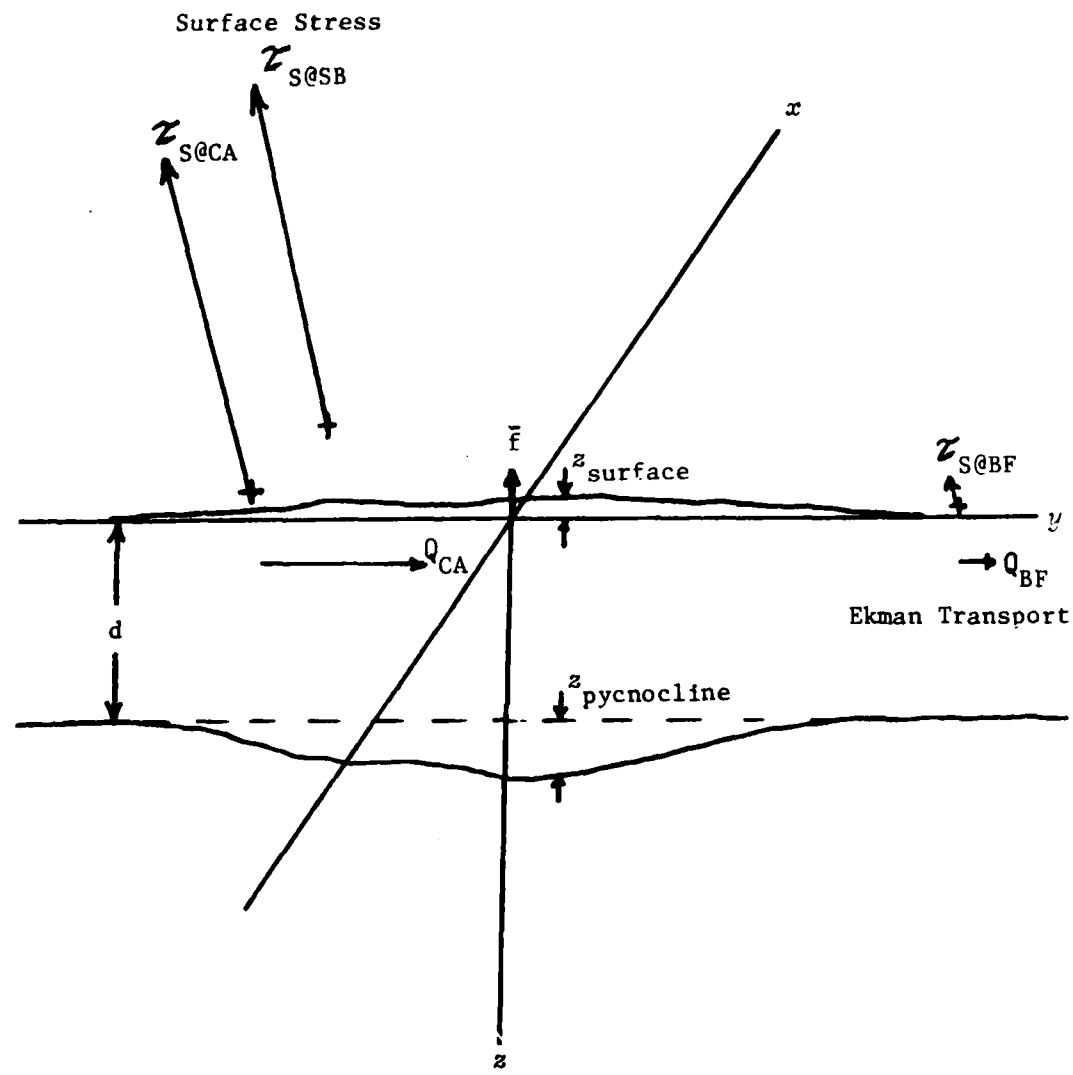


Figure 3.12. A simple two layer model of deepening of the seasonal pycnocline due to convergence in the mixed layer.

increased at Caribou and Snowbird while the motion at Blue Fox was negligible. This implies eastward Ekman transport in the mixed layer due to the northward surface stress at Caribou and Snowbird was not balanced by an equivalent transport near Blue Fox. The resultant convergence would have required the mixed layer depth to increase, just as observed. As the storm passed and the stress in the region around Blue Fox rose and that near Caribou and Snowbird decreased, the pycnocline depth would have had to decrease to balance divergence of Ekman transport. After the storm passed the energy imparted to the pycnocline would have been manifested as oscillations due to internal waves. The observed rebound and oscillations of the isopycnals is thus also consistent with this simple model. Furthermore, the model suggests the mixed layer depth responds not to local stress but the horizontal gradients of stress. Thus the depth may change before the local stress arises, just as observed on April 8.

Another mechanism which might drive the internal motions is the buoyancy flux under leads which opened during the storm. The increase in density in the mixed layer near leads, due to salt rejection by rapidly forming sea ice, can cause diverging currents in the mixed layer. The divergent circulations can in turn cause changes in the pycnocline depth.

These simple models neglect the time required to spin up the Ekman layer, the inertia of mixed layer and the restoring forces due to stratification. In the next chapter a sophisticated model of internal wave generation by surface stress, pressure, and buoyancy flux will be developed. The model will be run with forcing representative of actual

conditions in the Beaufort Sea at the time of the storm. The results indicate the response below the main pycnocline was largely due to internal wave motions driven by surface stress and buoyancy flux in leads.

3.4 Lead Convection Observed During the AMLE

On April 10 a lead broke through the AMLE camp. The photograph in Figure 3.13, taken the following day during evacuation, shows the camp orientation relative to the lead which by this time had widened to over 1 km. The relative current velocity at the time the lead opened was directed 20° true as shown, indicating the camp was downstream of the point 0.5 km to 1 km distant where the lead turned to the north and went around the experimental site. Figure 3.14 shows velocity and density profiles averaged over the last hour of operation along with a density profile obtained prior to the lead opening. No large changes in the velocity profiles were observed but changes in the density field were dramatic, mainly in the mixed layer where the density increased markedly.

Figure 3.15 which shows the salinity at 3 depths plotted versus time, yields an interesting history of the changes in the mixed layer density structure. The lead opened at approximately 1200 AST. The salinity first increased at the deepest depths. The density disturbance then moved up the water column, finally causing an increase in the mixed layer salinity starting at 1240. The salinity in the mixed layer increase by about 0.1°/oo while the initial density disturbance at depth gradually decreased. As can be seen by comparing the before and after density profiles of Figure 3.14 a decrease in density at

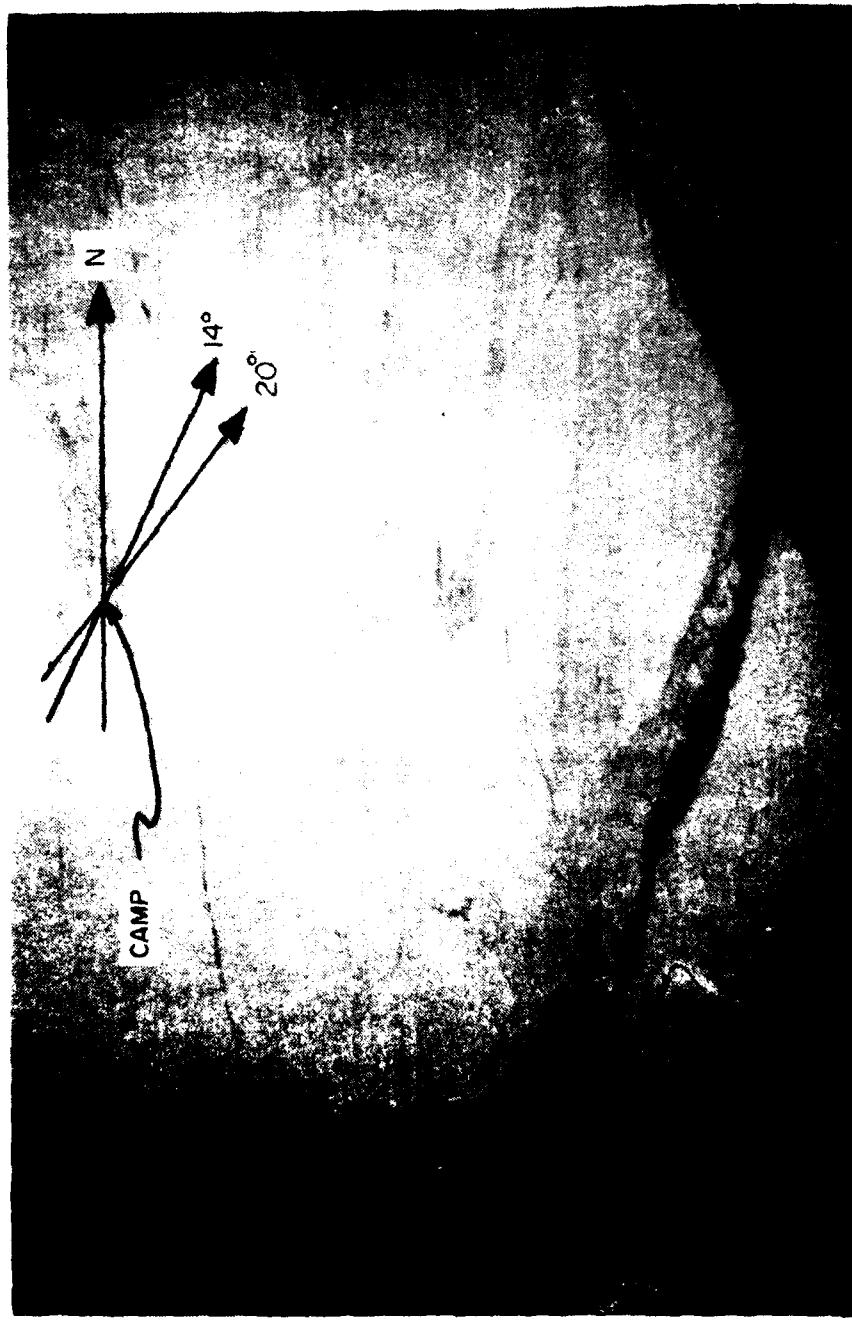


Figure 3.13. The AMLE camp as seen from the air during evacuation on April 11, 1976. When the lead opened on April 10, the current direction relative to the ice ranged from 20° True to 14° True.

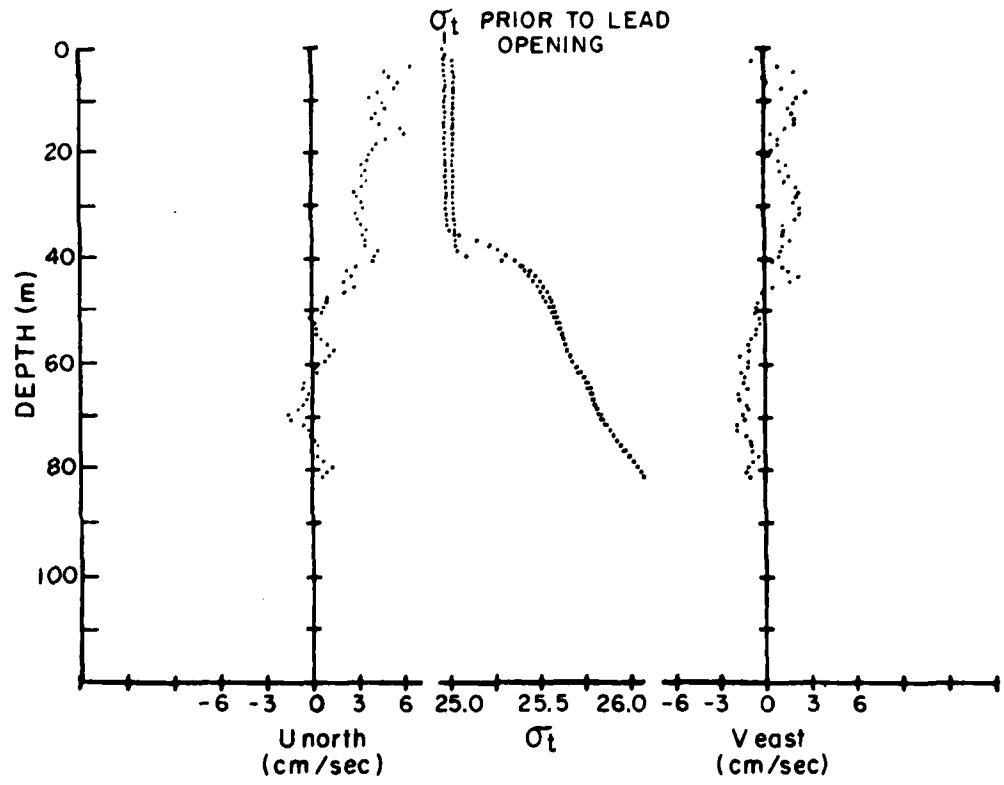


Figure 3.14. Velocity and σ_t as measured with the APS from 1430 to 1530, after the lead opened at the end of the experiment. Also shown is a σ_t profile made prior to the lead opening. There were no major changes in the velocity field. Air temperature = -16°C .

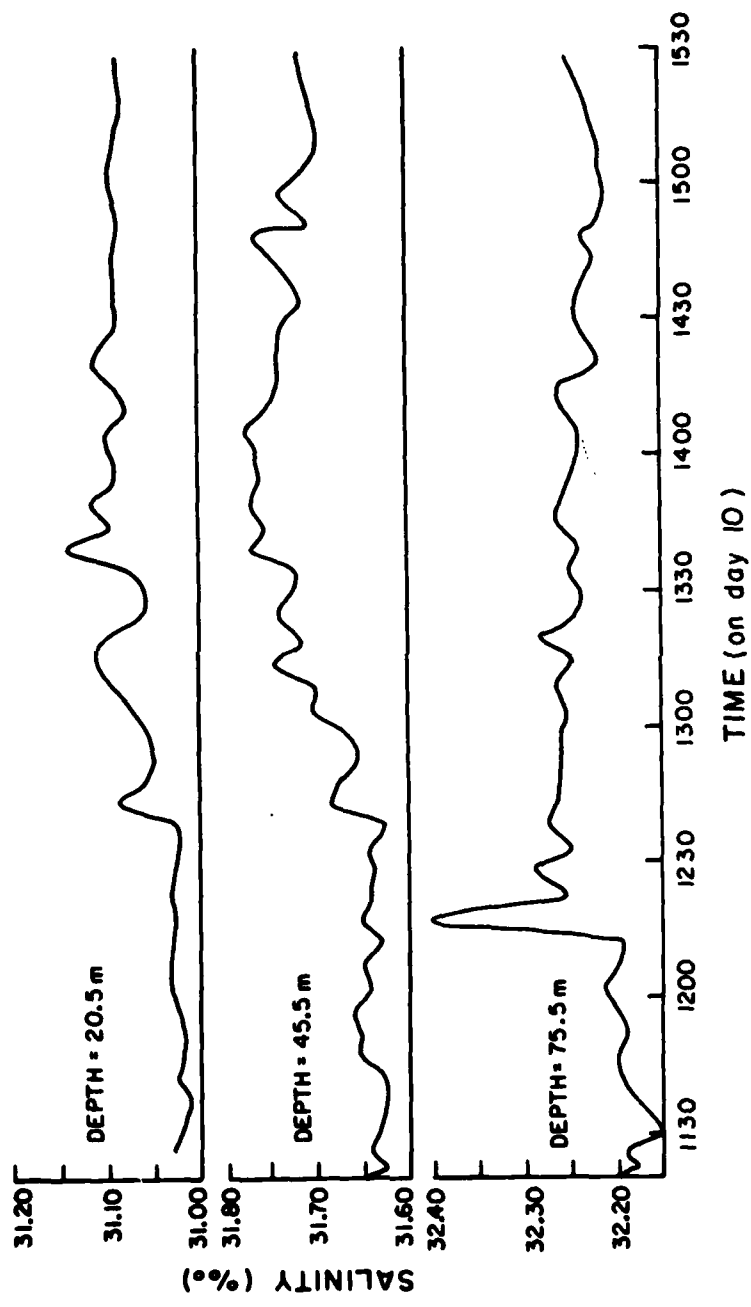


Figure 3.15. Salinity versus time at 20.5 m, 45.5 m, and 75.5 m. Mixed layer depth is 35.5 m and the lead opened ca. 1200 AST, April 10, 1976.

depths from 35 m to 41 m was caused by the deepening and sharpening of the pycnocline. This deepening may be due in part to turbulent mixing at the base of the mixed layer produced through vigorous convection directly under the lead.

The rapid increase in salinity at 75 m, which starts at 1215 in Figure 3.15, is associated with the marked rise shown in Figure 3.2 of all the isopycnals below 50 m. The manner in which the isopycnals rise together suggests the response at depth might be due to an internal wave driven by stress divergence across the lead or by buoyancy flux; the sense of the motion is appropriate to both forcing functions. However, results using the model developed in the next chapter indicate the theoretical response due to these factors is much slower than the observed response at depth. Alternatively it may be due to an isolated instance of penetrative convection, but it is difficult to imagine that a great enough salinity perturbation (more than 2⁰/oo is required) could develop in the mixed layer to drive a plume to an equilibrium depth of 75 m.

As a check on the source of the observed change in mixed layer salinity, the horizontal salt flux under the camp may be compared with the expected salt production in the lead. In order to calculate the total salt flux from a lead it is necessary to have upstream and downstream profiles of salinity and velocity. These measurements were only obtained for the downstream side, but it is possible to estimate the upstream salinity profile from measurements made prior to opening of the lead and to use this data with measured downstream velocity and salinity profiles to estimate the difference in salt flux across the

lead

$$\bar{q}(z) = [S_{\text{downstream}} - S_{\text{upstream}}] \bar{V} = \rho [\Delta S'(z)] V(z) \quad (3.4.1)$$

where ρ is the water density, S is salinity, and \bar{V} is the horizontal velocity. The integral of \bar{q} with depth equals the salt rejected in a strip of unit width across the lead. To estimate the upstream salinity profile, a linear curve fit was made to the salinity over each 1 m depth interval for 24 hours prior to the lead opening. The linear fit was used to extrapolate an upstream (or undisturbed) salinity profile. This profile was subtracted from measured profiles to estimate $\Delta S'(z)$ in equation (3.4.1). Figure 3.16 shows $\bar{q}(z)$ averaged over the last hour of data when, hopefully, the lead convection was approaching steady state. The velocity and measured salinity profile correspond to those of Figure 3.14. Also shown are error bars for $\bar{q}(z)$ calculated by using the extrapolated upstream salinity plus or minus the standard deviation of the linear curve fit. The salt flux in the mixed layer is significantly greater than the noise level while below the pycnocline the salt flux is negligible. At the pycnocline, the negative salt fluxes occur because $\Delta S'$ is negative due to the deepening of the pycnocline. The total salt flux (integral of \bar{q} over z) is $0.55 \text{ gm cm}^{-1} \text{ sec}^{-1}$ bearing 14°T to 20°T . This direction is shown in Figure 3.13.

The effective width of the lead contributing salt to the mixed layer can be estimated by dividing the total salt flux in the ocean by salt flux per unit area at the surface of open water. Determining the salt flux at the lead surface involves calculating the rate of ice growth and the salinity of the new ice. The difference between the

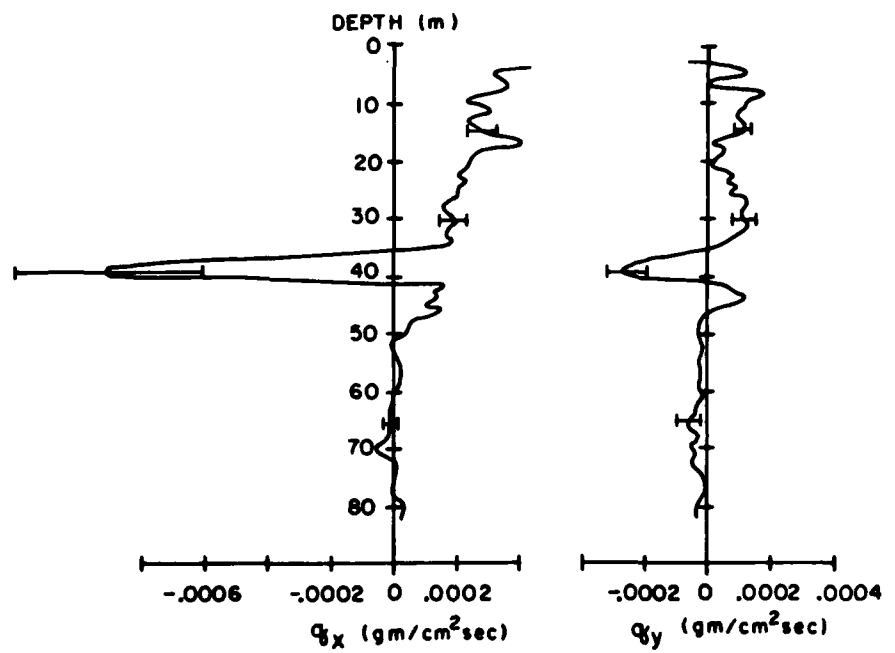


Figure 3.16. Salt flux = $\bar{q} = \bar{u} (S_{dn} - S_{up})$ at 1500, April 10.

salinity of the new ice and the water from which it was formed yields the salt rejected at the surface.

Several authors have dealt with the estimation of ice growth rates. Anderson (1961) gives an empirical expression for the ice growth rate based on field measurements,

$$\dot{h} = \frac{dh}{dt} = \frac{B_2(T_w - T_a)}{2h + B_1} \quad (3.4.2)$$

where T_w is the water temperature (assumed to be the freezing temperature) and T_a is the air temperature. B_1 equals 5.1 cm and B_2 equals $7.75 \times 10^{-5} \text{ cm}^{-2} \text{ sec}^{-1}$. Based on a theoretical examination of the heat flux through thin ice and open water, Maykut (personal communication, 1979) reports

$$\dot{h} = \frac{1}{\rho_i \lambda} \left(- \frac{k_i}{k_i + C_t + Ah} (C_t \theta + A\theta') \right) \quad (3.4.3)$$

where

$$k_i = 4.63 \times 10^{-3} \text{ cal cm}^{-1} \text{ sec}^{-1} \text{ }^{\circ}\text{C}^{-1}$$

= conductivity of ice

$$A = 8.68 \times 10^{-5} \text{ cal cm}^{-2} \text{ sec}^{-1} \text{ }^{\circ}\text{C}^{-1}$$

$$C_t = a_1 \rho_a C_p C_e U_a$$

$$= \{1.15 \times 10^{-4} (\text{cal cm}^{-2} \text{ }^{\circ}\text{C}^{-1} \text{ sec}^{-1}) / (\text{m sec}^{-1})\} U_a$$

$$U_a = \text{wind speed at 2 m in m sec}^{-1}$$

$$\theta = T_a - T_w$$

$$\theta' = T_e - T_w$$

$$T_e = \varepsilon^{1/4} T_a = (.7855 + .00312 G_c^{2.75})^{1/4} T_a$$

G_c = 10 x fraction of cloud cover

The θ term in (3.4.3) accounts for the sensible and latent heat loss while the θ' term accounts for heat loss due to long wave radiation. The heat required to produce one cubic centimeter of solid ice, $\rho_i \lambda$, is 72 cal. When predicting the growth rate of a porous ice sheet Maykut uses $\rho_i \lambda$ equal to 55 cal cm^{-3} . Lindsay (1976) has measured the sensible heat flux from open leads. The ice growth rate corresponding to his empirical formula for heat flux is

$$\dot{h} = \frac{1}{\rho_i \lambda} c_p \rho_a c_s u_a \theta \quad (3.4.4)$$

where

$$c_s = (2.6 + .11\theta/u_a^2) \times 10^{-3}$$

Converting these ice growth rates to salt flux requires an estimate of how much salt is rejected from the ice as it grows. Based on laboratory experiments, Cox and Weeks (1975) indicate the surface salt flux may be expressed as

$$F_s = \rho_i \dot{h} [1 - k_c] s_w \quad (3.4.5)$$

where

s_w = water salinity fraction

ρ_i = ice density = .9 gm/cm³

and

$$k_c = \begin{cases} 0.8439 + 0.0529 \ln h & h < 2 \times 10^{-5} \text{ cm sec}^{-1} \\ 0.26/[0.26 + 0.74 \exp(-7234h)] & h > 2 \times 10^{-5} \text{ cm sec}^{-1} \end{cases}$$

This formula is appropriate when the ice is of finite thickness. In fact, the surface of a lead is often kept ice free because wind stress moves surface water and ice crystals to the downwind edge of the lead. In such a situation the salinity of ice is effectively zero and k_c may be set to zero.

The salt flux has been calculated using equations (3.4.2), (3.4.3) and (3.4.4). Equation (3.4.5) was used to determine the salt flux as a function of ice growth rate, but k_c has been set to zero because the wind kept the surface ice free for several hours during the AMLE. The water temperature was -1.8°C , the air temperature was -16.8°C , and S_w was 31.0. The average 2 m wind speed was 4.5 m/sec and G_c in equation (3.4.3) is taken as 6. The results for these conditions and the three equations are given in Table 3.1. Also given are the lead widths over which these fluxes would have to act to produce a .55 gm/sec total salt flux.

Table 3.1
Salt Flux and Required Lead Widths

Model	Salt Flux, Qs	Required Lead Width
Anderson (3.4.2)	$7.3 \times 10^{-6} \text{ gm cm}^{-2} \text{ sec}^{-1}$	759 m
Maykut (3.4.3)	$4.0 \times 10^{-6} \text{ gm cm}^{-3} \text{ sec}^{-1}$	1382 m
Lindsay (3.4.4)	$2.5 \times 10^{-6} \text{ gm cm}^{-2} \text{ sec}^{-1}$	2209 m

Clearly there is a rather wide variation in the estimates of salt flux. The salt flux of equation (3.4.4) is low, probably because Lindsay's

equation accounts for only the loss of sensible heat. Maykut's equation (3.4.3) is based on a complete analysis of the thermodynamic exchanges at the lead surface and includes the effect of long wave radiation. It agrees well with the more sophisticated theoretical model used by Maykut (1978). Anderson's equation (3.4.2) produces the greatest ice growth and is based on field data. Because of the difficulty of measuring growth rates in open water, his results may be nothing more than an extrapolation from data for finite thickness. Because of the problems inherent in the other two equations, Maykut's equation (3.4.3) will be used henceforth.

In order to produce the observed total salt flux, a lead width of 1.4 km is required. This is much greater than the actual lead width of 100 m at 1500 on April 10. There are two probable reasons for the disparity. Most important, the flow past the lead was not perpendicular to it but rather parallel to the lead axis. The effective width of open water in such a case is very much greater than the actual lead width. Also, complexities in the circulation such as roll vortices may tend to concentrate the most highly saline water in streaks away from the lead. In any event the change in mixed layer salinity is consistent with the amount of salt released by a stretch of open water 1.4 km long.

The salinity data suggests that salt is rejected from the lead surface then mixed uniformly through the layer. The velocity data indicates more complicated processes may have been occurring. Although there were no large changes in the velocity structure, weak jets did appear in the mixed layer when the lead opened on April 10. These are

especially apparent in the u velocity profiles made around 1400 shown in Figure 3.3l. At 15 m depth there is a 2 cm sec^{-1} jet to the north, toward the lead. It persists from 1100 to the end of the experiment and is also shown in Figure 3.14. Figure 3.3l also displays a jet in u at 38 m depth which persists from 1100 to 1430. Its magnitude is about 2 cm sec^{-1} and it is directed south, away from the lead. The density disturbance in the mixed layer is due to salt rejected along the lead axis and advected past the camp while, because the lead veered around the camp to the north, manifestations of a lateral circulation pattern appear as jets in the u velocity profiles. The jet at 38 m is driven by the descending brine plume in the lead to the north of the camp and the jet at 15 m supplies an influx of mixed layer water to the lead surface. The density disturbances associated with these jets are obscured by the salt flux along the lead axis. Thus, the data suggests the observed pattern consists of simple entrainment of brine into the mixed layer due to a mean flow nearly parallel to the lead axis with a superimposed pattern of localized lead driven circulation perpendicular to the lead axis. Such a pattern has been predicted by Estoque and Bhumralkar (1969) using a numerical model of flow over a two-dimensional heat island; when the mean flow is along the axis of such a source, convective cells are still active perpendicular to the sides. Smith (1973) has suggested similar patterns of lead convection in order to explain jet-like features in other velocity data gathered in the Arctic.

AD-A091 046

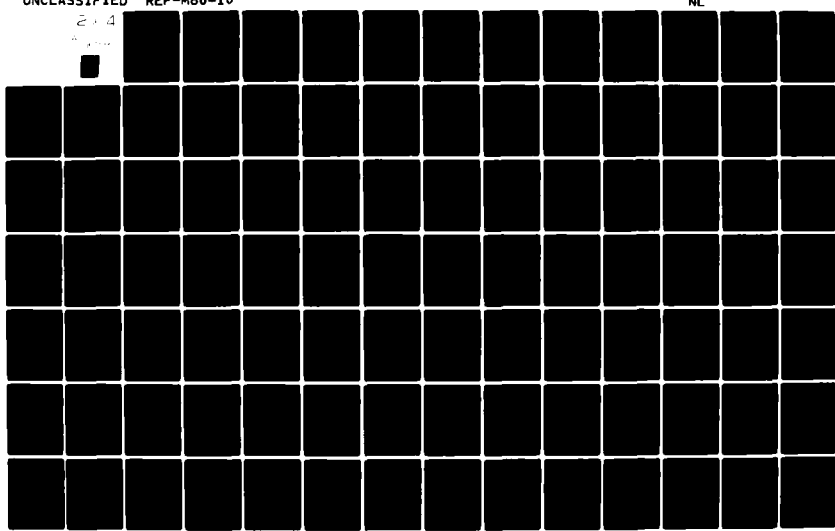
WASHINGTON UNIV SEATTLE DEPT OF OCEANOGRAPHY
FORCED INTERNAL WAVES IN THE ARCTIC OCEAN. (U)
MAY 80 J H MORISON
REF-M80-10

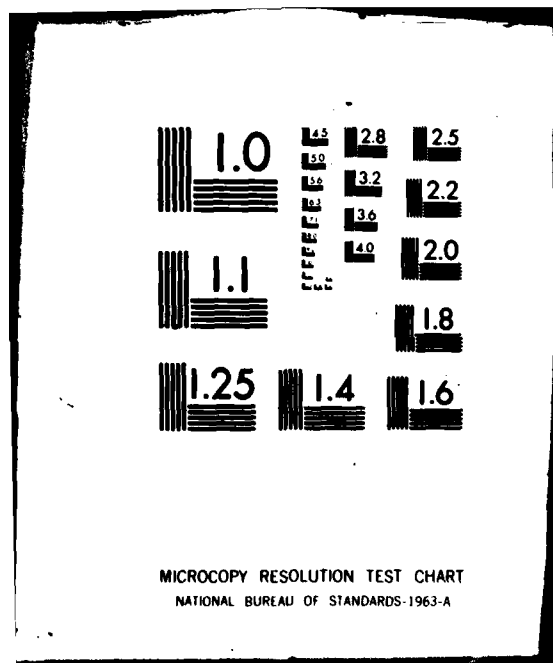
UNCLASSIFIED

F/6 8/3

N00014-75-C-0186
NL

2 x 4





Chapter 4

FORCED INTERNAL WAVES AND THE APRIL 8 STORM RESPONSE

4.1 Theoretical Models of Internal Wave Generation by Surface Forces

Numerous attempts have been made to determine the internal wave response to surface forcing. Free internal waves arise as a balance of buoyancy forces and fluid acceleration. These waves occur for a wide range horizontal and vertical scales with frequencies between the local Brunt-Väisälä frequency N and the inertial frequency f . The temporal character of forced internal waves depends to a large extent on the nature of the forcing. In theory, the permissible frequencies of forced waves vary over an infinite range. Therefore, numerous studies of forced internal waves have been made in order to explain a broad variety of internal motions. Thorpe (1975) gives a good review of work in this area.

Some of the earliest work involves the assumptions that (1) the ocean is composed of two layers and (2) shear stress can be treated as a body force. Veronis and Stommel (1956) deal with the general features of baroclinic and barotropic motions in a two layer ocean driven by atmospheric forcing. They give dispersion relations for motions at all time and length scales but focus attention on large scale, long period motions in which the p effect is important.

Kajiura (1958) and Geisler (1969) have determined the response of a two layer, f plane ocean to a hurricane moving at constant speed.

They use linear models and techniques discussed by Lighthill (1965, 1967). In contrast, O'Brien and Reid (1967) have determined the response of the ocean to a stationary hurricane using a two layer non-linear model. For these models the curl of wind stress is found to be the dominant forcing term and for realistic, hurricane intensity forcing the pycnocline may rise to the surface due to Ekman suction. In their studies of the response to a moving hurricane, both Geisler and Kajiura find the hurricane propagation speed is much less than the barotropic wave speed and greater than the baroclinic wave speed. Hence, the energy in the barotropic response radiates rapidly away from the storm while the baroclinic response moves as a wake behind the storm front. Prior to the work discussed later in this chapter, an attempt was made by the author to determine the ocean response which was moving with the storm of April 8. The resulting wake response at the pycnocline was only about 20 cm and did not lead the storm. Thus it was concluded that the two layer approximation and the assumption that the response was a wake moving at constant speed with the storm were not applicable to the experimental case.

The next most complicated set of models allows constant stratification and some of them even include a turbulent eddy viscosity to account for forcing by surface stresses. Commonly a Fourier transformation is used to eliminate the horizontal dimensions and time from the linearized equations of motion. This results in a differential equation in the vertical dimension which must be resolved to obtain the response for each horizontal wave number and frequency. Tomczak (1966, 1967) examines the response of an ocean with constant N and constant

eddy viscosity to surface stress and surface pressure. His model assumes zero surface displacement and he decomposes the solution in vertical wave numbers. He finds the curl of surface stress drives motions at frequencies below f and the divergence of surface stress is dominant at frequencies greater than f .

Krauss (1972a) uses a constant stratification and eddy coefficient and, after solving a fourth order equation for the vertical structure, gives transfer functions for the response at different depths as a function of horizontal wave number and frequency. His model uses the kinematic boundary conditions at the surface. In a similar work, Krauss (1972b) assumes a thin homogeneous surface layer overlies a layer of constant stratification. He uses a condition of zero displacement at the surface and obtains the response to a step change in surface stress. The zero surface displacement condition is not a rigid lid condition in that the pressure at the surface is also zero. Therefore, convergent inertial motions occur in the surface layer. These couple with low frequency internal waves in the lower layer to produce a beating phenomena in vertical velocity. If a more realistic surface boundary condition were used, vertical motions could not resonate at the inertial frequency (although horizontal velocities may). They would drive baroclinic and barotropic motions with resonant frequencies greater than f . The only beating which would occur would be between internal wave modes with nearly equal resonant frequencies.

More sophisticated models allow arbitrary stratification. Mork (1972, 1968) allows an arbitrary density distribution and uses an eddy coefficient inversely proportional to N . He decomposes the motion into

vertical normal modes in a manner similar to that of Fjeldstadt (1964) and obtains response functions for surface pressure and stress. Though the model employs an eddy coefficient, the eigenfunctions only satisfy a zero surface stress condition and the response of each mode is obtained by vertical integration of the stress profile. Thus, it appears the response is driven in the same manner as if a body force approximation were used. Mork (1972) compares his theory with a response measured off the coast of Norway but, because the observation site was on the continental slope, topographic effects had to be included. Doing so produced a very large (300 m) response in the first mode which seems to agree with the observations.

Leonov and Miropolskiy (1973) derive an expression for the internal wave response to surface pressure using the complete kinematic boundary condition. An inverse Laplace transform technique is used to separate the response into normal modes. They solve the equations for two special cases, constant N and a two layer ocean, but the theory is quite general.

Goodman and Levine (1977) use the pressure response of Leonov and Miropolskiy (1973) and the ratio of stress response to pressure response from Mork (1968) in order to study resonant forcing of internal waves. As will be discussed, they misinterpret the response function of Leonov and Miropolskiy. In spite of this, by including boundary effects, they produce a model response which agrees well with observations.

The most elaborate internal wave model is by Krauss (1976a and b). It allows arbitrary distributions of density and eddy diffusivity.

The complete linearized equations of motion are solved numerically for different cross-sections in a wave number-frequency space. Resonance peaks are found and identified with particular modes. Using a realistic stratification from the Baltic, the model response is found to have a maximum at the third mode. This contrasts sharply with the assumption, arising from constant N models, that the wind stress response decreases monotonically, with increasing mode number.

The works discussed above deal with the generation of internal waves by surface stress or pressure or both. Magaard (1973) derives an expression for the generation of internal waves by surface buoyancy fluxes such as evaporation, rainfall or salt rejection. He assumes a constant stratification and eddy diffusivity and uses coupled perturbation expansions to derive his result. He concludes the response due to buoyancy flux forcing is a small but significant fraction of that due to surface stress.

The goal of this chapter is to develop a model which might explain the generation of the internal wave motions observed during the April 8 storm. The high level of vertical structure observed in the storm response and the complicated stratification indicate the model should allow arbitrary stratification and be applicable for a large number of modes.

It is also desirable to use the true kinematic boundary condition at the surface. What is often called a rigid lid assumption in some of the works cited above is, in fact, not a true rigid lid but rather a zero displacement, zero pressure assumption. That is, not only is the surface displacement assumed zero but also the pressure

changes due to surface displacement are assumed zero. This is a poor assumption. When Ekman transport causes convergence in a surface mixed layer the pycnocline must be forced down. A pressure perturbation in the mixed layer is required to force this deflection and it can only be due to a small upward displacement at the surface. The displacement is very small but the pressure has an important effect on velocity in the mixed layer and should be included in the model.

Finally, the model must be simple enough to be run with realistic input data and produce outputs of vertical displacement and horizontal velocity over a period of about sixty hours. The model of Leonov and Miropolskiy (1973) is suitable for calculating the response to pressure but the results of Tomczak (1966, 1967), Krauss (1972a) and Mork (1968, 1972) indicate the pressure response is usually much smaller than the stress response.

In order to simplify the stress response model, the eddy coefficient approach will be avoided. The only models discussed above which allow arbitrary stratification and a realistic surface boundary condition in deriving the stress response are those of Mork (1968, 1972) and Krauss (1976a and b). Krauss' model is much too complex to be used to obtain a time response. The derivation of Mork's model is complicated a great deal by the inclusion of an eddy coefficient in what is only a marginally realistic manner. This added complication is not really necessary. The results of Krauss (1972b, 1976a and b) and the simple model of the previous chapter indicate deflections in the pycnocline are driven by Ekman pumping. Because the surface layer is unstratified or nearly so and because the stress goes to zero at its

base due to the strong stratification at the pycnocline, the total convergence is dependent only on the surface stress, not on the stress profile. Furthermore, the shear due to internal waves is zero in the unstratified surface layer. Because of this, internal waves probably have little direct effect on the stress profiles anyway. Thus, as pointed out by Geisler (1969), the stress may be assumed to act as a body force in the mixed layer. In fact, the stress response model by Mork (1968, 1972) probably amounts to a body force model in spite of the inclusion of an eddy coefficient. He decomposes the internal wave motions in normal modes which satisfy the zero surface stress condition. Thus, the solutions do not predict the true surface stress, only the internal wave response. His response is due to Ekman pumping driven by surface stress. Finally, use of the body force assumption avoids one problem encountered with the eddy coefficient models. That is, it is difficult to assess what effect errors in parameterizing the eddy coefficient may have on the model behavior. The eddy coefficients used by Mork and Krauss are not particularly realistic. Indeed realistic eddy coefficients for time varying boundary layer flows are only now being developed. It seems unwise to complicate a model with a crude parameterization of a poorly understood process when it is not necessary to do so.

In this work, stress will be assumed to act as a body force which matches an imposed stress at the surface and goes to zero at the pycnocline. Aside from these two conditions, the exact shape of the stress profile is left unspecified. In this way a simple model is developed which produces realistic behavior.

This approach can go awry if the surface stress is affected by the internal wave motions. With regard to wind stress forcing, the horizontal velocities due to internal waves are completely negligible relative to typical wind velocities; so, the surface stress (a function of the relative wind velocity), can be considered independent of the ocean response. Even for the case of ice stress on water, the ice velocity is expected to be much greater than the internal wave water velocity so the stress profile is independent of the internal wave response.

The only other problems created by not using an eddy coefficient approach is that the effect of frictional damping at the ocean bottom is ignored and the coupling of internal wave modes due to turbulent stress interaction is neglected. With regard to the first problem, the horizontal velocities at the ocean bottom are very small and bottom stress is not expected to be important during the initial generation of internal waves. The second problem is more complicated. As pointed out by Maurice Rattray (personal communication), turbulence should couple internal wave modes because when one mode produces turbulence and stress, the stress will excite motions in other modes. The simple eddy coefficient parameterization of Mork (1968, 1972) eliminates this coupling. Only a complicated numerical model such as Krauss' (1976a) can include this phenomena and the study of such an effect is beyond the scope of this work. Because the effect of internal waves on the stress profile is weak, the turbulent coupling of the modes is assumed to be negligible.

The model which will be developed here employs a thin

homogeneous surface layer (i.e., the mixed layer) overlying an ocean of arbitrary stratification. The kinematic boundary condition will be used. The response to forcing by surface stress will be derived in two ways, using normal mode decomposition and using an inverse Laplace transform technique. The pressure response of Leonov and Miropolskiy (1973) will be used and compared with one derived in Section 4.2 using normal mode decomposition.

In addition to deriving the response due to surface stress and pressure, another model will be derived in order to examine the effects of surface buoyancy flux. Actually the model is an extension of that by Magaard (1973) in that the same basic technique is used, but a real density distribution, rather than constant stratification, is employed.

4.2 Derivation of Response Functions for Internal Waves Driven by Surface Pressure and Stress

In this section the internal wave response to atmospheric pressure and surface stress is derived. Stratification is allowed to be arbitrary below a surface mixed layer of uniform density. Turbulent stresses are assumed negligible at the base of the mixed layer and below. Solutions are given as functions of time and horizontal wave numbers. A coordinate system with x to the north, y to the east, and z positive down is used. The ocean depth is H and the pycnocline depth is d (see Figure 3.12). (A list of symbols is given in Appendix C.)

If it is assumed that the motion is incompressible, that the waves are infinitesimal in amplitude and that the weak Bousinesq approximation holds, the equations of motion are

$$\rho_0 \left(\frac{\partial \bar{v}}{\partial t} + \bar{f} x \bar{v} \right) = -\Delta p + \frac{\partial \bar{\tau}}{\partial y} + \rho g \bar{k} \quad (4.2.1)$$

$$\Delta \cdot \bar{v} = 0 \quad (4.2.2)$$

and

$$\frac{\partial p}{\partial t} + w \frac{\partial \rho_0}{\partial z} = 0 \quad (4.2.3)$$

where

$$\frac{\partial \bar{\tau}}{\partial z} = - \frac{\partial}{\partial z} (\langle u' w' \rangle \bar{i} + \langle v' w' \rangle \bar{j} + \langle w' w' \rangle \bar{k}) \quad (4.2.4)$$

\bar{v} is the internal wave velocity perturbation vector

$$\bar{v} = u \bar{i} + v \bar{j} + w \bar{k}$$

and \bar{v}' is the turbulent velocity perturbation. The brackets, $\langle \rangle$, denote ensemble averaging. An f-plane ocean is assumed where f is the coriolis parameter,

$$\bar{f} = -f \bar{k}$$

The internal wave pressure perturbation about hydrostatic is p and the total density is

$$\rho = \rho_0(z) + \rho(x, y, z, t) + \rho'(x, y, z, t)$$

where ρ_0 is the mean density distribution, ρ is the internal wave perturbation and ρ' is the turbulent perturbation whose ensemble average is zero. The derivations of (4.2.1), (4.2.2) and (4.2.3) are given in Appendix B. The system of equations is similar to equation (2.18) given by Lumley and Panofsky (1964) and of the same form as (112.2), (112.4) and (112.3) in Krauss (1966).

Following Krauss (1966), the time derivative of the horizontal divergence of (4.2.1) can be combined with the curl of (4.2.1). Using the continuity conditions (4.2.2) yields

$$\rho_0 \left[\frac{\partial^3 w}{\partial t^2 \partial z} + f \frac{\partial w}{\partial z} \right] = \Delta_H \frac{\partial p}{\partial t} + f \left[\nabla_H \frac{\partial \bar{\tau}}{\partial z} \right]_z - \frac{\partial}{\partial t} \left[\nabla_H \cdot \frac{\partial \bar{\tau}}{\partial z} \right] \quad (4.2.5)$$

where Δ_H denotes the horizontal Laplacian, $\left(\frac{\partial^2}{\partial x^2} + \frac{\partial^2}{\partial y^2} \right)$, ∇_H denotes $\left(\frac{\partial}{\partial x} \bar{i} + \frac{\partial}{\partial y} \bar{j} \right)$, and $\left(\cdot \right)_z$ denotes a z component. Equation (4.2.5) is quite similar to Krauss' equation (112.6) except Krauss inconsistently uses f positive down. Taking the time derivative and horizontal Laplacian of the vertical component of (4.2.1) and using (4.2.3) yields

$$\rho_0 \Delta_H \frac{\partial^2 w}{\partial t^2} = -\Delta_H \frac{\partial^2 p}{\partial z \partial t} + \Delta_H \frac{\partial}{\partial t} \left[\frac{\partial \bar{\tau}}{\partial z} \right]_z - g_{dz} \frac{d\rho_0}{dz} \Delta_H w \quad (4.2.6)$$

Substituting this equation into the vertical derivative of (4.2.5) in order to eliminate the time derivative of p and letting $N^2 = \frac{g}{\rho_0} \frac{d\rho_0}{dz}$ gives the internal wave equation,

$$\frac{\partial^4 w}{\partial t^2 \partial z^2} + f^2 \frac{\partial^2 w}{\partial z^2} + \frac{N^2}{g} \left[\frac{\partial^3 w}{\partial t^2 \partial z} + f^2 \frac{\partial w}{\partial z} \right] + \frac{\partial^2}{\partial t^2} (\Delta_H w) + N^2 \Delta_H w = \frac{1}{\rho_0} \left[\Delta_H \frac{\partial}{\partial t} \left[\frac{\partial \bar{\tau}}{\partial z} \right]_z + f \left[\Delta_H \frac{\partial^2 \bar{\tau}}{\partial z^2} \right]_z - \frac{\partial}{\partial t} \left[\nabla_H \cdot \frac{\partial^2 \bar{\tau}}{\partial z^2} \right] \right] \quad (4.2.7)$$

In this application the vertical derivatives of stress in the boundary layer are very much greater than the horizontal derivatives so

$\Delta_H \left[\frac{\partial \bar{\tau}}{\partial z} \right]_z$ can be neglected in the forcing term on the right side of (4.2.7).

The boundary condition at the sea bottom is

$$w = 0 \quad @ z = H \quad (4.2.8)$$

The boundary condition of the sea surface is that the pressure be equal to atmospheric pressure. The incompressibility condition (equation B4) implies that, at the surface,

$$\frac{\partial p}{\partial t} = -wpg + \frac{\partial P_a}{\partial t} \quad @ z = 0$$

where P_a is the atmospheric pressure. Using this equation in (4.2.5) gives the boundary condition at the surface,

$$\frac{\partial^3 w}{\partial t^2 \partial z} + f^2 \frac{\partial w}{\partial z} + g \Delta_H w = \frac{1}{\rho_0} \left[\Delta_H \frac{\partial P_a}{\partial t} + f (\nabla_H \cdot \frac{\partial \tau}{\partial z}) \Big|_{z=0} \right. \\ \left. - \frac{\partial}{\partial t} (\nabla_H \cdot \frac{\partial \tau}{\partial z}) \Big|_{z=0} \right] \quad @ z = 0 \quad (4.2.9)$$

Equations (4.2.7), (4.2.8), and (4.2.9) are the basic equations to be solved in order to determine the internal wave response to surface stress and pressure. The biggest problem in solving these equations is that, strictly speaking, the stress terms are not decoupled from the velocity field. In this work it will be assumed that the stress field is determined strictly by the stress at the surface and is independent of the internal wave response. This amounts to an assumption that the stress acts as a body force but aside from being zero at the pycnocline and matching the surface stress, the details of the stress profile are

not specified. These assumptions are quite realistic. In the first instance the surface stress field is caused by wind or ice motion and the velocity defects associated with these forcings are typically much greater than the internal wave velocities. Also, the horizontal velocity perturbation is the sum of that due to the turbulent boundary layer motion and the internal wave response, but the turbulent stress is only important in the unstratified surface layer where the horizontal velocity component due to internal waves is constant and is not expected to contribute directly to the stress. The assumption that stress is negligible below the pycnocline is valid because strong stratification inhibits turbulence. McPhee (1974) has found this to be the case even during an Arctic storm.

To proceed, the equations are nondimensionalized by assuming

$$\rho_o = \rho_s r_o, \quad \rho_s = \rho_o @ z = 0 \quad (4.2.10)$$

$$x = Hx$$

$$y = Hy$$

$$z = Hz$$

$$t = f^{-1}t$$

$$\bar{\tau}(z) = \rho_s u_*^2 \bar{s}(z), \quad u_*^2 = \rho_s |\bar{\tau}(0)|_{\max}$$

$$w = Ww \quad W = \frac{u_*^2}{fH} \text{ for } u_*^2 \neq 0,$$

$$v = Wv$$

$$u = Wu$$

$$W = \frac{P_a |_{\max}}{\rho_s f H} \text{ for } u_*^2 = 0$$

$$p = P_d p$$

$$P_d = \rho_s WHf$$

$$P_a = P_d P_o$$

$$= P_a |_{\max} \text{ for } u_*^2 = 0$$

$$N^2 = f^2 N^2$$

$$= \rho_s u_*^2 \text{ for } u_*^2 \neq 0$$

$$\nabla_H \rightarrow H^{-1} \nabla_h$$

$$\frac{\partial}{\partial t} \rightarrow f \frac{\partial}{\partial t}$$

The (4.2.7) becomes

$$\begin{aligned} \frac{\partial^4 w}{\partial t^2 \partial z^2} + \frac{\partial^2 w}{\partial z^2} + \frac{N^2 H}{g} \left[\frac{\partial^3}{\partial t^2 \partial z} + \frac{\partial}{\partial z} \right] w + \frac{\partial^2}{\partial t^2} (\Delta_h w) \\ + \frac{N^2}{f^2} \Delta_h w = \frac{1}{r_0} \left[(\nabla_h \times \frac{\partial^2 \bar{s}}{\partial z^2}) - \frac{\partial}{\partial t} (\nabla_h \cdot \frac{\partial^2 \bar{s}}{\partial z^2}) \right] \end{aligned} \quad (4.2.11)$$

Equation (4.2.8) is

$$w = 0 \quad @ z = 1 \quad (4.2.12)$$

Noting that $r_0 = 1$ at the surface, and (4.2.9) becomes

$$\begin{aligned} \frac{\partial^3 w}{\partial t^2 \partial z} + \frac{\partial w}{\partial z} + \frac{g}{f^2 H} \Delta_h w = \Delta_h \frac{\partial p_0}{\partial t} \\ + (\nabla_h \times \frac{\partial \bar{s}}{\partial z}) - \frac{\partial}{\partial t} (\nabla_h \cdot \frac{\partial \bar{s}}{\partial z}) \quad @ z = 0 \end{aligned} \quad (4.2.13)$$

Alternatively, equations (4.2.7), (4.2.8) and (4.2.9) can be integrated in time assume zero initial conditions in order to obtain equations in terms of the displacement, ζ_w , where

$$\frac{\partial \zeta_w}{\partial t} = w$$

Nondimensionalizing the resulting equation assuming

$$\zeta_w = \zeta \frac{u_*^2}{f^2 H} \quad (4.2.14)$$

results in:

$$\frac{\partial^4 \zeta}{\partial z^2 \partial t^2} + \frac{\partial^2 \zeta}{\partial z^2} + \frac{N^2 H}{g} \left[\frac{\partial^3 \zeta}{\partial z \partial t^2} + \frac{\partial \zeta}{\partial z} \right] + \frac{\partial^2}{\partial t^2} (\Delta_h \zeta) \quad (4.2.15)$$

$$+ \frac{N^2}{f^2} \Delta_h \zeta = \frac{1}{r_0} \left[\int_0^t (\nabla_h \times \frac{\partial^2 \bar{s}}{\partial z^2}) d\xi - \nabla_h \cdot \frac{\partial^2 \bar{s}}{\partial z^2} \right]$$

$$\zeta = 0 \quad @ z = 1 \quad (4.2.16)$$

and

$$\frac{\partial^3 \zeta}{\partial t^2 \partial z} + \frac{\partial \zeta}{\partial z} + \frac{g}{f^2 H} \Delta_h \zeta = \quad (4.2.17)$$

$$\Delta_h \zeta|_0 + \int_0^t \nabla_h \times \frac{\partial \bar{s}}{\partial z}|_{z=0} d\xi - \nabla_h \cdot \frac{\partial \bar{s}}{\partial z}|_{z=0} \quad @ z = 0$$

This form of the equations has the advantage that, when estimates of actual stresses are used, the data can be integrated in time rather than differentiated in order to estimate the forcing term. Thus the forcing estimates will be less sensitive to noisy data.

These equations are solved by taking their Laplace transform (the Laplace variable is σ) and their two dimensional Fourier transform in the horizontal coordinates (variable is $\bar{k} = k_i^2 + k_j^2$). Assuming zero initial conditions (4.2.15) becomes

$$\frac{\partial^2 \phi}{\partial z^2} + \frac{N^2 H}{g} \frac{\partial \phi}{\partial z} - \frac{N^2 + \sigma^2}{\sigma^2 + 1} k^2 \phi + \frac{\Sigma''}{r_0 (\sigma^2 + 1)} \quad (4.2.18)$$

where $\phi(\sigma, \bar{k}, z)$ is the Laplace transform of the Fourier transform of ζ . k is the magnitude of \bar{k} , and

$$\Sigma''(\sigma, z) = \frac{\partial^2 \Sigma}{\partial z^2} = \mathcal{L} \left[\mathcal{F} \left[\int_0^t \nabla_h \times \frac{\partial^2 \bar{s}}{\partial z^2} d\xi - \nabla_h \cdot \frac{\partial^2 \bar{s}}{\partial z^2} \right] \right]$$

where $\mathcal{L} []$ denotes the Laplace transform and $\mathcal{F} []$ denotes the Fourier transform. Equation (4.2.16) becomes

$$\phi = 0 \quad @ z = 1 \quad (4.2.19)$$

and (4.2.17) becomes

$$\frac{\partial \phi}{\partial z} - \frac{g}{Hf^2} \frac{k^2}{(\sigma^2 + 1)} \phi = \quad @ z = 0 \quad (4.2.20)$$

$$\frac{1}{(\sigma^2 + 1)} \left[-k^2 \tilde{P}_o + \Sigma'_o \right] = \frac{\Pi(\sigma, \bar{k})}{(\sigma^2 + 1)}$$

where Σ'_o is $\Sigma'(\sigma, \bar{k}, 0)$ and \tilde{P}_o is the transformed atmospheric pressure.

There are two ways to solve (4.2.18), (4.2.19) and (4.2.20). A method which produces results which have a relatively simply physical interpretation can be obtained if the equations are decomposed into the eigenfunctions of the unforced equation with homogeneous boundary conditions. In order to do this the system of equations is first converted to one with homogeneous boundary conditions. Letting

$$\psi(\sigma, \bar{k}, z) = \phi + \frac{(\sigma^2 + 1)}{\sigma^2 + \omega_B^2} \frac{\Pi}{r_o(\sigma^2 + 1)} (1 - z) \quad (4.2.21)$$

Equation (4.2.18) becomes

$$\begin{aligned} \frac{\partial^2 \psi}{\partial z^2} + \frac{N^2 H}{g} \frac{\partial \psi}{\partial z} - \frac{N^2 + \sigma^2}{\sigma^2 + 1} k^2 \psi &= \frac{F}{r_o(\sigma^2 + 1)} = \\ \frac{1}{r_o(\sigma^2 + 1)} \Sigma'' - \frac{N^2 H}{g} \left(\frac{\sigma^2 + 1}{\sigma^2 + \omega_B^2} \right) \frac{\Pi}{r_o(\sigma^2 + 1)} & \\ - \frac{(N^2 + \sigma^2) k^2}{(\sigma^2 + \omega_B^2)} \frac{\Pi(1 - z)}{r_o(\sigma^2 + 1)} & \end{aligned} \quad (4.2.22)$$

where

$$\omega_B^2 = 1 + \frac{gk^2}{Hf^2}$$

Equation (4.2.19) yields

$$\psi = 0 \quad @ z = 1 \quad (4.2.23)$$

From (4.2.20) we obtain a homogeneous surface boundary condition for ψ ,

$$\frac{\partial \psi}{\partial z} - \frac{gk^2}{Hf^2(\sigma^2 + 1)} \psi = 0 \quad @ z = 0 \quad (4.2.24)$$

Equations (4.2.22), (4.2.23) and (4.2.24) with F set equal to zero comprise a second order eigenvalue problem. For a given k^2 , solutions exist only for a denumerably infinite number of values of the eigenvalue $\lambda_n = -\frac{k^2}{\sigma_n^2 + 1}$. The eigenfunction corresponding to each eigenvalue will be denoted ψ . Because the eigenvalue appears in the boundary condition, (4.2.24), the eigenfunctions are not precisely orthogonal but according to Mierovitch (1976) they obey a modified orthogonality relation. Namely, for $n \neq m$,

$$\begin{aligned} \int_0^1 (N^2 - 1) r_o \psi_n \psi_m dz &= \frac{-gr_o}{Hf^2} \psi_n \Big|_{z=0} \psi_m \Big|_{z=0} \\ &= -\frac{\psi_n'}{\lambda_n} \Big|_{z=0} \psi_m \Big|_{z=0} = -\psi_n \Big|_{z=0} \frac{\psi_m}{\lambda_m} \Big|_{z=0} \end{aligned}$$

The eigenfunctions are normalized by setting

$$\int_0^1 (N^2 - 1) r_o \psi_n^2 dz = 1$$

When this is done for a typical example, the maximum value of

$(\frac{\psi_n'}{\lambda_n} \psi_m) \Big|_{z=0}$ occurs for $n = 1$ and $m = 2$ and is about 6×10^{-4} , decreasing

with increasing n . Thus, the coupling between the modes is very weak and it will be assumed that

$$\int_0^1 (N^2 - 1) r_o \psi_n \psi_m dz = \delta_{nm} \quad (4.2.25)$$

This amounts to assuming a rigid lid for the purpose of decomposing the forcing, $\frac{F}{r_o(\sigma^2 + 1)}$ into modes. The rigid lid does, however, impose a pressure at the surface equal to that which would be produced by the actual surface deflection and the surface forcing, F , has been imposed by the change in variable from ϕ to ψ . The mode shapes correspond to those of the system with a free surface.

There is another problem due to the presence of the eigenvalue in the boundary condition. When the solution is decomposed into eigenfunctions, the boundary condition (4.2.24) cannot be satisfied exactly because the eigenfunctions satisfy the boundary condition only for $\sigma = \sigma_n$. The maximum error resulting from this mismatch has been found to be about 1 percent of the total pressure response and will be neglected.

Assuming a solution of the form,

$$\psi = \sum_{n=1}^{\infty} a_n \psi_n$$

and using the fact that ψ_n is the solution to the homogeneous problem equation (4.2.22) becomes

$$\sum_{n=1}^{\infty} a_n \left[\frac{(N^2 - 1)(\sigma^2 - \sigma_n^2)}{(\sigma_n^2 + 1)} \right] k^2 r_o \psi_n = F$$

Multiplying this result by ψ_m , integrating from $z = 0$ to $z = 1$, and using (4.2.25) yields

$$a_n = \frac{(\sigma_n^2 + 1)}{(\sigma^2 - \sigma_n^2)k^2} \int_0^1 F \psi_n dz$$

Therefore

$$\psi(\sigma, \bar{k}, z) = \sum_{n=1}^{\infty} \frac{(\sigma_n^2 + 1)}{(\sigma^2 - \sigma_n^2)k^2} \left[\int_0^1 F \psi_n dz \right] \psi_n(z) \quad (4.2.26)$$

Now the components of forcing for each mode, $\int_0^1 F \psi_n dz$ will be examined. From (4.2.22),

$$F = \Sigma'' - \frac{N^2 H}{g} \left(\frac{\sigma^2 + 1}{\sigma^2 + \omega_B^2} \right) \Pi - \frac{(N^2 + \sigma^2)k^2}{(\sigma^2 + \omega_B^2)} \Pi(1 - z)$$

For the Beaufort Sea, $N^2 H/g$ is of order 10^{-3} , N^2 is of order 6×10^2 , and the minimum value of k^2 is 4×10^{-4} . Therefore, the second term on the right side is always negligible compared to the last term.

Breaking Π down using (4.2.20), F can be written as

$$F = \Sigma'' - \frac{(N^2 + \sigma^2)k^2}{(\sigma^2 + \omega_B^2)} \Sigma'_0(1-z) + \frac{(N^2 + \sigma^2)k^4}{(\sigma^2 + \omega_B^2)} \tilde{\Sigma}'_0(1-z) \quad (4.2.27)$$

The forcing is divided into that due to stress and that due to surface pressure. In order to evaluate $\int_0^1 \Sigma'' \psi_n dz$, the stress profile must be considered in view of the assumed density profile. The stress is zero for depths greater than or equal to d . As has been mentioned in Chapter 3, the maximum boundary layer thickness was only 16 m during the AMLE, even less than the 20 m mixed layer depth. Therefore, the stress and stress gradient are assumed negligible at the bottom of the mixed layer. Also, because the mixed layer is unstratified, ψ'_n is virtually constant there. A scaling analysis applied to (4.2.18) indicates the

change in ψ'_n over the whole mixed layer is $k^2\delta^2$, where δ is the nondimensional mixed layer depth, d/H . For the largest k^2 to be considered, this change amounts to only 0.8 percent. With the above assumptions.

$$\begin{aligned} \int_0^1 \Sigma''\psi_n dz &= \int_0^\delta \Sigma''\psi_n dz = \Sigma'\psi_n|_0 - \int_0^\delta \Sigma'\psi'_n dz \\ &= \Sigma'\psi_n|_0 + \Sigma_0\psi'_n|_0 \end{aligned}$$

For realistic stress profiles and computed eigenfunctions the first term on the right is 1 percent to 10 percent of the second term and will be neglected, so

$$\int_0^1 \Sigma''\psi_n dz \approx \Sigma_0\psi'_n|_0 \quad (4.2.28)$$

Thus, the internal wave forcing due to the first term on the right of (4.2.27) is independent of the stress profile shape in the turbulent boundary layer. Furthermore, the integral of second term on the right of (4.2.27) multiplied times ψ'_n scales as

$$\frac{k^2}{\omega_B^2} \Sigma_0\psi'_n|_0 \delta \approx \frac{Hf^2}{g} \Sigma_0\psi'_n|_0 < 10^{-5} \Sigma_0\psi'_n|_0$$

and is completely negligible. Thus, the total forcing due to surface stress is completely independent of the stress profile shape. It is due only to surface stress (i.e. wind or ice stress) because the internal waves are driven by convergence and divergence in the mixed layer and these are, in turn, dependent only on the surface stress.

Neglecting the second term on the right of (4.2.27) and substituting this equation, along with (4.2.28), into (4.2.26) yields the

internal wave responses to surface stress and surface pressure. The stress response is

$$\psi_{\Sigma}(\sigma, \bar{k}, z) = \sum_{n=1}^{\infty} \psi_n(z) \frac{(\sigma_n^2 + 1)\psi_n'|_0}{(\sigma^2 - \sigma_n^2)k^2} \Sigma_0(\sigma, \bar{k}) \quad (4.2.29)$$

and the pressure response is

$$\psi_p(\sigma, \bar{k}, z) = \sum_{n=1}^{\infty} \psi_n(z) \frac{(\sigma_n^2 + 1)}{(\sigma^2 - \sigma_n^2)k^2} \cdot A \cdot k^4 \tilde{p}_0(\sigma, \bar{k}) \quad (4.2.30)$$

where

$$A = \int_0^1 \left(\frac{N^2 + \sigma^2}{\sigma^2 + \omega_B^2} \right) (1-z) \psi_n dz \quad (4.2.31)$$

To obtain the solutions as functions of time the inverse Laplace transforms (denoted \mathcal{L}^{-1}) of (4.2.29) and (4.2.30) must be taken. This can be done using standard theorems. For any two functions of time $x(t)$ and $y(t)$ with Laplace transforms $X(\sigma)$ and $Y(\sigma)$,

$$\mathcal{L}^{-1}[X(\sigma) \cdot Y(\sigma)] = \int_0^t x(t-\alpha) y(\alpha) d\alpha \quad (4.2.32)$$

Also,

$$\mathcal{L}^{-1} \left[\frac{\omega_n}{\sigma^2 + \omega_n^2} \right] = \sin \omega_n t \quad (4.2.33)$$

Recall that

$$\lambda_n = \frac{-k^2}{\sigma_n^2 + 1} \quad (4.2.34)$$

where λ_n is the eigenvalue (real) for the unforced problem and

$$\sigma_n = \pm i\omega_n$$

where ω_n is a real frequency, greater than unity (i.e. the free wave frequency is greater than the inertial frequency). Using these identities the inverse Laplace transform of ψ_Σ is

$$\psi_\Sigma(t, \bar{k}, z) = \mathcal{L}^{-1}[\psi_\Sigma] = \sum_{n=1}^{\infty} -\frac{\psi_n(z)\psi_n'|_0}{\lambda_n \omega_n} \int_0^t T_o(\alpha, \bar{k}) \sin \omega_n(t-\alpha) d\alpha \quad (4.2.35)$$

where T_o is the inverse Laplace transform of Σ_o or:

$$\begin{aligned} T_o &= \mathcal{F}[\tau_o] = \mathcal{F} \left[\int_0^t (\nabla_n x \bar{s}_o) d\xi - \nabla_n \cdot \bar{s}_o \right] \quad (4.2.36) \\ &= \mathcal{F} \left[\int_0^t -(\nabla_n x \bar{s}_s) d\xi + \nabla_h \cdot \bar{s}_s \right] \end{aligned}$$

\bar{s}_s is the normalized applied surface stress and, because z is positive down it is equal to minus the surface shear stress, \bar{s}_o .

In order to simplify taking the inverse Laplace transform of (4.2.30), note that ω_B , the characteristic frequency of the barotropic mode, is two orders of magnitude larger than the values of σ important in this problem. Also note that, for any function of time, $x(t)$ with $\dot{x}(0) = x(0) = 0$ and with Laplace transform $X(\sigma)$,

$$[\ddot{x}(t)] = \sigma^2 X(\sigma)$$

Then, using this relation, (4.2.33), and (4.2.34), the inverse Laplace transform of (4.2.30) is

$$\Psi_p(t, \bar{k}, z) = \mathcal{L}^{-1}[\psi_p] = \sum_{n=1}^{\infty} \left[\frac{-\psi_n(z)k^4}{\lambda_n} \left[\frac{1}{\omega_B^2 \omega_n} \int_0^1 N^2(1-z)\psi_n dz - \right. \right. \\ \left. \left. \frac{\omega_n}{\omega_B^2} \int_0^1 (1-z)\psi_n dz \right] \cdot \int_0^t P_1(\alpha) \sin \omega_n(t-\alpha) d\alpha \right] \quad (4.2.37)$$

where P_1 is the inverse Laplace transform of \tilde{P}_0 ,

$$P_1(t, \bar{k}) = \mathcal{F}^{-1}[P_0(t, x, y)] = \mathcal{L}^{-1}[\tilde{P}_0(\sigma, k)]$$

The responses from (4.2.35) and (4.2.37) may be added to obtain the total response to surface stress and pressure. The forcing must be Fourier decomposed in x and y and the solutions are expressed as Fourier components.

It is informative to derive the response function for stress forcing in an alternate way. The approach is analogous to that used by Leonov and Miropolskiy (1973) to determine the pressure response. The technique involves integrating the equations of motion explicitly. Non-dimensionalizing (4.2.5), using (4.2.10), and integrating in time yields

$$\frac{\partial^2 \zeta}{\partial t^2 \partial z} + \frac{\partial \zeta}{\partial z} = \frac{1}{r_0} \Delta_h p + \frac{1}{r_0} \left[\int_0^t \left(\nabla_n \times \frac{\partial \bar{s}}{\partial z} \right) d\xi - \nabla_n \cdot \frac{\partial \bar{s}}{\partial z} \right] \quad (4.2.38)$$

Taking the Laplace and Fourier transforms of this equation gives

$$(\sigma^2 + 1) \frac{\partial \phi}{\partial z} = -k^2 \tilde{p} + \Sigma' \quad (4.2.39)$$

where \tilde{p} is the Laplace-Fourier transform of p . Denoting $\phi(z=0)$ as

ϕ_0 and $\phi(z = \delta)$, as ϕ_δ , integration of (4.2.39) yields

$$(\sigma^2 + 1)(\phi_0 - \phi_\delta) = k^2 \int_0^\delta \tilde{p} d\xi + \Sigma_0 \quad (4.2.40)$$

If the non-dimensionalized vertical momentum equation is integrated in z from the surface and the turbulent vertical normal stress, s_z , is assumed zero at the surface, an expression for pressure results,

$$p - s_z = p|_{z=0} - r_0 \int_0^z \frac{\partial w}{\partial t} d\xi \quad (4.2.41)$$

Where $p|_{z=0}$ is the surface pressure. Assuming atmospheric pressure is zero, the incompressibility condition relates p_0 to ζ_0 . Substituting this relation into (4.2.41), taking the Laplace and Fourier transforms, and multiplying by k^2 yields

$$k^2 \tilde{p} = - \frac{g}{Hf^2} k^2 \phi_0 + k^2 E \quad (4.2.42)$$

where

$$E(\sigma, \bar{k}, z) = \mathcal{L} \left[\tilde{p} \left[-r_0 \int_0^z \frac{\partial w}{\partial t} d\xi + s_z \right] \right]$$

Inserting (4.2.42) into (4.2.40) gives

$$(\sigma^2 + 1)(\phi_0 - \phi_s) = - \frac{g\delta}{Hf^2} k^2 \phi_0 + k^2 \int_0^\delta E dz + \Sigma_0 \quad (4.2.43)$$

and inserting (4.2.42) into (4.2.39) yields, for $z = \delta$,

$$\phi_o = \frac{Hf^2}{gk^2} \left[(\sigma^2 + 1) \frac{\partial \phi_\delta}{\partial z} - \Sigma_\delta' + k^2 E_\delta \right] \quad (4.2.44)$$

Substituting (4.2.44) into (4.2.43) gives an expression relating ϕ_δ to the surface stress,

$$(\sigma^2 + 1) \left(\left[\frac{Hf^2}{gk^2} (\sigma^2 + 1) + \delta \right] \frac{\partial \phi_\delta}{\partial z} - \phi_\delta \right) = \Sigma_o \quad (4.2.45)$$

$$+ \underbrace{\left((\sigma^2 + 1) \frac{Hf^2}{gk^2} + \delta \right) \Sigma_\delta'}_{(a)} - \underbrace{(\sigma^2 + 1) \frac{Hf^2}{gk^2} E_\delta}_{(b)} + \underbrace{\delta k^2 E_\delta + k^2 \int_0^\delta E dz}_{(c)}$$

For the problem to be examined here, the neutral boundary layer thickness is less than the pycnocline depth and the term, (a) involving Σ_δ' can be neglected to an accuracy of better than 10 percent. Because s_z goes to zero at $z = \delta$, E_δ only involves an integral of vertical acceleration in the mixed layer. The motions are slow enough so that the pressure in the mixed layer is nearly hydrostatic and (b) and the first term of (c) are less than a few percent of Σ_o . Scaling arguments also indicate the second term in (c), which involves vertical accelerations and s_z , is always small relative to Σ_o and is negligible at horizontal wave numbers where stress forcing is important. Thus, to an accuracy of 10 percent (4.2.45) can be written as

$$(\sigma^2 + 1) \left(\frac{\delta \frac{gk^2}{Hf^2} + \sigma^2 + 1}{\frac{Hf^2}{gk^2}} \frac{\partial \phi_\delta}{\partial z} - \phi_\delta \right) = \Sigma_o \quad @ z = \delta \quad (4.2.46)$$

This equation and (4.2.19) can be used as a boundary condition for solution of the homogeneous internal wave equation, applicable for

z greater than δ ,

$$\frac{\partial^2 \phi}{\partial z^2} + \frac{N^2 H}{g} \frac{\partial \phi}{\partial z} - \frac{N^2 + \sigma^2}{\sigma^2 + 1} k^2 \phi = 0 \quad (4.2.47)$$

The homogeneous boundary condition corresponding to (4.2.46) is really the same as the homogeneous version of (4.2.20),

$$(\phi^2 + 1) \frac{\partial \phi_0}{\partial z} - \frac{gk^2}{Hf^2} \phi_0 = 0 \quad @ z = 0 \quad (4.2.48)$$

In order to see this, recall that the internal wave equation (4.2.47) implies ϕ' is constant in the mixed layer, so, the above equation can be written as

$$(\sigma^2 + 1) \frac{\partial \phi_\delta}{\partial z} - \frac{gk^2}{Hf^2} \left(\phi_\delta - \frac{\partial \phi_\delta}{\partial z} \delta \right) = 0$$

which can be rewritten as

$$\frac{\delta \frac{gk^2}{Hf^2} + \sigma^2 + 1}{gk^2/Hf^2} \frac{\partial \phi_\delta}{\partial z} - \phi_\delta = 0 \quad @ z = \delta \quad (4.2.49)$$

Equation (4.2.49) is the homogeneous version of (4.2.46). Therefore, functions satisfying the free wave conditions for the whole water column [equations (4.2.47), (4.2.48) and (4.2.19)] also satisfy the free wave conditions for $z \geq \delta$ [equations (4.2.47), (4.2.49) and (4.2.19)].

To solve for the forced response for $z \geq \delta$, equations (4.2.46), (4.2.47) and (4.2.19), a method similar to that of Leonov and Miropol-skiy (1973) is used. It is assumed that

$$\phi_{\Sigma} = C_{\Sigma}(k^2, \sigma^2) v(k^2, \sigma^2, z)$$

where v satisfies (4.2.19) and (4.2.47) and is of arbitrary amplitude (v' is an arbitrary constant at $z = 1$). For σ equal to the eigenfrequency, v also satisfies the boundary conditions (4.2.48) and (4.2.49).

So,

$$v = \psi_n @ \sigma = \sigma_n \quad (4.2.50)$$

In general,

$$C_{\Sigma}(k^2, \sigma^2) = \frac{\Sigma_0}{(\sigma^2 + 1) \left[\left(\frac{Hf^2}{gk^2} (\sigma^2 + 1) + \delta \right) \frac{\partial v_{\delta}}{\partial z} - v_{\delta} \right]}$$

where v_{δ} and $\frac{\partial v_{\delta}}{\partial z}$ denote v and $\frac{\partial v}{\partial z}$ at $z = \delta$. Then

$$\phi_{\Sigma} = \frac{v \Sigma_0}{(\sigma^2 + 1) \left[\left(\frac{Hf^2}{gk^2} (\sigma^2 + 1) + \delta \right) \frac{\partial v_{\delta}}{\partial z} - v_{\delta} \right]} \quad (4.2.51)$$

To take the inverse Laplace transform of (4.2.51), recall (4.2.32). Then

$$\Phi_{\Sigma}(t, \bar{k}, z) = \int_0^+ R(t - \alpha) T_0(\alpha) d\alpha \quad (4.2.52)$$

and the function R is

$$R(t, \bar{k}, z) = \mathcal{L}^{-1} \left[\frac{v}{(\sigma^2 + 1) \left(\left(\frac{Hf^2}{gk^2} (\sigma^2 + 1) + \delta \right) \frac{\partial v_\delta}{\partial z} - v_\delta \right)} \right] \quad (4.2.53)$$

$$= \frac{1}{2\pi i} \int_{\sigma_{r-i} - \infty}^{\sigma_r + i\infty} \frac{v e^{\sigma t}}{(\sigma^2 + 1) L_o} d\sigma$$

The last integral is based on the definition of the inverse Laplace transform. σ_r is a real constant to the right of any singularities of the integrand in the complex σ plane. L_o is

$$L_o = \left(\left(\frac{Hf^2}{gk^2} (\sigma^2 + 1) + \delta \right) \frac{\partial v_\delta}{\partial z} - v_\delta \right)$$

To integrate (4.2.53), consider the complex σ plane in Figure 4.1. The poles of the integrand are at the zeros of L_o . These zeros occur at the values of σ , $\sigma = \pm i\omega_n$, corresponding to the eigenfrequencies of the homogeneous problem defined by equations (4.2.47), (4.2.49) and (4.2.19) or equations (4.2.47), (4.2.48) and (4.2.19). The eigen frequencies, ω_n , are greater than 1 and less than the maximum N . At first it appears that there are poles at $\sigma = \pm i$ but in fact these are canceled by zeros in L_o at $\sigma = \pm i$. This is so because the non-dimensional frequency equal to unity corresponds to the inertial frequency and free inertial oscillations involve no vertical motion. Furthermore, examination of equation (4.2.45) shows that $(\sigma^2 + 1)L_o$ is really an approximation for a term which, if (c) of (4.2.45) were included, would not be zero at $\sigma = \pm i$. At the other poles, neglect of the terms

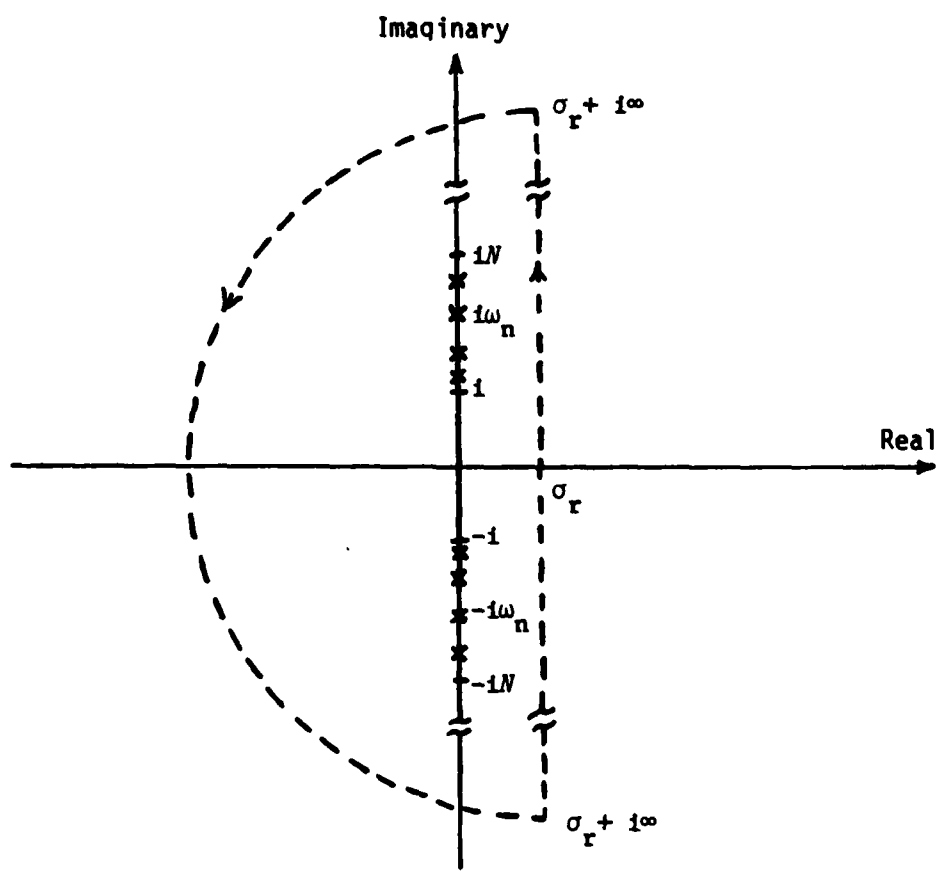


Figure 4.1. Contour of integration in the complex σ plane for solving the stress forced problem.

(b) and (c) would produce a very slight shift in eigenfrequencies but, by using (4.2.47), (4.2.48), and (4.2.19) to solve for the eigenfrequencies, this problem is avoided.

To perform the integration of equation (4.2.53), the line of integration from $\sigma_r - i\infty$ to $\sigma_r + i\infty$ is extended around the poles by adding the semicircular loop at $|\sigma| = \infty$. The magnitude of v is arbitrary but finite and L_o is non zero for $|\sigma| > N$. So, as σ goes to infinity, the magnitude of the integrand around the semicircle goes as $\sigma/(\sigma^2 + 1)$ and is zero for $\sigma = \infty$. Therefore, the integral (4.2.53), is equal to the integral around the closed contour and can be evaluated using the calculus of residues.

From Churchill (1960) the countour integral taken counterclockwise around a group of poles is equal to $2\pi i$ times the sum of the residues of those poles. Also, if a function $f(\sigma)$ is of the form:

$$f(\sigma) = \frac{x(\sigma)}{y(\sigma)}$$

and has a simple pole at σ_o so that $y'(\sigma) \neq 0$, then the residue of $f(\sigma)$ at σ_o is

$$b = \frac{x(\sigma_o)}{y'(\sigma_o)}$$

The integrand of equation (4.2.53) is of this form. So.

$$R(t, \bar{k}, z) = \sum_{\text{all } \sigma_n} - \frac{\psi_n^{\sigma_n t}}{2\sigma_n \lambda_n L'_o} \quad (4.2.54)$$

$\lambda = \lambda_n$

where

$$L'_o = \frac{\partial L_o}{\partial \lambda} \quad (4.2.55)$$

and

$$\lambda = \frac{-k^2}{\sigma^2 + 1}$$

Equations (4.2.54) and (4.2.55) may be somewhat confusing. Remember, L_o is a function of v evaluated at δ and, as λ goes to λ_n , v changes in such a way that L_o goes to zero and v becomes ψ_n , the eigenfunction.

$L'_o|_{\lambda=\lambda_n}$ is the rate, evaluated at $\lambda = \lambda_n$, at which L_o goes to zero with changes in λ . The amplitude of v has no effect on equation (4.2.53) because the amplitude of v in the numerator cancels the amplitude of v in L'_o .

For each value of n there are two poles. Combining the residues at each value of n yields

$$R(t, \bar{k}, z) = \sum_{n=1}^{\infty} -\frac{\psi_n}{2\lambda_n L'_o|_{\lambda=\lambda_n}} \left(\frac{1}{i\omega_n} e^{i\omega_n t} - \frac{1}{i\omega_n} e^{-i\omega_n t} \right)$$

The zeroeth mode, ($n = 0$), corresponds to the barotropic wave mode and can be ignored to get the internal wave response corresponding to Ψ_{Σ} in the previous derivation. (The difference between Ψ and Φ is due to barotropic motion.) Then after some trigonometric manipulations it can be shown that

$$R(t, \bar{k}, z) = \sum_{n=1}^{\infty} \frac{-\psi_n \sin \omega_n t}{\lambda_n \omega_n L'_o|_{\lambda=\lambda_n}}$$

so, neglecting the barotropic motions, equation (4.2.52) becomes

$$\Psi_{\Sigma}(t, \bar{k}, z) = \sum_{n=1}^{\infty} \left[\frac{-\psi_n}{\lambda_n \omega_n L'_0} \right]_{\lambda=\lambda_n} \int_0^t T_0(\alpha) \sin \omega_n(t-\alpha) d\alpha \quad (4.2.56)$$

The solution for pressure response which is analogous to (4.2.56) is given by Leonov and Miropolskiy (1973). They solve the homogeneous internal wave equation with the boundary condition of equation (4.2.20) but with Σ_0 equal to zero. After correction of a factor of two error and modification to allow the use of a different form of L_p , their solution is

$$\Psi_p(t, \bar{k}, z) = \sum_{n=1}^{\infty} \frac{k^2 \psi_n}{\lambda_n \omega_n L'_p} \int_0^t P_1(\alpha) \sin \omega_n(t-\alpha) d\alpha \quad (4.2.57)$$

where

$$L'_p = \left. \frac{\partial L_p}{\partial \lambda} \right|_{\lambda=\lambda_n} = \left. \frac{\partial}{\partial \lambda} \left[\frac{\partial u}{\partial z} - \frac{gk^2}{Hf^2(\sigma^2 + 1)} u \right] \right|_{z=0}$$

The method of solution used to obtain equations (4.2.56) and (4.2.57) decomposes the solution into eigenfunctions of the homogeneous problem and takes the inverse Laplace transform in one operation. The orthogonality of the eigenfunctions is not a factor in the derivations. Equations (4.2.35) and (4.2.37) are derived in a different way but are of the same form as (4.2.56) and (4.2.57) and both types of solution have been computed numerically. The details will be given in

Sections 4.4 and 4.5 but the important point is: (4.2.35) and (4.2.56) produce virtually identical results as do (4.2.37) and (4.2.57). In general

$$\Psi_{\Sigma} = \sum_{n=1}^{\infty} \frac{\psi_n}{\lambda_n \omega_n} R_{\Sigma} \int_0^t T_o(\alpha) \sin \omega_n(t - \alpha) d\alpha \quad (4.2.58)$$

and

$$\Psi_p = \sum_{n=1}^{\infty} \frac{\psi_n}{\lambda_n \omega_n} R_p \int_0^t k^2 p_i(\alpha) \sin \omega_n(t - \alpha) d\alpha \quad (4.2.59)$$

where the response factors are

$$R_{\Sigma} = \frac{-1}{L_o' \Big|_{\lambda=\lambda_n}} \approx -\psi_n' \Big|_{z=0} \quad (4.2.60)$$

and

$$R_p = \frac{1}{L_p' \Big|_{\lambda=\lambda_n}} \approx -k^2 \left[\frac{1}{\omega_B^2} \int_0^1 N^2 (1 - z) \psi_n dz - \frac{\omega_n^2}{\omega_B^2} \int_0^1 (1 - z) \psi_n dz \right] \quad (4.2.61)$$

The response of (4.2.58) and (4.2.59) are given in terms of the eigenfunctions of the free waves and the forcings are convolved with the resonant response for each mode. The stress response is driven by the curl and divergence of surface stress, T_o in (4.2.36), while the pressure response is driven by the Laplacian of the applied surface pressure $k^2 p_i$.

The response factors derived using the method of Leonov and Miropolskiy are inversely related to the sharpness of the resonance peak. For example consider the pressure forced case; if the homogeneous boundary condition is nearly satisfied for a broad range of frequencies about a particular eigenfrequency, L'_p is small and, if there is any energy in P_1 near the eigenfrequency, the model response is large. If the resonance is sharp, L'_p is large and not much energy goes into the mode. The same argument applies to the stress forced problem.

The response factor derived for stress using the normal mode decomposition is understandable in terms of power input. As will be shown, the horizontal velocity due to motion of mode n is proportional to ψ'_n . So, horizontal stress (proportional to Σ_o) times ψ'_n is proportional to the power input to the mode. The power is integrated in time to produce the modal displacement which is a measure of potential energy. Therefore, the larger the modal horizontal velocity, ψ'_n , the greater the amount of energy that can be put into the mode. This solution is similar to that of Mork (1968, 1972) in that the response is proportional to ψ'_n . Goodman and Levine (1973) indicate the response is inversely proportional to ψ'_n . Their erroneous result is due to a misunderstanding of L'_p . It must be remembered that u is a function not only of z , but of λ (or σ) as well. Only at $\lambda = \lambda_n$ (or $\sigma = \sigma_n$) is $u = \psi_n$. Generally

$$L'_o \Big|_{z=\delta} = \frac{Hf^2}{\lambda^2 g} \frac{\partial u}{\partial z} \Big|_{z=\delta} + \left(-\frac{Hf^2}{\lambda g} + \delta \right) \frac{\partial \tilde{u}}{\partial z} \Big|_{z=\delta} - \tilde{u} \quad (4.2.62)$$

and

$$L'_p \Big|_{z=\delta} = \frac{\partial \tilde{U}}{\partial z} \Big|_{z=\delta} - \lambda \frac{g}{Hf^2} \tilde{U} \Big|_{z=\delta} - \frac{g}{Hf^2} U \quad (4.2.63)$$

where

$$\tilde{U} = \frac{\partial U}{\partial \lambda} \quad (4.2.64)$$

When L'_o and L'_p are evaluated at $\lambda = \lambda_n$, the λ go to λ_n and the U go to ψ_n in equations (4.2.62) and (4.2.63) but \tilde{U} is not zero as Goodman and Levine claim. In this work the function \tilde{U} is evaluated for $\lambda = \lambda_n$ and terms involving it are found to dominate equations (4.2.62) and (4.2.63). The differential equations and boundary conditions for determining \tilde{U} are given in Section 4.4.

The response factor derived for pressure using normal mode decomposition is inversely proportional to the surface stiffness as represented by ω_B^2 . The response is largest for modes that have large values of ψ_n in the upper ocean. Since the pressure acts vertically, it is to be expected that the amount of energy going into a mode increases as the modal vertical velocity (proportional to ψ_n) increases near the surface.

Before applying equations (4.2.58) through (4.2.61) to an actual problem the expressions for horizontal velocity in a forced internal wave will be derived. The Laplace transform in time and Fourier transform in the horizontal dimensions of the horizontal components of momentum equation (4.2.1), yields expressions for the transformed velocities,

$$\mu = - \frac{i}{r_0} \frac{(\sigma k - \lambda)}{(\sigma^2 + 1)} \tilde{p} + \frac{1}{r_0(\sigma^2 + 1)} (\sigma \theta'_x - \theta'_y)$$

and

$$v = - \frac{i}{r_0} \frac{(k + \sigma\ell)}{(\sigma^2 + 1)} \tilde{p} + \frac{1}{r_0(\sigma^2 + 1)} (\theta'_x + \sigma\theta'_y)$$

The variables μ and v are the transformed u and v , and θ'_x and θ'_y are the transformed s_x and s_y . For both equations, the second term on the right gives the solution for a horizontally homogeneous boundary layer while the first term on the right gives the solution due to pressure perturbations. In this study, attention is focused on the velocities driven by the internal wave pressure perturbations,

$$\mu_p = - \frac{i}{r_0} \frac{(\sigma k - \ell)}{(\sigma^2 + 1)} \tilde{p} \quad (4.2.65)$$

and

$$v_p = - \frac{i}{r_0} \frac{(k + \sigma\ell)}{(\sigma^2 + 1)} \tilde{p} \quad (4.2.66)$$

The transformed pressure, \tilde{p} , can be calculated using the non-dimensionalized vertical momentum equation,

$$\frac{\partial^2 \zeta}{\partial t^2} = - \frac{1}{r_0} \frac{\partial p}{\partial z} - N^2 \zeta$$

Here, the vertical turbulent stress gradient, $\partial s_z / \partial z$, is neglected because it is zero below δ and, along with $\partial^2 \zeta / \partial t^2$ and $N^2 \zeta$, is very small in the mixed layer. Taking the Laplace and Fourier transforms of this equation and considering only the baroclinic components of motion yields

$$(\sigma^2 + N^2) \psi = - \frac{1}{r_o} \tilde{p}'$$

Using equations (4.2.58) and (4.2.59), ψ can be expressed as an expansion in the normal modes of oscillation or

$$\sum_{n=1}^{\infty} (\sigma_n^2 + N^2) a_n \psi_n = - \frac{1}{r_o} \tilde{p}'$$

Using the homogeneous wave equation, (4.2.47), which each ψ_n satisfies for $\sigma = \sigma_n$, and noting that $\frac{N^2}{g} \frac{\partial \psi_n}{\partial z} \ll \frac{\partial^2 \psi_n}{\partial z^2}$ everywhere, this equation can be rewritten as

$$\tilde{p}' = - r_o \sum_{n=1}^{\infty} a_n \frac{(\sigma_n^2 + 1)}{k^2} \underbrace{\left(\frac{N^2 + \sigma_n^2}{N^2 + \sigma_n^2} \right)}_{(a)} \frac{\partial^2 \psi_n}{\partial z^2} \quad (4.2.67)$$

Over most of the water column $N^2 \gg \sigma^2$ and, where N^2 is zero, $\frac{\partial^2 \psi_n}{\partial z^2}$ is virtually zero. So, for the sake of determining the forced horizontal velocity, vertical accelerations may be ignored in computing the pressure gradient. Thus (a) in (4.2.67) is approximately one and integration yields

$$\tilde{p} = - r_o \sum_{n=1}^{\infty} \frac{a_n (\sigma_n^2 + 1)}{k^2} \psi_n' \quad (4.2.68)$$

In integrating (4.2.67) the constant of integration has been set to zero in order to satisfy the equation relating the baroclinic surface pressure and displacement,

$$\tilde{p}(z = 0) = - \frac{g}{Hf^2} \psi(z = 0)$$

Using (4.2.68) in equations (4.2.65) and (4.2.66) yield equations for μ_p and v_p in terms of the eigenfunction derivatives. These are

$$\mu_p = \sum_{n=1}^{\infty} \frac{i(\sigma k - \ell)(\sigma_n^2 + 1)}{k^2(\sigma^2 + 1)} a_n \psi'_n \quad (4.2.69)$$

and

$$v_p = \sum_{n=1}^{\infty} \frac{i(k + \sigma \ell)(\sigma_n^2 + 1)}{k^2(\sigma^2 + 1)} a_n \psi'_n \quad (4.2.70)$$

For an unforced response, σ goes to σ_n and (4.2.69) and (4.2.70) become the usual equations for the horizontal velocity in free waves. Equations (4.2.58) and (4.2.59) imply:

$$a_n = \frac{1}{\lambda_n \omega_n} (R_s \Sigma_o + R_p k^2 \tilde{p}_o) \cdot \frac{\omega_n}{(\sigma^2 + \omega_n^2)} \quad (4.2.71)$$

Combining this with equations (4.2.69) and (4.2.70) yields expressions for the velocities with poles at the inertial frequency and at the internal wave eigenfrequency. The resonance at the inertial frequency arises because inertial motion is always a solution of the inviscid horizontal momentum equations and can be superimposed on any other solution. In physical terms, if an internal wave response is caused by surface forcing of any type, the resulting pressure perturbations excite inertial motions as well. In this indirect way surface forces can excite inertial motion below the surface mixed layer. In contrast

to the results of Krauss (1972b), no beating between inertial and internal wave frequencies can occur in the vertical motion but it may occur in the horizontal velocity.

The inverse Laplace transforms of u_p and v_p can be computed using (4.2.69), (4.2.70) and (4.2.71). They are

$$u_p = ikv_a - ilu_a \quad (4.2.72)$$

and

$$v_p = iku_a + ilv_a \quad (4.2.73)$$

where

$$u_a = \sum_{n=1}^{\infty} \frac{\psi_n'}{k^2} \int_0^t x_n(\alpha) [\sin \omega_n(t - \alpha) - \omega_n \sin (t - \alpha)] d\alpha \quad (4.2.74)$$

and

$$v_a = \sum_{n=1}^{\infty} \frac{\psi_n'}{k^2} \int_0^t x_n(\alpha) [\omega_n \cos \omega_n(t - \alpha) - \omega_n \cos (t - \alpha)] d\alpha \quad (4.2.75)$$

with

$$x_n(\alpha) = \frac{1}{\lambda_n \omega_n} [R_\Sigma T_o(\alpha, \bar{k}) + R_p k^2 P_1(\alpha, \bar{k})] \quad (4.2.76)$$

The two frequency components of the velocity response are apparent in equations (4.2.74) and (4.2.75). The impulse response [$X_n(x) = \text{unit impulse}$], is a sum of inertial and internal wave motions. The inertial component is equal for both u and v . The current hodograph for the

internal wave component is an ellipse with the ratio of the major to the minor axis equal to ω_n .

In Section 4.4 the steps necessary to implement equations (4.2.58) through (4.2.61) and (4.2.74) through (4.2.76) will be discussed. However, Section 4.3 will first deal with one other type of forced response, that due to surface buoyancy flux.

4.3 Forcing of Internal Waves by Buoyancy Flux at the Surface

When the surface water in an open lead freezes, salt is rejected from the newly formed ice. The salt combines with sea water to form a dense brine which sinks beneath the lead. This process is important in the generation of internal waves because the buoyancy flux creates a density disturbance in the mixed layer. Horizontal variations in mixed layer density cause perturbations in the velocity field and convergence and divergence in this field can in turn drive internal waves. This section is devoted to deriving the internal wave response to buoyancy flux.

Magaard (1973) has developed a theoretical model of internal wave generation by buoyancy flux. He assumes constant stratification, a rigid lid at the ocean surface and constant eddy diffusivity. He has found that, under conditions typical of temperate oceans, the response due to buoyancy flux is a small but significant fraction of the response due to surface stress. In this study a method similar to that of Magaard is used. However, in an effort to make the results more realistic, the stratification is assumed arbitrary below the surface mixed layer and the kinematic boundary condition is used at the

surface. The eddy diffusivity is assumed infinite in the mixed layer and zero below. The ocean is assumed to be of uniform depth.

Using the non-dimensionalization of (4.2.10) with the additional condition that the scale of the density perturbation, $\rho = \rho^s r$, is

$$\rho^s = \frac{fW\rho_s}{g} \quad (4.3.1)$$

the component form of (4.2.1) becomes

$$\frac{\partial u}{\partial t} + v = - \frac{1}{r_o} \frac{\partial p}{\partial x} \quad (4.3.2)$$

$$\frac{\partial v}{\partial t} - u = - \frac{1}{r_o} \frac{\partial p}{\partial y} \quad (4.3.3)$$

$$\frac{\partial w}{\partial t} = - \frac{1}{r_o} \frac{\partial p}{\partial z} + \frac{r}{r_o} \quad (4.3.4)$$

Equation (4.2.2) becomes

$$\frac{\partial u}{\partial x} + \frac{\partial v}{\partial y} + \frac{\partial w}{\partial z} = 0 \quad (4.3.5)$$

The diffusion equation for buoyancy comes from (B11). It is

$$\frac{\partial r}{\partial t} + r_o N^2 w = \delta_d r_o \frac{\partial F}{\partial z} \quad (4.3.6)$$

where

$$\delta_d = \frac{\rho_s F_s}{\rho_s H g f} \quad (4.3.7)$$

and

$$F_s F = - \frac{g}{\rho_0} \langle \rho' \omega' \rangle$$

F is the non-dimensional buoyancy flux and F_s is the scale flux (e.g. buoyancy flux at the surface for $t = 0$). The vertical velocity is zero at the ocean bottom [equation (4.2.12)]. Assuming zero atmospheric pressure fluctuations and zero surface stress, the boundary condition at the surface is the homogeneous version of equation (4.2.13),

$$\frac{\partial^3 w}{\partial t^2 \partial z} + \frac{\partial w}{\partial z} + \frac{g}{f^2 H} \Delta_h w = 0 \quad @ z = 0 \quad (4.3.8)$$

Setting the surface pressure and stress to zero is not meant to imply they are really zero. Rather, in this linearized approach, the response due to buoyancy flux is analyzed separately and may be added to the responses due to pressure and stress. In fact, the nature of the diffusion process in the boundary layer is dependent on the surface stress, but a very simple eddy coefficient parameterization is used here and the non-linear coupling is neglected.

As mentioned previously, it is hypothesized that the eddy coefficient for vertical diffusion is infinite above the pycnocline and zero below. So, when salt is released at the surface, it mixes instantaneously through the mixed layer. For negative buoyancy flux, such as that from leads, this is fairly realistic because the unstable nature of the process forces plumes of dense brine to descend rapidly through the mixed layer. Here, for the sake of simplicity, the brine is assumed to mix uniformly in the vertical. The horizontal dispersion of the brine is assumed to be due only to movement of the lead. In order

for this to be a valid approximation, the lead motion must be faster than convectively driven spreading. During periods of high ice velocity this is probably a valid assumption, but during periods of low ice velocity it will under estimate the amount of horizontal spreading.

Following Magaard's approach, it is assumed that any parameter, γ , of the solution to equations (4.3.2) through (4.3.8) can be divided into two parts. One part is representative of the diffusive boundary layer motion, γ_B , and another part is representative of the non-diffusive internal wave motion, γ_I . It is also assumed that the non-dimensional diffusive boundary layer thickness, δ_d , is small and that the parameters can be expanded in powers of δ_d . Therefore

$$\gamma = \gamma_B + \gamma_I \quad (4.3.9)$$

and

$$\gamma_B = \gamma_B^{(0)} + \delta_d \gamma_B^{(1)} + \delta_d^2 \gamma_B^{(2)} \dots \dots \quad (4.3.10)$$

$$\gamma_I = \gamma_I^{(0)} + \delta_d \gamma_I^{(1)} + \delta_d^2 \gamma_I^{(2)} \dots \dots$$

It is assumed that the surface buoyancy flux occurs only at zero order in the boundary layer solution and because the solution is to describe a boundary layer phenomena, all parameters γ_B go to zero for $z/\delta_d \gg 1$. (In fact, a simple solution is used for which $\gamma_B = 0$ for $z/\delta_d \geq 1$.) For the boundary layer equations, an expansion of the vertical scale is employed

$$z = \delta_d \xi \quad (4.3.11)$$

With this change of variable the boundary layer equations are

$$\frac{\partial u_B}{\partial t} + v_B = - \frac{\partial p_B}{\partial x} \quad (4.3.12)$$

$$\frac{\partial v_B}{\partial t} - u_B = - \frac{\partial p_B}{\partial y} \quad (4.3.13)$$

$$r_o \delta_d \frac{\partial w_B}{\partial t} = - \frac{\partial p_B}{\partial \xi} + \delta_d r_B \quad (4.3.14)$$

$$\delta_d \left(\frac{\partial u_B}{\partial x} + \frac{\partial v_B}{\partial y} \right) + \frac{\partial w_B}{\partial \xi} = 0 \quad (4.3.15)$$

and

$$\frac{\partial r_B}{\partial t} + r_o N^2 w_B = r_o \frac{\partial F_B}{\partial \xi} \quad (4.3.16)$$

The internal wave equations are

$$\frac{\partial u_I}{\partial t} + v_I = - \frac{1}{r_o} \frac{\partial p_I}{\partial x} \quad (4.3.17)$$

$$\frac{\partial v_I}{\partial t} - u_I = - \frac{1}{r_o} \frac{\partial p_I}{\partial y} \quad (4.3.18)$$

$$\frac{\partial w_I}{\partial t} = - \frac{1}{r_o} \frac{\partial p_I}{\partial z} + \frac{r_I}{r_o} \quad (4.3.19)$$

$$\frac{\partial u_I}{\partial x} + \frac{\partial v_I}{\partial y} + \frac{\partial w_I}{\partial z} = 0 \quad (4.3.20)$$

and

$$\frac{\partial r_I}{\partial t} + r_o N^2 w_I = 0 \quad (4.3.21)$$

Because the boundary layer solution goes to zero for $\xi \gg 1$, the internal wave solution for w_I must also go to zero at the bottom in order to satisfy the bottom boundary condition. At the surface, the boundary condition of equation (4.3.8) requires

$$\left. \left(\frac{\partial^3 w_I}{\partial t^2 \partial z} + \frac{\partial w_I}{\partial z} + \frac{g}{f^2 H} \Delta_h w_I \right) \right|_{z=0} = 0 \quad (4.3.22)$$

$$- \left. \left(\delta_d^{-1} \left(\frac{\partial^3 w_B}{\partial t^2 \partial \xi} + \frac{\partial w_B}{\partial \xi} \right) + \frac{g}{f^2 H} \Delta_h w_B \right) \right|_{\xi=0}$$

The surface boundary condition of (4.3.22) couples the boundary layer and internal wave solutions.

To determine the boundary layer solutions, recall that the eddy coefficient is assumed infinite in the mixed layer so the density perturbation is uniform with depth there. As a result, the surface density disturbance must scale with the integral over time of the surface buoyancy flux divided by mixed layer depth. Therefore ρ^s is set equal to the change in density under the lead in a period equal to the inertial time scale;

$$\rho^s = \frac{F_s \rho_s}{d g f}$$

Through this relation and (4.3.1), F_s fixes the scale of motion

$$F_s = f^2 d w \quad (4.3.23)$$

and according to (4.3.7),

$$\delta_d = \frac{d}{H} = \delta$$

Also, if there is to be no variation in the mixed layer density, the flux gradient must be constant. In order to satisfy this condition and that of zero flux at the pycnocline,

$$F_B = \begin{cases} F_0 (1 - \xi) & \xi \leq 1 \\ 0 & \xi > 1 \end{cases}$$

where F_0 is the non-dimensional buoyancy flux, F , at $z = \xi = 0$.

Considering the zero order perturbation terms of the boundary layer solution, equation (4.3.14) requires

$$\frac{\partial p_B^{(0)}}{\partial \xi} = 0$$

and (4.3.15) implies

$$\frac{\partial w_B^{(0)}}{\partial \xi} = 0$$

The boundary conditions for $\xi \geq 0$ require $w_B^{(0)} = p_B^{(0)} = 0$. Then (4.3.12) and (4.3.13) imply $u_B^{(0)}$ and $v_B^{(0)}$ are zero. Equation (4.3.16) yields the zero order density disturbance as a direct function of the buoyancy flux,

$$r_B^{(0)} = \begin{cases} - \int_0^t F_0(\theta) d\theta & \xi \leq 1 \\ 0 & \xi > 1 \end{cases}$$

Examining the terms of first order in (4.3.15) yields $\frac{\partial w_B^{(1)}}{\partial \xi} = 0$ and the boundary conditions for $\xi \gg 1$ again imply $w_B^{(1)} = 0$. Then, because the buoyancy flux occurs only at zeroeth order, (4.3.16) implies the first order density derivative with time is zero; so $r_B^{(1)} = 0$. Equation (4.3.14) at first order yields

$$\frac{\partial P_B^{(1)}}{\partial \xi} = r_B^{(0)} = \begin{cases} - \int_0^t F_o(\theta) d\theta & \xi \leq 1 \\ 0 & \xi > 1 \end{cases}$$

Assuming $P_B^{(1)} = 0$ for $\xi \gg 1$ yields

$$P_B^{(1)} = \int_1^\xi \int_0^t -F_o(\theta) d\theta d\xi' = \int_0^t (1 - \xi) F_o(\theta) d\theta \quad \xi \leq 1 \quad (4.3.24)$$

and $P_B^{(1)} = 0$ for $\xi > 1$. This expression is analogous to that derived by Magaard except the actual expression for the buoyancy flux is used.

As shown by Magaard, the first order terms for horizontal velocity can be expressed as functions of pressure by taking the Laplace transform of (4.3.12) and (4.3.13), rearranging terms and taking the inverse Laplace transform of the resultant expression. Doing so results in

$$u_B^{(1)} = - \frac{\partial P_B^{(1)}}{\partial x} * \cos t + \frac{\partial P_B^{(1)}}{\partial y} * \sin t$$

and

$$v_B^{(1)} = - \frac{\partial P_B^{(1)}}{\partial y} * \cos t - \frac{\partial P_B^{(1)}}{\partial x} * \sin t$$

where * denotes a convolution integration such as that in equation (4.2.32).

Proceeding to the second order terms of (4.3.15) yields

$$\frac{\partial w_B^{(2)}}{\partial \xi} = - \left(\frac{\partial u_B^{(1)}}{\partial x} + \frac{\partial v_B^{(1)}}{\partial y} \right) = \left(\frac{\partial^2 p_B^{(1)}}{\partial x^2} + \frac{\partial^2 p_B^{(1)}}{\partial y^2} \right) * \cos t$$

Integrating this equation and using $w_B^{(2)} = 0$ for $\xi \gg 0$, the surface velocity is found to be non-zero at second order. It is

$$w_B^{(2)} \Big|_{\xi=0} = - \frac{1}{2} \Delta_h \left[\int_0^t F_o(\theta) d\theta * \cos t \right] \quad (4.3.25)$$

Also

$$\frac{\partial w_B^{(2)}}{\partial \xi} \Big|_{\xi=0} = + \Delta_h \left[\int_0^t F_o(\theta) d\theta * \cos t \right] \quad (4.3.26)$$

Thus, at second order, vertical velocity perturbations arise at the surface in the boundary layer solutions. Only the mixed layer density is non-zero at zero order. Just as in Magaard (1973), the zero order density gradients cause pressure and horizontal velocity disturbances at first order which drive the vertical velocity disturbance at second order. The only difference here is that the boundary layer disturbances are confined to a mixed layer of depth, d . In view of the large stratification of the pycnocline, this is more reasonable than using a constant eddy coefficient. The velocity perturbations are zero at the pycnocline but the internal wave solutions, required to satisfy (4.3.22), (4.3.25) and (4.3.26), will cause motion there.

Equations (4.3.17) through (4.3.21) can be combined to produce an internal wave equation for w_I similar in form to (4.2.11). The boundary condition of the bottom is $w_B = 0$ and at the surface, equations (4.3.22), (4.3.25), (4.3.26) and (4.3.10) yield

$$\left. \left(\frac{\partial^3 w_I}{\partial t^2 \partial z} + \frac{\partial w_I}{\partial z} + \frac{g}{f^2 H} \Delta_h w_I \right) \right|_{z=0} = (4.3.27)$$

$$\left. \left(-\delta \left(\frac{\partial^2}{\partial t^2} + 1 \right) + \delta^2 \frac{g}{2f^2 H} \Delta_h \right) \left(\Delta_h \int_0^t F_o(\theta) d\theta \right) * \cos t \right.$$

The zero order terms of the internal wave solution are zero because all boundary conditions are zero. At first order the solution is forced by the

$$\left. \left(\frac{\partial^2}{\partial t^2} + 1 \right) \frac{\partial w_B^{(2)}}{\partial \xi} \right|_{\xi=0}$$

term of the boundary layer solution and at second order it is forced by the $\frac{g}{2f^2 H} w_B^{(2)}|_{\xi=0}$ term. Here the two are combined to solve directly for the total response. This is valid because the equations are linear.

Taking the Laplace and Fourier transform of the time integral of (4.3.27) yields

$$\left. \left[\frac{\partial \psi_I}{\partial z} - \frac{gk^2}{f^2 H(\sigma^2 + 1)} \psi_I \right] \right|_{z=0} = \frac{-k^2 P_B}{\sigma^2 + 1} \quad (4.3.28)$$

where P_B is an equivalent transformed pressure,

$$P_B = - \frac{\delta(\sigma^2 + 1 + \frac{\delta g k^2}{2f^2 H}) B_o}{\sigma(\sigma^2 + 1)} \quad (4.3.29)$$

B_o is the Laplace and Fourier transformed F_o . The solution for the internal wave response to buoyancy flux is thus equivalent to that for pressure, equation (4.2.5), but with an effective buoyancy flux pressure, P_{iB} , substituted for P_i . The inverse Laplace transform of (4.3.29) gives this effective pressure in terms of the Fourier transform of the surface buoyancy flux. Namely,

$$P_{iB}(t, \bar{k}) = -\delta \int_0^t \beta_o(\bar{k}, \alpha) [\cos(t - \alpha) + \omega_G^2 [1 - \cos(t - \alpha)]] d\alpha \quad (4.3.30)$$

where

$$\omega_G^2 = 1 + \frac{\delta g k^2}{2f^2 H}$$

and β_o is the Fourier transformed surface buoyancy flux,

$$\beta_o(\bar{k}, t) = \mathcal{F} [F_o(x, y, t)]$$

4.4 Calculation Techniques and General Results for N^2 , Eigenfunctions and Response Integrals

There are three basic steps in determining the forced internal wave responses. First, the Brunt-Väisälä frequency distribution must be determined for the region in question. Second, the eigenvalues, λ_n , and eigenfunctions, ψ_n , must be determined for use in equations (4.2.58) through (4.2.61). The response functions of (4.2.60) and (4.2.61) are

determined at the same time. Finally, the convolution integrals of (4.2.58) and (4.2.59) must be computed for forcing functions at several horizontal wave numbers. The results from different wave numbers are multiplied by the correct trigonometric functions to obtain the response at a particular location.

Density data from several sources was required to determine the N^2 distribution. Data from the AMLE has been used for the upper 80 m. For depths from 80 m to 145 m, data from the AIDJEX camps Snowbird and Blue Fox has been used (no data from Caribou was available), and hydrocast data from T-3 has been used for depths below 645 m.

Data from the AMLE was used for the near surface region because it was the only available data which adequately resolved the sharp seasonal pycnocline. N^2 was computed at 1 m depth intervals for each of three tape average density profiles from data tapes made at 1700 and 2242 on April 7 and at 0206 on April 8. The total time covered is four hours just prior to the April 8 storm. This period was chosen as the maximum interval which gave a realistic N^2 distribution representative of the undisturbed density field at the beginning of the event. A longer averaging time would have obscured the sharp changes in structure at the top pycnocline. The Brunt-Väisälä frequency was calculated for the upper 80 m using

$$N^2 = \frac{g}{\rho_0} \frac{d\rho_0}{dz} = \frac{g}{\rho_0} \frac{d\sigma_t}{dz} 10^3$$

This method gives satisfactory values because the adiabatic temperature changes are negligible over such shallow depths.

Figure 4.2 shows N in cycles/hour as determined for all depths. By convention, N , rather than N^2 , has been plotted but N^2 is the physical variable of interest. The values of N^2 calculated for each of the three tape average density profiles were averaged together to obtain the points between 20 m and 80 m. The average stratification was very slightly negative for depths less than 20 m and has been assumed zero. For depths between 33 m and 80 m, N is greater than 3 cycles/hour and the values vary smoothly with depth. The peak value is 21 cycles/hour at 38 m. The x at 60 m and 70 m indicate average values of N from Snowbird and Blue Fox calculated using a more sophisticated scheme described below. The agreement between N calculated from the two sources is quite good.

Between 20 m and 33 m the Brunt-Väisälä frequency varies from 1 cycle/hour to 3 cycles/hour. The values there are relatively noisy because the stratification is weak and variations due to density errors are relatively greater. In computing the average N^2 from the three tapes, the standard deviation has also been computed for each depth. The average standard deviation for all points above 80 m is .0023 sec^{-2} . This is about 15 percent of the average N^2 below 20 m and amounts to an error in N of about 2.8 cycles/hour. Thus, it is not surprising that the points look noisy above 33 m. A smoother plot could be achieved for this region by averaging over a longer time or a greater depth span. However, it is more important to use an N^2 profile which represents well the vertical variations in the instantaneous structure in the upper ocean (and particularly at the top pycnocline) than it is to use a profile which is smoother in some averaged sense.

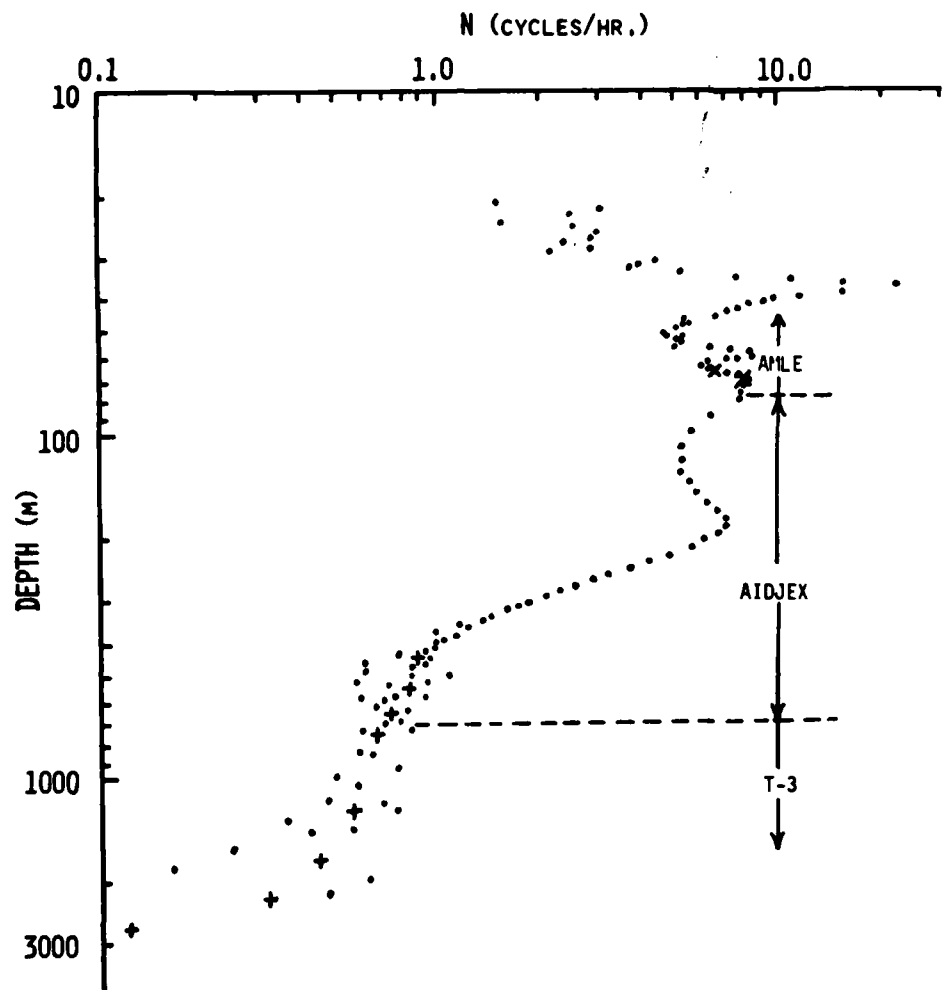


Figure 4.2. The Brunt Väisälä frequency, N , as a function of depth for the Beaufort Sea. Density data are from the AMLE experiment (AMLE), the AIDJEX camps Snowbird and Blue Fox (AIDJEX) and T3 (T3). + indicates 100 m block average above 650 m and 500 m block averages below.

In calculating the eigenfunctions, N^2 is used in an integral sense. This being the case, the errors between 20 m and 33 m occur over such a shallow depth span that they have a negligible effect. It should also be added that, at the point of maximum N^2 , the standard deviation was less than 5 percent.

The data for N^2 between 80 m and 645 m was gathered during four hydrocasts made between 0800, April 7, 1976 and 0800 April 9, 1976. The samples were taken at the AIDJEX camps Blue Fox and Snowbird by a group under the direction of Ken Hunkins. The data was given to the author in the form of 10 m averages by Miles McPhee of the AIDJEX office. The four density profiles for each camp were averaged and $N^2(z)$ was calculated for each site.

A program written by William Bendiner of the Applied Physics Laboratory (APL), University of Washington, was used to calculate N^2 for depths greater than 80 m. The program uses a technique developed by N. P. Fofonoff of Woods Hole Oceanographic Institution and calculates N^2 as

$$N^2 = \frac{-g}{\alpha_0} \left[\frac{\partial \alpha}{\partial T} \left(\frac{dT}{dz} + \Gamma \right) + \frac{\partial \alpha}{\partial S} \frac{dS}{dz} \right]$$

where T is in situ temperature, Γ is the adiabatic lapse rate, $\left(\frac{-\partial T}{\partial z} \right)_{a}$, S is salinity and $\alpha = \frac{1}{\rho}$. The method avoids round-off errors associated with comparing the actual density gradient and the adiabatic density gradient, which are nearly equal at great depths. The program was used with the equations of state of Ekman (1908) and Knudsen (1901) and an equation for the adiabatic lapse rate by Fofonoff.

The values of N^2 for the average density profiles at Snowbird

and Blue Fox, calculated using this program, agree quite well. They were averaged together to obtain an N^2 profile for the site at Big Bear. These values are plotted in Figure 4.2. The values at 60 m and 70 m agree with the AMLE data. Values of N^2 vary quite smoothly between 80 m and 350 m. Below 350 m N drops below 1 cycle/hour and, using the 10 m data point spacing, errors in temperature and salinity produce a rather noisy profile. Unlike the small region between 20 m and 33 m, it is unnecessary to maintain fine depth resolution below 350 m because there are no sharp changes in the density structure. Therefore, in order to reduce the noise level, 100 m block averages of N^2 (+ in Figure 4.2), were used to represent the true N^2 profile.

The only density data available for the AMLE camp location at depths greater than 500 m are from hydrocasts made at T-3 between June 1965 and May 1966 (Tripp, 1966, 1967). Data from three different cruises were used, T3-W01 in July and August of 1965 at 75°N-142°W, T3-W02 in November and December of 1965 at 75°N-144°W and T3-W03 in April and May of 1966 at 75°N-156°W. N^2 was calculated for 65 pairs of points using the program from APL. Only pairs of points from the same cast were used to calculate each value of N^2 . Most of the corresponding values of N are shown as dots below 650 m in Figure 4.2. Many points below 2000 m were off scale. The spacing between data points was 100 m to 200 m but the stratification is extremely weak below 650 m and, even with this large spacing, the N profile is noisy. In order to smooth the profile the values of N^2 were averaged over 500 m blocks to produce the points shown as + in Figure 4.2.

Values of N^2 at 1 m depth intervals below 80 m, were

interpolated from the averaged AIDJEX and T-3 data (+ in Figure 4.2) using a program written by J. G. Dworski of the Department of Oceanography, University of Washington. The program employs the interpolation scheme of Akima (1970). The plot of Figure 4.3 shows the interpolated N on a logarithmic depth scale while Figure 4.4 shows the same thing with a normal depth scale. The interpolated N was less than zero below 2853 m and was arbitrarily set to zero. Using NOAA chart #C&GS 9400, the ocean depth has been estimated to be 3250 m.

Figure 4.3 is obviously quite similar to Figure 4.2 and gives a detailed view of the strongly stratified, upper 200 m. Figure 4.4 shows the N profile in a more realistic perspective. The profile can be broken into four main regions; the unstratified surface layer, the top pycnocline where N is on the order of 20 cycles/hour, the main pycnocline with N approximately 6.5 cycles/hour, and the weakly stratified deep layer below 500 m. The differences in N^2 between these regions is even more exaggerated than the differences in N . The stratification (i.e. N^2) at the top pycnocline is nearly ten times that in the main pycnocline where the stratification is, in turn, one hundred times greater than that in the deep water and surface layer. The top pycnocline is of course subject to change in position and stratification as the mixed layer changes depth. The main pycnocline is representative of a transition in water types from Arctic Surface Water through Intermediate and Pacific Water to Atlantic Water. The dip in N^2 at 100 m in Figure 4.3 is associated with the higher temperature of the Pacific Water. The core of the Atlantic Water is at about 500 m. This depth corresponds to the top of the weakly stratified deep layer. According

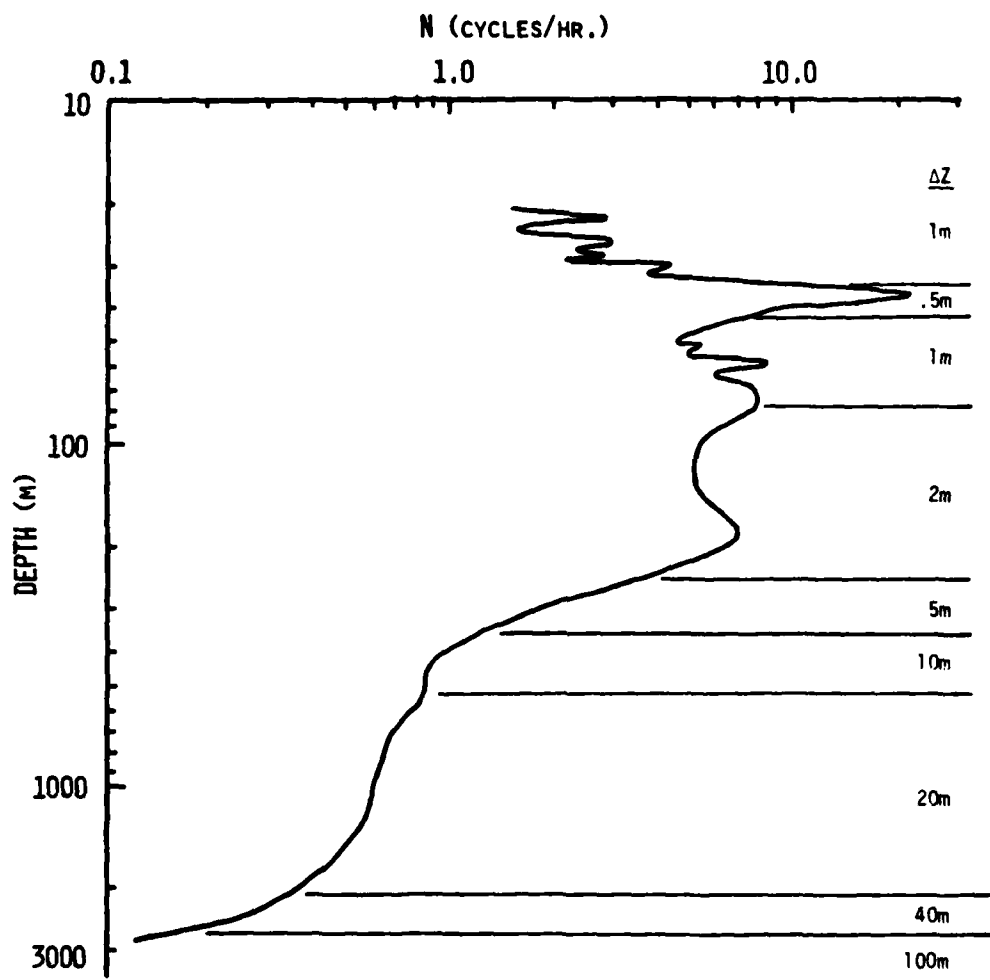


Figure 4.3. Interpolated values of N on a logarithmic depth scale.

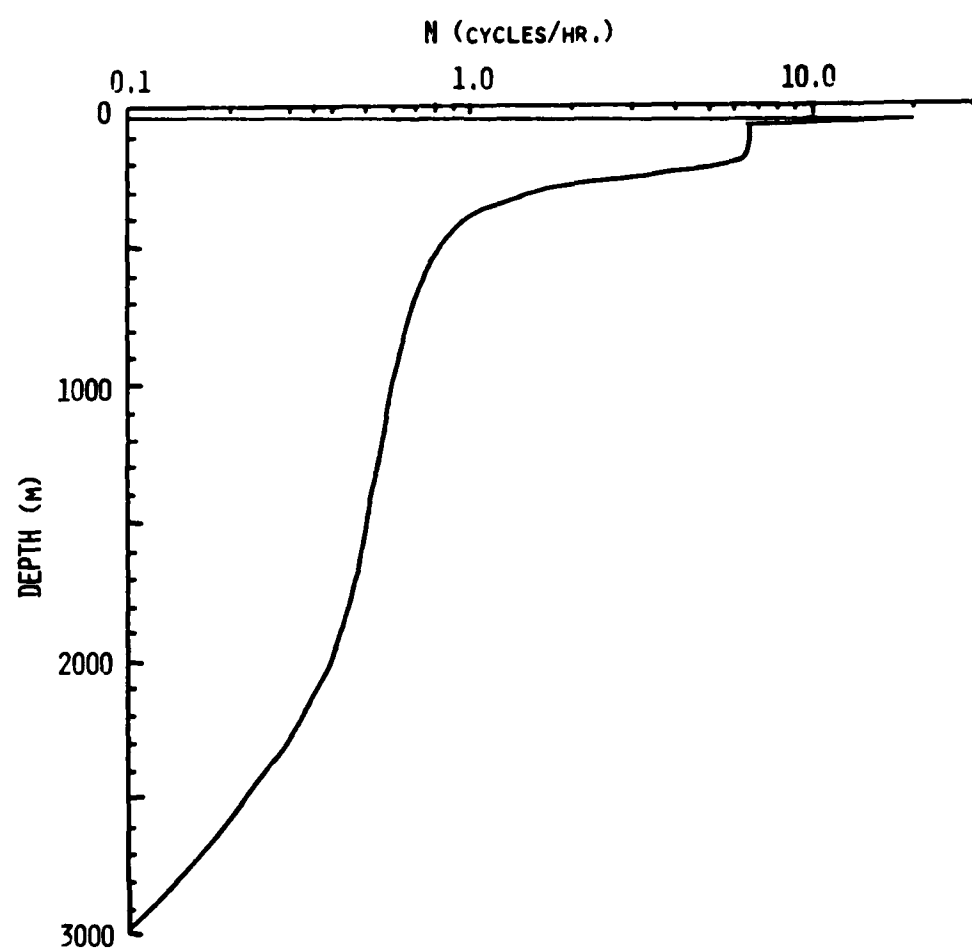


Figure 4.4. Interpolated values of N on an arithmetic depth scale.

to the classification of Coachman (1963), the Arctic Bottom Water lies below 900 m and, as can be seen in Figure 4.4, the density of this water is nearly the same as that at the core of the Atlantic Water.

The profiles of N in Figures 4.2, 4.3 and 4.4 indicate that models employing constant stratification cannot represent the true stratification very well. In fact, the region of strongest stratification is so thin it appears that a two layer model might be better than a constant stratification model. The model being discussed here uses the actual stratification. In subsequent calculations, N^2 is normalized by dividing by f^2 ($f = 1.3906 \times 10^{-4}$) and is written as N^2 . The depth is normalized to unity.

Given the profile of N^2 determined above, the eigenfunctions, ψ_n , and response factors, R_Σ and R_p , for equations (4.2.58) to (4.2.61) can be determined. The eigenfunctions, ψ_n , of the homogeneous internal wave equation can be calculated in a two step procedure. First a finite difference scheme is used to obtain approximate eigenvalues for the first few modes. Then an iterative scheme is used to obtain refined values for the eigenvalues and the eigenfunctions. Initial estimates of the eigenvalues at higher mode numbers are generated by the iterative program along with values for the response factors of equations (4.2.60) and (4.2.61). The solution scheme is a modified version of that used by Rattray et al. (1969).

Unlike that in Rattray et al. (1969), the problem here is to decompose the equations (4.2.47), (4.2.48) and (4.2.23) into normal modes for fixed values of k^2 instead of fixed values of σ^2 . In order to isolate the eigenfrequency at one term in the equation of motion,

equation (4.2.47) must be rewritten as

$$\frac{\partial^2 \psi}{\partial z^2} + \frac{N^2}{g} \frac{\partial \psi}{\partial z} - k^2 \psi + \lambda (N^2 - 1) \psi = 0 \quad (4.4.1a)$$

or, for $\lambda = \lambda_n$

$$\frac{\partial^2 \psi_n}{\partial z^2} + \frac{N^2}{g} \frac{\partial \psi_n}{\partial z} - k^2 \psi_n + \lambda_n (N^2 - 1) \psi_n = 0 \quad (4.4.1b)$$

where λ_n is the eigenvalue,

$$\lambda_n + \frac{-k^2}{\sigma_n^2 + 1}$$

and the corresponding boundary conditions are:

$$\frac{\partial \psi_n}{\partial z} + \lambda_n \frac{g}{Hf^2} \psi_n = 0 \quad @ z = 0 \quad (4.4.2)$$

and

$$\psi_n = 0 \quad @ z = 1 \quad (4.4.3)$$

The form of the equation of motion given in (4.4.1b) has the advantage that, for long wavelengths, $k^2 \psi_n$ is negligible and the eigenvalues and eigenfunctions are independent of wave number.

To find approximate values of λ_n for the first m modes, the water column is divided into m equally spaced intervals of length $h = 1/m$. In this case m has been set at 50 but only the first ten or so eigenvalues are actually used. Equations (4.4.1b), (4.4.2) and (4.4.3) can then be written in finite difference form,

$$[\tilde{\psi}(j-1) - 2\tilde{\psi}(j) + \tilde{\psi}(j+1)]/h^2 - k^2\tilde{\psi}(j) + \lambda M_j \tilde{\psi}(j) = 0 \quad (4.4.4)$$

$$[\tilde{\psi}(0) - \tilde{\psi}(-1)]/h + \lambda G \tilde{\psi}(0) = 0 \quad (4.4.5)$$

and

$$\psi(m) = 0 \quad (4.4.6)$$

where

$$\tilde{\psi}(j) = \psi(jh)$$

$$G = \frac{g}{hf^2}$$

and

$$M_j = N^2(jh) - 1$$

Equation (4.4.5) can be used to eliminate $(j-1)$ from (4.4.4) evaluated at $j = 0$. Similarly, (4.4.6) can be used in (4.4.4) evaluated at $j = m - 1$ to eliminate $\tilde{\psi}(m)$. Then the system of equations can be expressed in matrix form,

$$(\underline{A} - \mu \underline{I}) \underline{\tilde{\psi}} = 0 \quad (4.4.7)$$

where I is the identity matrix and

$$\underline{A} = \begin{bmatrix} (1+k^2h^2)b & -b & 0 & \dots & \dots & \dots & \dots & \dots & 0 \\ -a_1 & (2+k^2h^2)a_1 & -a_1 & 0 & \dots & \dots & \dots & \dots & 0 \\ 0 & -a_2 & (2+k^2h^2)a_2 & -a_2 & \dots & \dots & \dots & \dots & 0 \\ \dots & \dots \\ 0 & \dots & \dots & \dots & -a_{m-2} & (2+k^2h^2)a_{m-2} & -a_{m-2} & \dots & \dots \\ 0 & \dots & \dots & \dots & -a_{m-1} & (2+k^2h^2)a_{m-1} & \dots & \dots & \dots \end{bmatrix} \quad (4.4.8)$$

where $a_j = 1/M_j$, $b = 1/(M_0 + m)$

$$\mu = h^2\lambda \quad (4.4.9)$$

\underline{A} is an m by m matrix and $\tilde{\psi}$ is a column vector ($mx1$) made up of $\tilde{\psi}(j)$, $j = 0, 1, 2, \dots, m-1$. Equation (4.4.7) has solutions only for m values of μ , the eigenvalues of the matrix \underline{A} . Equation (4.4.9) relates the eigenvalues of \underline{A} to the eigenvalues λ_n . Thus, to obtain initial estimates for the first few λ_n , the matrix \underline{A} is formed and a standard matrix eigenvalue program (QREIG from the Boeing Library, University Academic Computer Center) is used to calculate the λ_n approximations. The differences between the process used here and that of Rattray et al. (1969) is in the form of (4.4.4) and the diagonal elements of \underline{A} .

Estimates obtained in the above manner are usually good for the first five to ten modes if m is 50. The first approximations for eigenvalues at higher mode numbers are calculated on the basis of the asymptotic behavior of the eigenvalues as n becomes large. As a first approximation (4.4.5) can be replaced with a rigid lid condition and the effect of λ on the boundary condition ignored. According to

(4.4.1b), the eigenvalue must increase as the ratio of ψ_n'' to ψ_n . The number of zero crossings of ψ_n is n so ψ_n''/ψ_n increases as n^2 . Therefore,

$$\lambda_n \approx \frac{n^2}{(n-1)^2} \lambda_{n-1}$$

Using this equation, a first approximation for an eigenvalue may be derived from the eigenvalue at the next lower mode.

Once first approximations (λ_n^0) of the eigenvalues are obtained, accurate eigenvalues and the eigenfunctions are calculated using an iterative approach. Given an approximation, λ_n^l , to the eigenvalue, λ_n with error, ϵ_n^l ,

$$\lambda_n = \lambda_n^l + \epsilon_n^l \quad (4.4.10)$$

equation (4.4.1a) can be numerically integrated forward in z from $z = 0$ to $z = 1$ for $\lambda = \lambda_n^l$. At the upper boundary ψ is set to an arbitrary constant, C , and (4.4.2) with $\lambda_n = \lambda_n^l$ is used to obtain the initial condition for $\partial\psi/\partial z$. The result is a function $\psi_s(z, \lambda_n^l)$ satisfying (4.4.1a) and (4.4.2) for $\lambda_n = \lambda_n^l$. Because of the error in the eigenvalue, (4.4.3) will not be satisfied; $\psi_s(1, \lambda_n^l)$ will be non zero. The eigenvalue estimate can be improved by determining ϵ_n^l and subtracting it from the current estimate. To calculate the error, consider the first two terms of the Taylor series expansion of $\psi_s(z = 1)$ with λ about λ_n^l .

$$0 = \psi_n(z = 1) = \psi_s(1, \lambda_n^l) \approx \psi_s(1, \lambda_n^l) + \left. \frac{\partial \psi_s}{\partial \lambda} \right|_{\lambda=\lambda_n^l} \lambda_n^l \epsilon_n^l$$

Therefore,

$$\varepsilon_n^l = - \frac{\psi_s(l, \lambda_n^l)}{\tilde{v}_s(l, \lambda) \Big|_{\lambda=\lambda_n^l}} \quad (4.4.11)$$

where

$$\tilde{v}_s = \frac{\partial \psi_s}{\partial \lambda}$$

The term $\psi_s(l, \lambda_n^l)$ is known but, in order to determine ε_n^l , the value of $\tilde{v}_s(l, \lambda_n^l)$ must be calculated. Differentiating (4.4.1a) and evaluating at $\lambda = \lambda_n^l$ yields

$$\frac{\partial^2 \tilde{v}_s}{\partial z^2} + \frac{N^2}{g} \frac{\partial \tilde{v}_s}{\partial z} - k^2 \tilde{v}_s + \lambda_n^l (N^2 - 1) \tilde{v}_s = - (N^2 - 1) \psi_s \quad (4.4.12)$$

Since $\psi_s(z = 0)$ is an arbitrary constant,

$$\tilde{v}_s(0) = 0 \quad @ z = 0 \quad (4.4.13)$$

and differentiation of the boundary condition, (4.4.2), with respect to λ_n implies

$$\frac{\partial \tilde{v}_s}{\partial z} \Big|_{z=0} = - \frac{g}{Hf^2} \psi_s \Big|_{z=0} = - \frac{g}{Hf^2} C \quad @ z = 0 \quad (4.4.14)$$

To solve for \tilde{v}_s equation (4.4.12) can be integrated from the surface to the bottom using (4.4.13) and (4.4.14) as initial conditions. The solution of ψ_s is used as a forcing term on the right of (4.4.12).

Knowing how to solve for \tilde{U}_s , the iterative scheme becomes clear. Given an initial estimate of the eigenvalue, (4.4.1a) is integrated forward from $z = 0$ to $z = 1$. Then (4.4.12) is integrated forward in z from the initial conditions (4.4.13) and (4.4.14). The values of ψ_s and \tilde{U}_s evaluated at $z = 1$ are used in (4.4.11) to determine the eigenvalue error, ϵ_n^λ , which is then used in (4.4.10) to determine a new estimate for the eigenvalue. The process is repeated until the error is sufficiently small. In this study, iterations were terminated when $\epsilon_n^\lambda < 10^{-4} \lambda_n^\lambda$. When conversion occurs the final value of ψ_s is proportional to ψ_n . The eigenfunctions are normalized by numerically integrating

$$\int_0^1 (N^2 - 1) r_o \psi_s^2 dz = D_n$$

and dividing the computed ψ_s by $\sqrt{D_n}$ to obtain the ψ_n .

To perform the numerical integration of (4.4.1a), the second order differential equation is converted to two first order differential equations, one with ψ as the variable and the other with $\partial\psi/\partial z$ as the variable. Thus, when the integration and normalization are completed both ψ and $\partial\psi/\partial z$ are known. The response factor on the far right of (4.2.60) is given with no further effort. The response factor on the far right of (4.2.61) is obtained by numerical integration.

In order to obtain the response factors containing L'_o and L'_p in (4.2.60) and (4.2.61), equations (4.2.62) and (4.2.63) must be evaluated. The function \tilde{U} in these equations satisfies (4.4.12) for $\lambda_n^\lambda = \lambda$ and $\psi_s = \psi$. However the boundary conditions which \tilde{U} must satisfy are

different. It is assumed that at $z = 1$, \tilde{v} is zero and has a derivative equal to a constant. Therefore \tilde{v} has the boundary conditions

$$\begin{aligned}\tilde{v} &= 0 \\ \frac{\partial \tilde{v}}{\partial z} &= 0 @ z = 1\end{aligned}\quad (4.4.15)$$

To evaluate \tilde{v} at $\lambda = \lambda_n^l$, λ_n^l is changed to λ_n and ψ_s is changed to ψ_n in (4.4.12). This equation is integrated numerically from $z = 1$ to obtain \tilde{v} and $\partial \tilde{v} / \partial z$ evaluated at $z = \delta$ and $z = 0$. With these values, L'_o and L'_p can be evaluated using (4.2.62) and (4.2.63).

The method of calculating L'_o and L'_p described above is quite useful. It can be used for arbitrary stratification. Leonov and Miro-polskiy (1973) posed their pressure solution in terms of L'_p but only gave solutions for two simplified types of stratification. The method of calculating L'_o and L'_p used here permits the determination of the forced response for any stratification once the eigenfunction is known.

The numerical integrations used in computing the eigenfunctions were performed with a fourth order Runge-Kutta, variable step size routine. (RKINIT of the Boeing Library, University of Washington Academic Computer Center). Values of ψ_n were computed at 291 grid points with a spacing inversely proportional to N . Figure 4.3 shows the grid size distribution in meters. (Actually the values shown should be divided by the depth, 3250 m, to give the true step size.) The smallest (.5 m) is at the pycnocline and the largest (100 m) is at the bottom. The integration routine uses a variable step size which is set by the program when integrating from one grid point to another and

tests indicate the results are insensitive to grid spacing. The form of (4.4.1b) is such that using a step size inversely proportional to N produces an equal number of ψ_n values between each zero crossing. With 291 points the minimum number of points between zero crossings was four for the fiftieth mode. The use of a variable grid size greatly increases the computation speed over the constant grid size scheme of Rattray et al. (1969).

As a check on the programs, eigenvalues, eigenfunctions, and response factors were computed assuming constant stratification. The results were compared to theoretical values for constant N and a rigid lid boundary condition. For short wavelengths ($k \gg 1$) the agreement between the program and the theory is better than 1 percent. For long wavelengths ($k < 1$) the first two modes show differences of less than 10 percent and, for mode 3 and higher, the differences are less than 1 percent. Long wavelengths and low modes produce the largest surface deflections and thus are expected to be slightly different from the rigid lid theory.

Figure 4.5 shows eigenvalues determined using the realistic N^2 distribution corresponding to the N profiles of Figures 4.3 and 4.4. The eigenvalues, eigenfunctions, and response factors have been calculated at eleven horizontal wavelengths from 1.375 km to 995.6 km. Given the assumed depth of 3250 m, the range of wave numbers is 14.8 to 5.8×10^{-2} . The wave number closest to unity is at a wavelength of 22 km, for which $k = .92$. Figure 4.5 shows only the highest wave number case and the $k = .92$ case. For k less than unity the eigenvalues are virtually independent of wave number because the $-k^2\psi_n$

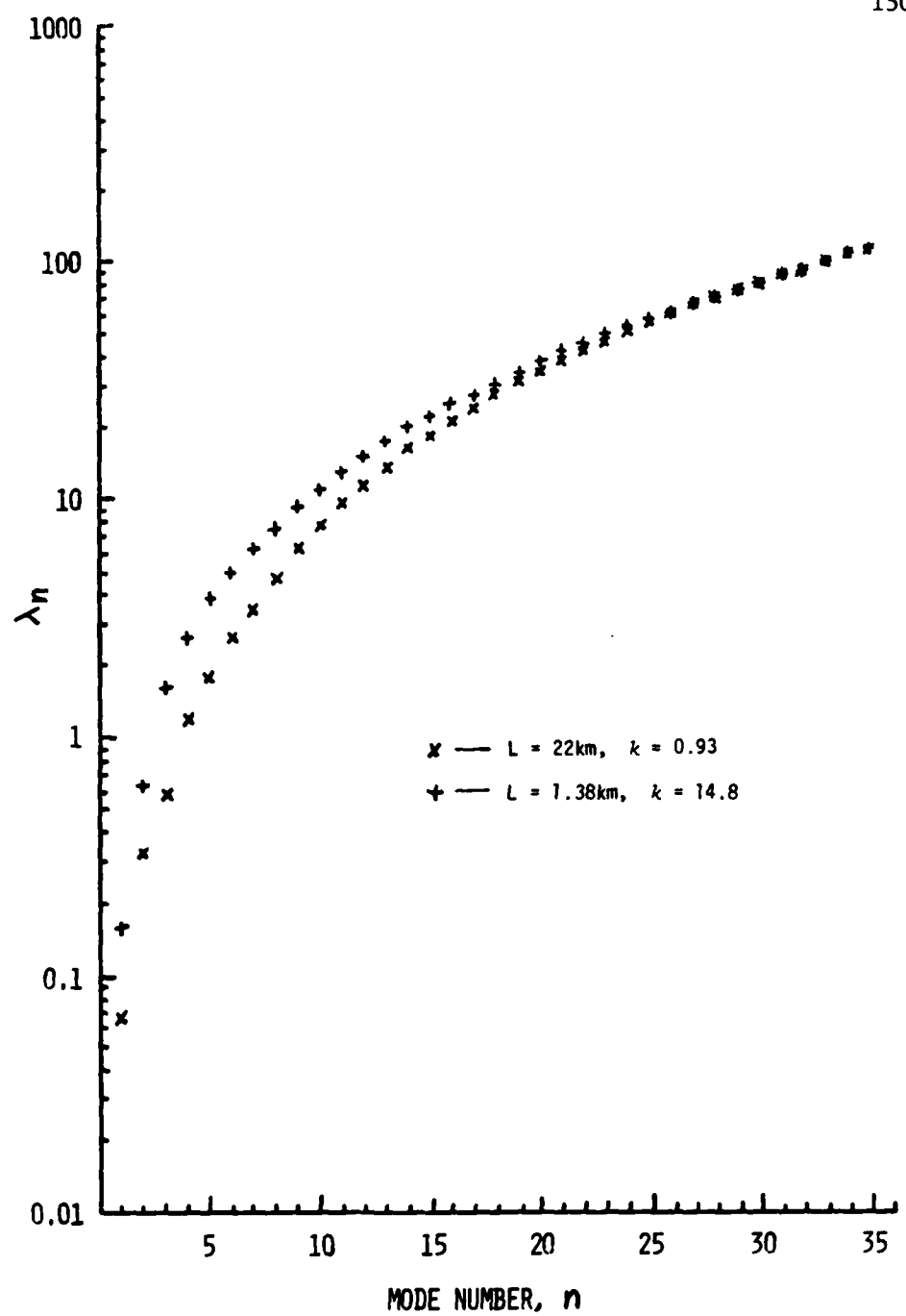


Figure 4.5. Eigenvalues for the Beaufort Sea, $k = 14.8$ and $k = .92$. The eigenvalues are virtually independent of k for $k < 1$.

term is small in (4.4.1b) even for $n = 1$. Also, for small k , λ_n is nearly proportional to n^2 over all n . For the high wave number case λ_n must be larger at small n in order to balance the $-k^2\psi_n$ term with the $\lambda_n(N^2 - 1)\psi_n$ term in (4.4.1b). The deviation from an n^2 dependence is greatest for the first ten modes. For mode numbers greater than 25 the eigenvalues are nearly independent of k .

Figures 4.6a and 4.6b show the eigenfunctions and eigenfunction derivatives for modes 1 through 4 for $k = .92$. Figures 4.7a and 4.7b show the same thing for $k = 14.8$. None of the eigenfunctions bear much resemblance to the usual trigonometric mode shapes associated with the eigenfunctions for constant stratification. All the eigenfunctions display the highest curvatures in the upper 250 m where the stratification is the greatest. This is understandable in view of equation (4.4.1b); ψ_n'' is proportional to N^2 .

The eigenfunction shears are generally large near the surface. This is because the displacements have local maxima high in the pycnocline while the surface displacements are nearly zero. Horizontal velocity is proportional to the eigenfunction derivative. Therefore, horizontal forces acting near the surface will be relatively effective in driving internal waves compared to horizontal forces acting in the interior. On the other hand, vertical forces applied near the surface will be relatively ineffective on driving internal waves because the maximum vertical motion occurs in the interior.

One qualitative difference between the mode shapes at the two wave numbers stands out. The amplitude of the eigenfunctions for $k = 14.8$ are very small below 1000 m while some of the largest

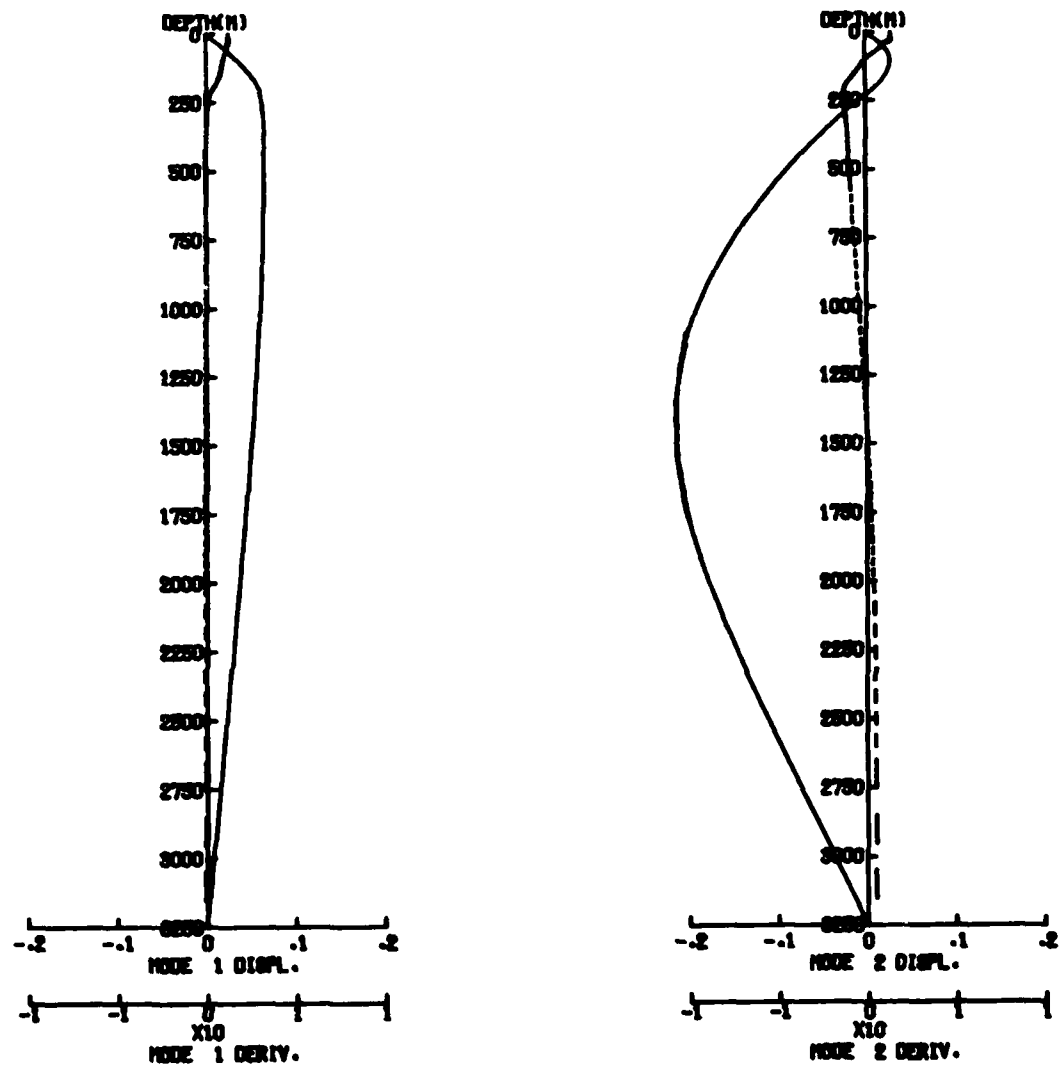


Figure 4.6. Eigenfunctions and eigenfunction derivatives for $k = .92$, modes one through four.

4.6a. Modes one and two.

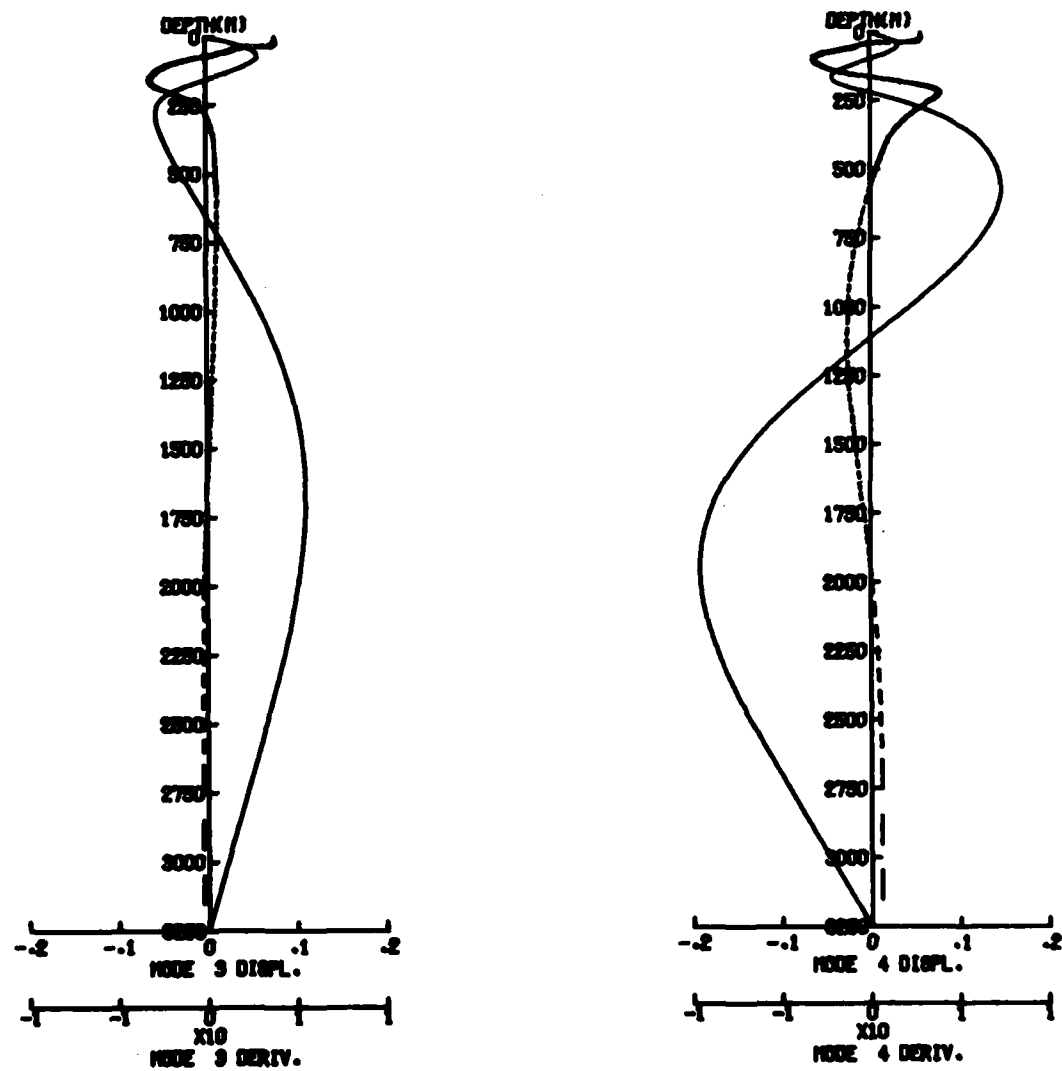


Figure 4.6. Continued

4.6b. Modes three and four.

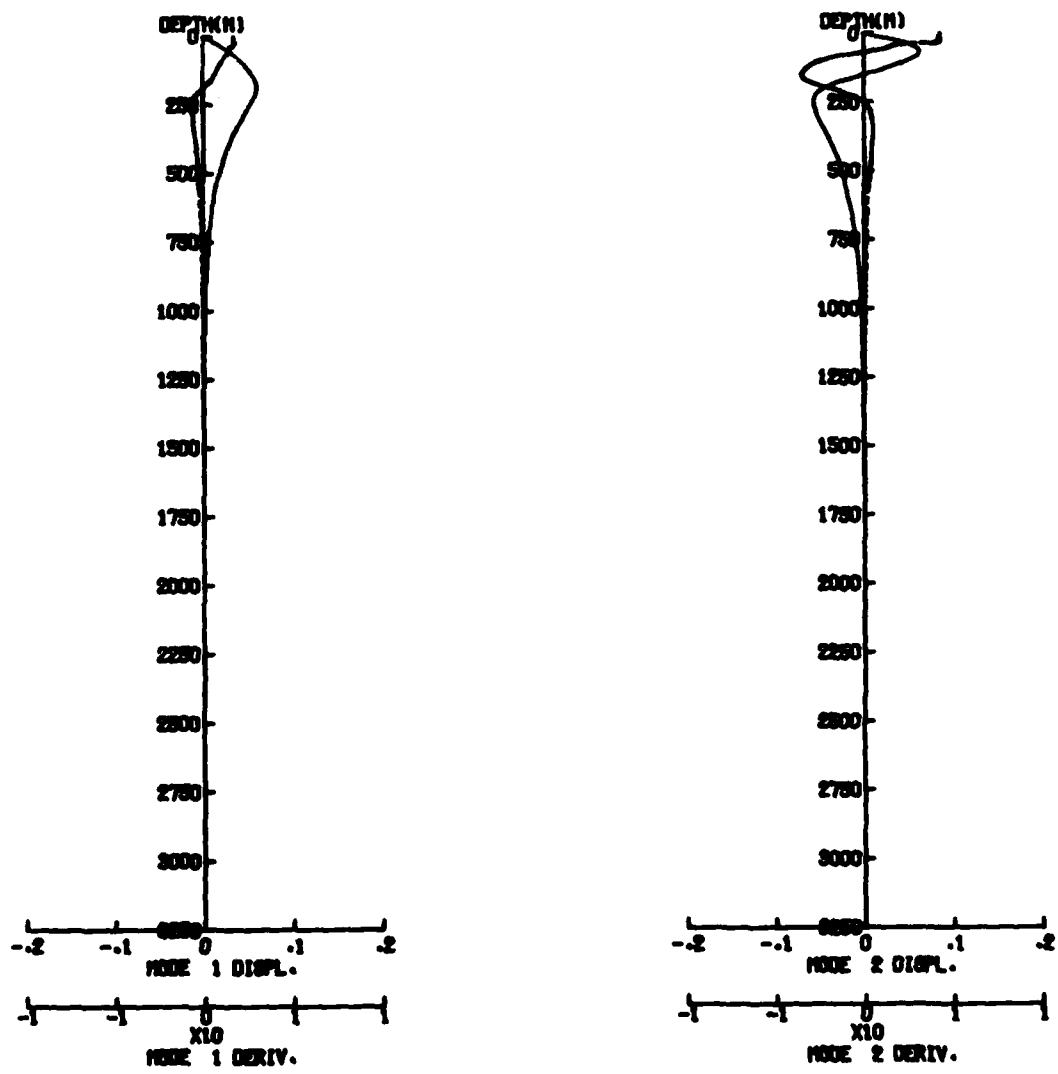


Figure 4.7. Eigenfunctions and eigenfunction derivatives for $k = 14.8$, modes one through four.

4.7a. Modes one and two.

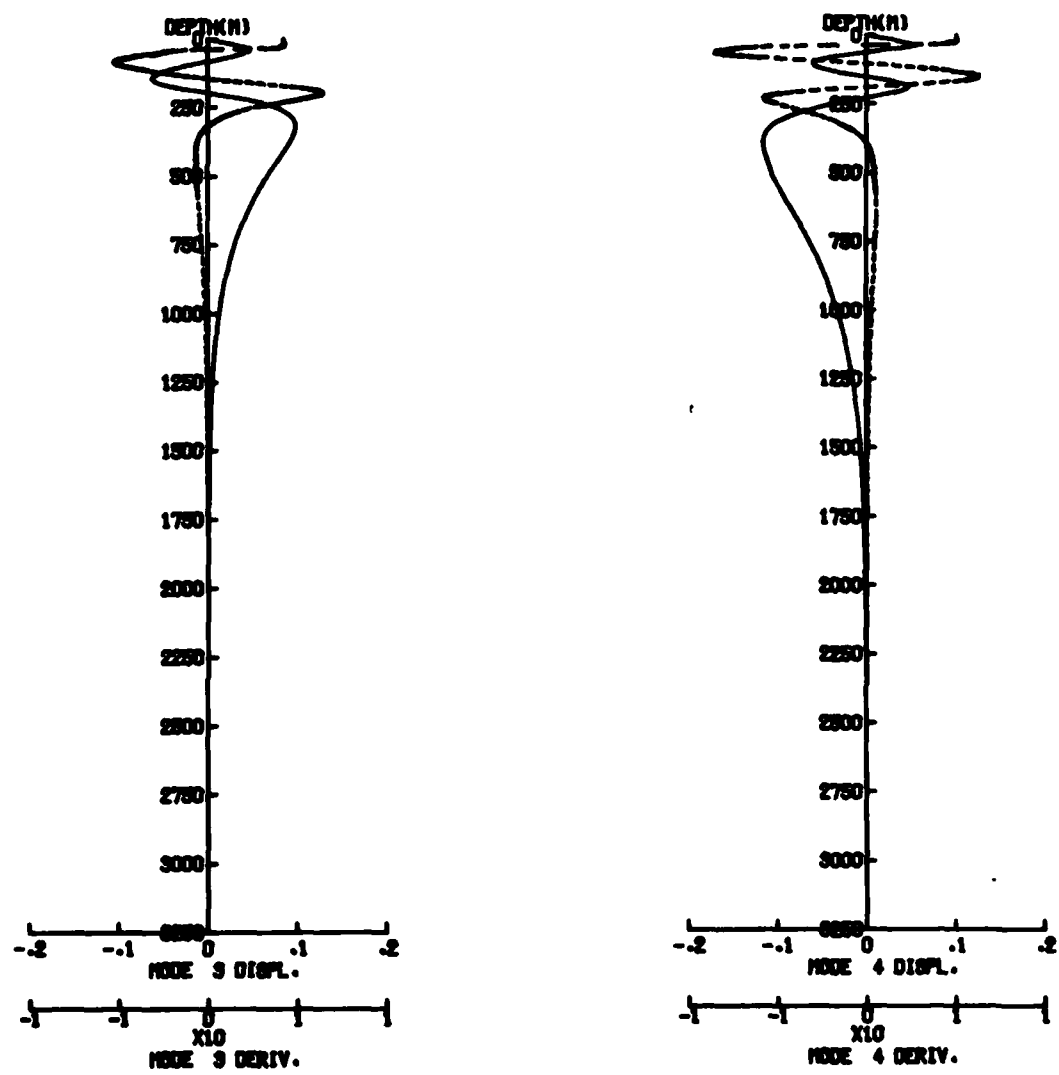


Figure 4.7. Continued

4.7b. Modes three and four.

amplitudes are found in the interior for $k = .92$. The reason for this can be seen in equation (4.4.1b). The presence of the $k^2\psi_n$ term implies that where k^2 is greater than $\lambda_n(N^2 - 1)$, the solution must behave like a decaying exponential. Where k^2 is less than $\lambda_n(N^2 - 1)$ the solution will display oscillatory solutions. Below 150 m the stratification drops monotonically. So, for a given wave number and eigenvalue, there is a critical depth below which k^2 is less than $\lambda_n(N^2 - 1)$ and the mode shape must appear as a decaying exponential. For $k = 14.8$ this depth is 425 m for mode 1 and 630 m for mode 4. These are depths below which the eigenfunctions in Figures 4.7a and 4.7b begin to decay. The critical depth for $k = .92$, mode 1 is 2320 m and for mode 4, the depth is 2775 m. Thus the eigenfunctions for $k = .92$ appear harmonic over most of the water column. The critical depth increases with increasing mode number because λ_n increases with n but it will be shown that the response is small at high mode numbers. So, the total response is always concentrated at shallow depths for high wave numbers.

This variation in the mode shapes with wave number does not occur if the stratification is a constant. For such a case the mode shapes are always harmonic and the eigenvalues are large enough to ensure k^2 is less than $\lambda_n(N^2 - 1)$. The case for real stratification is more akin to that of a two layer ocean model. For wavelengths which are short compared to the water depth ($k \gg 1$), interfacial waves on a pycnocline decay exponentially below the pycnocline and their presence is not felt at depth. Long interfacial waves ($k \ll 1$) appear as shallow water waves below the pycnocline and their influence is

constant with depth. The real ocean response is much like this; short waves do not penetrate as deeply as long waves.

Figure 4.8 is a plot of the modal response to surface stress as a function of mode number for three wave numbers, k equal to 14.8, .92, and 5.8×10^{-2} . The modal response is the response factor, R_{Σ} , divided by $\lambda_n \omega_n$. As shown by (4.2.58) it is a measure of the response of each mode that is independent of time, depth and forcing. Figure 4.9 is a plot of the modal response to pressure for the same three wave numbers. The response factors R_{Σ} and R_p were calculated using both of the formulations given in equations (4.2.60) and (4.2.61). As discussed above, the factors were computed in the same program used to calculate the eigenfunctions and the two types of formulation give identical results.

Figure 4.8 shows several things. First, the modal response increases with decreasing wave number. This is especially true for wave numbers greater than 1. For small wave numbers the response factors and eigenvalues become independent of k and ω_n goes asymptotically to unity with decreasing k . Therefore, the modal responses for $k \ll 1$ are nearly constant. For $k \gg 1$, the eigenfunctions and eigenvalues are strongly dependent on k . The most important effect is that of increasing λ_n and ω_n with increasing k . The eigenvalues (and hence ω_n) must increase to balance the effect of the $k^2 \psi_n$ term in (4.4.1b). This behavior is similar to that of surface waves or interfacial waves in that ω_n increases with increasing wave number. The increase in λ_n and ω_n with increasing k cause the decrease in modal response. In most second order systems the natural frequency increases

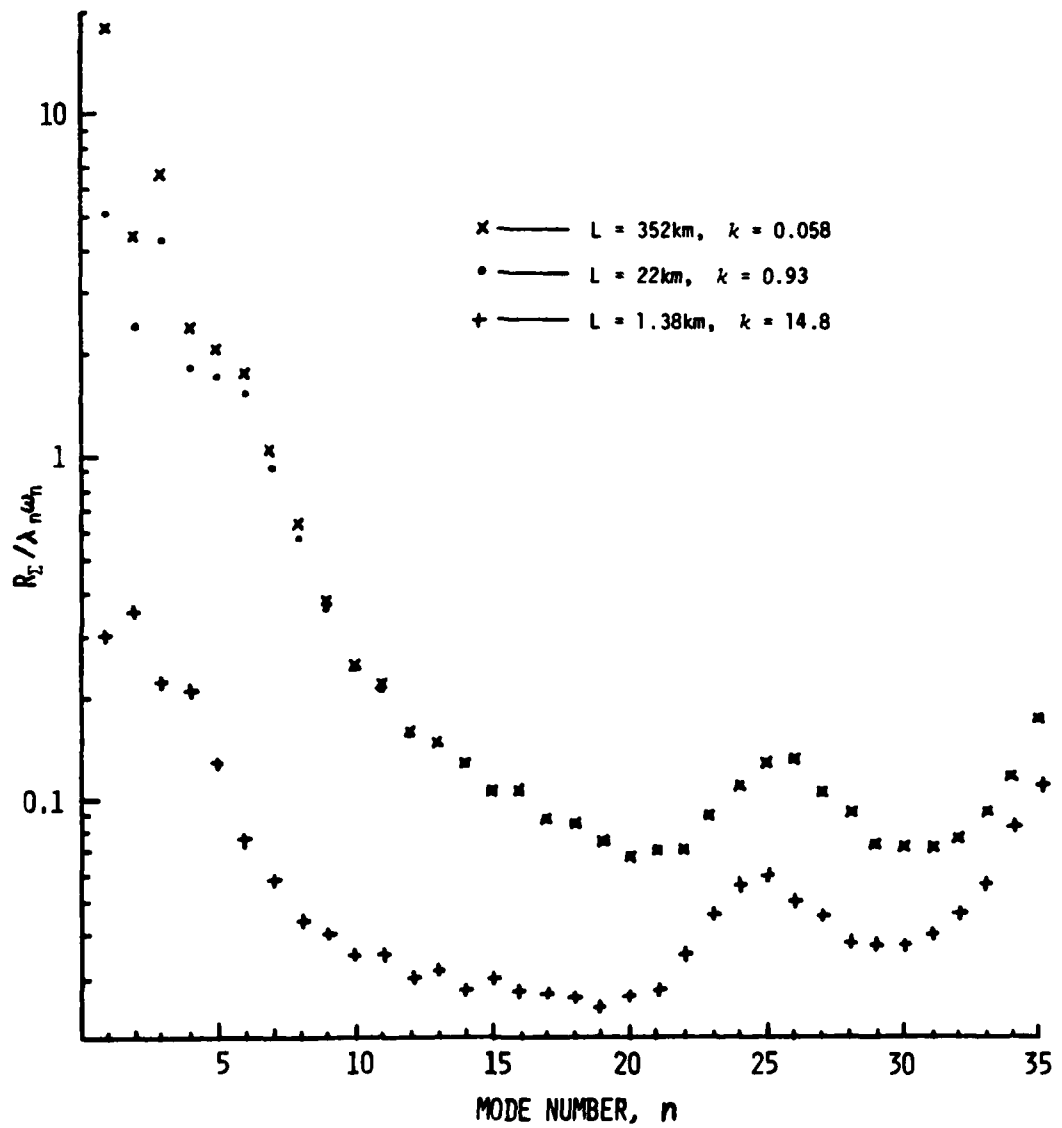


Figure 4.8. The modal responses to surface stress, $R_{\Sigma} / \lambda_n \omega_n$.

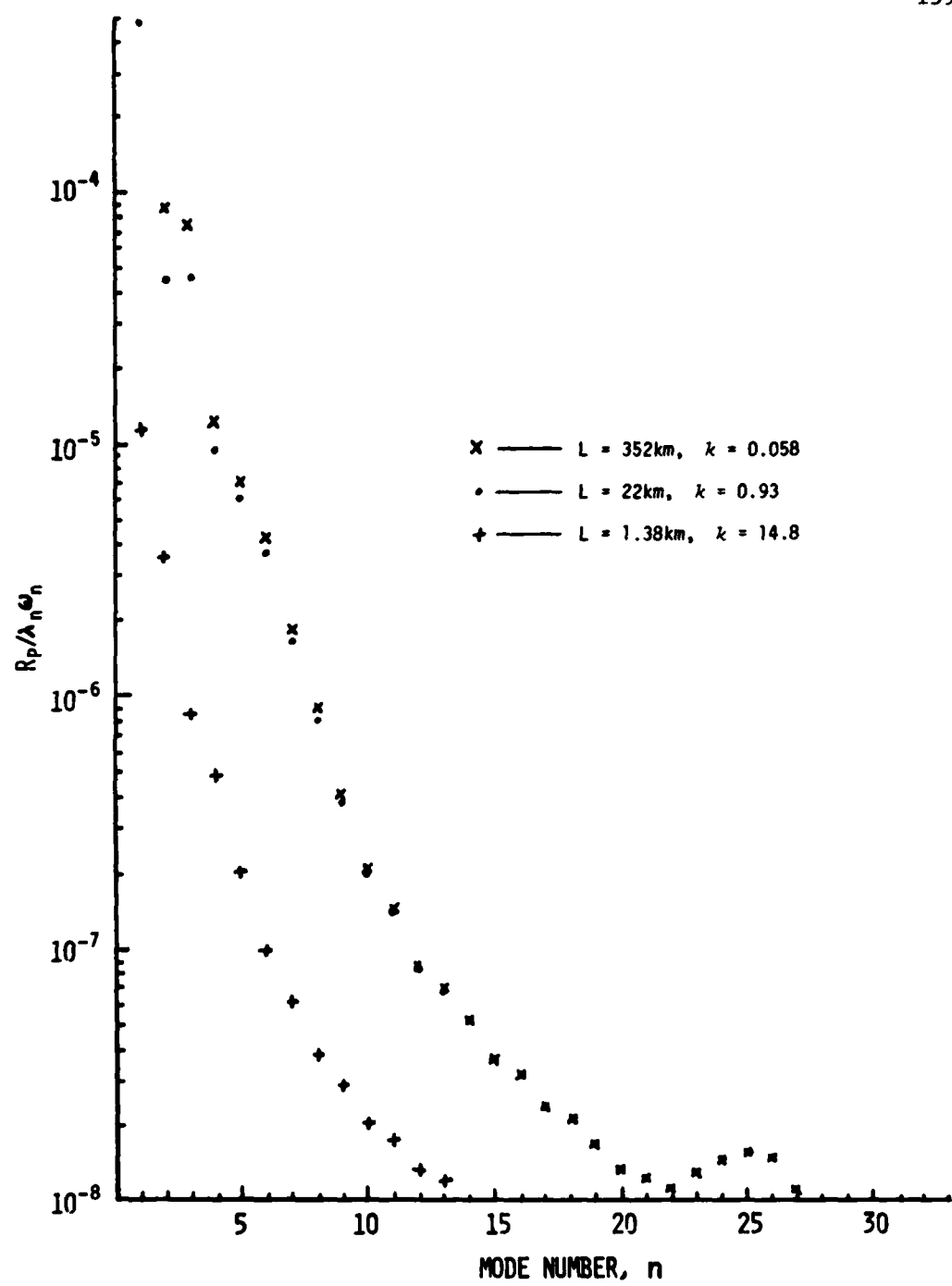


Figure 4.9. The modal response to surface pressure, $R_p/\lambda_n \omega_n$.

with the stiffness of the system. Thus, it is not surprising that increased ω_n implies a decreased forced response.

Second, the modal responses generally decrease very rapidly with increasing mode number. Beyond mode 12 the responses are less than one percent of the maximum response. Increases in the mode number have an effect similar to that of increasing k . As has been shown, λ_n increases as n^2 and for large λ_n , ω_n goes to one. The eigenfunction derivative increases proportionally with n . Combining these effects indicates the modal response must vary as the inverse of n .

Finally, the modal response does not decrease monotonically with n . For the low wave number cases, the response of the third mode is higher than that of the second mode. For the high wave number case the response of the second mode is greatest. At high mode numbers there are oscillations about a decreasing modal response. This is in sharp contrast to a model with constant stratification which will produce a modal response which decreases monotonically. For such a model the value $\psi_n'|_{z=0}$ is exactly $n\pi$ but here, $\psi_n'|_{z=0}$ does not vary smoothly with n .

Figure 4.9 shows the modal response for pressure forcing. The plots share the same general characteristics with the plots of modal response to surface stress; the response decreases with increasing wave number and mode number. The main difference between the pressure response and the stress response is the much larger decrease in pressure response beyond the first few modes. The response drops to one percent of the maximum by mode 4 for the small wave number cases because the pressure response is proportional to the average value of the

eigenfunction near the surface and this value is relatively large for the first few modes.

Computation of the convolution integrals of equations (4.2.58), (4.2.59), (4.2.74) and (4.2.75) is the final step in determining the internal wave response. The most straight forward method is to use a numerical integration scheme such as RKINIT. This approach has been used for forcing functions which are very complicated functions of time. For each point in time, t , the forcing function $[T_o(\alpha) \text{ or } k^2 p_i(\alpha)]$ is multiplied by $\sin \omega_n(t - \alpha)$ and $\cos \omega_n(t - \alpha)$ and integrated in α from 0 to t . The total computation time is proportional to the square of the total number of time steps. When calculating the response for a large number of modes and wavelengths the integration time can become quite large.

It is possible to use a more efficient scheme if the forcing function can be represented as a polynomial in time. This is possible for most smoothly varying forcing functions. If such is the case, advantage may be taken of the identities:

$$\int_0^\beta \theta^j \sin \theta d\theta = -\theta^j \cos \theta \Big|_0^\beta + j \int_0^\beta \theta^{j-1} \cos \theta d\theta \quad (4.4.16)$$

and

$$\int_0^\beta \theta^j \cos \theta d\theta = \theta^j \sin \theta \Big|_0^\beta - j \int_0^\beta \theta^{j-1} \sin \theta d\theta \quad (4.4.17)$$

to determine the convolution integrals analytically.

For a forcing function, $Q(t)$, which is represented by a

polynomial of order m ,

$$Q(\alpha) = \sum_{i=0}^m A_i \alpha^i \quad (4.4.18)$$

The convolution integrals,

$$I_1 = \int_0^t Q(\alpha) \sin \omega_n (t - \alpha) d\alpha \quad (4.4.19)$$

and

$$I_2 = \int_0^t Q(\alpha) \cos \omega_n (t - \alpha) d\alpha \quad (4.4.20)$$

can be rewritten as

$$I_1 = \sum_{i=0}^m A_i \frac{1}{\omega_n^{i+1}} \sum_{j=0}^i \gamma_{ij} \int_0^\beta \theta^j \sin \theta d\theta \quad (4.4.21)$$

and

$$I_2 = \sum_{i=0}^m A_i \frac{1}{\omega_n^{i+1}} \sum_{j=0}^i \gamma_{ij} \int_0^\beta \theta^j \cos \theta d\theta \quad (4.4.22)$$

where

$$\theta = (t - \alpha) \omega_n$$

$$\beta = t \omega_n$$

and

$$\gamma_{ij} = \frac{i!(-1)^j}{(j!)[(i-j)!]} \beta^{i-j}$$

The integrals of equations (4.4.21) and (4.4.22) can be expressed strictly in powers of β , $\sin \beta$ and $\cos \beta$. This is done by first evaluating them at $j = 1$ using the identities (4.4.16) and (4.4.17),

$$\int_0^\beta \theta \sin \theta d\theta = -\beta \cos \beta + \sin \beta \quad (4.4.23)$$

and

$$\int_0^\beta \theta \cos \theta d\theta = \beta \sin \beta + \cos \beta - 1 \quad (4.4.24)$$

The integral (4.4.16) at $j = 2$ is evaluated by subtracting $\beta^2 \cos \beta$ from the integral (4.4.17) at $j = 1$. The integral for (4.4.17) at $j = 2$ is evaluated by subtracting the integral of (4.4.16) at $j = 1$ from $\beta^2 \sin \beta$. The process is repeated until the integrals are evaluated for all values of j . Given these integrals, (4.4.21) and (4.4.22) can be used to replace the convolution integrals of (4.4.19) and (4.4.20) with double summations of polynomials in β , $\cos \beta$ and $\sin \beta$.

For any value of t , the powers of β , $\cos \beta$, and $\sin \beta$ can be computed very rapidly on a computer. For a tenth order expansion and 120 points in time, the power series solution is five times as fast as direct integration. For the power series approach computation time increases linearly with the number of time steps but as the square of m . Therefore, if the forcing is represented with a low order polynomial or if many time steps are used, the power series approach is

fastest. In calculating the convolution integrals used in this work, the two schemes were compared for identical inputs and were found to produce identical output. For most problems the forcing was simple enough to allow the power series approach to be used.

In this section the techniques used to calculate the internal wave responses to surface forcing have been discussed and some of the general results have been presented. The eigenfunctions for the Beaufort Sea are fairly complex due to the nature of the ocean stratification. The eigenfunctions change shape as the wave number becomes large and the wave penetration depth decreases. The modal responses tend to decrease with increasing wave number and with increasing mode number. The convolution integrals for the time response are best performed using a power series expansion of the forcing.

4.5 The Wave Number Frequency Response

Figure 4.8 illustrates how the model response to surface stress varies with mode number. It also gives some idea of how the response varies with wavelength, but in order to determine the important length and time scales for stress forcing it is best to examine the wave number frequency response for a fixed depth and mode number. The wave number frequency response (WFR) is the magnitude of the response to a force equal to $\sin ky \sin \omega t$ where ω is the non-dimensional frequency ($\omega = 1$ corresponds to the inertial frequency). The WFR for stress forcing may be obtained by equating σ with $-i\omega$ in equation (4.2.29). Using (4.2.60), the WFR for the vertical displacement of mode n is

$$\left| \zeta_p \right|_{n,\omega,k} = \left| \frac{R_\Sigma}{\omega_n \lambda_n} \psi_n(z) \frac{\omega_n}{\omega^2 - \omega_n^2} \right| \quad (4.5.1)$$

The corresponding WFR for the velocity components u_p and v_p of (4.2.69) and (4.2.70) are

$$\left| u_p \right|_{n,\omega,k} = \left| \frac{R_\Sigma}{\lambda_n \omega_n} \psi_n'(z) \frac{k \omega_n}{(\omega^2 - \omega_n^2)(\omega^2 - 1)\lambda_n} \right| \quad (4.5.2)$$

and

$$\left| v_p \right|_{n,\omega,k} = \omega \cdot \left| u_p \right|_{n,\omega,k} \quad (4.5.3)$$

The corresponding WFRs for surface pressure forcing ($k^2 p_1$) are identical with the substitution of R_p for R_Σ .

Figure 4.10 is a three-dimensional perspective plot of the WFR for the mode 1 displacement at the pycnocline due to surface stress. The figure is quite similar to those by Krauss (1972b). Resonant peaks occur at points in k, ω space corresponding to the dispersion equation for free waves and the resonant frequency asymptotically approaches the inertial frequency as k becomes small. Where values near resonance exceed 0.4 the peaks are truncated in the figure. For any one wave-number, the frequency response is that of an undamped second order oscillator. As such, the response drops off at frequencies greater than the resonant frequency because the forces required to overcome fluid inertia become large. For frequencies less than the resonant frequency the pressure due to convergence in the mixed layer works

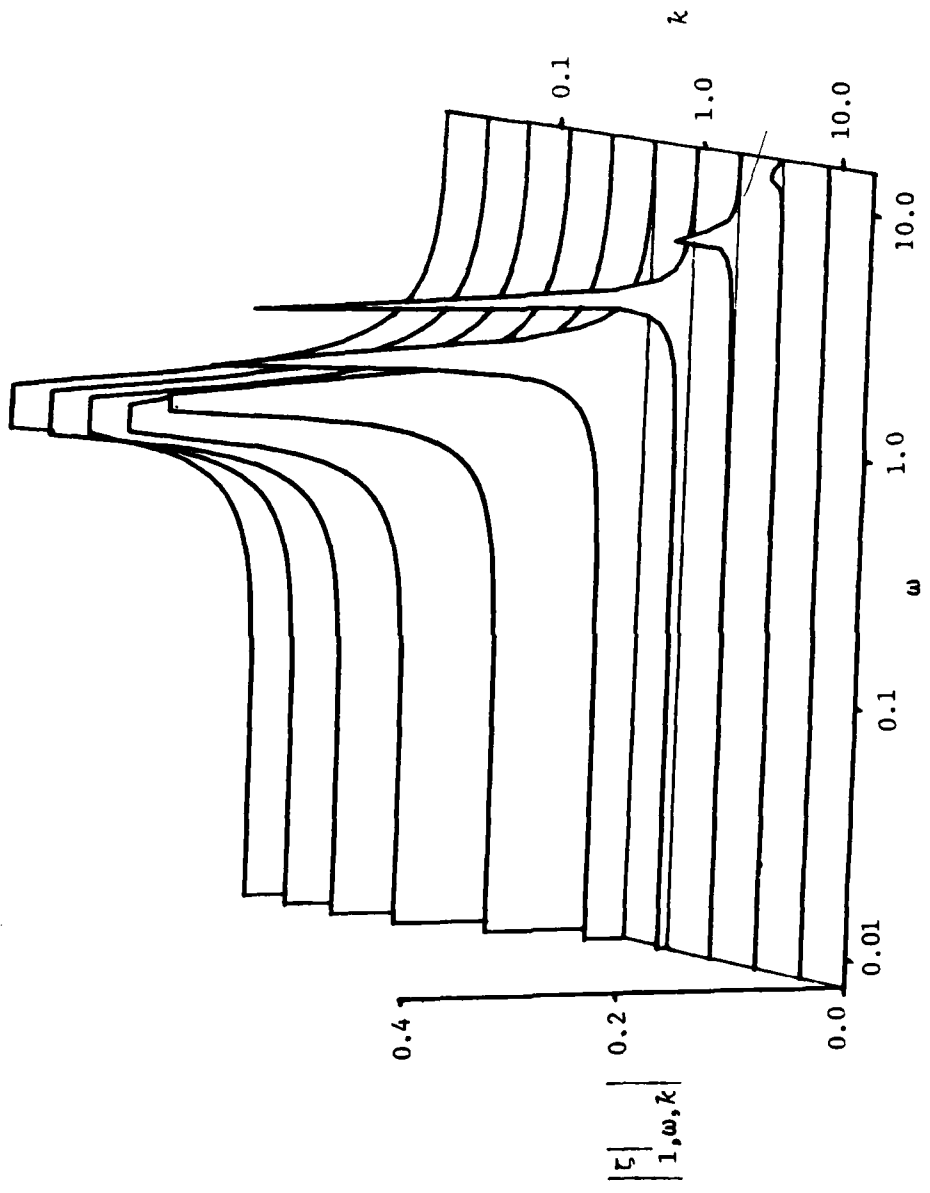


Figure 4.10. Three-dimensional perspective plot of the wave number frequency response for displacement at the pycnocline, $k = .92$, mode one. The variable k is the wave number normalized by ocean depth and ω is frequency normalized by the inertial frequency.

against buoyancy in the stratified fluid below and the buoyancy force is independent of frequency. So, the response is constant with respect to ω at low frequency. As has been pointed out, the response decreases with increasing wave number because the stiffness is proportional to k^2 . Expressed another way the forcing term acts against the Laplacian of pressure due to buoyancy forces and a given forcing will produce larger displacements if k^2 (the Fourier transform analog of Δ) is small. For extremely low values of k the buoyancy forces have a negligible effect on the role of convergence and for such cases at low frequency the vertical deflection is determined solely by the rate of convergence (or divergence) due to Ekman transport. Then the pressure required to force the pycnocline down is so small as to have no effect on the role of convergence in the mixed layer and the simple argument at the end of Section 3.3 applies.

$$\rho_0 f^2 w_{\text{pycnocline}} = - \bar{f} \cdot [\nabla \bar{x}(z = 0)]$$

The response is thus independent of wave number and the WFR appears as a level plateau for $\omega < 1$ and $k < .2$ in Figure 4.10.

Figure 4.11 shows the WFR for $\mu_{1,\omega,k}$ of equation (4.5.2) for mode 1 only. It is the mixed layer ($z = 10$ m) velocity perpendicular to the wave-number vector (or parallel to the wave crests) and is geostrophically driven. The figure shows resonant peaks at the internal wave resonant frequencies and at the inertial frequency. The peaks merge asymptotically for small k and the response at high frequencies and large wave-numbers is small because the vertical deflections (and hence driving pressures) are small. The intriguing thing about the

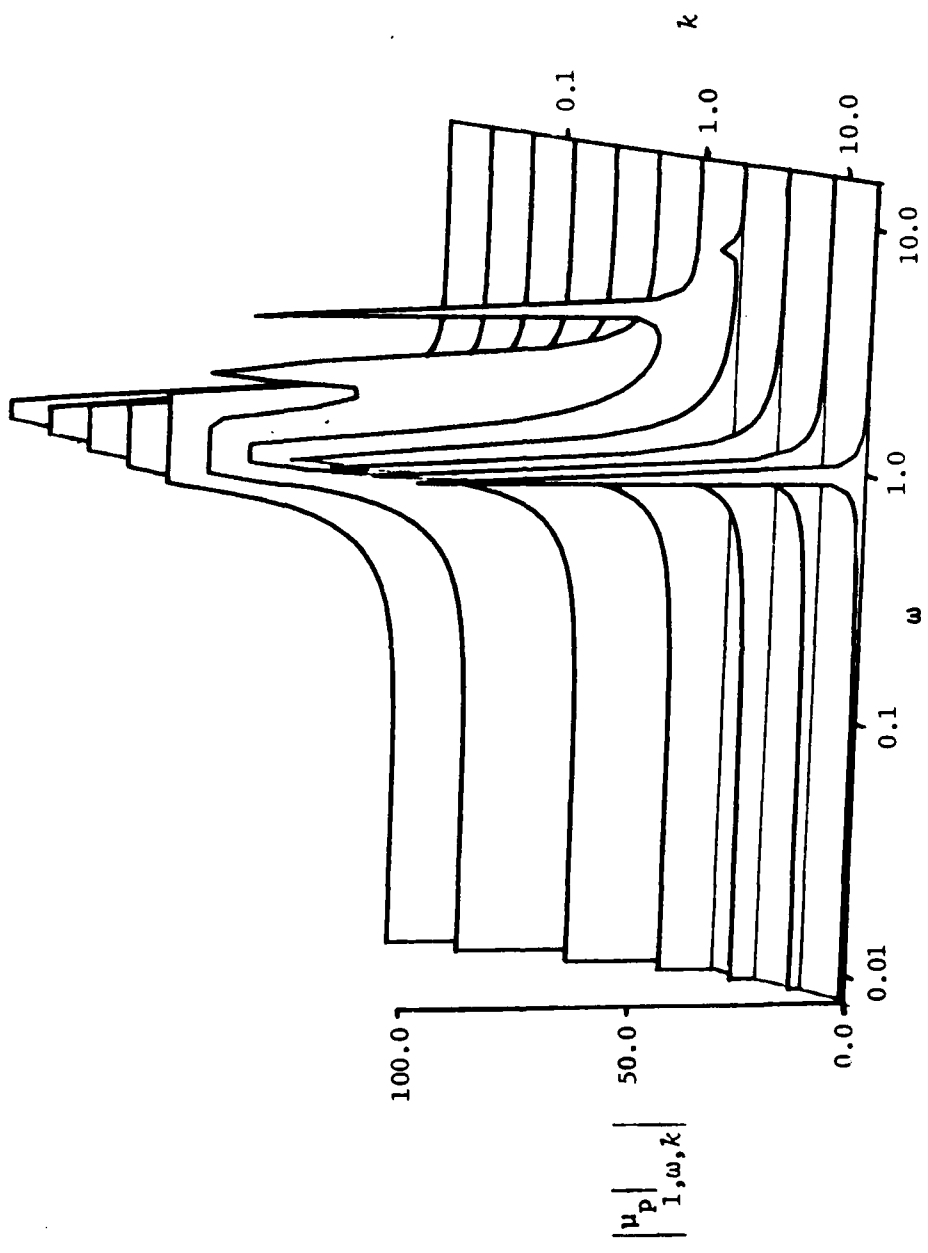


Figure 4.11. Three-dimensional perspective plot of the wave-number frequency response for velocity, u_p , in the mixed layer $k = .92$, mode one.

response is that, for frequencies less than the inertial frequency, it is a maximum around $k = 0.2$. The mixed layer velocity is driven by the surface pressure gradient. The pressure disturbance is proportional to the displacement near the pycnocline which, as shown in Figure 4.10, is a large constant for small wave-numbers. Thus, as the wave number decreases beyond the point where the vertical displacement first reaches a maximum, the pressure gradient and the geostrophically driven velocity must decrease.

Figure 4.12 is a perspective view of the WFR for $v_p|_{1,\omega,k}$ (see equation 4.5.3), the mode 1 velocity at 10 m aligned with the wave number vector. This velocity is small at low frequencies because currents and pressure are geostrophically balanced. For $\omega > 1$, $v_p|_{1,\omega,k}$ is greater than $\mu_p|_{1,\omega,k}$ but is still small because the total response is small. The pattern of resonance and the location of the velocity maximum for low frequencies are the same as for $\mu_p|_{1,\omega,k}$.

The WFR for the mode 3 displacement at the pycnocline is shown in Figure 4.13. The general pattern is quite similar to that of Figure 4.10. The response for the third mode is slightly larger than that for the first mode. This is the same result obtained by Krauss (1976). (This is true for the steady state forced response but in simulations of responses starting from zero, the third mode displacements are slightly smaller than the first mode because the third mode resonant frequency is lower.)

The displacement response for mode 3 becomes constant with wave number as a slightly larger wave number than that of mode 1 and the maximum in the WFR for $\mu_p|_{3,\omega,k}$ is also at a larger wave number than for

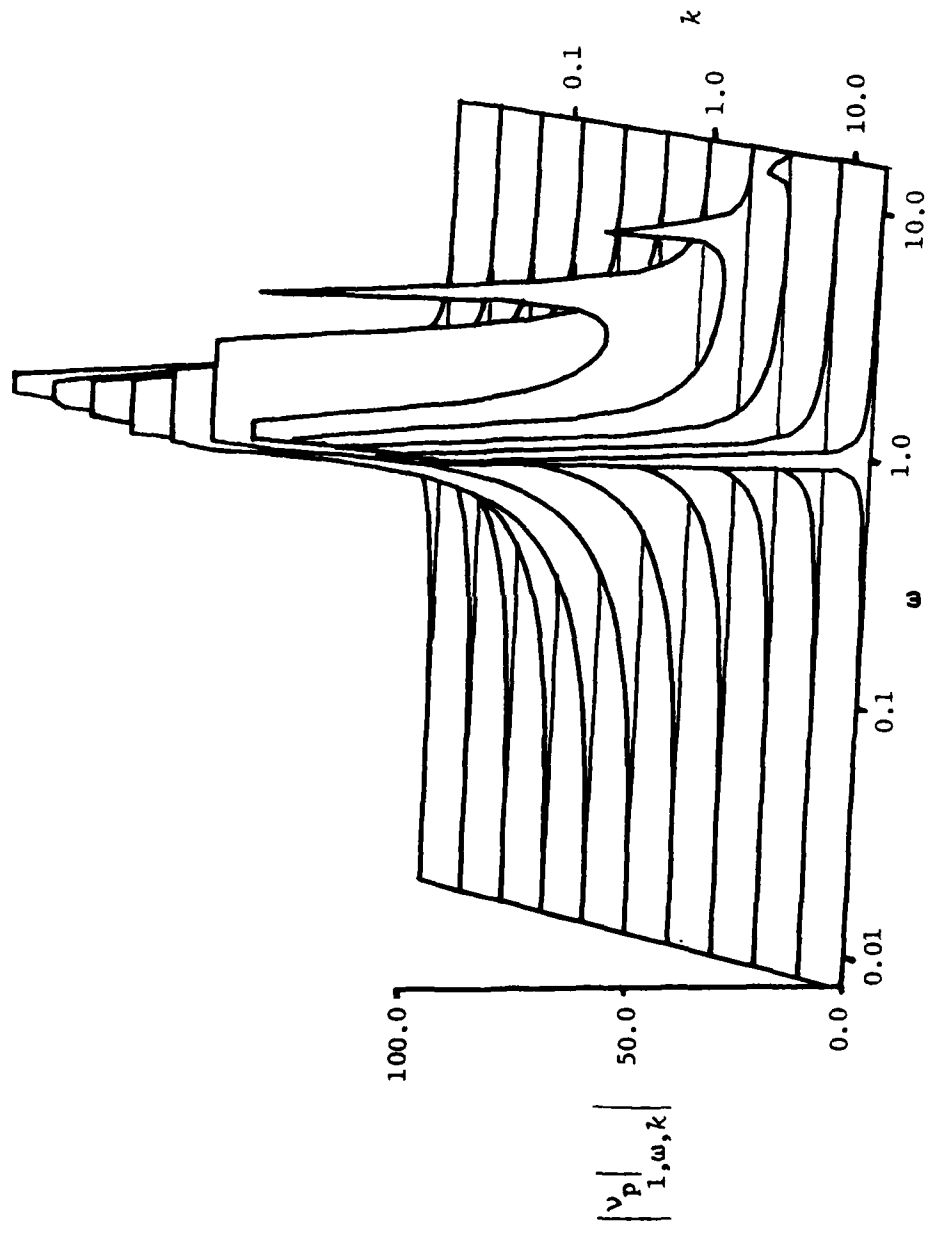


Figure 4.12. Three-dimensional perspective plot of the wave-number frequency response for velocity, v_p , in the mixed layer $k = .92$, mode one.

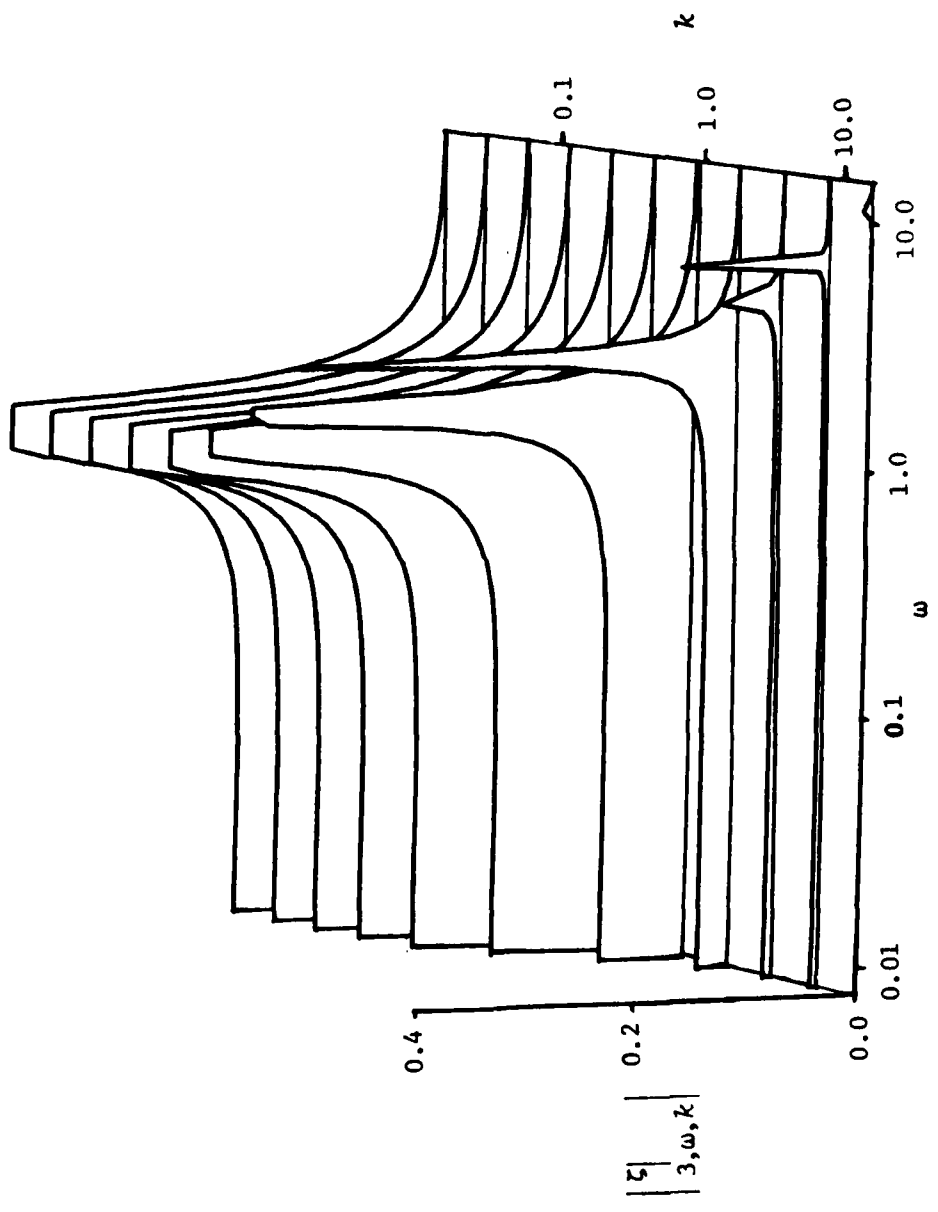


Figure 4.13. Three-dimensional perspective plot of the wave number frequency response for displacement at the pycnocline, $k = .92$, mode three.

$\mu_p|_{1,\omega,k}$. This is because for higher mode numbers, buoyancy forces are small relative to Coriolis forces (ω_n goes to 1 for large n). The critical wave number where the maximum velocity response occurs for a particular mode can be estimated by taking the derivative of (4.5.2) with k assuming ω is negligible and k is small enough so that R_Σ , λ_n and ψ'_n do not vary. Doing so, it can be shown that the critical wave numbers, $k_c(n)$, are those for which

$$k_c^2(n) = \lambda_n(k_c) \quad (4.5.4)$$

This is not surprising because λ_n is equal to the inverse square of the non-dimensionalized Rossby radius of deformation for mode n . This characteristic length scale (C_n/f in dimensional form where C_n is a modal wave speed) decreases with increasing mode number. For the first five modes the critical wave numbers and length scales are given in Table 4.1.

Table 4.1
Wave Numbers for Maximum Velocity Response

Mode	1	2	3	4	5
k_c	.26	.57	.76	1.10	1.35
$L_c = \frac{2\pi H}{k_c}$ (km)	78.5	35.8	26.5	18.6	15.7
Rossby Radius, r_n (km)	12.5	5.7	4.22	2.95	2.5

A number of studies such as Sanford (1975), Gonella (1972), and Webster (1968) indicate that inertial motions become incoherent at spatial scales of more than about 10 km. This may be because the WFR

is maximum at length scales on the order of the modal Rossby radius. A storm acting on the ocean surface over a broad range of length scales excites velocity disturbances which are maximum at length scales on the order of 10 km or less (wavelengths on the order of 70 km or less). Once the forcing stops, these disturbances oscillate at natural frequencies nearly equal to the inertial frequency.

In closing this section it should be noted that the shape of the WFR for pressure forcing ($k^2 P_i$) is the same as that for stress forcing so the discussion above also applies to the pressure forced case. However, while the shear stress forcing is proportional to k , the pressure forcing varies as k^2 . Also, the buoyancy flux response involves an equivalent pressure which is itself proportional to k^2 , so the buoyancy flux forcing ($k^2 P_{\text{equiv}}$) is proportional to k^4 . Thus, though the WFRs have the same shape for stress, pressure, and buoyancy flux, the high wave number forcing is of relatively greater importance for pressure and buoyancy flux.

4.6 Internal Waves Forced by Surface Stress During the April 8 Storm

In this section the internal wave response to a realistic surface stress pattern will be examined but first scaling arguments will be given to show the response to atmospheric pressure is negligible and a model forcing representative of the April 8 storm will be developed.

The atmospheric pressure response is much less than the surface stress response because the pressure response factor is very much less than the stress response factor. From (4.2.58) and (4.2.59) it is apparent that the response to surface stress and surface pressure are

identical except for the differences in the forcing and the response factor ($R_{\Sigma} T_o$ vs. $R_p k^2 P_i$). The stress forcing in dimensional form varies between 10^{-7} and 10^{-6} dynes cm^{-3} . Normalizing by $H/\rho_s u_*^2$ for $u_* = 1$ yields a typical value for T_o of 3×10^{-2} . The value of $k^2 P_i$ has been estimated from the National Weather Service surface pressure map for the polar region of 0343 GMT, April 9, 1976 (1743 AST, April 8, 1976). Using the normalization of (4.2.10) it is found to be about 0.7. However, the pressure response factor, R_p , is four orders of magnitude less than the stress response factor R_{Σ} , at comparable wavelengths (i.e., 100 km). Thus the atmospheric pressure response is over two orders of magnitude less than the stress response and may be neglected. In contrast, it will be shown in Section 4.7 that the response to surface buoyancy flux, which is similar to a pressure response, is comparable in magnitude to the response to surface stress.

Deriving a realistic forcing function, T_o in (4.2.36), requires solving problems in two areas. First, the application of the model to an ice-covered ocean requires a decision as to whether the surface stress is estimated from wind stress on the ice or ice stress on the water. Second, the forcing over a large range of wave numbers must be modeled using a relatively small number of data points in the horizontal coordinates.

With regard to the first problem, when the ice cover is broken or "free" with a large percentage of open water, internal ice stresses are negligible and the ice/water mixture above the mean draft of the ice is free to converge and diverge as if there were no ice present. For such a case, the surface stress is best taken to be equal to the

wind stress on the surface. When the ice is closely packed or "locked up," convergence in the ice/water layer above the mean ice draft is inhibited by internal ice stress and it is more appropriate to use the stress of the ice on the water as the effective surface stress for the model. The ice "free" case is probably applicable to summer conditions when internal ice stresses are negligible. The ice "locked up" case might be applicable in mid-winter. During the AMLE the ice was initially "locked up" and the satellite photographs of Figures 3.7 and 3.8 indicate the ice diverged during the storm. Conditions were probably somewhere between "free" and "locked up." Therefore, it is wise to first make estimates of both types of forcing, wind stress on ice and ice stress on water, and compare them.

The forcing has been computed in both ways for Big Bear using wind velocity and ice velocity measured at the three AIDJEX camps. The stress of the ice on the water has been estimated at the three camps using (3.3.1) and the wind stress on the ice has been calculated using $\tau_a = \rho_a a_w |\bar{v}_{10}| \bar{v}_{10}$ where \bar{v}_{10} is the wind velocity at 10 m and $a_w = 0.0027$. This drag law for wind over sea ice is the same as that used in the AIDJEX ice models (Pritchard et al., 1976) and was derived using the momentum integral technique with pibal data from the AIDJEX experiment (Eric Leavitt, personal communication). The uncertainty in the drag coefficient may be as great as ± 33 percent (Pritchard et al., 1976). The ice camps formed a triangular array centered around Big Bear so using data from the three points, a two dimensional linear fit for stress has been computed. The coefficients of this fit determine an average stress curl and divergence in the triangle. In order to

calculate the internal wave forcing, τ_o , for the triangle, the stress curl was integrated in time starting at a time when conditions were calm. (In this case integration was begun at 0000, April 8.) The integrated stress curl and stress divergence were then combined using (4.2.36) to yield τ_o .

The dimensional form of τ_o for both types of forcing are shown in Figure 4.14. The ice forced and wind forced curves are remarkably similar in form. Both indicate a negative forcing on April 8 with a change to positive forcing on April 9 and 10. The negative forcing occurs because the northward ice velocity and wind velocity increased first at Caribou and Snowbird causing positive surface stress curl [negative surface shear stress curl, see (4.2.36)]. The forcing becomes positive because the northerly wind and ice velocity at Blue Fox became large late on April 8. Negative forcing tends to drive the pycnocline down and positive forcing draws it up so the sense of the forcing both before and after 24.0 hours is appropriate to cause the observed oceanic response.

The obvious difference between the two types of forcing is that the amplitude of the wind forcing is larger. On April 8 the wind forcing magnitude is twice as large as the ice forcing and after April 8 it is as much as three times larger. If the ice were massless and supported no internal stress, wind and water stress would balance and the two curves would be identical. The differences here are due both to internal ice stress and Coriolis force acting on the ice.

In spite of the differences between the two types of forcing it appears that, if the goal of this modeling effort is to decide if the

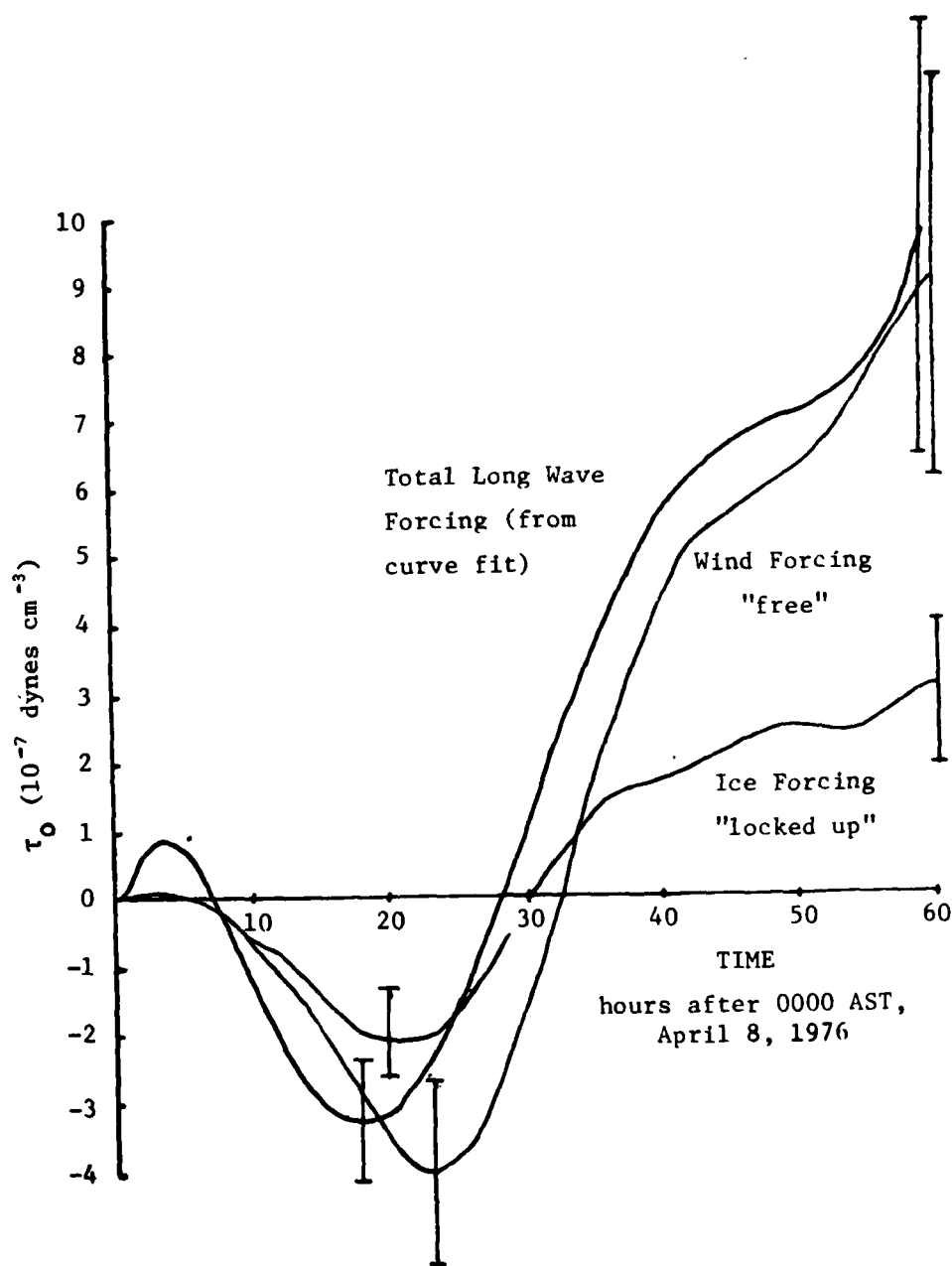


Figure 4.14. The internal wave forcing at Big Bear. The forcings due to wind stress and ice stress calculated for the triangle Caribou, Blue Fox, and Snowbird are shown. Also shown is the total long wave forcing at the AMLE camp derived from two dimensional 2×2 harmonic fit to the AIDJEX buoy data. Typical uncertainty limits are shown based on uncertainty in drag coefficients. Note the general agreement between estimates made in three different ways.

observed oceanic response could be due to forced internal waves, either type of forcing may be used. It must be kept in mind that the forcing so derived is an approximation to the actual forcing.

There is one consideration which indicates the forcing is best estimated from ice stress on the water. When a storm passes over an ice covered ocean, the ice typically breaks into irregular floes with dimensions on the order of ten kilometers. These floes are interspersed with large leads. For example, Figures 4.7 and 4.8 plainly show five large leads between Big Bear and Blue Fox on April 8 and 9 and faint traces of five more leads are visible between Big Bear and Caribou. To be visible in the photographs the leads must be about 2 km wide. They are separated by an average distance of 22 km. The stress on the water under a particular ice floe is relatively constant and large horizontal gradients in surface stress only occur in the large leads. Thus, the forcing τ_o , which is proportional to horizontal derivatives of stress, will be largest in narrow bands and have intermediate and high wave number components, which are substantial even if the wind stress forcing has no component at short wavelengths. The internal wave forcing for an ice covered area is unique in this regard. In order to account for the intermediate and high wave number forcing, the stress of ice on water will be used to estimate the forcing.

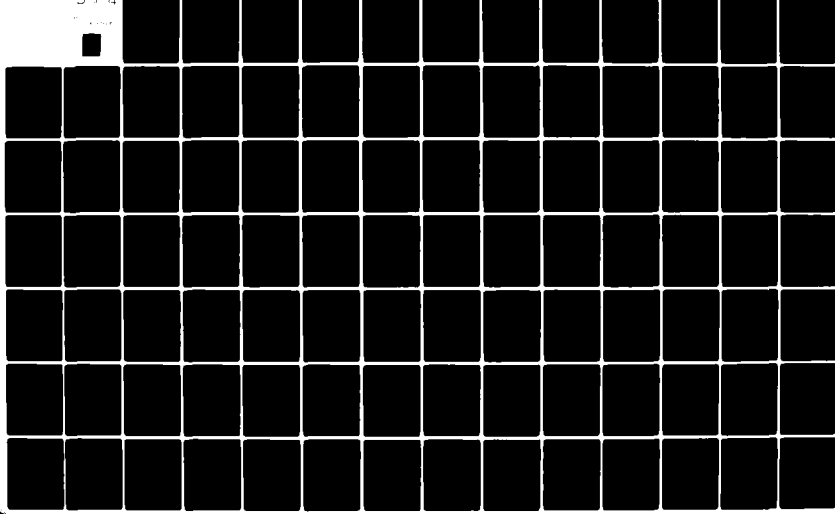
The second problem in deriving a model forcing is estimating the appropriate values over a broad range of wave numbers. The paragraph above points out the magnitude of the intermediate and high wave number forcing and Figures 4.10 through 4.13 indicate the response functions are greatest over a broad range of intermediate and small

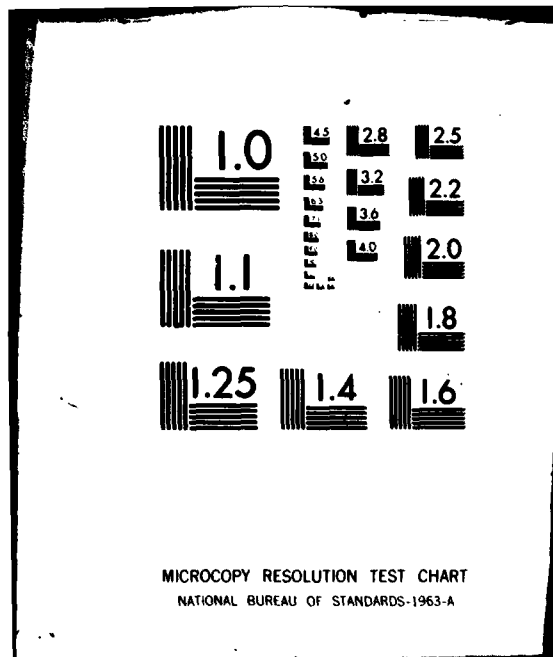
AD-A091 046 WASHINGTON UNIV SEATTLE DEPT OF OCEANOGRAPHY
FORCED INTERNAL WAVES IN THE ARCTIC OCEAN. (U)
MAY 80 J H MORISON
UNCLASSIFIED REF=M80-10

F/6 8/3

N00014-75-C-0186
NL

3 x 4





wave numbers. Unfortunately, data is available for estimating only the lowest wave number forcing at Big Bear. This information consists of ice position and velocity as measured over a large scale grid with AIDJEX satellite navigation buoys. The grid spacing is too large to resolve the forcing at less than a 200 km wavelength and so the intermediate and high wave number forcing must be hypothesized. Observations of lead patterns and a knowledge of the long wave forcing provide some basis for estimating the unknown components and fix upper bounds on the forcing. However, many of the particulars of the forcing have been determined with the idea of trying to maximize the agreement between the theoretical and observed responses. Thus, in principal, agreement between theory and data is only a necessary condition, not a sufficient condition, to prove the observed response is due to forced internal waves. The implications of this will be discussed further.

The long wave forcing due to ice stress on water has been estimated from the AIDJEX buoy data. As described by Thorndike and Cheung (1977) a network of satellite navigation buoys was maintained in the Beaufort Sea from March 1975 to May 1976. Figure 4.15 shows the array as it existed during the AMLE. Buoy locations are indicated by the squares at the corners of the triangles. They form an array approximately 600 km in the north-south direction and 800 km in the east-west direction. Position and velocity data from each of the buoys was obtained from the AIDJEX data bank and used in (3.3.1) to calculate the surface stress at each location. The array was then broken into 39 triangular segments with intersections at the buoy locations and the stress curl and divergence were calculated for each triangle. Using

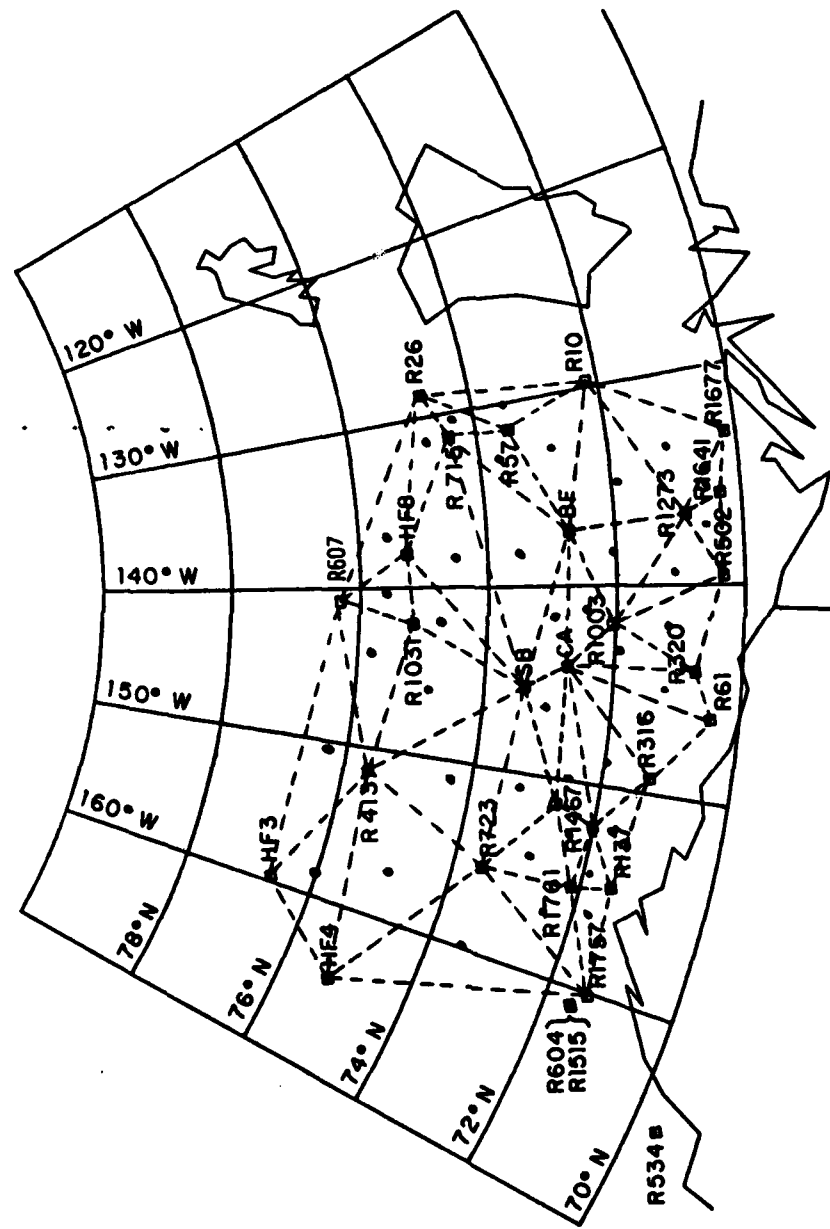


Figure 4.15. The AIDJEX buoy array at the time of the AMLE. Triangles indicate grids over which the internal wave forcing due to ice stress was calculated.

the integral of the stress curl with time, starting at 2300 on April 7, the dimensional form of τ_o [(4.2.36) gives the non-dimensional form] was computed for each triad of buoys. The forcing functions were assumed to apply at the average position of the three buoys making up the array and these points are indicated by dots in Figure 4.15.

Through this process, τ_o is described at discrete points in time and space. In order to apply the forcing to the model, the Fourier transform, T_o of τ_o must be estimated. Long wavelength components of τ_o are approximated by

$$\tau_{oa}(x, y, t) = \sum_{k=-K}^K \sum_{l=-L}^L A(t) e^{i(kx + ly)}$$

or for τ_{oa} a real number

$$\tau_{oa}(x, y, t) = \sum_{k=0}^K \sum_{l=0}^L \left\{ \begin{array}{l} T(t) \cos kx \cos ly + \\ 1k l \\ T(t) \sin kx \sin ly + T(t) \cos kx \sin ly + T(t) \sin kx \cos ly \end{array} \right\} \quad (4.6.1)$$

$$\begin{array}{lll} 2k l & 3k l & 4k l \end{array}$$

where x and y are non-dimensional distances centered at the AMLE site. With this approximation for the long wavelength components of τ_o , the Fourier transform, T_o , can be replaced by the coefficients, T_{ikl} , of a two-dimensional Fourier series. The responses derived using each of these coefficients are the response coefficients of a Fourier series of an identical form. Where ik and il appear in the velocity response equations, (4.2.72) and (4.2.73), they represent differentiation of the series in x and y respectively.

The series of (4.6.1) has been fit to the forcing from the

AIDJEX buoy data using a least squares technique. The maximum wavelength is 704 km and coefficients for the first two harmonics in each direction have been determined. The shortest wavelength for which forcing has been determined is thus 352 km. The fundamental wavelength was chosen because it nearly equaled the minimum dimension of the buoy array and the lead spacing of 22 km is its sixth harmonic. The coefficients were determined at three hour intervals from 0200 April 8 to 1400 April 10 and the approximation of (4.6.1) accounts for about 50 percent of the total variance at the 39 data points.

As mentioned in Section 4.4 the forcing functions are best represented by polynomials in time. So the Fourier coefficients of (4.6.1) were approximated with sixth order polynomials using a least squares curve fitting program. The errors in doing so amount to less than 10 percent of the values. Figure 4.14 shows a plot of the sum of the polynomial fits for T_{1kl} . Because the coordinate system is centered at Big Bear, only the coefficients T_{1kl} produce any vertical disturbance there. The trigonometric terms of the other coefficients in (4.6.1) are all zero. Thus the plot of Figure 4.14 is representative of the total long wavelength forcing at $x = y = 0$. Comparison with the other plots in Figure 4.14 indicates the long wavelength forcing at Big Bear is comparable to the wind forcing and stress forcing estimated from the AIDJEX manned camp triangle. This inspires confidence in the values especially since the "wind forcing" is based on a completely different data set than the other two types of forcing.

In order to estimate the short wavelength forcing the ice is assumed to be broken into strips 20 km wide with 2 km gaps or leads

between them. This is a crude representation of the pattern observed in Figures 3.6, 3.7 and 3.8. Because stress is constant under each strip, the forcing is zero there and is concentrated in the narrow leads. Figure 4.16 shows a sketch illustrating an approximation to this situation. The forcing is represented as a square wave of constant amplitude symmetric around Big Bear with an average value equal to the total long wave forcing. A series such as τ_L can be composed into a Fourier series. From Lathi (1965),

$$\tau_L = \tau_m + \sum_{n=1}^{\infty} 2\tau_m S_a \left(\frac{n\pi\Delta L}{L} \right) \cos \frac{2\pi n}{L} y \quad (4.6.2)$$

where

$$S_a(\theta) = \frac{\sin \theta}{\theta} \quad (4.6.3)$$

and τ_m is both the average forcing over the region and, by nature of the geometry of the situation, the scale for the fluctuations about the mean.

In this work τ_m is approximated with the total long wavelength forcing, τ_{oa} , at Big Bear because it is the best estimate of the large scale average forcing. The model of Figure 4.16 thus relates the short wavelength forcing to the long wavelength forcing. The approximation is only applicable over a radius about Big Bear which is small relative to the shortest wavelength component of the long wave forcing (i.e., a 35 km radius about Big Bear). However, it should be pointed out that the scheme does not create energy at short wavelengths out of nothing. Rather it reconstructs the energy in the spectrum which is filtered

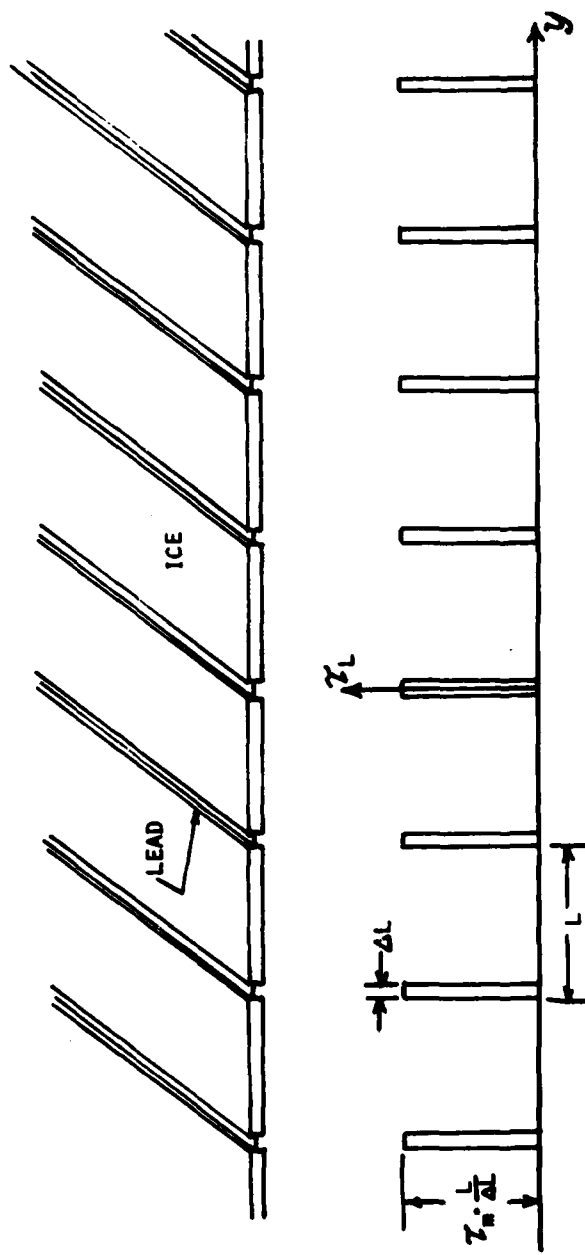


Figure 4.16. Sketch illustrating the model of lead distribution near the AMLE camp at Big Bear on April 8, 1976 and the assumed small scale distribution of forcing.

out of the position measurements by the large station spacing.

For $\Delta L = 2$ km and $L = 22$ km the first five values of $S_a(n)$ are given in Table 4.2.

Table 4.2

$S_a(n)$ for $n = 1 \rightarrow 5$

n	1	2	3	4	5
$S_a(n)$.9865	.9465	.8821	.7962	.6932

For such narrow pulses the wave number spectra obviously drops off very slowly with increasing wave number. Using equations (4.6.2) and (4.6.3) the forcing for wavelengths 22, 11, 5.5, 2.75 and 1.375 km have been estimated. Because of the broad band nature of the signal, the short wavelength components are all nearly twice the total long wavelength forcing.

The only remaining harmonic wavelengths unaccounted for are the intermediate values, 176 km, 88 km, and 44 km. The actual forcing is not really the same in each lead as shown in Figure 4.16, but undoubtedly varies with an amplitude of the same order as the magnitude of the pulses. These variations are due to variation of the intermediate wavelengths which are not resolved by the navigation buoy triangles and are not included in the approximation of (4.6.2). Here their amplitude is assumed equal to that of the 22 km component. The intermediate and short wave forcing components are assumed to be cosines in y which sum constructively at $y = 0$. This will yield a response at $y = 0$ with a

maximum possible amplitude. Presumably the sine components may be of similar magnitude but they produce no displacement at Big Bear ($y = 0$).

Using the forcing functions described above, equation (4.2.58) was solved for vertical displacement using formulas (4.4.16) through (4.4.24) to compute the convolution integral. The first 49 normal modes were used and the 49th mode was found to have a response equal to about 2 percent of the first mode. The result of this computation for the upper 100 m of the water column is shown in Figure 4.17.

In Figure 4.17 the response of isopycnals initially positioned at 5 m intervals from 5 m depth to 85 m depth are shown along with the observed response as functions of time starting at 0000 AST on April 8, 1976. In addition the response of the seasonal pycnocline is represented by the response at 38 m. The response generally resembles the total long wave forcing function of Figure 4.14 because the forcing is dominated by frequencies lower than the natural frequencies of the internal wave modes and the forced response follows the forcing. The maximum response occurs near the seasonal pycnocline. The isopycnal at 38 m rises initially then drops to 0.70 m below its initial position by 14.5 hours. Subsequently the pycnocline rises steadily to 1.6 m above its initial position by 60.0 hours. During the rise, three weak oscillations occur about 10.0 hours apart.

The predicted response at the pycnocline is similar to the observed response in that it involves an initial depression followed by rebound with oscillation at frequencies slightly greater than the inertial frequency. Just as was suggested in the simple explanation of the observed response, during the initial stages of the storm, the

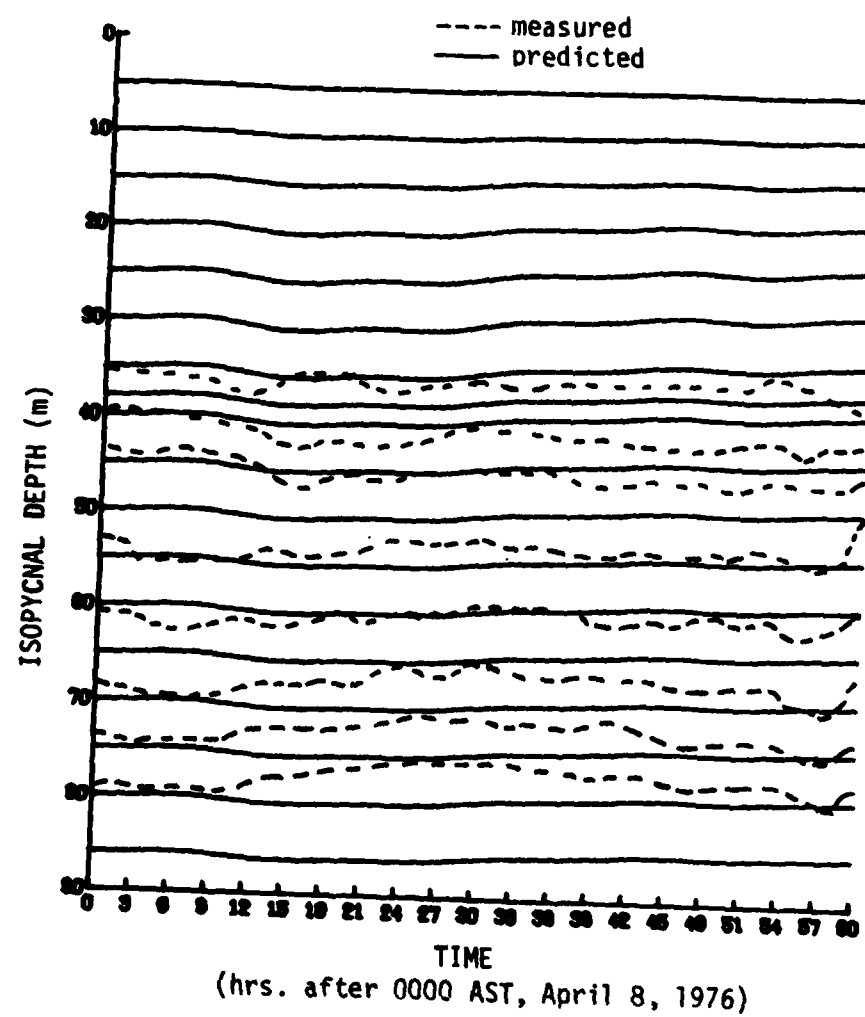


Figure 4.17. The predicted isopycnal response to surface stress and observations at Big Bear in the upper 90 m of the water column. The time scale starts at 0000 AST, April 8, 1976.

northwesterly ice motion to the west of Big Bear forces the pycnocline down due to Ekman pumping. After the storm passes Big Bear, reversal of the stress curl causes the pycnocline to be pumped back up. The oscillations occur with a period of about 10 hours. The frequency is greater than the inertial because the fluctuations are due to free oscillations of the internal wave modes.

The predicted and observed response of the seasonal pycnocline agree fairly well in phase. The maximum observed depression occurs between 11.0 hours and 15.0 hours, depending on which isopycnal is being considered, and the maximum depression in the theoretical response occurs at 14.5. Both the observed and predicted response begin before the wind speed starts to increase. This occurs for two reasons. The pycnocline motion is forced by the integral of the surface stress curl and the response is greatest at large length scales. Thus, the response at the pycnocline starts, not when the local wind stress begins to rise, but when the integral of stress curl averaged over a large distance (ex. 200 km) begins to rise. As a storm moves toward a site such as the AMLE camp, the large scale components of the integral of stress curl rise locally before the storm front arrives.

The observed and predicted responses also reach maxima more than five hours before the local wind speed reaches a maximum at 19.7 hours. For the most part, this is because the April 8 storm intensified after passing Big Bear and, as a result, the integral of stress curl went to zero and changed sign before the region of maximum stress arrived.

It should be added that the vertical velocity and components of

the horizontal velocity are proportional to the stress curl, not the integral of stress curl, and thus, lead the peak stress even more than the vertical displacement does. This is the most likely explanation for the observations by J. D. Smith (personal communication) indicating that the relative water velocity begins to rise a few hours before the local wind during the passage of an arctic storm.

Aside from the qualitative agreement in the form of the response and phase relationships, the predicted and observed responses disagree in several ways. An obvious deficiency is that the predicted response is significantly smaller than the observed response. The second problem is that the predicted response continues to rise after the storm passes Big Bear while the observed response stops and levels off at or slightly below the initial position. Finally, the predicted response is relatively constant with depth at least with regard to phase, while the observed response shows marked differences above and below 50 m. These dissimilarities will be discussed in order.

The maximum depression of the predicted response is 0.7 m while the observed response is 2 m at 38 m depth and 3 m at 45 m depth. Thus the predicted response in the first 24 hours is a factor of three to four too small. One explanation for this is that the forcing components at wavelengths of 176 km and less are too small. This is actually unlikely. The forcings at these scales have been estimated in a simple way from the long wavelength forcing by assuming the stress curl and divergence occur in a few narrow leads and that the variations between the forcing in leads is of the same order as the forcing in individual leads. Table 4.3 shows the contribution to the total predicted

Table 4.3
Contributions to the Stress Response at Different Wavelengths

Wavelength (km)	Short	Intermediate	Long wave > 352.0	Total						
	1.375	2.75	5.5	11.0	22.0	44.0	88.0	176.0	352.0	Total
Pycnocline Depression at 14.5 hrs (cm)	.6	2.0	4.1	5.9	8.5	12.2	14.5	16.8	7.7	72.3

displacement of the pycnocline due to the various short and intermediate wavelength forcings along with the total long wavelength response. The intermediate length forcings combine to produce 60 percent of the total response. The response at each is about twice the total due to long wavelength forcing because the intermediate scale forcings are assumed to be equal to the 22 km forcing (twice the total long wavelength forcing). It is conceivable that the Big Bear camp was in a region of very intense surface stress gradients and the intermediate scale forcing should be three or four times as large. However, the forcing at 176 km is already nearly an order of magnitude greater than the individual long wavelength components and, in this regard, further increases are difficult to justify. The model probably is yielding the maximum conceivable response of the pycnocline due to surface stress. As will be shown in the next chapter the addition of forcing by buoyancy flux is necessary to account for the magnitude of the observed response at the pycnocline.

The predicted rise of the isopycnals after the storm are most likely due to an incorrect estimate of the intermediate wavelength forcing. The large increase in the total long wavelength forcing is caused by a rapid northwesterly ice motion at Blue Fox. If this ice motion is due to localized activity at Blue Fox the intermediate scale forcing at Big Bear should not reflect the large positive forcing after April 8. If the intermediate and small scale forcings simply returned to the level achieved at 14.5 hours and remained there, the predicted response would only rise to .6 m below equilibrium by 60 hours. In order to achieve a response similar to that observed at 45 m the

forcing at wavelengths of 176 km and shorter should drop to -10^{-6} dynes cm^{-3} by 18.0 hours and then rise to -4.0×10^{-7} dynes cm^{-3} by about 24.0 hours. After that time the intermediate and small scale forcing should remain nearly constant.

Although imposing the artificial forcing discussed above would force the response to resemble the observed pycnocline displacement it would not recreate the observed variations in response with depth. The observed response is quite different above and below 50 m. The isopycnals above 50 m indicate initial depression followed by partial rebound while the 25.6 isopycnal drops 1 m between 0.0 hours and 2.0 hours and rises slowly back to the initial position by 24.0 hours. The 26.0 isopycnal drops slightly at first but for the most part is characterized by a slow rise of about 4.0 m between 11.0 hours and 32.0 hours. The predicted response displays the same general pattern, depression and rebound, at all depths and only the amplitude changes, decreasing with depth below the seasonal pycnocline. The response at 80 m is 60 percent of the response at 38 m. The rise of the isopycnals predicted by the model might be representative of the observed rise of isopycnals below 50 m but the phase of the predicted rise lags the observed by about 10 hours. Modifications to the intermediate wavelength forcing would not have a substantial effect on vertical structure because the forcing acts slowly and the mode shapes at all the important wavelengths are nearly identical. Therefore, changes in the intermediate scale forcing have a similar effect at all depths. It would seem that an entirely different process is acting at depths below 50 m.

Figure 4.18 shows the response to surface stress throughout the

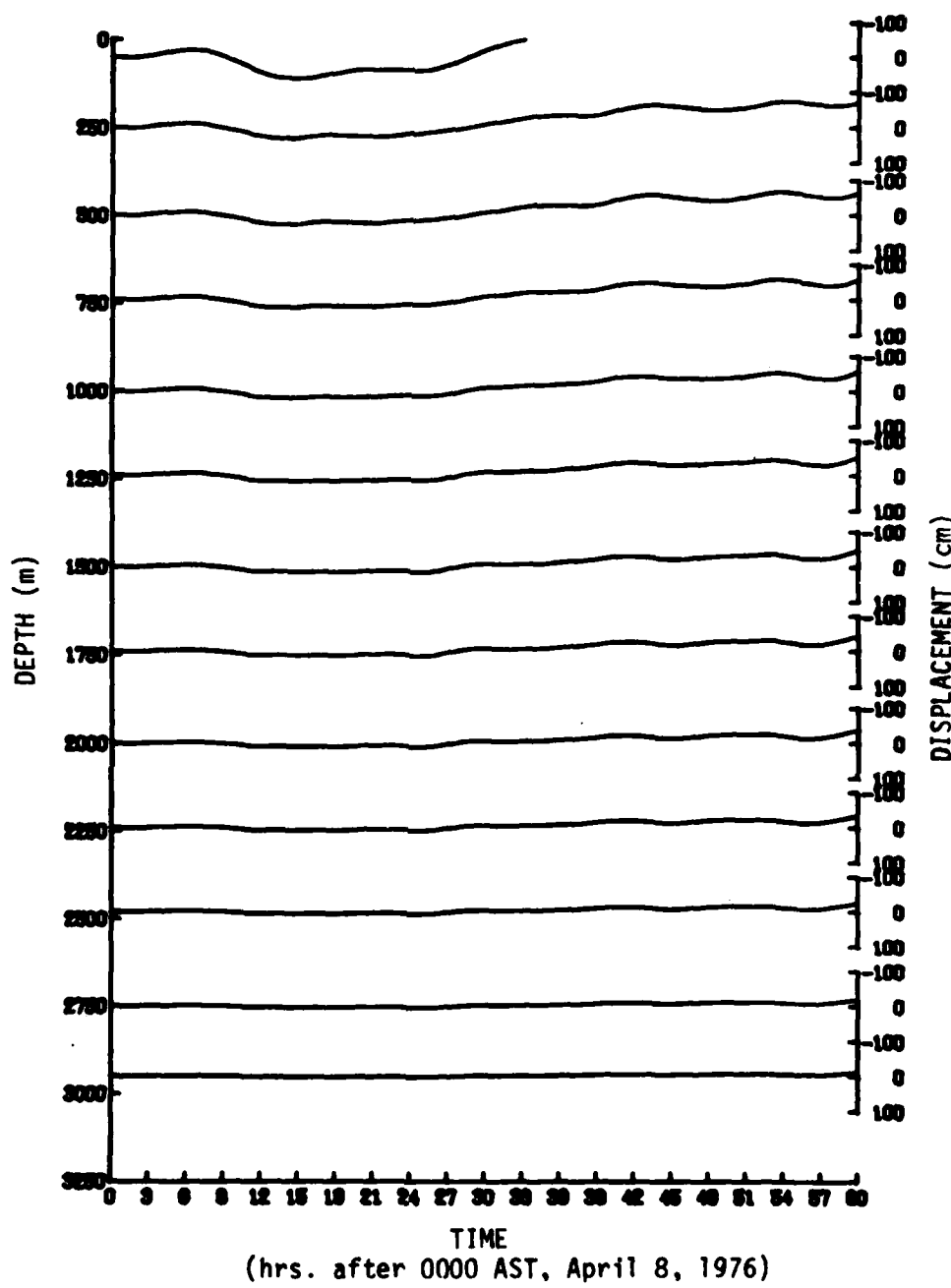


Figure 4.18. The predicted response to surface stress at Big Bear over the whole ocean depth. The time scale starts at 0000 AST, April 8, 1976.

water column. The vertical scales for the displacements are given on the right and the initial depths are on the left. The upper line is the displacement at 50 m depth. The interesting thing about the plot is that the response is confined to the upper 250 m. It decays smoothly with depth in spite of the inclusion of a large number of modes with significant amplitude at depth. In fact, all the modal responses reinforce near the pycnocline but interact destructively below. It is in one sense disappointing that all the interesting high modal structure is wiped away in the total response. However, the result is intuitively satisfying in that convergence in the mixed layer results in a simple downward deflection of the pycnocline, and, for rapid changes in forcing, produce little motion at depth.

The simplicity of the response also suggests the pycnocline deflection might be predictable using a two layer model but such a model would be incapable of producing the rapid decay in response with depth shown in Figure 4.18. For long wavelengths, letting N go to zero below the pycnocline would produce vertical deflections which would decay linearly with depth (shallow water wave) while the disturbance actually decays more rapidly with depth, not because the waves are short, but because they are transient in time and cannot penetrate the weak stratification of the main pycnocline instantaneously. If a two layer model were to be used effectively to study forced transient behavior, the lower layer should be made artificially shallow (ex. 250 m) so that energy input may remain concentrated near the surface during the initial response. The artificially shallow layer would take the place of the stratification below the top pycnocline in the complete model.

Figure 4.19 shows u velocity contour plots produced by the stress forced internal wave model. The velocities are those produced by the $\cos kx \sin ly$ and $\sin kx \cos ly$ components of long wave forcing [T_{3kl} and T_{4kl} in (4.6.1)] plus intermediate and short wave forcing components with magnitudes equal to those used to produce the displacement plots. The velocity is thus not directly related to the displacements shown in Figures 4.17 and 4.18 but is representative of the type of velocity field one would expect to be associated with such displacements. Figure 4.20 shows v velocity contours in time and depth for the same forcing as used to derive the u velocity. The left hand plots in both Figure 4.19 and 4.20 represent absolute velocity while the plots on the right show the velocity relative to the average velocity in the mixed layer.

Both the u and v velocity fluctuations are largest in the mixed layer. This is because all modes respond by producing vertical displacement in the same direction at the top pycnocline and, as a result, the modal velocities, proportional to the gradient of vertical displacements, add constructively in the mixed layer. Below the top pycnocline the model velocities interfere. Almost all of the velocity fluctuation is due to motion at the intermediate wavelengths because the forcing is greatest for these components and, as was shown in Figure 4.11, the velocity response (u_p or v_p) is greatest at intermediate wavelengths.

The u velocity initially increases to 1.5 cm sec^{-1} at 15.0 hours. The northerly velocity is geostrophically driven by sea surface tilt upwards to the east. (The pycnocline slopes down to the east.)

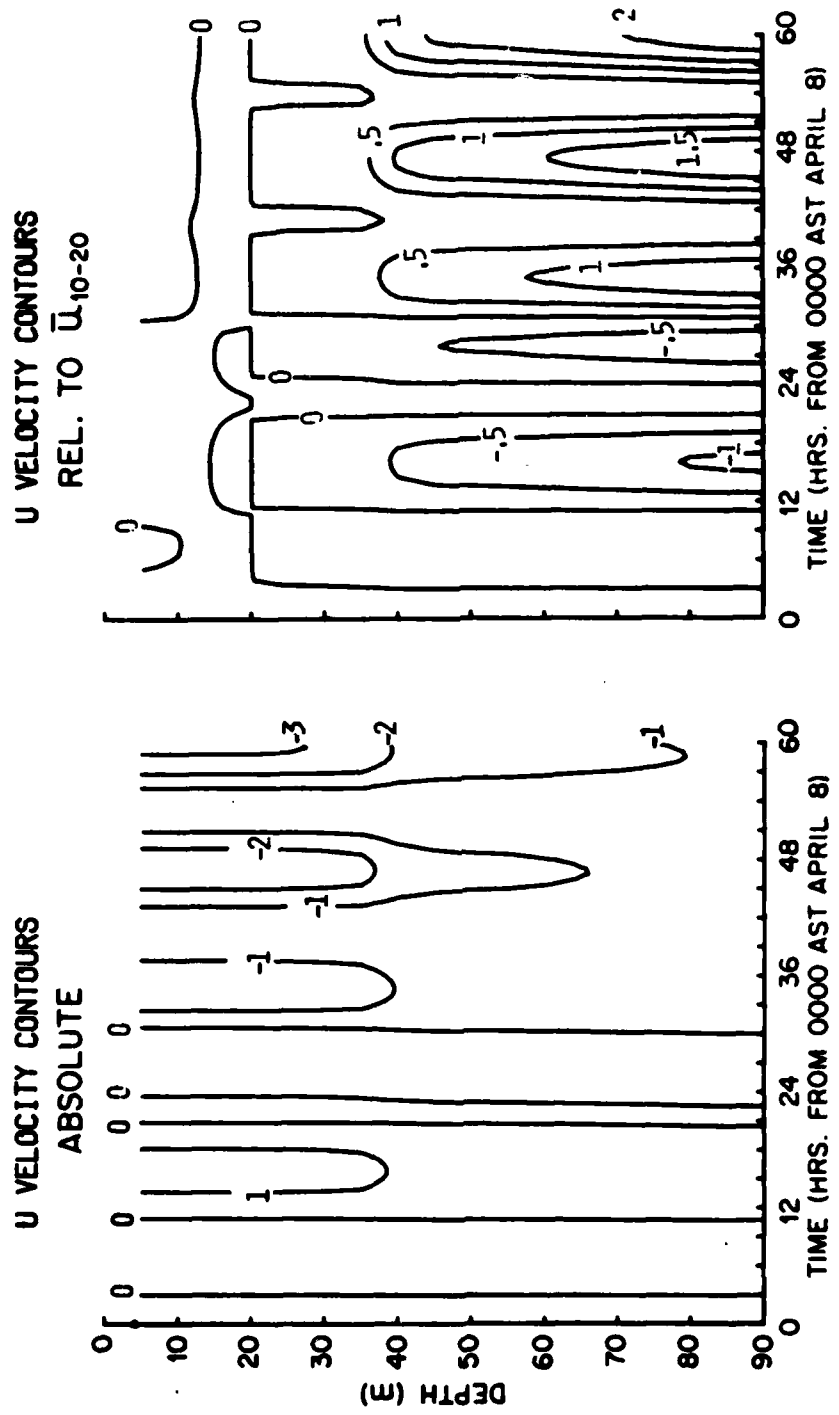


Figure 4.19. Contour plots of absolute and relative u velocity due to stress response. The time scale starts at 0000 AST, April 8, 1976.

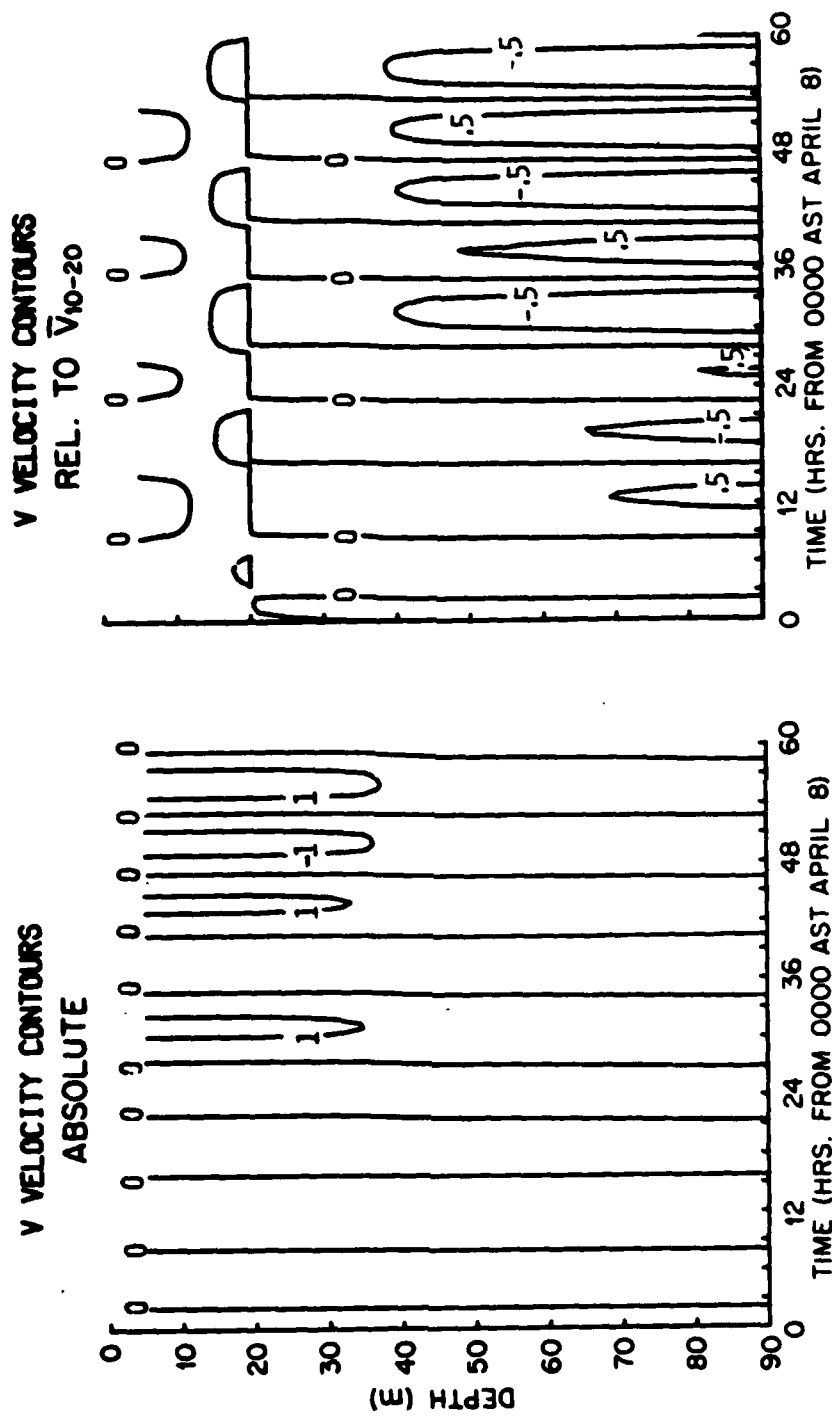


Figure 4.20. Contour plots of absolute and relative v velocity due to stress response. The time scale starts at 0000 AST, April 8, 1976.

When the trend in vertical displacement reverses after 24.0 hours, the average u velocity in the surface layer becomes negative and oscillates with a growing amplitude. By 60.0 hours the amplitude of the oscillations is about 1.4 cm sec^{-1} and the average velocity is -1.6 cm sec^{-1} . The v velocity displays similar oscillations of the same amplitude. The oscillations occur at or near the inertial period and the v velocity lags the u velocity so as to produce inertial motion. The average v velocity is nearly zero. It should be noted that the fluctuations in v in the mixed layer do not satisfy continuity. The mass balance there is maintained by the addition of the boundary layer flow which forces the pycnocline down (or up). The v velocity due to the forced internal wave solution is driven by the opposing pressure gradient which is set up by sea surface tilt. This velocity is about 10 percent of the boundary layer velocity and is neglected in zero surface displacement models.

The oscillatory behavior is perhaps the most important feature of the velocity plots. Vertical bands of velocity maxima appear in both the predicted velocity contours shown in Figures 4.19 and 4.20 and the observed velocity contours of Figures 3.9 and 3.10. In both the observed and predicted data, the oscillations occur at or near the inertial frequency. The observed oscillations occur at a frequency slightly greater than the inertial frequency, but this is probably due to the qualitative manner in which the oscillations are identified, the short time over which they were observed and the influence of other velocity disturbances. In contrast, oscillations of both predicted and observed vertical displacement occur at periods significantly shorter

than the inertial period (six hours to ten hours for the observed and ten hours for the predicted). The energy content of vertical displacement in the inertial frequency range is much smaller than that at the natural frequencies of the internal wave modes. Thus, the displacement oscillations appear at frequencies higher than the inertial period. However, there is some energy at the inertial frequency in the forced displacements and this energy excites inertial motion in the horizontal velocity. Unlike inertial motions directly excited by stress in the mixed layer, these inertial motions penetrate the pycnocline. This is shown in both the observed and predicted velocity contours but is especially apparent in the u velocity plot of Figure 4.19 where oscillations extend as deep as 80 m. The phenomena is not as apparent in the v velocity plot of Figure 4.20 because of the choice of contour interval. Energy at the inertial frequency is transmitted across the pycnocline, not by turbulent momentum transfer, but rather by the inertial frequency component of the forced vertical displacements.

Aside from their general oscillatory character, the theoretical and observed velocity contours do not compare very well. The amplitude of the oscillations and mean values for the theoretical contours are about one half or one third of the observed motions and the phases of the oscillations are different. The latter problem is understandable inasmuch as the velocity predictions were only intended to be representative of the types of velocity patterns that might be encountered during the storm.

In summary, the response due to surface stress at the top pycnocline is similar to the observed response in sense and phase. The

velocity response of the model is also similar in character (if not phase) to the observed pattern, but the theoretical responses in both displacement and velocity are a factor of two or three smaller than the observed motions. This is in spite of the fact that, in developing the theoretical forcing function, an effort was made to maximize the response. Also the theoretical and actual vertical displacement disagree below 50 m and after 24.0 hours. Therefore, though the response to surface stress is significant it cannot account for all the observed motions. Additional phenomena must have been active in order to produce the observed response of April 8.

The next section considers the effects of surface buoyancy flux on internal wave motions. It will be shown that this type of forcing may cause displacements comparable to those due to surface stress and, when combined with the theoretical response to surface stress, produces a motion at the seasonal pycnocline similar to that observed on April 8.

4.7 Response to Buoyancy Flux

The second possible cause of the observed disturbances is the generation of internal wave motions by buoyancy flux in leads. It has already been hypothesized that, during the April 8 storm, an array of large leads opened at intervals of approximately 22 km. Such a pattern would produce a buoyancy flux pattern which can be broken into Fourier harmonics just as was the short wavelength stress forcing.

In examining the short wavelength forcing due to stress, the motion of the lead system was ignored. Doing so was permissible for

that case because only the shortest wavelength components (wavelength ≤ 11.0 km) are affected by ice motion and these produce little response. Also, only high mode numbers ($n > 15$) have phase speeds as low as the typical ice velocity. These high modes produce responses with amplitudes two orders of magnitude less than those of the low modes. So, even if they were driven as resonance for one day they would only increase by one order of magnitude and would still be small. In contrast, the proper application of the buoyancy flux model requires that the ice velocity be accounted for in some manner because, in the model, horizontal spreading of the surface layer density disturbance is due only to movement of the buoyancy flux source. Lateral diffusion due to turbulence and convective circulation is ignored. If it is assumed that the leads and buoyancy flux pattern are as shown in Figure 4.16 but that the ice is moving at a constant velocity v_i perpendicular to the leads, the buoyancy flux can be decomposed into Fourier harmonics:

$$F_{BO} = \left\{ \sum_{j=1}^{\infty} c_j \cos \frac{2\pi j}{L} (y - v_i t) + F_{BL} \frac{\Delta L}{L} \right\} H(t) \quad (4.7.1)$$

where

$$c_j = 2 F_{BL} S_j \frac{\Delta L}{L} \quad (4.7.2)$$

and F_{BL} is the buoyancy flux in each lead. A more convenient form for the fluctuating buoyancy flux is the non-dimensional form,

$$F_B = \sum_{j=1}^{\infty} A_j (\cos \omega_j t \cos \ell_j y + \sin \omega_j t \sin \ell_j y) H(t) \quad (4.7.3)$$

where

$$\omega_j = \frac{j2\pi H}{L} \frac{v_i}{Hf} = \ell_j \frac{v_i}{Hf}$$

Using (4.3.23) and the relation between W and u_*^2 in (4.2.1), the non-dimensional magnitude A_j is found for a velocity scale corresponding to $u_* = 1$,

$$A_j = \frac{c_j}{F_s} = \frac{c_j}{u_*^2 \delta f} = \frac{c_j}{\delta f}$$

The Laplace transform of this equation is

$$B_o = \sum_{j=1}^{\infty} A_j \left(\left(\frac{\sigma}{\sigma^2 + \omega_j^2} \right) \cos \ell_j y + \left(\frac{\omega_j}{\sigma^2 + \omega_j^2} \right) \sin \ell_j y \right) \quad (4.7.4)$$

and the equivalent pressure forcing is

$$\begin{aligned} P_{IB} &= \frac{-\delta(\sigma^2 + \omega_G^2)}{\sigma(\sigma^2 + 1)} B_o \\ &= \sum_{j=1}^{\infty} A_j \delta \left(\frac{(\sigma^2 + \omega_G^2)}{(\sigma^2 + \omega_j^2)(\sigma^2 + 1)} \cos \ell_j y \right. \\ &\quad \left. + \frac{\omega_j(\sigma^2 + \omega_G^2)}{\sigma(\sigma^2 + \omega_j^2)(\sigma^2 + 1)} \sin \ell_j y \right) \end{aligned} \quad (4.7.5)$$

When this equivalent pressure is used to drive vertical displacements the results are satisfactory but the $\frac{1}{\sigma^2 + 1}$ term causes a resonant growth of inertial motions in the velocity solution. For this reason σ^2 is assumed small relative to unity. Such an approximation amounts to an assumption that the boundary layer motions are quasi-geostrophic.

That is, accelerations in the boundary layer are assumed small relative to the Coriolis acceleration. Also σ is much less than ω_G . Making these assumptions the Laplace transform equation for displacement is

$$\psi_p = \sum_{j=1}^{\infty} \sum_{n=1}^{\infty} - \frac{\psi_n R A_j \delta k_j^2}{\lambda_n \omega_n} \cdot \frac{\omega_n \omega_G^2}{(\sigma^2 + \omega_n^2)(\sigma^2 + \omega_j^2)} \cdot (\cos \lambda_j y + \frac{\omega_j}{\sigma} \sin \lambda_j y) \quad (4.7.6)$$

Using (4.2.69) and (4.2.70), the equations for velocity are

$$\mu_p = \sum_{j=1}^{\infty} \sum_{n=1}^{\infty} \frac{\psi_n' R k_j^2 A_j \delta \lambda_j}{\omega_n \lambda_n^2} \cdot \frac{\omega_n \omega_G^2}{(\sigma^2 + 1)(\sigma^2 + \omega_n^2)(\sigma^2 + \omega_j^2)} \cdot (\sin \lambda_j y - \frac{\omega_j}{\sigma} \cos \lambda_j y) \quad (4.7.7)$$

and

$$v_p = \sum_{j=1}^{\infty} \sum_{n=1}^{\infty} \frac{\psi_n' R k_j^2 A_j \delta \lambda_j}{\omega_n \lambda_n^2} \cdot \frac{\omega_n \omega_G^2 \sigma}{(\sigma^2 + 1)(\sigma^2 + \omega_n^2)(\sigma^2 + \omega_j^2)} \cdot (- \sin \lambda_j y + \frac{\omega_j}{\sigma} \cos \lambda_j y) \quad (4.7.8)$$

The inverse transforms for displacement and the velocities are

$$\begin{aligned} \zeta = & \sum_{j=1}^{\infty} \sum_{n=1}^{\infty} - \frac{\psi_n R A_j \delta k_j^2}{\lambda_n \omega_n} \cdot \left[\left(\frac{A_d}{\omega_n} \cos \omega_n t + \frac{B_d}{\omega_j} \sin \omega_j t \right) \cos \lambda_j y \right. \\ & \left. + \left(\frac{A_d \omega_j}{\omega_n^2} (1 - \cos \omega_n t) + \frac{B_d}{\omega_j} (1 - \cos \omega_j t) \right) \sin \lambda_j y \right] \end{aligned} \quad (4.7.9)$$

$$u_p = \sum_{j=1}^{\infty} \sum_{n=1}^{\infty} \frac{\psi_n^* R_p k_j^2 A_j \delta \ell_j}{\omega_n^2 \omega_j^2} (u_1 \sin \ell_j y - u_2 \cos \ell_j y) \quad (4.7.10)$$

and

$$v_p = \sum_{j=1}^{\infty} \sum_{n=1}^{\infty} \frac{\psi_n^* R_p k_j^2 A_j \delta \ell_j}{\omega_n^2 \omega_j^2} (-v_1 \sin \ell_j y + v_2 \cos \ell_j y) \quad (4.7.11)$$

where

$$A_d = -B_d = \frac{\omega_n \omega_G^2}{\omega_j^2 - \omega_n^2} \quad (4.7.12)$$

$$u_1 = \frac{A_v}{\omega_n} \sin \omega_n t + \frac{B_v}{\omega_j} \sin \omega_j t + c_v \sin t \quad (4.7.13)$$

$$u_2 = \frac{A_v \omega_j}{\omega_n^2} (1 - \cos \omega_n t) + \frac{B_v}{\omega_j} (1 - \cos \omega_j t) + c_v \omega_j (1 - \cos t) \quad (4.7.14)$$

$$v_1 = A_v \cos \omega_n t + B_v \cos \omega_j t + c_v \cos t \quad (4.7.15)$$

$$v_2 = \omega_j u_1 \quad (4.7.16)$$

$$A_v = \frac{A_d}{(1 - \omega_n^2)} \quad (4.7.17)$$

$$B_v = \frac{B_d}{(1 - \omega_j^2)} \quad (4.7.18)$$

and

$$c_v = \frac{\omega_n \omega_G^2}{(\omega_n^2 - 1)(\omega_j^2 - 1)} \quad (4.7.19)$$

To simulate conditions at Big Bear, only the first three harmonics, wavelengths = 22, 11, and 5.5 km, have been used. As will be shown, the 5.5 km wavelength appears to be the shortest wavelength for which it is appropriate to neglect horizontal diffusion. Equations (4.7.9) through (4.7.11) were evaluated numerically for several positions and ice velocities. The buoyancy flux in the leads was calculated from the ice growth rate. This was estimated using equations (3.4.3) and (3.4.5). For the -15°C temperature difference between the air and the sea water on April 8 and a 5 m/sec wind speed, the salt flux from open water is $4.36 \times 10^{-6} \text{ gm cm}^{-2} \text{ sec}^{-1}$. This corresponds to a buoyancy flux of $-3.3 \times 10^{-3} \text{ cm}^2 \text{ sec}^{-3}$. It was assumed for the purposes of calculating the response with the analytic expressions (4.7.9), (4.7.10) and (4.7.11) that the leads opened at 0000 AST on April 8, remained open for 24 hours, and then closed abruptly. The assumption of an open water condition produces a maximum buoyancy flux but corresponds to the common situation in which wind blows grease ice to one side of an open lead keeping the lead surface ice free. When the wind stops, the ice cover begins to grow and the buoyancy flux decreases rapidly. The model is linear so the cessation of forcing is implemented in the model by adding the response to a step forcing of opposite sign at 24.0 hours to the response continuing from 0.0 hours.

Figure 4.21 and 4.22 are plots of isopycnal responses as a function of time, assuming the ice velocity is initially 5 cm/sec in the negative y direction and then goes to zero at 24.0 hours. The response is that which would be observed from a point moving with the ice but initially at -12.38 km. Figures 4.23 and 4.24 illustrate the same

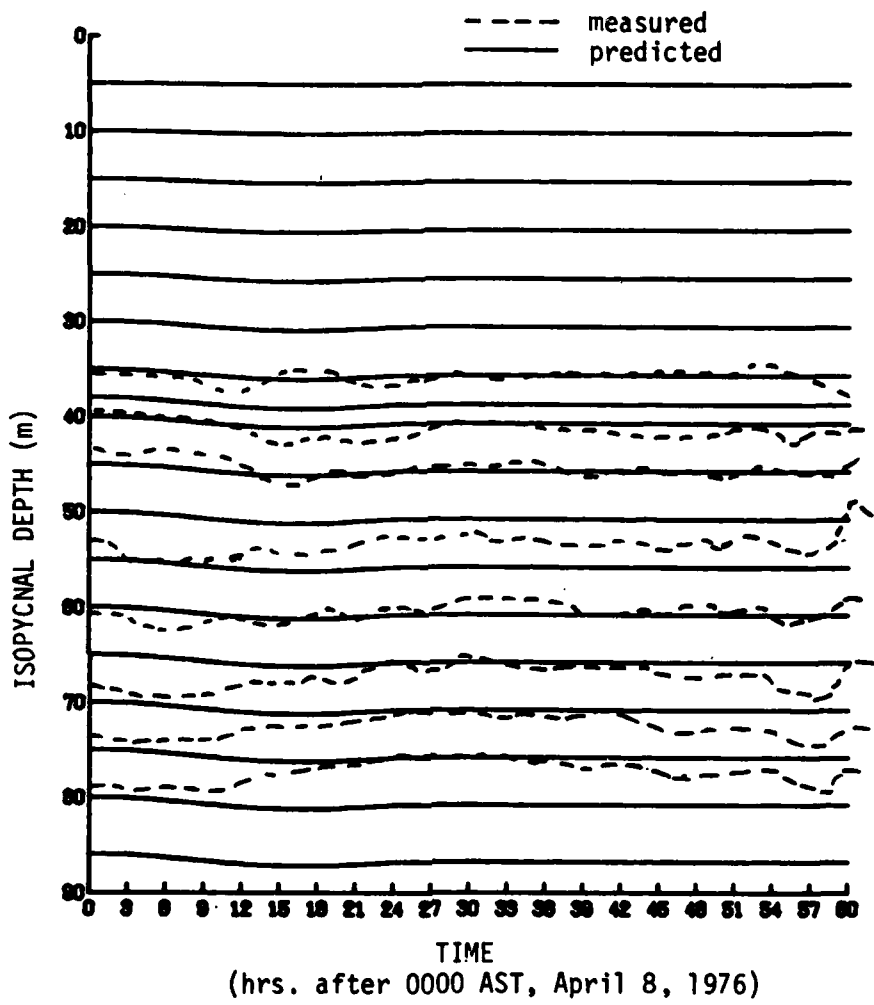


Figure 4.21. Predicted isopycnal responses in the upper 90 m of the water column to buoyancy flux in leads open on April 8. The response is as viewed from ice moving at -5 cm sec^{-1} for 24 hours and stopped thereafter. The initial position is -12.375 km. Dashed lines represent observations. Note relatively better agreement at 45 m and above.

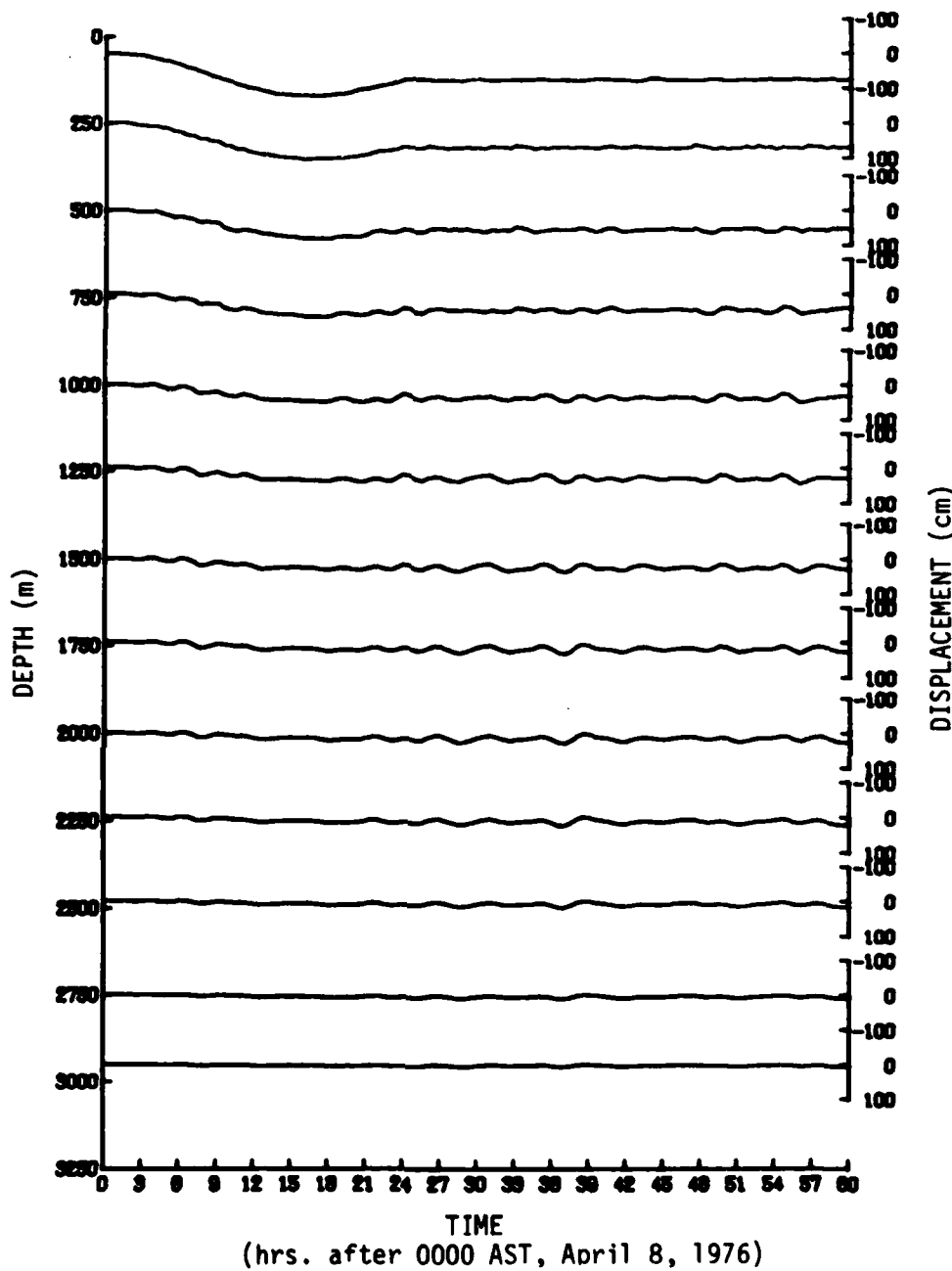


Figure 4.22. Predicted isopycnal response over the full ocean depth to buoyancy flux conditions identical to those of Figure 4.21.

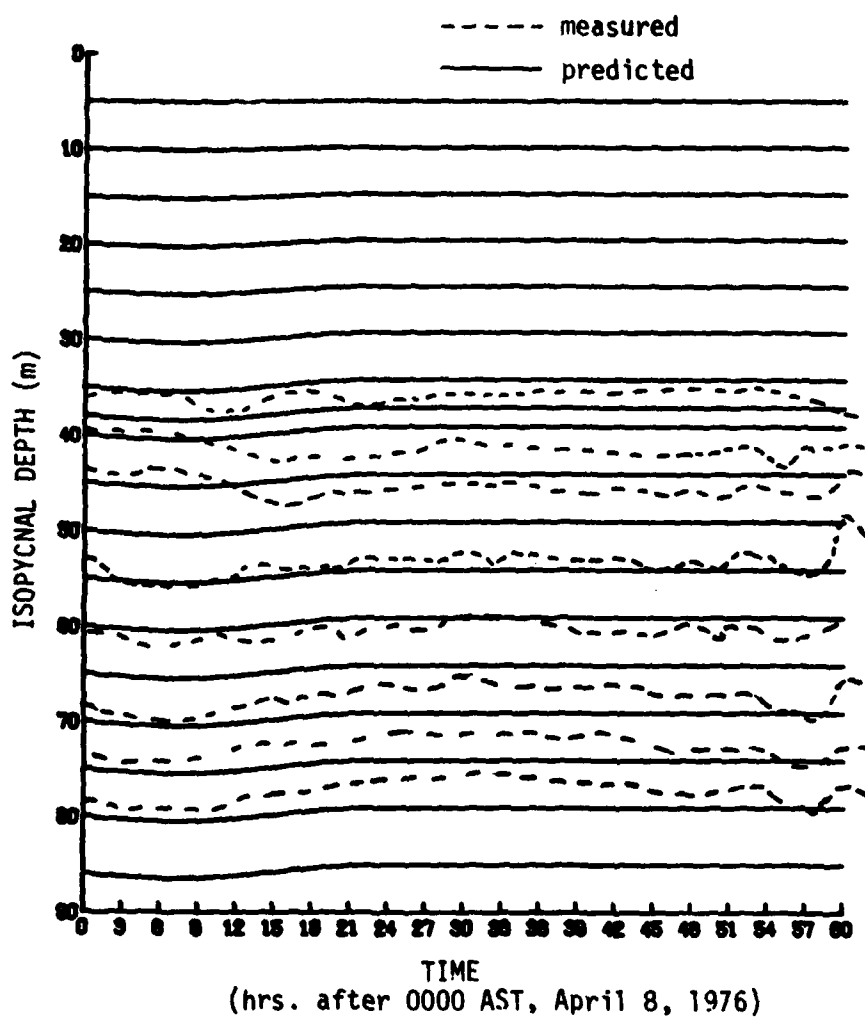


Figure 4.23. Predicted isopycnal responses in the upper 90 m of the water column for conditions identical to those of Figure 4.21 except the initial position of the observation point is -8.25 km. Dashed lines represent observation. Note relatively better agreement in form at 60 m and below.

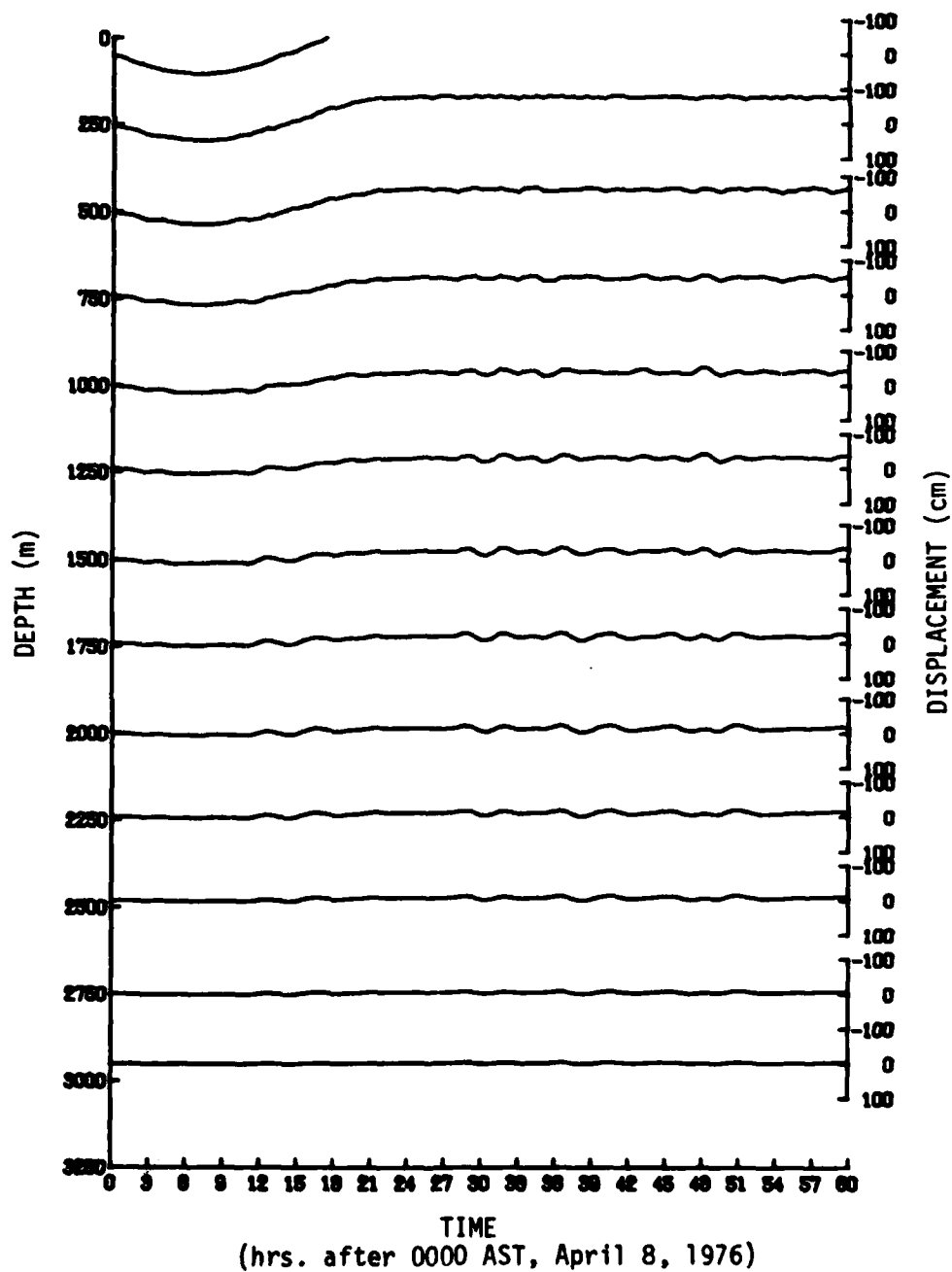


Figure 4.24. Predicted isopycnal responses over the full ocean depth for conditions identical to those of Figure 4.21 except the initial position of the observation point is -8.25 km.

situation except for an initial position of -8.25 km. Figures 4.21 and 4.23 show only the response in the upper 80 m while Figures 4.22 and 4.24 show the response over the whole water column.

The values of the independent parameters (ice velocity and position) used in making the figures were chosen in part with the idea of trying to duplicate certain aspects of the experimentally observed behavior. Figure 3.5 shows the assumed ice velocity pattern to be a crude compromise between the ice velocities indicated by navigation data and current meter data, but, in fact, neither the true velocity pattern nor the lead position and configuration is known precisely. As comparison of Figures 4.21 and 4.23 indicates, the response as viewed from the ice varies significantly with the assumed initial position and ice velocity. Thus, rather than attempting to show the response for all combinations of independent parameters it has been decided to select cases which most nearly reproduce important features of the observed response. Figures 4.21 and 4.22 are representative of the type of behavior observed above 50 m while Figures 4.23 and 4.24 are representative of that below 50 m. The fact that the shapes of the responses are so different for different positions and velocities is important. Obviously the response is concentrated at small length scales because the forcing occurs at short length scales. The response varies with initial position and velocity because the wavelengths are comparable to the distance traveled by the ice in one day.

Figure 4.21 indicates the pycnocline initially deepens 1.2 m by 15.0 hours then rebounds to .75 m below the initial depth by 24.0 hours. The response resembles that observed at the top pycnocline

during the storm. The initial depression and rebound are similar although the magnitude of the response is about half the observed response.

Comparing Figures 4.21 and 4.22 with Figures 4.17 and 4.18, one discovers a basic difference between the buoyancy flux response and the surface stress response. While the surface stress response is a maximum at the seasonal pycnocline and decays rapidly below that depth, the buoyancy flux increases with depth down to 250 m. The buoyancy flux produces internal motion as would a surface pressure disturbance. Because the pressure response (Figure 4.9) decreases much more rapidly with increasing mode number than does the surface stress response (Figure 4.8), the vertical structure in Figures 4.21 through 4.24 tends to be dominated by the low order modes. As a result, fewer modes are important to the total response and the maximum response occurs deep in the water column. The high frequency oscillations superimposed on the general response are due to natural oscillations of the low order modes. For example, the oscillations at mid-depth in Figure 4.22 occur with a period of about 3.5 hours which nearly corresponds to the natural frequency of the fourth mode for the 5.5 km wavelength and the second mode for the 11.0 km wavelength. The high frequency oscillations appear to beat, indicating they are the result of a combination of several modes with nearly equal natural frequencies. Finally, with regard to Figure 4.22, the low frequency motion or trend toward deepening of the isopycnals extends deeper than the initial response. The isopycnal deflection at 60 hours decreases nearly linearly with depth while the initial depression below the final equilibrium depth is

negligible below 1,000 m. One would expect this to occur; the penetration depth of high frequency disturbances driven at the surface is less than low frequency disturbances.

Figures 4.23 and 4.24 show the same response as Figures 4.21 and 4.22 but observed from a different location. At this position the pycnocline initially deepens .5 m until 8.0 hours when it begins to rise, finally reaching a depth 0.9 m shallower than the initial depth. The response resembles that observed below 50 m on April 8, 1976 but is about one half the magnitude of the observed response.

The most important aspects of the buoyancy flux response are that it varies so much over short distances and that it is of the same order as the stress response. Actually the two characteristics are related. Magaard (1973) found the buoyancy flux response to be a small but significant fraction of the stress response. The most fundamental difference between the situation he discussed and that studied here is that, due to the unique geometry of Arctic leads, the length scales for buoyancy flux forcing are smaller for an ice covered ocean than for a temperate ocean. Equation (4.7.6) indicates the displacement response is proportional to k^4 (note: $\omega_G \propto k$). This effect is partially offset by a decrease in R_p with increasing k but the response to buoyancy flux still increases with increasing k . Thus, the buoyancy flux is large precisely because the length scales over which the forcing acts are small.

In fact the predicted response could be made even larger by adding even higher wave number components but this would not be realistic because horizontal dispersion of the salinity disturbance, which

has been neglected in the model, should reduce the high wave number forcing. Salt rejected during freezing at the surface of a lead is spread horizontally, not only by motion of the ice pack, but also by convective circulations in the mixed layer. Smith (1973) indicates these circulations may easily extend a couple of kilometers from the lead. The model neglects this effect and the edges of the density disturbance in the mixed layer are assumed to remain sharp, giving rise to forcing at very high wave numbers. In reality, the convective circulations must smooth the edges of the disturbance, eliminating forcing with characteristic lengths shorter than a few kilometers. As will be shown below, the modeled velocities give an indication of the minimum wavelength suitable for inclusion in the forcing.

Figure 4.25 shows the u velocity pattern as seen from the moving ice initially at $y = -12.38$ km and Figure 4.26 shows the corresponding v velocity pattern. The plot on the left in each figure is a contour plot of absolute velocity and the plot on the right is the velocity relative to the average velocity in the mixed layer. The u velocity in the mixed layer initially drops to -12 cm sec^{-1} by 8.5 hours then rises gradually to 7 cm sec^{-1} by 24.0 hours. After forcing stops at 24.0 hours the average value of u is 6 cm sec^{-1} and oscillations occur about this average value with an amplitude of 4 cm sec^{-1} . The mean u velocity is maintained by a geostrophic balance with the steady state vertical displacement which varies in the y direction only.

The v velocity in the mixed layer initially increases to 10 cm sec^{-1} by 12.5 hours then decreases to 4 cm sec^{-1} by 24.0 hours. After the buoyancy flux stops, the average value of v goes to zero and only

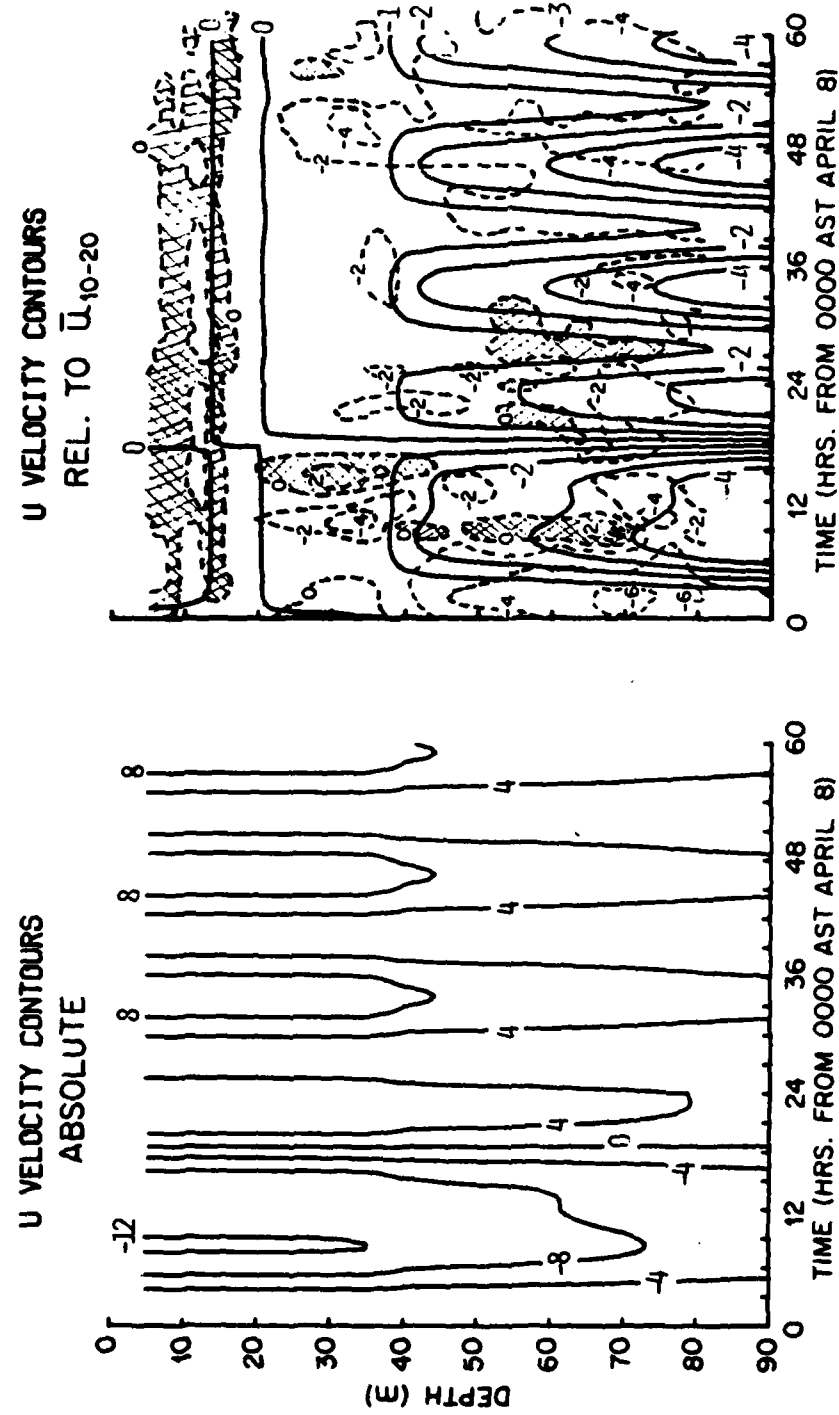


Figure 4.25. Contour plots of absolute and relative u velocity due to buoyancy flux response. The solid lines indicate predictions and the dashed lines indicate observations from Figure 3.9. The motion is that which would be observed from a platform moving as described for Figure 4.21.

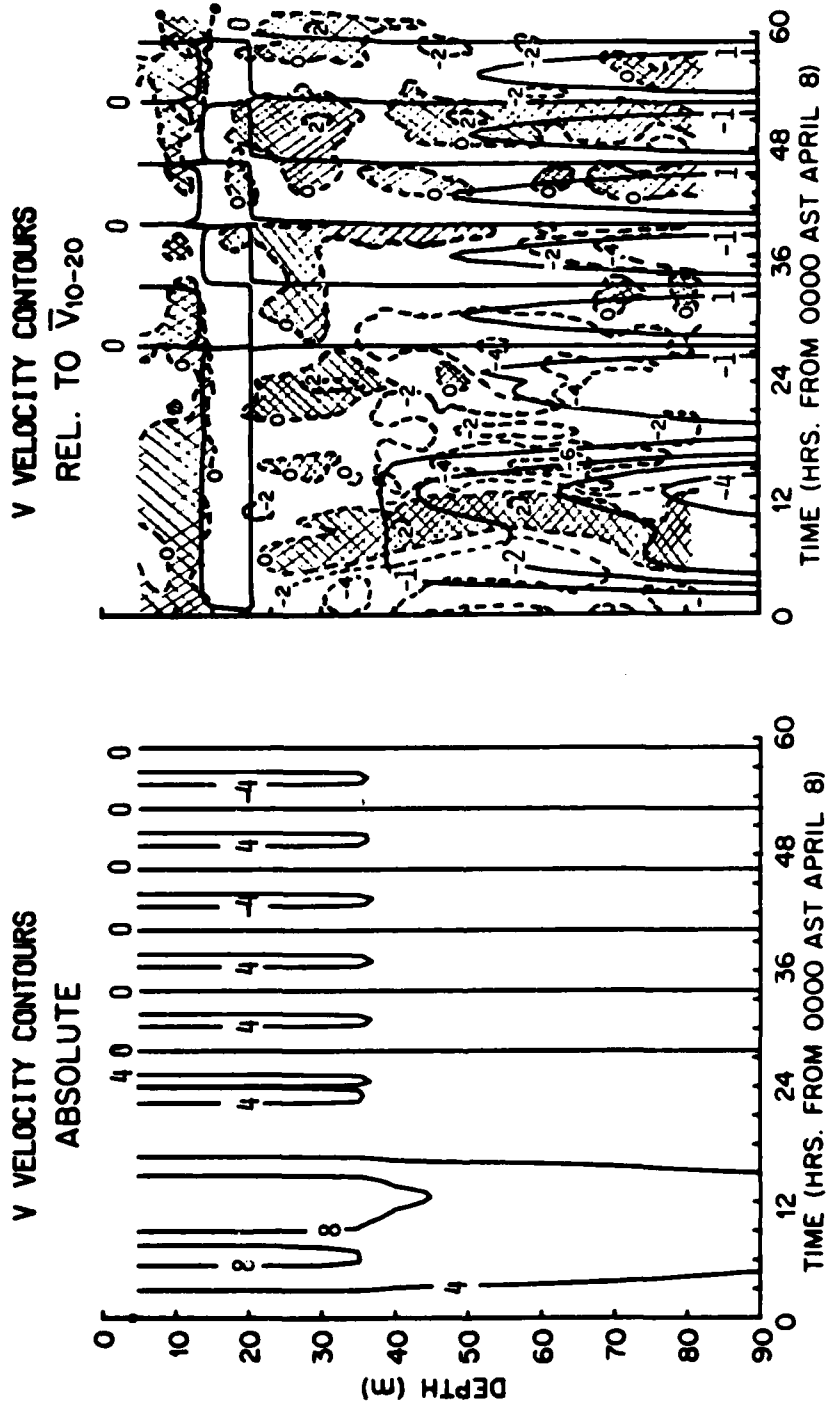


Figure 4.26. Contour plots of absolute and relative v velocity due to buoyancy flux response. The solid lines indicate predictions and the dashed lines indicate observations from Figure 3.12. The motion is that which would be observed from a platform moving as described in Figure 4.21.

inertial oscillations of 4 cm sec^{-1} amplitude are observed.

The relative velocity contours bear a resemblance to the observed relative velocity contours of Figures 3.9 and 3.10. (The observed contours are indicated by dotted lines in Figures 4.25 and 4.26.) Because the buoyancy flux response is dominated by low modes, the shear is relatively weak and thus, the amplitudes of the relative velocities in the upper 90 m are significantly less than the absolute velocities. The inertial frequency oscillations appear as shears of nearly 2 cm sec^{-1} amplitude between 20 m and 90 m. The relative u velocity is offset by -2 cm sec^{-1} after 24.0 hours and the predicted oscillations in u are of the same size as the observed oscillations. The only area of disagreement is the phase; the predicted +4 cm/sec peak at 10.0 hours leads the observed motions by two hours or so and the observed oscillation at 25.0 hours is not predicted by the model. The oscillations in u after 39.0 hours are not as sharply defined as those predicted by the model. Figure 4.26 indicates the modeled perturbations in v match the observed motions quite well in phase even during the storm. The difference is the observed velocities are offset -2 cm/sec while the predicted velocities oscillate about zero. As with the experimental data and the velocities predicted for the stress forced problem, the inertial oscillations show only a gradual change across the pycnocline indicating energy at the inertial frequency is transferred across the top pycnocline. As explained in the previous section, this transfer is achieved by pressure fluctuations rather than by turbulent momentum transfer.

In spite of the fair agreement between the observed and

predicted relative velocities, the absolute velocities seem rather high, being of the same order as typical boundary layer velocities. As a matter of fact, the peak velocities due to these waves are even higher, nearly 25 cm sec^{-1} at some locations. The high velocities are due to the 5.5 km component of the motion and if it is eliminated from the model, the peak internal wave velocities are on the order of 5 cm sec^{-1} and the vertical displacements are about 0.5 m, values which are quite reasonable. The reason for this can be seen by examining equations (4.7.7) and (4.7.8). The ratio between velocity and displacement increases in proportion to k . So, for very high wave numbers, the horizontal velocity in the mixed layer becomes unreasonably large.

In a crude way, the increase in velocity with wave number gives some indication of the minimum wavelength suitable for inclusion in the forcing and consequently the length scale over which horizontal spreading of the salinity disturbance near a lead is important. If high horizontal velocities were to occur at high wave numbers in the mixed layer the motions would tend to spread out the density disturbance, thus drastically reducing the high wave number forcing. This feedback mechanism is not included in the model; the shape of the density disturbance is unaffected by the horizontal velocity in the mixed layer. For wavelengths less than 5.5 km the model produces horizontal velocities much larger than those observed in nature indicating density disturbances due to leads must smooth out to wavelengths no less than 5.5 km. The length scale corresponding to this is about 1 km and is of the same order as Smith's estimate (Smith, 1973a) of the spreading lengths due

to convection.

The results above indicate it is safe to assume the internal wave driven buoyancy flux produce vertical displacements from 0.5 m to 1.0 m with velocities on the order of 5 to 10 cm sec^{-1} . Clearly such disturbances are a significant factor in the response of the upper ocean to storms.

4.8 A Combined Stress and Buoyancy Flux Response

Obviously both stress forcing and buoyancy flux forcing were active simultaneously during the April 8 storm. In order to explore the effects of a combination of both kinds of forcing, the response to surface stress developed in Section 4.6 has been combined with the response to buoyancy flux as predicted for $y = -12.38$. The assumed location of the ice camp relative to the idealized lead pattern is different for the stress forced and buoyancy flux forced components but the response is realistic anyway because the stress response at short wavelengths, where such a difference would matter, is small. The results are basically due to stress forcing at long wavelengths and buoyancy flux at short wavelengths. The combined vertical displacement is shown in Figure 4.27 along with the observed response. The predicted response displays a maximum depression at the top pycnocline of 1.9 m at 15.0 hours. By 60.0 hours the isopycnals rise with oscillations to a depth about 0.8 m less than the initial depth. The response is of the same general shape as that of the stress forced problem but the magnitude of the initial depression is much closer to the observed amplitude and the subsequent rise of the isopycnals is more gradual. Thus, the

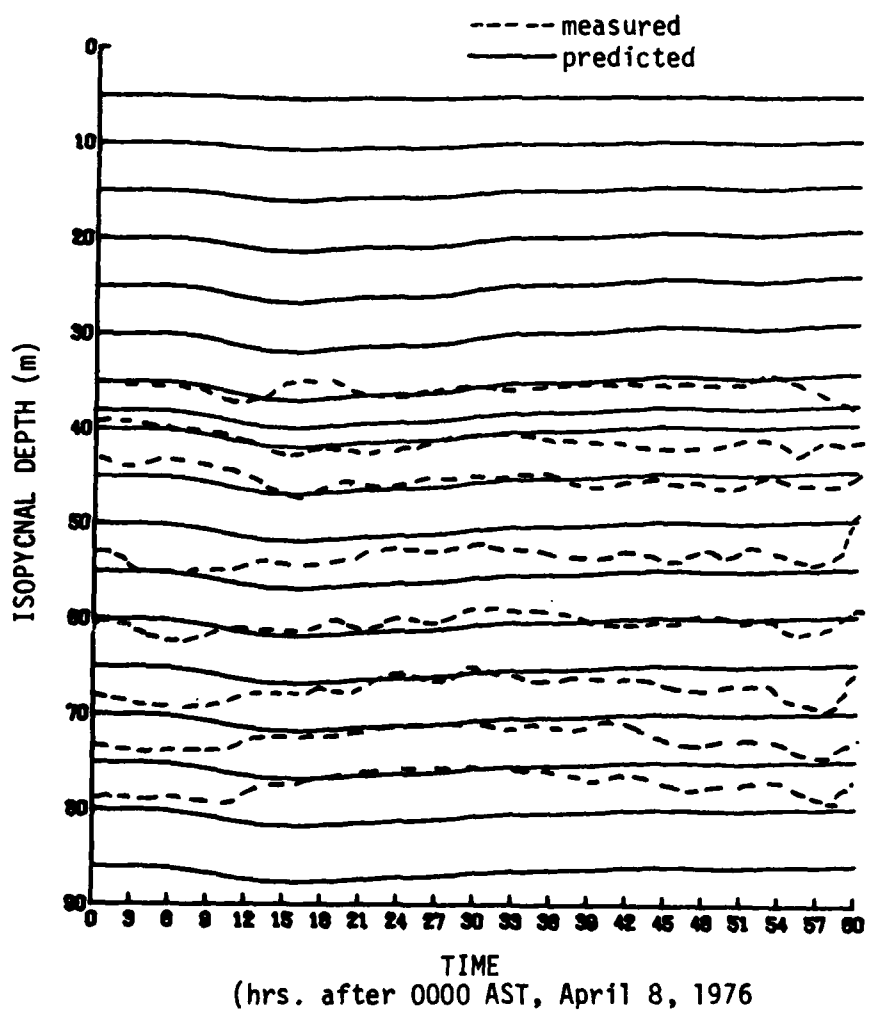


Figure 4.27. Combination of the stress forced isopycnal response of Figure 4.17 and the buoyancy flux forced isopycnal response of Figure 4.21. Also shown is the observed response of April 8.

agreement with the observed displacements is fairly good above 50 m, especially at 45 m.

Both the stress response and buoyancy flux response are constant in shape with depth. Thus it has proven impossible to simultaneously match the response below 50 m and at the pycnocline by combining the two. Because the buoyancy flux response increases slightly with depth in the upper 80 m, the difference above and below 50 m was thought to be explainable by superimposing the stress response and the buoyancy flux response at $y = -8.25$ km (Figure 4.23). As it turns out the result is a slightly modified version of the response in Figure 4.23. This is because the increase in the buoyancy flux response is dominant and changes only slightly with depth below the pycnocline.

There are a couple of possible explanations for the difference between the response at the pycnocline and that below 50 m. One is that the camp was advected past a stationary disturbance below 50 m. For example, the results of the previous section indicate buoyancy flux under leads may drive disturbances below the pycnocline with amplitudes on the order of one meter and at short wavelengths (i.e. 5 to 20 km). Such disturbances persist after buoyancy flux stops. If such a feature were created well before the storm and the manifestations of it at the pycnocline were reduced due to turbulent mixing, it would appear to an observer moving over it as a transient response below the pycnocline.

Another explanation is that the model of the response to buoyancy flux in leads is not complete. As has been pointed out, the circulation in the mixed layer near the lead has been included in a very crude way. In fact lead driven circulation probably involves

vertical displacement at the pycnocline which is not modeled here. While the internal wave response involves a rise in the pycnocline under a lead, the convective accelerations below the lead would require the existence of a local region of high pressure and hence a local downward deflection of the top pycnocline. Thus while the internal wave response may cause a rise in the isopycnals below the pycnocline, the neglected convective circulation in the mixed layer would cause a drop at the pycnocline and the complete buoyancy flux response would show more variation with depth than the model. A behavior similar to this was observed on April 10 when a lead broke through the AMLE camp (see Figure 4.27, observed response). The observed initial rise in the isopycnals below 40 m was even more rapid than can be predicted with the model. Because of the nonlinear nature of the convective accelerations, the error in neglecting convection is probably only important near the lead.

The combined velocity response corresponding to Figures 4.17 and 4.21 is dominated by the buoyancy flux response and is similar to that of Figures 4.25 and 4.26. As has been pointed out, the predicted absolute velocities are somewhat high, but the relative velocity pattern is similar to the observed pattern.

As was mentioned previously, the combined response of Figure 4.27 is somewhat artificial. Because the exact character of both the buoyancy flux forcing and the surface stress forcing is unknown, they were chosen in part with the idea of making the modeled response agree with the observed response. In spite of this and in spite of the discrepancies between the modeled and observed responses, the results do

indicate that at least the forced internal motions discussed here cause significant motions in the upper pycnocline and must make some contribution to the storm response. Also the fact that they produce disturbances which persist after a storm is over implies they cause a great deal of horizontal structure in the density and velocity fields over a large range of wavelengths. Perhaps the most unique result of the last two sections is that, due to the strong forcing in closely spaced leads, the buoyancy flux response may be greater than the stress response in an ice covered ocean.

Chapter 5

SUMMARY AND CONCLUSIONS

The primary thrust of this dissertation has been the elucidation of the role of forced internal waves in the dynamics of the upper Arctic Ocean. The work was motivated by measurements made with the Arctic Profiling System during the Arctic Mixed Layer Experiment. Observations made during a storm on April 8, 1976 indicate that a forced internal response caused deepening of the pycnocline. The downward deflection of the isopycnals was initiated before the storm began at the AMLE camp and a maximum deflection on the order of 2 m occurred five hours before the maximum wind speed (9 m sec^{-1}) was achieved. After reaching maximum deflection, the isopycnals tended to rebound and oscillate with periods of about 10 hours. The horizontal velocity fluctuations, measured relative to the average velocity between 10 m and 20 m, display oscillations near the inertial period.

In attempting to explain the observed response of April 8, theoretical models have been developed for the internal wave response to surface stress, atmospheric pressure, and buoyancy flux. The models allow arbitrary stratification and a realistic surface boundary condition. The total response is determined as a sum of responses of normal modes evaluated at a number of horizontal wavelengths.

The stress response derivation is unique in that it employs the actual stratification observed in the Beaufort Sea and a simple body force approximation for shear stress. This works because the stress is negligible below the weakly stratified surface layer. The response of

each mode is derived using two approaches, a normal mode decomposition and integration of the equations of motion in the mixed layer. The latter method is original but it involves an inverse Laplace transformation technique similar to that used by Leonov and Miropolskiy (1973). The results of the two types of derivation are the same. The actual forcing function for vertical displacement is the sum of the stress divergence and the time integral of stress curl.

The response to surface pressure has been derived for arbitrary stratification using normal mode decomposition. The results are compared with those obtained using the method of Leonov and Miropolskiy (1973) and the two approaches are found to yield identical results.

The internal wave response to buoyancy flux has also been derived in an extension of the method used by Magaard (1973). Arbitrary stratification is used and vertical diffusion is assumed to occur instantaneously in a thin surface mixed layer. The results indicate the buoyancy flux forcing can be converted to an equivalent surface pressure forcing and the internal wave response can be found using the pressure response.

The transfer functions relating modal vertical displacements and the forcing functions have resonances at the internal wave natural frequencies and the transfer functions for modal horizontal velocity display resonances at the internal wave natural frequencies and at the inertial frequency. There is a maximum in each modal velocity transfer function at a length scale corresponding to the Rossby radius of deformation for that mode.

In applying the model to the events of April 8, scaling

arguments have been used to show that the response to atmospheric pressure is negligible. The internal wave response is dominated by surface stress and buoyancy flux and this study is unique in that these forcing functions are estimated on the basis of real data. When using stress and buoyancy forcing functions representative of conditions on April 8, internal wave responses can be produced which reproduce most of the features shown in the observed data records.

The theoretical response to surface stress only agrees with the observations in the form and phase of the initial response at the top pycnocline. The model also predicts oscillations in velocity similar to those observed experimentally. However, the maximum possible displacement which can be predicted is 0.7 m, about one-third of the observed response. Also, the form of the theoretical and observed responses at the top pycnocline differ after 24.0 hrs. and the predicted vertical displacements vary little with depth while the observed response below 50 m is different from that above. In short, though the model results indicate the stress response is an important component of the storm response it cannot account for all the observed motions.

There are a couple of difficulties which arise in solving the stress forced problem. These suggest areas for future work. The first problem involves estimating the forcing. In this study the model forcing was estimated using navigation data from the AIDJEX buoy array and, while that network was the most complete one ever designed, the grid spacing was still too large to estimate the forcing at intermediate length scales. So, the model forcings at these length scales had to be inferred from those at larger length scales. Future studies of

Arctic mixed layer dynamics would benefit from a knowledge of the ice motion over a broader range of length scales, especially the intermediate scales, 10 km to 100 km.

The other problem, which is shared with the buoyancy flux forced model, is that horizontal variations in density structure, which the model ignores, may trap internal wave energy in certain regions. The model results (particularly for buoyancy flux forcing) indicate there exist persistent variations in isopycnal depth, on the order of 1 m, at short length scales. The effect of such variations on forced internal waves should be assessed with a model which incorporates horizontal variations in the density field.

The buoyancy flux component of the internal wave response is especially important in the Arctic. The situation is unique in an ice covered ocean as opposed to a temperate ocean in that the buoyancy flux in leads produces forcing at relatively short wavelengths. Therefore, because the vertical displacement response is proportional to k^4 , the theoretical buoyancy flux response estimated for April 8 is fairly large (1.2 m) relative to the maximum stress response (0.7 m). Because of the short wavelengths involved, the form of the buoyancy flux response varies markedly with horizontal position, but unfortunately it cannot produce the variations in vertical displacement with depth observed on April 8.

The two major problems with the buoyancy flux response model are an imprecise knowledge of the lead distribution around the ice camp and the neglect of horizontal dispersion in the mixed layer. The absence of a detailed map of the lead distribution around the AMLE camp has

necessitated the use of a hypothetical distribution. In future experimental studies of the Arctic mixed layer, the lead patterns over a 60 km grid should be measured periodically by aerial photography.

Neglecting horizontal dispersion around the leads causes several difficulties. Because, lead convection tends to smooth out the density disturbances and eliminate high wave number forcing, neglecting the effect results in an unrealistically large response for very large values of k . Also, the lead convection component of motion must involve vertical motion at the pycnocline and thus, a combined internal wave, lead convection response would probably show more variation in vertical displacement with depth than the internal wave response alone, at least near the lead. Including a lead convection response might account for the differences in displacement above and below 50 m displayed in the measurements.

In order to produce a response comparable in magnitude to the observed motions, the buoyancy flux response and the surface stress response must be combined. Doing so, the model compares favorably with the data, at least with regard to the pycnocline displacement. It is natural that a combined model should produce the best agreement with data because both stress forcing and buoyancy flux were active during the storm. However, like the stress response, the combined model response differs from the observations below 50 m.

A likely explanation for the departures of the theoretical response from the actual response is that the effects of small scale disturbances left over from previous lead activity have not been accounted for. The theoretical results presented here indicate the buoyancy flux

from leads cause forced internal wave motions at short wavelengths (of order 10 km) and these disturbances persist in some form after buoyancy flux stops. They involve isopycnal displacements on the order of one meter throughout the main pycnocline. Velocity disturbances of several centimeters per second occur and, though they are maximum at the surface, they extend well into the main pycnocline. Furthermore the lead convection process in the mixed layer (which is highly idealized in the model) responds to similar surface density gradients and should produce comparable mixed layer velocity perturbations, some fraction of which must persist after the lead closes. The features left over from lead activity near the top pycnocline might be modified or smoothed out by turbulent mixing due to surface stress. As a result of the processes described above, the upper Arctic Ocean must be characterized by a great deal of variability down to horizontal length scales of 5 km to 10 km and the presence of these "fossil" disturbances should have an important effect on the observed response, particularly where the immediate ocean response to a storm is small or after an extended period of time. The storm response measured from a moving ice camp may consist of equal parts of an immediate storm response and a long term apparent response due to movement of the ice over the small scale disturbances generated by prior lead activity. This was probably the situation on April 8. The initial disturbance of the seasonal pycnocline was due to the immediate effects of surface stress and buoyancy flux in leads. However, the magnitude of the immediate storm response decreased below the seasonal pycnocline, and after 24.0 hours the displacement of the ice camp relative to any "fossil" disturbances would

have become quite large. Thus, the changes due to passage through such fossil disturbances might account for the deviations between observation and theory.

It is useful to consider briefly the magnitude of the forced response which might be encountered under other typical Arctic conditions. This yields both some idea of what type of initial storm responses might be expected and rough bounds on the magnitude of the small scale "fossil" disturbances. The stress forcing function increases in proportion to the stress magnitude and duration and varies inversely with the storm scale. While stress levels during the April 8 storm were about $.25 \text{ dyne cm}^{-2}$ and the duration was only one day, it is not uncommon for stresses to reach 1 dyne cm^{-2} during storms which may last for several days. Under such a situation, assuming the horizontal scales of such a storm were comparable to those of the April 8 storm, the pycnocline displacement could be on the order of 6 m or 7 m.

The response to buoyancy flux may also be greater than that discussed here. Buoyancy flux increases almost linearly with decreasing air temperature and increasing wind speed. Thus, for a day on which the temperature difference between the air and the water was -30 degrees and the wind velocity was 10 m sec^{-1} , the buoyancy flux in leads might be expected to produce deflections of the isopycnals on the order of 4 m, even if the wavelength components shorter than 10 km were ignored. The "fossil" disturbance corresponding to such a response would be of sufficient magnitude to explain a great deal of the difference between the observed and predicted response discussed above.

How do the variations in pycnocline depth and velocity for

these extreme cases compare with the general variability observed in the Arctic Ocean? Smith and English (1973) have found from the analysis of three year's hydrographic data from T3 that the amplitude of the annual variation in mixed layer depth is 4 m. The variability about the annual cycle is on the same order. Thus, the variations in density structure due to the most energetic internal waves are comparable to the long term variations in density structure and are presumably the cause of the large variability.

Two points of general interest regarding forced internal waves should be mentioned. First, both the buoyancy flux forcing and surface stress forcing produce inertial oscillations. The oscillations are greatest in the mixed layer but may extend through the pycnocline without the existence of turbulent stress there. This seems odd at first because free oscillations in the vertical cannot occur at the inertial period. However, it must be remembered that the vertical motions being discussed here are forced or transient motions and do possess energy at the inertial frequency. This motion excites inertial frequency resonance in the horizontal velocity. Similar phenomena may explain observations of inertial motion below the pycnocline. Sanford (1975) has found inertial period motion at high mode numbers and at great depth. These motions are probably excited not by stress but by the pressure disturbances due to forced internal waves. The inertial motions should be expected to be most prevalent at high mode numbers because the internal wave natural frequencies approach the inertial period for high mode numbers. Sanford observes that the horizontal velocities are quite different at a spatial scale of 10 km. This may be due to the

fact that the velocity response is a maximum for length scales less than the maximum modal Rossby radius (approximately 10 km).

A second point of interest is the fact, observed both experimentally and theoretically, that the internal wave response begins before the local wind speed increases. According to the theoretical work on waves driven by surface stress, there are two combined reasons for this. The vertical displacement is driven by stress curl and divergence, not local stress, and the response is greatest for large scale forcing. When a sharply defined storm front moves into a region, the stress divergence and integral of stress curl, averaged over some large length scale (> 200 km), may begin to rise before the leading edge of the storm arrives at a particular station within the region. For example, consider an idealized storm with a very sharp front which causes a wind stress curl pattern resembling a delta function. Suppose the storm moves so slowly as to be virtually stationary. The forcing function may be broken into an infinite number of wave components but the ocean responds the most to the long wave components. These components will not sum to zero in front of the storm and the response will start and continue there even while local conditions are completely calm.

During the April 8 storm the displacement response at the pycnocline not only began before the storm started at Big Bear, but also peaked before the peak wind speed was achieved. This is explained in part by the fact that the peak in forcing due to stress divergence tends to lead the peak stress. However, the integral of stress curl is usually the dominant forcing term and the phase of this term relative to peak stress will vary for different types of storms. The April 8

storm intensified after passing Big Bear and as a result the stress curl went to zero and changed sign before the region of maximum stress reached there. Hence, the maximum forcing and response occurred before the local wind stress occurred. In general the region of pycnocline response can be expected to spread beyond the boundaries of the storm. In addition the peak in internal wave forcing and response may tend to lead the storm center. The vertical velocity is driven simply by stress curl and will thus tend to lead the local stress. As a result some components of horizontal velocity will also lead the local stress.

In summarizing the work on forced internal waves, it can be said that, at the very least, motions forced by a combination of surface stress and buoyancy flux played an important part in the observed storm response. Several factors indicate this is true. First, even though, in the absence of complete data on the forcing, forcing functions were estimated in an idealized way, the estimates are reasonable and the magnitude of the resultant model responses are comparable to the observed motions. Second, the presence of stress forced internal waves would explain why the oceanic response leads the atmospheric forcing. Third, forced internal waves result in oscillations in vertical displacement after the storm with periods shorter than the inertial and such oscillations were observed after the April 8 storm. Finally, forced internal waves produce inertial motions which extend through the pycnocline and evidence of such motions also exists in the observed velocity profiles. Because it is possible to duplicate so many aspects of the observed storm response it can be concluded that forced internal waves were an important component of the observed response.

It has also been suggested that the deviations of the model from the observations may be due to the presence of "fossil" disturbances generated by forced internal motions prior to the storm. Under cases of extreme forcing, internal waves may be generated with an amplitude of several meters.

Gaining a further understanding of forced internal waves will require effort in two areas. First, in order to verify the model of stress generated internal waves given here, an experiment should be performed to simultaneously measure the stress forcing and ocean response. This would require establishment of a navigation network with a grid scale of about 20 km extending over a scale of 200 km. Oceanographic measurements conducted within the array could be used to measure the response to the forcing measured by the navigation array. Second, with regard to the buoyancy flux forced waves, a more sophisticated model should be developed which would account for the effects of horizontal diffusion and convection in the mixed layer. The validity of such a theory could be tested with the same experimental scheme outlined above if accurate measurements of lead activity were made.

In addition to providing the impetus for a study of forced internal waves, data gathered during the AMLE gives some idea of the importance of lead convection in the mixed layer. On April 10, observations were made of the direct effects of a lead which opened through the AMLE camp. They indicate the mixed layer salinity increased about 0.1 ‰ downstream of the open lead. Calculation of the salt flux at the lead surface and comparison with salinity and velocity profiles downstream indicate the total flux was confined to the mixed layer.

Maykut's formulation for determining salt flux appears quite reasonable. The measured salinity variation is comparable to the average annual variation in mixed layer salinity, estimated to be 0.18 ‰ by Smith and English (1973).

Perhaps more important than the direct observations of lead convection are the data illustrating its general effect on mixed layer density structure. Prior to the April 8 storm, after a prolonged period of quiet conditions, the mixed layer was slightly stratified. During the storm the stratification was eliminated. The stratification must build up due to lead convection. Starting with an unstratified mixed layer, water with increased salinity from the surface of refreezing leads falls through the mixed layer, mixing with surface water along the way, and comes to rest in an equilibrium position near the top pycnocline. As the process continues, water with different salinities settles out at various equilibrium depths thereby causing the observed stratification. The effect on the mean flow field is apparent in the observed velocity profiles. The presence of slight stratification permits baroclinic velocity features such as jet-like maxima and shears in the mixed layer with magnitudes up to 3 cm sec^{-1} .

Another effect which is not as readily apparent under the calm conditions prevailing during the AMLE is the way stratification modifies the turbulent boundary layer. Smith and Long (1976) illustrate how stratification not only produces baroclinic pressure gradient effects (thermal wind) in the boundary layer but changes the eddy coefficient so as to decrease the boundary layer thickness and increase the turning angle and structure at the bottom of the boundary layer.

Because of the importance of lead convection both to the buoyancy forced internal wave problem and to an understanding of mixed layer and boundary layer processes, it should be the subject of both experimental and theoretical study in future years. Experiments should focus on examining the velocity and density fields in and around leads and theoretical work should focus on the effects of wind velocity, ice velocity, ambient stratification, and freezing rates on the convective circulation patterns.

Finally, some mention should be made of the Arctic Profiling System. It has been found to be a useful instrument for making accurate vertical profiles of velocity and density rapidly. The novel feature of the device is that it is capable of producing measurements of horizontal velocity with 1 cm sec^{-1} accuracy and zero threshold while being lowered at speeds between 50 cm sec^{-1} and 100 cm sec^{-1} . Three current sensors are used in such a way that all three water velocity components are measured and the horizontal components are extracted during data processing. The current sensors are arranged such that the lowering velocity keeps each one rotating at well above the threshold speed. Thus, the threshold for the measurement of horizontal velocity is zero and high lowering speeds may be used even in weak currents. Also, measurement of three velocity components permits corrections to be made for the deviation of each of the current sensors from a perfect cosine angle of attack response. The system is superior to those employing single rotors and direction vanes because, even when lowered at high speed, the response time is very short and features with a depth span of only one or two meters can be resolved. Even better

resolution (e.g., 20 cm) would be possible were it not necessary to average out oscillations of the instrument.

One of the main concerns in using a profiling current meter system is the effect of the probe motion on the velocity measurements. The instruments in the IRU are satisfactory for determining orientation of the APS but the rate gyros are not sufficiently accurate to permit computation of the rectilinear velocity of the probe. However, comparison of the APS data with velocity data from fixed current meters indicates that, for current speeds less than 15 cm sec^{-1} and maximum depths less than 100 m, lateral motion of the probe is negligible. For future experiments involving higher velocities and greater depths it may be advantageous to increase the weight of the probe and use a smaller diameter cable. Doing so will require multiplexing all signals from the probe up a single wire.

Use of an automatic winch has proven to be a major benefit in making repeated profiles at high frequency. During the AMLE the automatic cycling feature allowed the winch to be run unattended and only one person was required to operate the data acquisition system. This permitted continuous sampling to be maintained even in view of the many non-scientific tasks which had to be performed to maintain the ice camp. Continuous sampling should be a major component in future Arctic Ocean oceanographic experiments because, as the AMLE data shows, significant activity occurs at time scales on the order of a few hours. These motions must be monitored every half hour in order to ensure that they are resolved by the data and not aliased into lower frequency information.

REFERENCES

Akima, H., 1979. A new method of interpolation and smooth curve fitting based on local procedures. Journal of the Association of Computing Machinery, 12, 589-602.

Anderson, D. L., 1961. Growth rate of sea ice. Journal of Glaciology, 3, 1170-1172.

Badgley, F. I., 1966. Heat budget at the surface of the Arctic Ocean. Proceedings of the Symposium on the Arctic Heat Budget and Atmospheric Circulation, Ed. J. O. Fletcher. The RAND Corp., Santa Monica, California. RM 5289-NSF. 215-246.

Brown, W. P. and E. G. Kerut, 1978. Air dropable RAMS (ADRAMS) Buoy. AIDJEX Bulletin No. 40, 21-28.

Churchill, R. V., 1960. Complex Variables and Applications, New York: McGraw-Hill.

Coachman, L. K., 1963. Water masses of the Arctic. Proceedings of the Arctic Basin Symposium. Washington, D. C.: Arctic Institute of North America, 143-167.

Coachman, L. K. and K. Aagaard, 1974. Physical Oceanography of Arctic and Subarctic Seas. Marine Geology and Oceanography of the Arctic Seas, Ed. Yvonne Herman, New York: Springer Verlag.

Coachman, L. K. and C. A. Barnes, 1962. Surface water in the Eurasian Basin of the Arctic Ocean. Arctic, 15(4), 251-277.

Coon, M. D., G. Maykut, R. S. Pritchard, D. A. Rothrock, and A. S. Thorndike, 1974. Modeling the pack ice as an elastic-plastic material. AIDJEX Bulletin No. 24, 1-106.

Cox, G. F. N. and W. F. Weeks, 1975. Brine Drainage and Initial Salt Entrainment in Sodium Chloride Ice. CRREL Research Report 345, Hanover, New Hampshire, 85 pp.

Denman, K. L., 1973. A time-dependent model of the upper ocean. J. Phys. Oceanogr., 3, 173-184.

Ekman, V. W., 1908. Die Zusammendrückbarkeit des Meerwassers. Conseil Perm. Intern. p. l'Expl. de la Mer, Pub. de Circonference, No. 43, 47 pp.

Estoque, M. A. and C. M. Bhumralkar, 1969. Flow over a localized heat source. Monthly Weather Review, 97(12), 850-859.

Etkin, B., 1972. Dynamics of Atmospheric Flight, New York: Wiley, 579 pp.

Evans, D. L. and T. Rossby, 1976. Observations of shear and density fine structure in the Sargasso Sea. EOS, 57(12), 929. Abstract of talk given at 1976 Fall Annual Meeting of the AGU, San Francisco, California.

Fjeldstad, J. E., 1964. Internal waves of tidal origin. Geof. Publ. 25, 1-73.

Geisler, J. E., 1969. Linear theory of the response of the two layer ocean to a moving hurricane. Geophysical Fluid Dynamics, 1, 249-272.

Gonella, J., 1972. A rotary-component method for analysing meteorological and oceanographic vector time series. Deep-Sea Research, 19, 833-846.

Goodman, L. and E. R. Levine, 1977. Generation of oceanic internal waves by advecting atmospheric fields. Journal of Geophysical Research, 82(12), 1711-1717.

Hunkins, K., 1974. Subsurface eddies in the Arctic Ocean. AIDJEX Bulletin No. 23, 9-36.

Kajiura, K., 1958. Response of a boundless two-layer ocean to atmospheric disturbances. Ph.D. dissertation, Oceanography Department, Texas A & M University.

Knudsen, M., 1901. Hydrographic Tabellen, Coepnhagen, 63 pp.

Kraus, E. B. and J. S. Turner, 1967. A one-dimensional model of the seasonal thermocline, II, the general theory and its consequences. Tellus, 19, 98-106.

Krauss, W., 1966. Methoden und Ergebnisse der theoretischen Ozeographie, B. II--Interne Wellen. Berlin: Gebruder Borntraeger, 248 pp.

Krauss, W., 1972a. On the response of a stratified ocean to wind and air pressure. Dt. Hydrogr. Z., 25(2), 46-60.

Krauss, W., 1972b. Wind-generated internal waves and inertial-period motions. Dt. Hydrogr. Z., 25(6), 241-250.

Krauss, W., 1976a. On currents, internal and inertial waves in a stratified ocean due to variables winds. Part 1. Dt. Hydrogr. Z., 29(3), 87-96.

Krauss, W., 1976b. On currents, internal and inertial waves in a stratified ocean due to variable winds. Part 2. Dt. Hydrogr. Z., 29(4), 120-135.

Leonov, A. I. and Yu. Z. Miropolskiy, 1973. Resonant excitation of internal gravity waves in the ocean by atmospheric-pressure fluctuations. Bull. (IZV.), Acad. Sci. USSR, Atmospheric and Oceanic Physics, 9(8), English translation, 480-485.

Lighthill, M. J., 1965. Group velocity. J. Inst. Maths. Applics., 1, 1-28.

Lighthill, M. J., 1967. On waves generated in dispersive systems by travelling forcing effects with applications to the dynamics of rotating fluids. J. Fluid Mech., 27(4), 725-752.

Lindsay, R. W., 1976. Wind and temperature profiles taken during the Arctic Leads Experiment. M. S. thesis, University of Washington, Dept. of Atmospheric Sciences.

Lumley, J. L. and H. A. Panofsky, 1964. The Structure of Atmospheric Turbulence. New York: Wiley, 239 pp.

Magaard, L., 1973. On the generation of internal gravity waves by a fluctuating buoyancy flux at the sea surface. Geophysical Fluid Dynamics, 5, 101-111.

Maykut, G. A., 1978. Energy exchange over young sea ice in the Central Arctic. Journal of Geophysical Research, 83(C7), 3646-3658.

McPhee, M. G., 1974. An experimental investigation of the boundary layer under pack ice. Ph.D. dissertation, University of Washington, 164 pp.

McPhee, B. G., 1975. Ice-ocean momentum transfer for the AIDJEX ice model. AIDJEX Bulletin No. 29, 93-111.

McPhee, M. G. and J. D. Smith, 1976. Measurement of the turbulent boundary layer under pack ice. Jour. of Phys. Oceanogr., 6 (5), 696-711.

Meirovitch, L., 1967. Analytical Methods in Vibrations. New York: McMillan.

Morison, J. H., 1978. The Arctic Profiling System. (Synopsis of a poster session display.) Proceedings of the Working Conference on Current Measurement. University of Delaware, February 1978.

Morison, J. B., 1957. O-rings and interference seals for static application. Machine Design, Feb. 7, 1957.

Mork, M., 1968. The response of stratified ocean to atmospheric forces. Report, University of Bergen, Geofs. Inst.

Mork, M., 1972. On oceanic response to atmospheric forces. Extrait Rapp. Proces. Verb. Cons. Cons. Int. Explor. Mer., 162, 184-190.

Newton, J. L., K. Aagaard and L. K. Coachman, 1974. Baroclinic eddies in the Arctic Ocean. Deep-Sea Research, 21, 707-719.

O'Brien, J. J. and R. O. Reid, 1967. The non-linear response of a two-layer, baroclinic ocean to a stationary, axially-symmetric hurricane: Part 1. Upwelling induced by momentum transfer. JAS, 24, 197-207.

Perkins, H. T. and J. C. VanLeer, 1976. Cyclosonde measurements during GATE, Data Report, University of Miami Rosenstiel School of Marine and Atmospheric Science.

Pollard, R. T., P. B. Rhines and R. O. R. Y. Thompson, 1973. The deepening of the wind-mixed layer. Geophys. Fluid Dyn., 4, 381-404.

Pritchard, R. S., M. Coon and M. G. McPhee, 1976. Simulation of sea ice dynamics during AIDJEX. AIDJEX Bulletin No. 34, 93.

Rattray, M. Jr., J. G. Dworski and P. E. Kovala, 1969. Generation of long internal waves at the continental slope. Deep-Sea Research, supplement to Vol. 16, 179-195.

Sanford, T. B., 1975. Observations of the vertical structure of internal waves. Journal Geophysical Research, 80(27).

Schaus, R. H. and J. A. Galt, 1973. A thermodynamic model of an Arctic lead. Arctic, 26(3), 208-221.

Smith, J. D., 1973. Lead driven convection in the Arctic Ocean. (Abstract of oral presentation given at the Fall Annual Meeting of the American Geophysical Union, San Francisco, California, December 10, 1973.) EOS, 54(11), 1108-1109.

Smith, J. D. and T. S. English, 1973. Seasonal variations of density and depth of the mixed layer in the Arctic Ocean. (Abstract of oral presentation of the 20th Pacific Northwest Regional Meeting of the American Geophysical Union, Missoula, Montana, October 19, 1973.) EOS, 55(2), 76.

Smith, J. D., 1974a. Turbulent structure of the surface boundary layer in an ice covered ocean. Proceedings of the 1972 ICES Symposium on the Physical Processes Responsible for the Dispersal of Pollutants in the Sea, with Special Reference to the Nearshore Zone. Rapports et Proces - Verbaux Series, Ed. J. W. Talbot and G. Kullenberg.

Smith, J. D., 1974b. Oceanographic investigations during the AIDJEX lead experiment. AIDJEX Bulletin No. 27, 125-133.

Smith, J. D., 1978. Measurements of turbulence in ocean boundary layers. Proceedings of the Working Conference on Current Measurement, University of Delaware, February 1978.

Smith, J. D. and C. E. Long, 1976. The effect of turning in the bottom boundary layer on continental shelf sediment transport. Mémoires Société Royale des Science de Liège, 6^e série, tome X, pp. 369-396.

Thorndike, A. S., D. A. Rothrock, G. Maykut and R. Colony, 1975. The thickness distribution of sea ice. Journal of Geophysical Research, 80(33), 4501-4513.

Thorndike, A. S. and J. Y. Cheung, 1977. AIDJEX measurements of sea ice motion 11 April 1975 to 14 May 1976. AIDJEX Bulletin No. 35, 1-149.

Thorndike, A. S. and R. Colony, 1977. Estimating the deformation of sea ice. AIDJEX Bulletin No. 37, 25-36.

Thorpe, S. A., 1975. The excitation, dissipation, and interaction of internal waves in the deep ocean. J. Geophys. Res., 80(3), 328-338.

Tomczak, V. M. Jr., 1966. Winderzeugte interne wellen, insbesondere im periodenbereich oberhalb der trägeheitsperoide. Dt. Hydrogr. Z., 19(1), 1-21.

Tomczak, V. M. Jr., 1967. Über den Einfluss fluktuerender windfelder auf ein stetig geschichtetes meer. Dt. Hydrogr. Z., 20(3), 101-129.

Tripp, R. B., 1966. Physical, Chemical and Current Data from Fletcher's Ice Island (T3): Beaufort Sea Area June 1965-January 1966. University of Washington Department of Oceanography Technical Report No. 157.

Tripp, R. B., 1967. Physical and Chemical Data from Fletcher's Ice Island (T3): Beaufort Sea Area: January-May 1966. University of Washington Department of Oceanography Technical Report No. 187.

Veronis, G. and H. Stommel, 1956. The action of variable wind stresses on a stratified ocean. J. Marine Res., 15(1), 43-75.

Webster, F., 1968. Observations of inertial-period motions in the deep-sea. Rev. Geophys., 6, 473-490.

Appendix A

APS SENSOR CALIBRATION AND DATA PROCESSING

A.1 Calibration of the APS Sensors

Current meters of the type used on the APS had undergone continual development and calibration for several years prior to their use in the triplet configuration shown in Figure 2.4. The variation in response of the sensors with angle of attack had been measured (Smith, 1974a; McPhee, 1974), but only for rotations about the axis of the current meter support tube. Referring to Figure A.1, this is the yaw angle, α , which is, in fact, the projection of the total angle of attack, β , onto the Y-Z plane. When used in the APS the sensors encounter the major component of velocity, the lowering velocity, at an angle of 55 degrees measured about an axis perpendicular to the support tube or, referring again to Figure A.1 the velocity vector lies nearly on the X-Y plane and θ is about 55 degrees. α is generally much smaller than θ . Although it was believed the angular response in θ and α should be nearly the same, it was decided that a series of calibration tests should be made to determine the angular response in the θ direction. Also the sensors had not been recalibrated since the conversion from the optical pickup, McPhee (1974) and Smith (1974a), to the new Hall effect pickup and it was felt that a complete calibration test of the new units would be appropriate.

This appendix is largely devoted to discussion of the current meter calibrations. Much of the calibration information will be useful

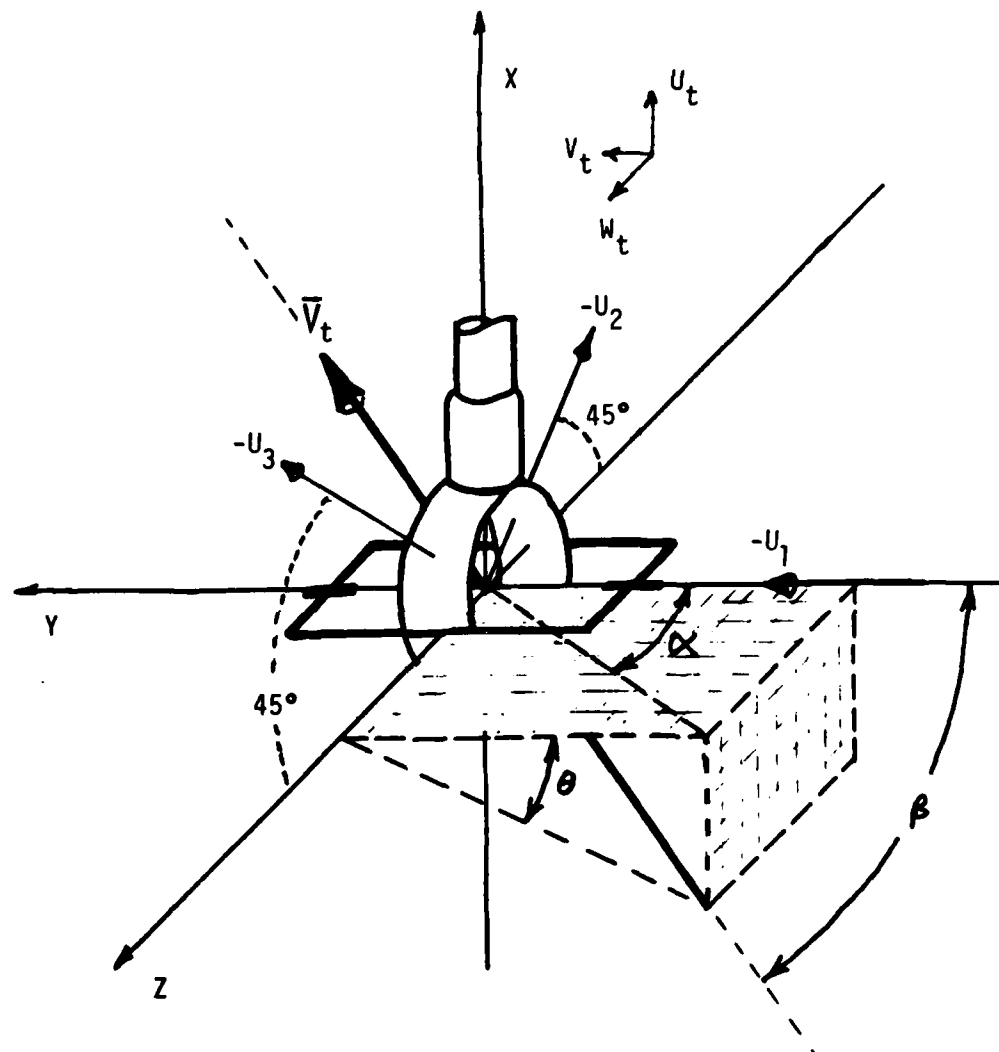


Figure A.1. Current meter angles of attack. For a total velocity vector, \bar{V}_t , impinging on a current meter sensor at a total angle of attack, β , the yaw angle, α , is the projection of β on the y - z plane and the pitch angle θ is the projection of β on the x - y plane.

to other users of these current meters even if they are not used in the APS configuration. Before proceeding with this topic, the calibration of the other sensors in the APS will be discussed.

The Guideline CTD used in the APS was calibrated before the AMLE by NOIC in Bellevue, Washington. Specifications for it and the other sensors in the APS are given in Table A.1. In the field the pressure sensor offset is determined and adjusted while placing the sensor at some specified shallow depth (ex. 2 m). Some care must also be taken to keep the conductivity cell clean. Given this minimal amount of care the CTD is very stable and appears to conform to the manufacturers specifications as listed in Table A.1.

The calibrations as given by NOIC are

$$\begin{aligned} C &= (10.71924 \cdot V_c + 42.8606) \text{ mmho cm}^{-1} \\ T &= (9.98869 \cdot V_t + 0.001) {}^\circ\text{C} \\ D &= (49.044 \cdot V_d - .4218) \text{ m} \end{aligned} \quad (\text{A.1.1})$$

where C is conductivity, T is temperature and D is depth. The output voltages are V_c , V_t and V_d . V_c ranges from zero to minus three volts and V_t and V_d range from zero to plus three volts.

The sensitivity and bias of each accelerometer was determined in a manner recommended by the manufacturer after the units were connected to the filter-range resistor circuit installed in the IRU. Each accelerometer was placed upright on a plate leveled to 1/4 degree. The unit was rocked slightly until a maximum output was achieved. The process was repeated with the accelerometer inverted and the minimum voltage output measured. The sensitivity is computed by numerically adding

Table A.1

Instruments in Arctic Profiling System

A. CTD, Guildine model 8101A	
1) Temperature Sensor	accuracy = $\pm .02^\circ\text{C}$ resolution = $\pm .003^\circ\text{C}$ time constant = 300 msec
2) Conductivity Sensor	accuracy = $\pm .04 \text{ mmho/cm}$ resolution = $\pm .0005 \text{ mmho/cm}$ time constant = 300 msec
3) Pressure Sensor	accuracy = 20 cm of H_2O resolution = 5 cm of H_2O time constant < 200 msec
B. Current Meter - 3 component mechanical	accuracy = $\pm 2\%$ (batch, 1% individual) time constant < 250 msec typical
C. IRU, Inertial Reference Unit	
1) Accelerometers, Sundstrand QFlex, 3 each in triaxial mount	accuracy = $\pm .0008 \text{ g}$ resolution = $\pm .000001 \text{ g}$ time constant = 3 msec
2) Rate Gyro Hamilton Standard, 2 each in orthogonal, pitch and roll rate, mount	accuracy = $\pm .2^\circ/\text{sec}$ resolution = $< .03^\circ/\text{sec}$ time constant < 50 msec
3) Gyro Compass, Humphrey North Seeking Type	accuracy = $\pm 2^\circ$ resolution = $\pm .2^\circ$ time constant < 50 msec

the two voltages and dividing by two. The bias is computed by numerically subtracting the inverted reading from the upright reading and dividing by two. The calibrations determined in this way for the AMLE are

$$\begin{aligned} a_1 &= (V_{a1} + 0.0035)/5.0065 \text{ g} \\ a_2 &= (V_{a2} + .0060)/5.2460 \text{ g} \\ a_3 &= (V_{a3} + .0045)/5.1715 \text{ g} \end{aligned} \quad (\text{A.1.2})$$

where a_i are the accelerations in g's and V_{ai} is the output voltage for accelerometer i . The accuracy figures listed in Table A.1 were supplied by the manufacturer.

The rate gyro units were calibrated by Sandia Laboratories in Albuquerque, N. M., the same group which donated the units. The calibration for the unit used was:

$$\begin{aligned} r_1 &= (24.15 \cdot V_{r1}) \text{ degree sec}^{-1} \\ r_2 &= (26.64 \cdot V_{r2}) \text{ degree sec}^{-1} \end{aligned} \quad (\text{A.1.3})$$

The accuracy listed in Table A.1 is degraded from the manufacturer's specifications by excessive cross axis sensitivity. The resolution measured at Sandia was slightly better than the manufacturer's specification.

The calibration of the gyrocompass is determined by the voltage applied across the output potentiometer. During the AMLE this voltage was set so that

$$\gamma = (.01381 \cdot V_b - 180^\circ) \quad (\text{A.1.4})$$

where γ is the magnetic bearing and V_b is the compass output voltage ranging from 0.0 to 4.79 volts. The accuracy listed in Table A.1 is specified by the manufacturer.

The instruments in the IRU were aligned with the current meter axes in the following way. The compass lubberline, accelerometer #1, and rate gyro axis #2 were aligned relative to one another using lubber marks on the case of each device. The profiling instrument was assembled and attached on a gimble assembly which allowed the instrument to swing about a single axis. The instrument was twisted until number 2 accelerometer indicated a null voltage so that the axis of accelerometer #1 was perpendicular to the swing axis. This direction could be plotted on a piece of paper below the instrument and was found to deviate from the #1 or forward current meter axis by 4 degrees. The 4 degree correction was subsequently used during reduction of the current meter data.

The current meters were calibrated using a 16 m wave tank and tow cart. The arrangement is illustrated in Figure A.2. The tank is .6 m wide and .5 m deep and the cart was timed over a 8.0 m section, 1.0 m being allowed at each end for acceleration and deceleration. The cart is .6 m square and is equipped with hard rubber tires which roll on tubular rails fixed to the top of the tank and it is powered by a Graham .25 hp AC electric motor through a variable speed gearbox. The velocity of the cart is determined by measuring the travel time between two magnets fixed to the tank 8.0 m apart. Two reed switches mounted on the cart (only one is shown in Figure A.2) sense the passage of the magnets and activate a start-finish circuit which in turn controls an

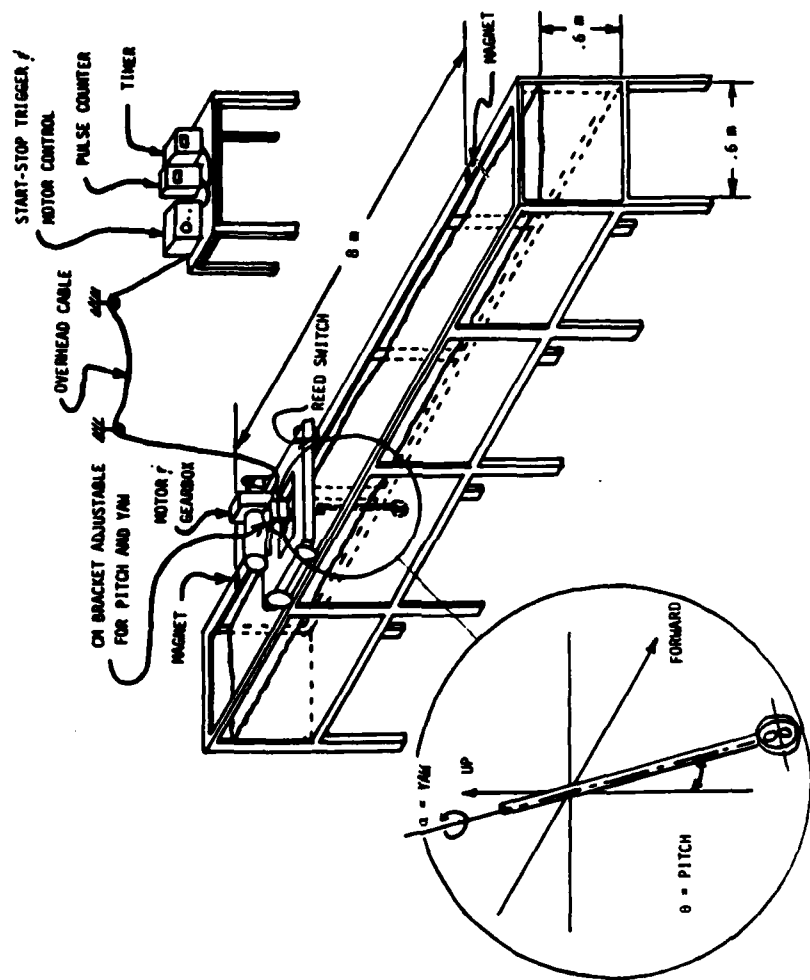


Figure A.2. Current meter calibration facility. The test tank and motor driven cart are shown.

Itron 680 timer. The motor-gearbox can be adjusted to produce constant velocities between 0.9 and 100.0 cm/sec. At a given gear setting, the elapsed time from run to run varied by less than .01 sec (<1%).

A current meter to be calibrated is suspended from the cart with the sensor in the center of the water column. The mounting bracket is adjustable in two angular directions. As shown in Figures A.1 and A.2, the yaw angle is taken about an axis along the current meter tube. When the current meter is suspended vertically from the cart α corresponds to the current meter yaw in the traditional sense but the term has been generalized here to describe rotation in the y-z plane of Figure A.1, no matter what the current meter orientation is. Similarly, Figure A.2 shows that what is defined as the current meter pitch angle, θ , is indeed pitch in the traditional sense when the meter is mounted on the test cart.

The current meter output is carried via an overhead cable to the start-stop trigger circuitry. This unit not only starts and stops the Itron timer but simultaneously starts and stops a counter which records the total number of current meter pulses which occur while the cart travels the 8 m test section. Cart velocity is taken as 8 m divided by the transit time and current meter output frequency is the number of pulses divided by the transit time.

In calibrating the current meters it has been found that at zero angle of attack, the rotation frequency, f , and component velocity, U , are linearly related. With the cart moving at speed S_c and the zero current meter angle of attack the current meter component velocity is

$$U = a f + b = S_c \quad (A.1.5)$$

where f is the current meter output frequency and a and b are calibration constants. If the current meter were an ideal sensor, the same expression would hold relating the velocity component, U , along the current meter rotor axis and the rotation frequency, regardless of the yaw angle of the meter. Then

$$U(\alpha) = a f(\alpha) + b = S_c \cos \alpha$$

However, the sensors are not perfect and a small correction $G_\alpha(a)$ must be made, so

$$U = (a f + b) G_\alpha(\alpha) = S_c \cos \alpha \quad (A.1.6)$$

Similarly if the current meter moves through the water at a pitch angle, θ :

$$U = (a f + b) G_\theta(\theta) = S_c \cos \theta \quad (A.1.7)$$

Both G_α and G_θ are close to one for most angles of attack. Note that to obtain the parameter many investigators term the "cosine response" one must divide G_α (or G_θ) into $\cos \alpha$ (or $\cos \theta$). Here G_α is termed the yaw correction and G_θ is termed the pitch correction.

In any practical application the velocity vector will impinge on the sensor with both a pitch and a yaw. If the sensor were radially symmetric G_α and G_θ would be the same and the angle of attack correction would be determined solely by the total angle of attack, β , where, from Figure A.1,

$$\tan^2 \beta = \tan^2 \alpha + \tan^2 \theta \quad (A.1.8)$$

In fact the sensor is not radically symmetric and $G_\theta(\beta) \neq G_\alpha(\beta)$. Thus the general equation must be written

$$U = (a f + b) G(\alpha, \theta) \quad (A.1.9)$$

As will be shown G_θ and G_α , though not equal, are not too different. For this reason $G(\alpha, \theta)$ is taken as a linear interpolation between G_α and G_θ , each evaluated at the total angle β . Referring to Figure A.3, $G(\alpha, \theta)$ can be expressed as a function of the two variables $\tan \alpha$ and $\tan \theta$ or as a function of their vector magnitude, $\tan \beta$, and the angle ϵ .

$$\epsilon = \tan^{-1} \frac{\tan \alpha}{\tan \theta} \quad (A.1.10)$$

It is assumed that $G(\alpha, \theta)$ can be determined by interpolating linearly along the radius of magnitude $\tan \beta$. Therefore

$$G(\alpha, \theta) = G_\theta(\beta) + \frac{2\epsilon}{\pi} [G_\alpha(\beta) - G_\theta(\beta)] \quad (A.1.11)$$

This equation reduces to the proper form at $G_\theta = G_\alpha$ and yet allows a rational adjustment for the effect of unequal G_θ and G_α . The method shown above allows the angle of attack corrections to be determined by independent determination of the yaw and pitch corrections.

In order to determine the calibration constants a and b , test tank runs were made with α and θ set to zero. These "head on" runs were made with four different current meters at eight cart speed settings. Actually, the cart speed is different going in opposite

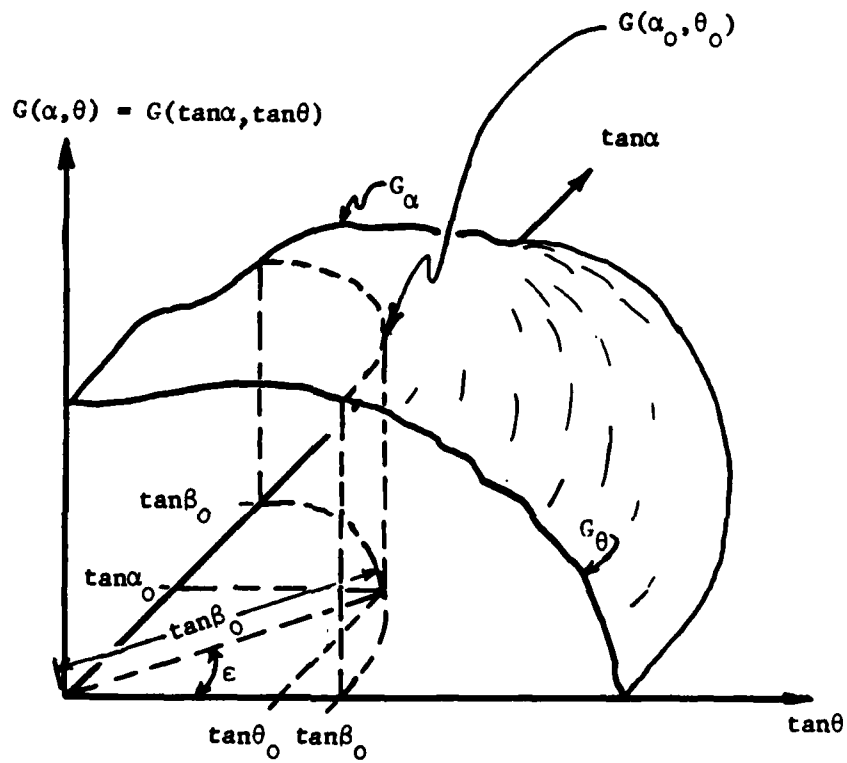


Figure A.3. A three-dimensional perspective sketch of $G(\alpha, \theta)$ vs. $\tan \alpha$, $\tan \theta$. G_θ is the intersection of $G(\alpha, \theta)$ with the $\tan \alpha = 0$ plane and G_α is the intersection of $G(\alpha, \theta)$ with the $\tan \theta = 0$ plane. $G(\alpha, \theta)$ is determined by linear interpolation along the arc of radius $\tan \beta$, $\tan \beta^2 = \tan \alpha^2 + \tan^2 \theta$.

directions so two speeds were achieved at each motor setting. The result of these calibration runs is shown in Figure A.4. The line is a least square linear fit to the data and yields:

$$a = 3.601 \text{ cm sec}^{-1} \text{ Hz}^{-1} \quad (\text{A.1.12})$$
$$b = 1.089 \text{ c. sec}^{-1}$$

Note that these constants apply to rotors with two magnets. The variance about the curve is $0.24 \text{ cm}^2/\text{sec}^2$ for an error of $\pm 0.49 \text{ cm/sec}$. Almost all of this error was due to differences between individual current meters. When any one sensor was run repeatedly at the same speed the same number of total pulses seldom varied by more than one. Over the 8 meter test section a total of about 200 pulses occurs. Therefore, the resolution of the total scheme is about 0.5 percent and the variation of any one current meter moving in a given direction at a particular speed is nearly obscured by the resolution of the technique. Comparing sequences of runs at different speeds with an individual current meter shows the response for runs in one direction to be nearly linear but the output varies with direction by about 1.0 percent or $.2 \text{ cm/sec}$ whichever is greater (i.e., a varied by 1.0 percent and b by less than $.2 \text{ cm/sec}$). The scatter in the response of the meters taken as a group reflects this type of error. The scatter increases linearly with speed and there is a minimum error of about $\pm 0.3 \text{ cm/sec}$. Therefore, the error in calibration is ± 1.2 percent ($.49 \text{ cm/sec}$ divided by the average calibration speed of 40 cm/sec) or $\pm 0.3 \text{ cm/sec}$, whichever is greater.

In performing the calibrations two possibilities for improving

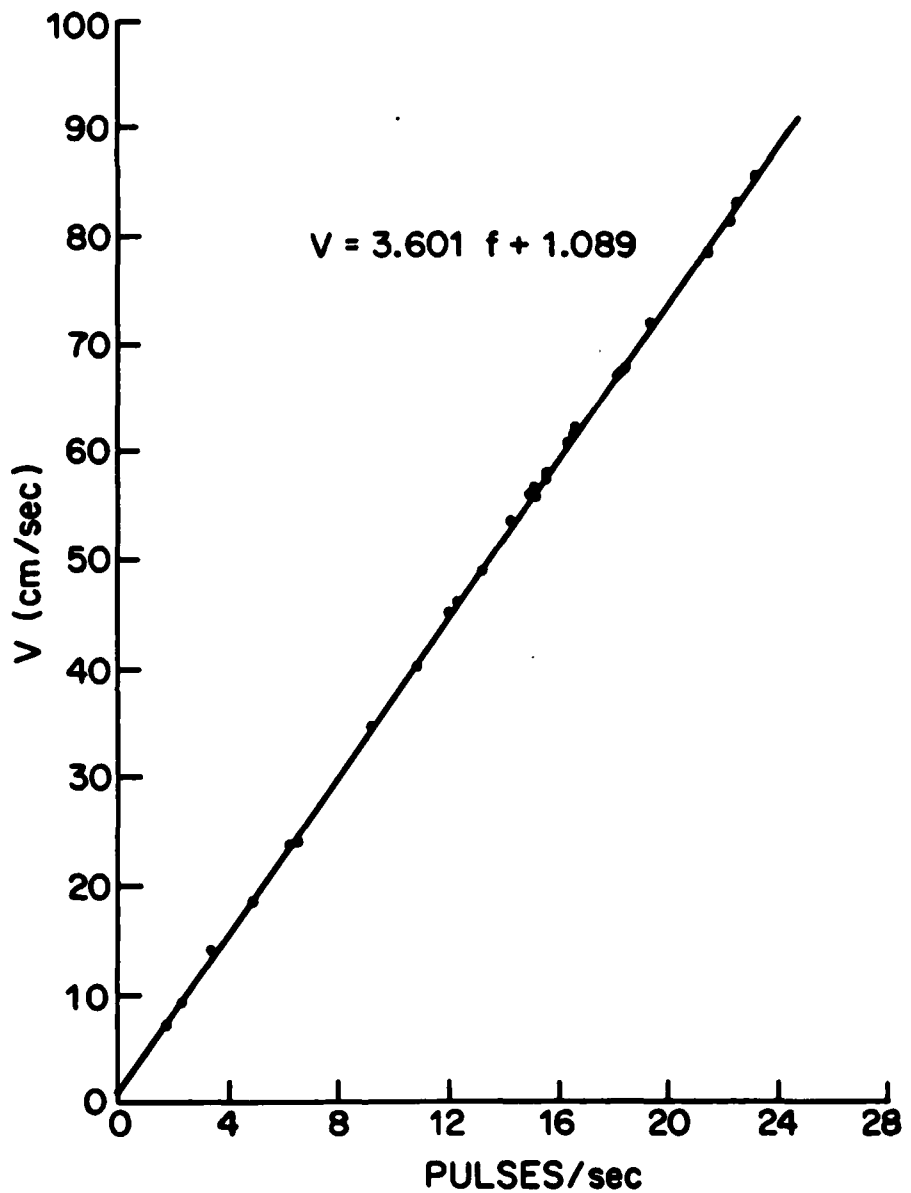


Figure A.4. Head on calibration for mechanical current meters.

the current meters came to light. The variation in performance with direction was found to be due to an asymmetry in the rotors. The plastic rotors are injection molded and in the forming process the edge of the blades on one side become more rounded than the edges on the other side. The sharp edges should be sanded smooth to produce symmetric rotors. This was done with one current meter and the unit produced virtually identical results moving in opposite directions.

The current meter to current meter variation could be duplicated by removing the rotor from a sensor and replacing it. The only parameter that this process could possibly change is the bearing end play. For this reason it is suggested that a more positive method of adjusting the end play be provided and that the clearance be set to some standard value with a dial indicator before each experiment.

In addition to the head on calibrations described above, low speed calibration tests were made, largely in an attempt to determine the current meter threshold. For these tests, runs were made at 18 different speeds from around 1 cm/sec to 20 cm/sec. The slowest the cart was able to go was 0.9 cm/sec and the current meter was turning smoothly at that low speed. Thus, the current meter threshold appeared to be at least as small as .9 cm/sec. Using two different current meters it was found that for slow speed

$$a = 3.64 \text{ cm/sec}^{-1} \text{ Hz}$$

$$b = .8 \text{ cm/sec}$$

So the low speed calibration is slightly different from, but within the error bounds of, the full range calibration. This low range calibration

is different from the high speed calibration in a sense opposite from that described in Smith (1974a) and McPhee (1979). In these works, a was found to be lower and b higher for low speeds than for high speeds. The reason for this difference is not obvious but the sensor system has been changed. The units previously employed an optical pickup while those described here employ the Hall effect pickup. The magnets in the tips of the rotors increase the inertia of rotors and this may allow them to keep spinning when the bearings suffer moments of increased friction. More important is the lengthy effort that is made to balance the rotors equipped with magnets. This probably results in a decrease in the current meter threshold velocity, and an increased output at low speed.

The angle of attack corrections were determined by running current meters through the tank at fourteen values of α and θ and using equations (A.1.6) and A.1.7) to determine G_α and G_θ respectively. A set of runs were made with three different current meters in a high speed range. The high speed range corresponded to a cart speed of 55.5 cm/sec in one direction and 60 cm/sec in the other and was meant to approximate the lowering speed of the APS. Low speed runs were made at 7.0 and 13.4 cm/sec with two different current meters. In calculating the angle of attack corrections, the head on calibration (a and b) for the individual current meter was used. It has been assumed that, in this way, the variation in head on calibration is eliminated from the angle of attack corrections. Once the angle of attack corrections were determined for each meter and each angle of attack, the results for each angle of attack were averaged to a single value. A least

squares fit was made to this data with a seventh order polynomial.

Figure A.5 shows the seventh order polynomial curve fits for the yaw correction. Due to the sensor symmetry in yaw, the correction is the same for positive and negative α . Also shown are all the data points that went into the 55-60 cm/sec curve fit. The variation about the curve fit is ± 2.0 percent. As shown by the different curves for the low speed range, there is some variation in the angle of attack correction with speed. The variation appears to increase at lower speed, the variation between 7.0 and 13.4 cm/sec being about the same as the difference between the high speed calibrations and the 13.4 cm/sec calibration. The calibration compares fairly well with that of Smith (1974a) and McPhee (1974). The earlier calibration does not show the roll off at high angles of attack. This roll off is necessary because of the form of equations (A.1.6) and (A.1.7). As θ or α goes to 90 degrees the corresponding correction must go to zero because b is finite. A better form for the equations might be

$$U = a(\alpha) \cdot f + b(\alpha)$$

and

$$U = a(\theta) \cdot f + b(\theta).$$

In practice this is not much of a problem because angles of attack greater than 70 degrees are seldom encountered. Usually the triplet orientation is adjusted so all current meters read approximately the same; so, the angle of attack is about 55 degrees.

Figure A.6 shows a similar set of curves for the pitch

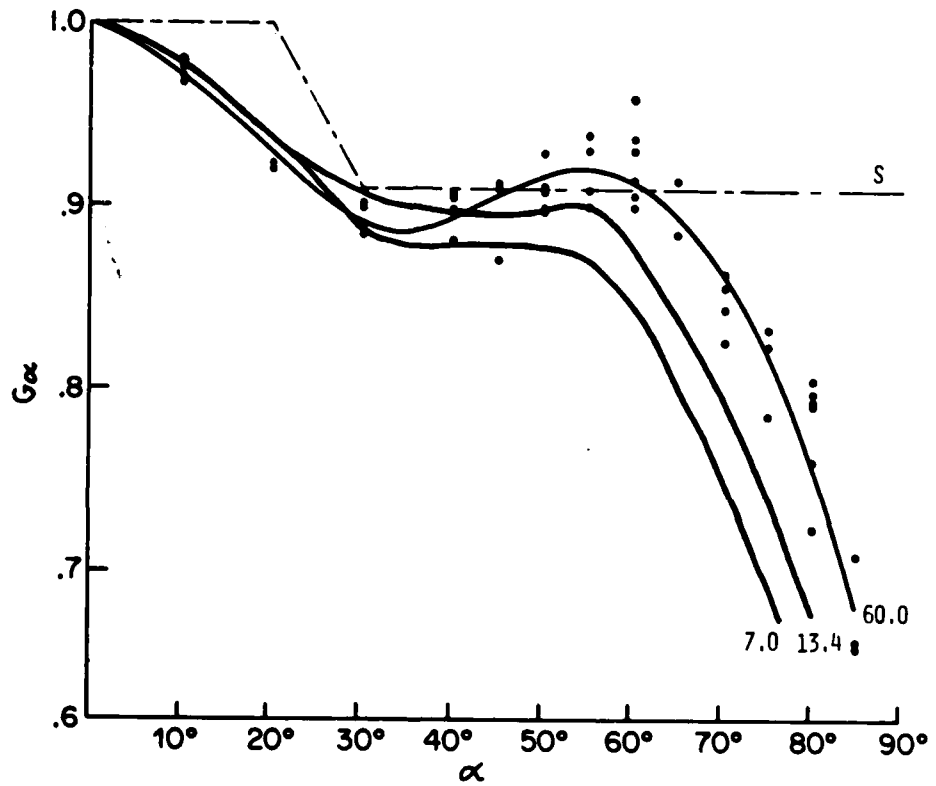


Figure A.5. Yaw correction coefficients. Seventh order fits for cart speeds of 7.0, 13.4, and 55-60 cm sec^{-1} . Points are the data for the 55-60 cm sec^{-1} fit. Also shown (S) is the fit described by Smith (1974a) and McPhee (1974).

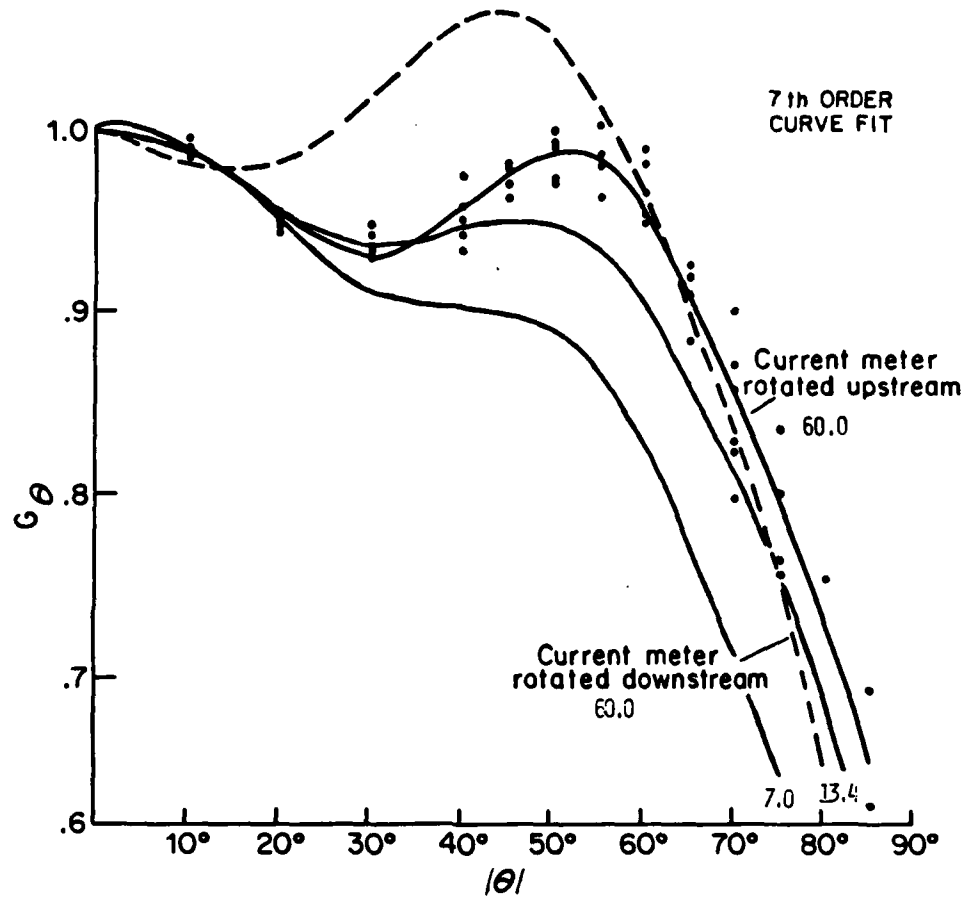


Figure A.6. Pitch correction coefficients. Seventh order fits for cart speeds of 7.0, 13.4, and 55-60 cm sec^{-1} . The points are data for the 55-60 cm sec^{-1} fit. The dashed line is the 55-60 cm sec^{-1} fit for negative pitch.

correction. As one can see the yaw and positive pitch corrections are quite similar, differing by only a few percent. Also shown is the seventh order curve fit for negative pitch and $S_c = 60 \text{ cm sec}^{-1}$. The current meter is not symmetric with pitch because of the support tube location; so the correction for positive and negative pitch are different. Seldom do the current meters encounter negative pitch so corrections for all three speeds are shown only for positive pitch. In the negative pitch orientation, the current meter rod leads from the sensor cage into the flow. Apparently this forces the flow to be aligned perpendicular to the rotor axis and the sensed speed is decreased. Hence the correction is greater than one for most negative pitch angles.

Table A.2 lists the coefficients of the seventh order curve fits for G_α and G_θ . With this information and the formulas of (A.1.12), equations (A.1.8) to (A.1.11) can be used to calculate the velocity component measured by a current meter, given the rotation frequency and angle of attack. The accuracy of the calculation is about ± 2 percent. In practice the angle of attack must be calculated using the velocity data from a triplet of current meters. Thus the calculation of velocity requires some sort of iterative scheme.

The iterative process begins with the assumption of zero angle of attack for all three current meters. Initial estimates, v_1 , v_2 , and v_3 , of the current meter component velocities, are made using (A.1.9) with $G(\alpha, \theta)$ set equal to one:

$$v_i = a f_i + b \quad i = 1, 2, 3 \quad (\text{A.1.13})$$

Table A.2
Angle of Attack Correction Polynomial Coefficients

$$\text{for } G_{\alpha} = \sum_{i=1}^8 \gamma_{\alpha i} |\alpha|^{i-1} \quad \text{and} \quad G_{\theta} = \sum_{i=1}^8 \gamma_{\theta i} \theta^{i-1}, \quad \theta > 0$$

i	1	2	3	4	5	6	7	8
$\gamma_{\alpha i} \text{ for } S_c =$								
7.0	1.006	-4.218x10 ⁻¹	3.500	-1.660x10 ⁻¹	3.416x10 ⁻¹	-3.401x10 ⁻¹	1.624x10 ¹	-3.007
13.4	1.004	-2.375x10 ⁻¹	1.577	-8.887	1.957x10 ⁻¹	-1.972x10 ⁻¹	9.205	-1.626
57.5	1.002	-3.475x10 ⁻¹	2.712	-1.460x10 ⁻¹	3.277x10 ⁻¹	-3.460x10 ⁻¹	1.734x10 ¹	-3.357
$\gamma_{\theta i} \text{ for } S_c =$								
7.0	.996	-1.287x10 ⁻¹	2.544	-1.646x10 ⁻¹	3.903x10 ⁻¹	-4.317x10 ⁻¹	2.262x10 ¹	-4.566
13.4	.998	1.114x10 ⁻¹	-8.231x10 ⁻²	-1.462	9.404	-1.343x10 ⁻¹	7.753	-1.625
57.5	1.003	-2.021x10 ⁻¹	2.730	-1.705x10 ⁻¹	4.089x10 ⁻¹	-4.490x10 ⁻¹	2.296x10 ¹	-4.461

where a and b are as given in (A.1.12). Then, in order to calculate improved velocity estimates, U_1 , U_2 and U_3 , the angles of attack must be calculated. Figure A.7 shows a sketch of the APS triplet and the numbering system used to identify the current meters. Note that

$V_i = U_i$ for the first iteration but V_i is defined by (A.1.13) while U_i is the current best estimate of velocity and changes with each new iteration until it converges and is taken as the final velocity. Figure A.1 shows the orientation of U_1 , U_2 and U_3 as they appear in the reference frame of current meter number 1. In general, for any current meter,

$$\theta = \tan^{-1} \frac{U_t}{V_t} \quad (A.1.14)$$

and

$$\alpha = \tan^{-1} \frac{W_t}{V_t} \quad (A.1.15)$$

for current meter number 1

$$\theta_1 = \tan^{-1} \frac{1}{\sqrt{2}} \left(\frac{U_3 + U_2}{U_1} \right) = \tan^{-1} c \quad (A.1.16)$$

$$\alpha_1 = \tan^{-1} \frac{1}{\sqrt{2}} \left(\frac{U_3 - U_2}{U_1} \right) = \tan^{-1} h \quad (A.1.17)$$

$$c = \frac{1}{\sqrt{2}} \left(\frac{U_3 + U_2}{U_1} \right) \quad (A.1.18)$$

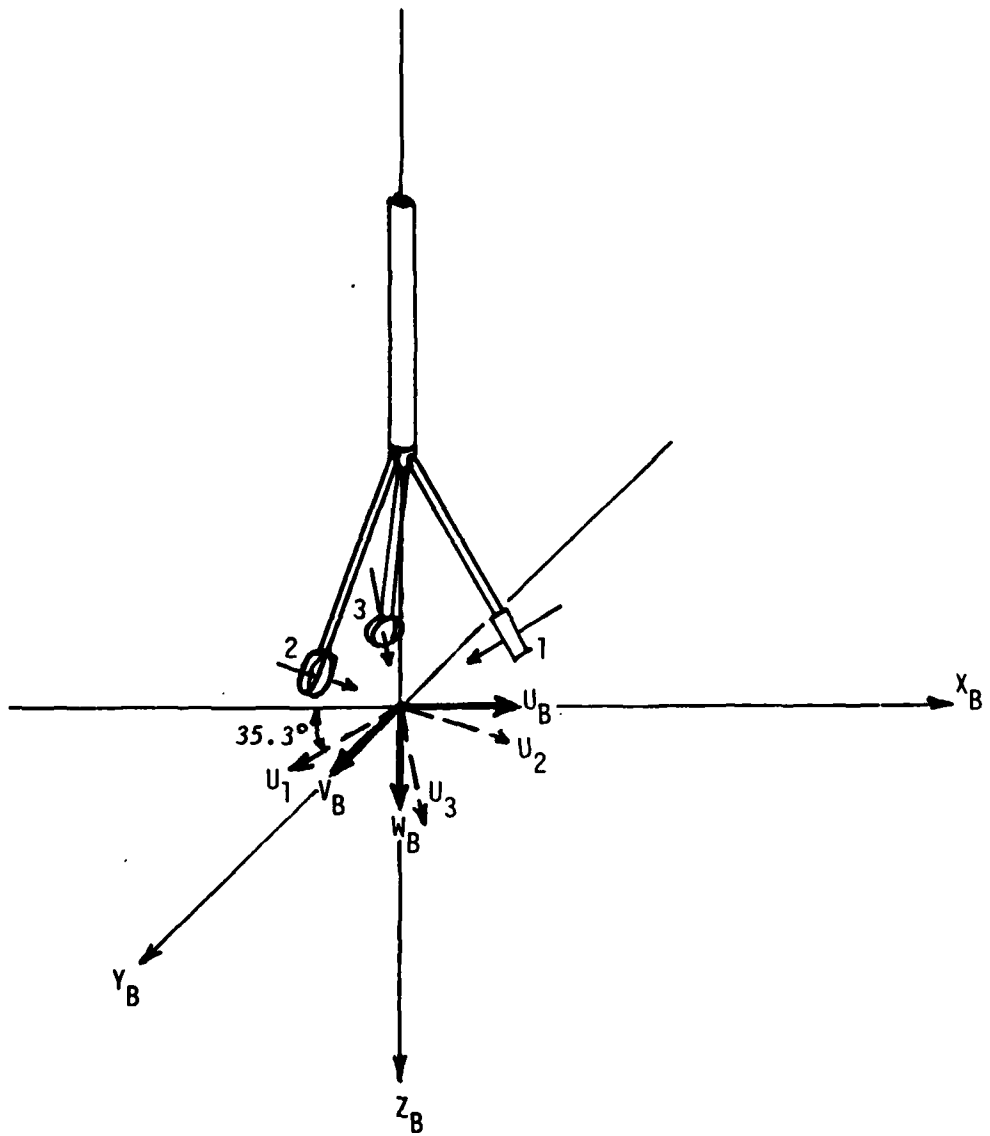


Figure A.7. Sketch of the APS triplet showing the numbering convention used to identify the current meters.

$$h = \frac{1}{\sqrt{2}} \left(\frac{U_3 - U_2}{U_1} \right) \quad (A.1.19)$$

Similarly the pitch and yaw angles for the other two current meters are

$$\theta_2 = \tan^{-1} \frac{1}{\sqrt{2}} \left(\frac{U_1 + U_3}{U_2} \right) = \tan^{-1} \left[\frac{1 + \frac{1}{\sqrt{2}} (C + h)}{C - h} \right] \quad (A.1.20)$$

$$\alpha_2 = \tan^{-1} \frac{1}{\sqrt{2}} \left(\frac{U_1 - U_3}{U_2} \right) = \tan^{-1} \left[\frac{1 - \frac{1}{\sqrt{2}} (C + h)}{C - h} \right] \quad (A.1.21)$$

$$\theta_3 = \tan^{-1} \frac{1}{\sqrt{2}} \left(\frac{U_2 + U_1}{U_3} \right) = \tan^{-1} \left[\frac{1 + \frac{1}{\sqrt{2}} (C - h)}{C + h} \right] \quad (A.1.22)$$

and

$$\alpha_3 = \tan^{-1} \frac{1}{\sqrt{2}} \left(\frac{U_2 - U_1}{U_3} \right) = \tan^{-1} \left[\frac{\frac{1}{\sqrt{2}} (C - h) - 1}{C + h} \right] \quad (A.1.23)$$

Once these formulas are used with the initial velocity estimates, equations (A.1.8), (A.1.10) and (A.1.11) can be used to calculate total of angle attack corrections for each current meter. These corrections can then be used to calculate improved velocity estimates using (A.1.9). The process is repeated until the velocity estimates converge.

A procedure which is less time consuming involves first performing the iterative procedure with hypothetical data and fitting the angle of attack corrections to the initial velocity measurements.

Then, during data processing the curve fits can be used to determine the angle of attack corrections without going through the iteration process. This technique was used in analyzing the APS data. An array of hypothetical initial values, C_o and h_o , of C and h were input to a program which calculated the angle of attack corrections using the technique described in the previous paragraph. The final values of the three angle of attack corrections were least squares fit to the initial values of C and h with a polynomial second order in h_o and seventh order in C_o ,

$$G_i = \sum_{j=1}^8 C_o^{j-1} \left[\sum_{k=1}^3 A_{ijk} h_o^{k-1} \right] \quad (A.1.24)$$

In this way, the angle of attack correction for each current meter is expressed as a function on the initial velocity estimates, namely

$$G(\alpha_i, \theta_i) = G_i(C_o, h_0) \quad i = 1, 2, 3 \quad (A.1.25)$$

where

$$C_o = \frac{a(f_3 + f_2) + 2b}{(a f_1 + b) \sqrt{2}} \quad (A.1.26)$$

$$h_o = \frac{a(f_3 - f_2)}{(a f_1 + b) \sqrt{2}} \quad (A.1.27)$$

Advantage can be taken of the fact that, because the corrections are symmetric in α ,

$$G(\alpha, \theta) = G(-\alpha, \theta) \quad (A.1.28)$$

and θ_1 is independent of h ; so,

$$G_1(C_o, h_o) = G_1(C_o, -h_o) \quad (A.1.29)$$

Also, from

$$\theta_2(C, h) = \theta_3(C, -h) \quad (A.1.30)$$

$$|\alpha_2(C, h)| = |\alpha_3(C, -h)| \quad (A.1.31)$$

it is found that:

$$G_2(C_o, -h_o) = G_3(C_o, h_o) \quad (A.1.32)$$

Therefore it is only necessary to calculate the correction coefficients G_1 , G_2 and G_3 for positive h_o (C_o is always positive).

Figure A.8 shows $G_1(C_o, h_o)$ as calculated for the APS. Figure A.9 shows $G_2(C_o, h_o) = G_3(C_o, -h_o)$. When the device is lowered through still water, C_o equals $\sqrt{2}$ and h_o equals zero. At this point G_1 , G_2 and G_3 are equal. In practice C_o is usually between about 1.0 and 2.0 and h_o is between $\pm .4$ so that minimum correction coefficient is about 0.8. Table A.3 gives the values of A_{ijk} used on constructing G_1 , G_2 , and G_3 for the APS.

It should be noted that the functions G_1 , G_2 , and G_3 depend on the current meter triplet configuration because the equations relating the angles of attack to the current meter velocities are unique to each triplet. Only the APS triplet has been discussed here but similar corrections were derived for the fixed mast triplets and the low speed angle of attack corrections shown in Figure A.5 and A.6. In

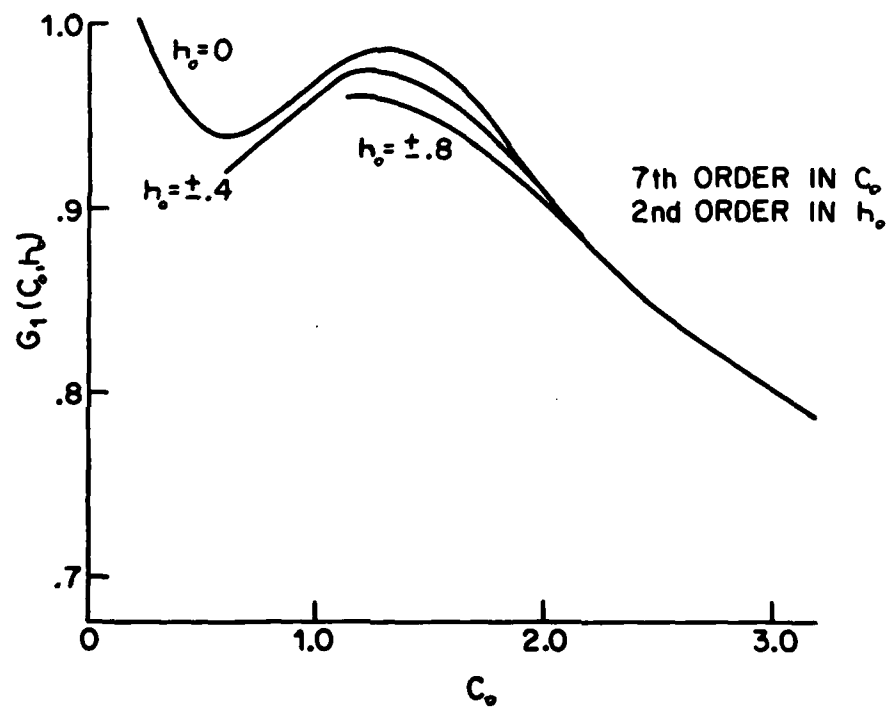


Figure A.8. $G_1(C_0, h_0)$ for APS triplet. This is the angle of attack correction for current meter 1 given the initial values of C and h .

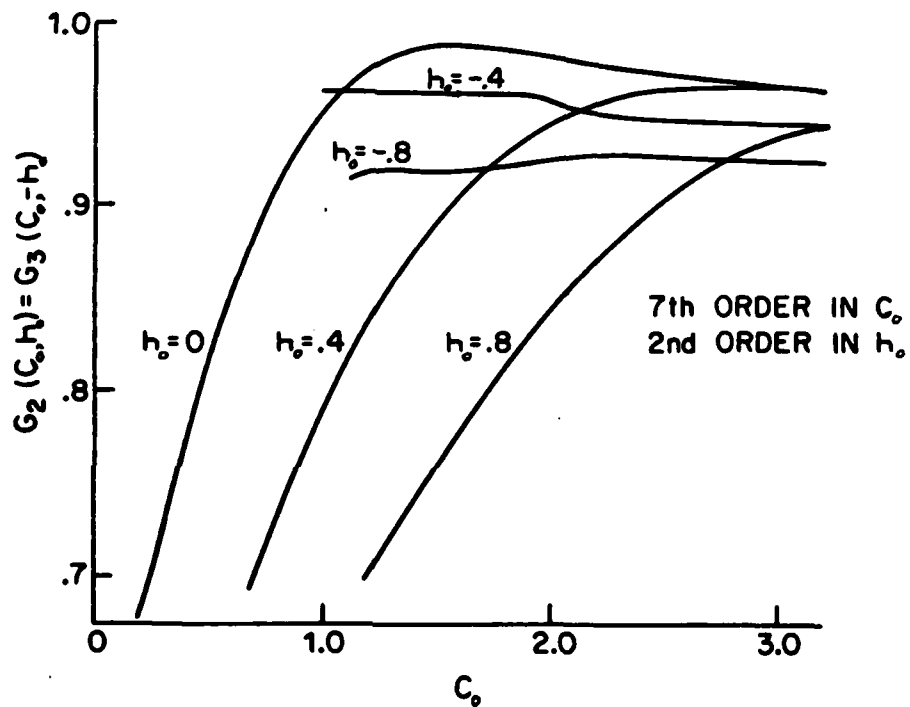


Figure A.9. $G_2(C_o, h)$ for APS triplet. This is the angle of attack correction for current meter 2 given the initial values of C and h . $G_3(C_o, h_o) = G_2(C_o, -h_o)$.

Table A.3
Coefficients for APS Triplet Angle
of Attack Corrections

 A_{1jk}

$i \setminus k$	1	2	3
1	1.070	1.655	-2.998
2	-3.083×10^{-1}	-1.101×10^1	1.822×10^1
3	-4.373×10^{-1}	2.585×10^1	-3.999×10^1
4	1.824	-3.005×10^1	4.385×10^1
5	-1.857	1.920×10^1	-2.671×10^1
6	8.448×10^{-1}	-6.850	9.175
7	-1.819×10^{-1}	1.279	-1.662
8	1.514×10^{-2}	-9.722×10^{-2}	1.235×10^{-1}

 $A_{2jk}(h \geq 0) = A_{3jk}(h \leq 0)$

$i \setminus k$	1	2	3
1	5.397×10^{-1}	-1.194	-4.551×10^{-1}
2	8.218×10^{-1}	4.521	-1.297
3	-7.524×10^{-1}	-1.041×10^1	7.615
4	6.554×10^{-1}	1.141×10^1	-1.086×10^1
5	-4.776×10^{-1}	-6.427	7.037
6	2.048×10^{-1}	1.946	-2.355
7	-4.418×10^{-2}	-3.024×10^{-1}	3.982×10^{-1}
8	3.725×10^{-3}	1.895×10^{-2}	-2.699×10^{-2}

 $A_{3jk}(h \geq 0) = A_{2jk}(h \leq 0)$

$j \setminus k$	1	2	3
1	5.746×10^{-1}	-1.270	2.149
2	5.239×10^{-1}	1.221×10^1	-1.833×10^1
3	1.035×10^{-1}	-2.807×10^1	4.166×10^1
4	-4.715×10^{-1}	2.947×10^1	-4.441×10^1
5	2.972×10^{-1}	-1.672×10^1	2.575×10^1
6	-8.333×10^{-2}	5.303	-8.362
7	1.083×10^{-2}	-8.869×10^{-1}	1.431
8	-5.031×10^{-6}	6.099×10^{-2}	-1.005×10^{-1}

processing the APS data on the NOVA 1200 computer it was found that using the pre-derived angle of attack corrections was an order of magnitude faster in computer time than going through the iterative procedure.

The following section will deal with calculating the current meter output frequencies applying the calibrations discussed here and using the orientation data to calculate the horizontal water velocity.

A.2 Analysis of APS Data from the AMLE

This section is devoted to an explanation of how the raw current meter data from the APS is converted to measurements of horizontal velocity. For most of the experiment only data from the APS was recorded but during periods when the fixed current meters were above threshold, the data from them was included in the current meter records. Also, noise problems created by the gyrocompass were severe during the AMLE and it was necessary to shut the compass off while recording every other tape in order to insure adequate density data was gathered. Thus, several, slightly different data handling schemes have been used to convert raw data tapes into sequences of profiles. First, the basic scheme for converting a raw data tape made with only APS current meters and a functioning compass will be discussed. The reduction of the CTD data will be mentioned as one aspect of handling the analog data. Modifications for other cases and more advanced data reduction will be discussed at the end of the section. Figure A.10 is a block diagram of the basic data reduction scheme used for analyzing the APS data. Steps 2 through 5 are computations required to convert raw

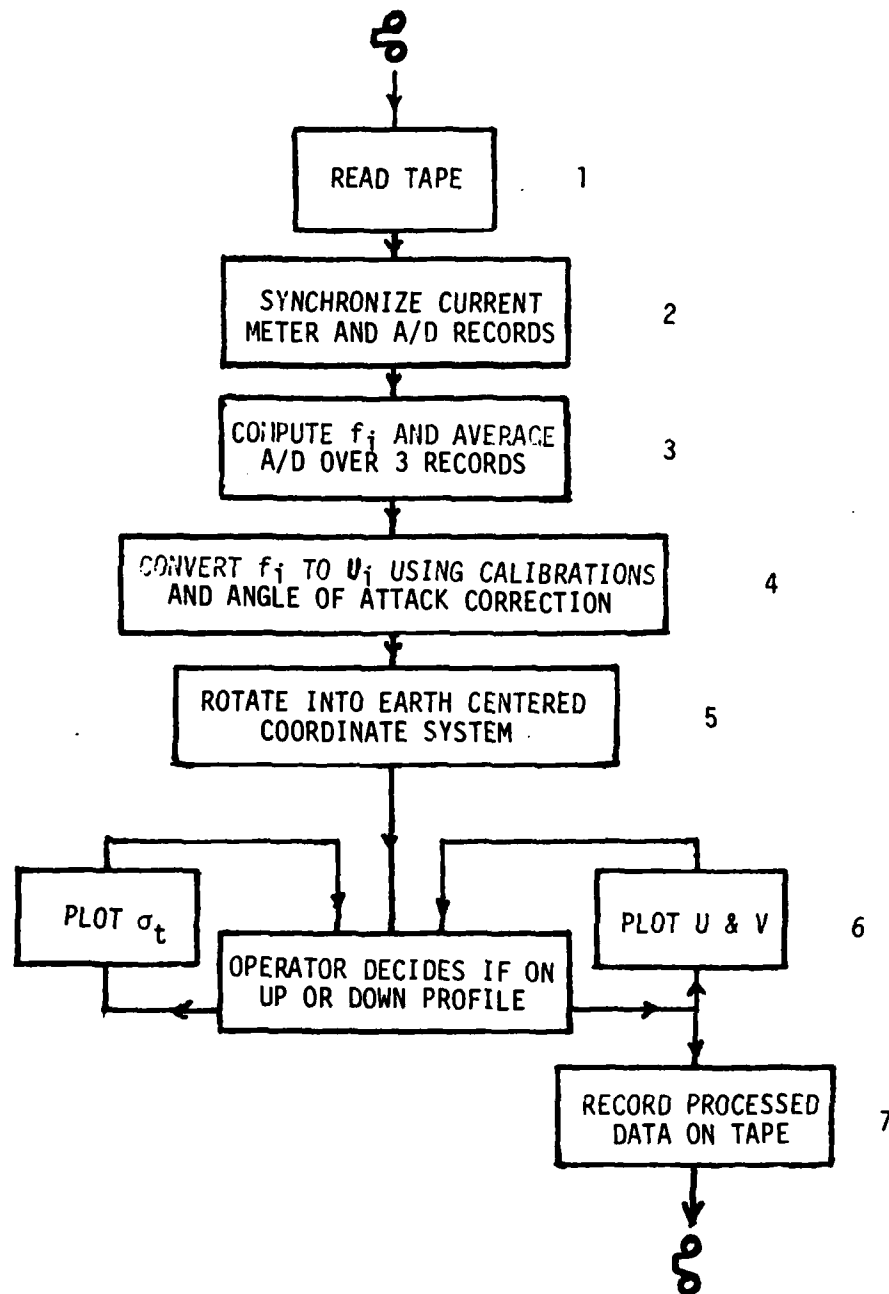


Figure A.10. Block diagram of data reduction scheme used for analyzing APS data.

data to useful information.

The first operation in analyzing a raw data tape is synchronizing the A/D and current meter records. The A/D data is stored on the raw tapes in separate records made asynchronously with the current meter records. During data acquisition the number of the A/D buffer currently being filled is recorded at the beginning of each current meter record. The current meter records are written at the highest priority. That is, an A/D buffer which has just been filled is not written on tape until the current meter buffer presently being filled is written. When analyzing a raw data tape it is thus possible to synchronize the A/D and current meter data by going to a current meter record appearing immediately after an A/D record (or go the first current meter record on tape) and reading the A/D buffer number. This number must refer to a location in the next A/D record. Once corresponding times have been located in the A/D and current meter records they may be treated as two parallel strings of data and it is possible to step through them in equal time increments using buffers to store data as one set of records gets ahead of the other. Synchronization is usually required only at the beginning of a tape.

The next step in data reduction is the determination of current meter output frequency. In order to justify the technique used to make this conversion it is necessary to discuss some of the noise problems encountered with the APS current meter and analog data. It is also necessary to discuss the way in which the profiler oscillates as it is lowered through the water. Figure A.11 is a plot of raw frequency data from the three APS current meters. The raw data consists of periods of

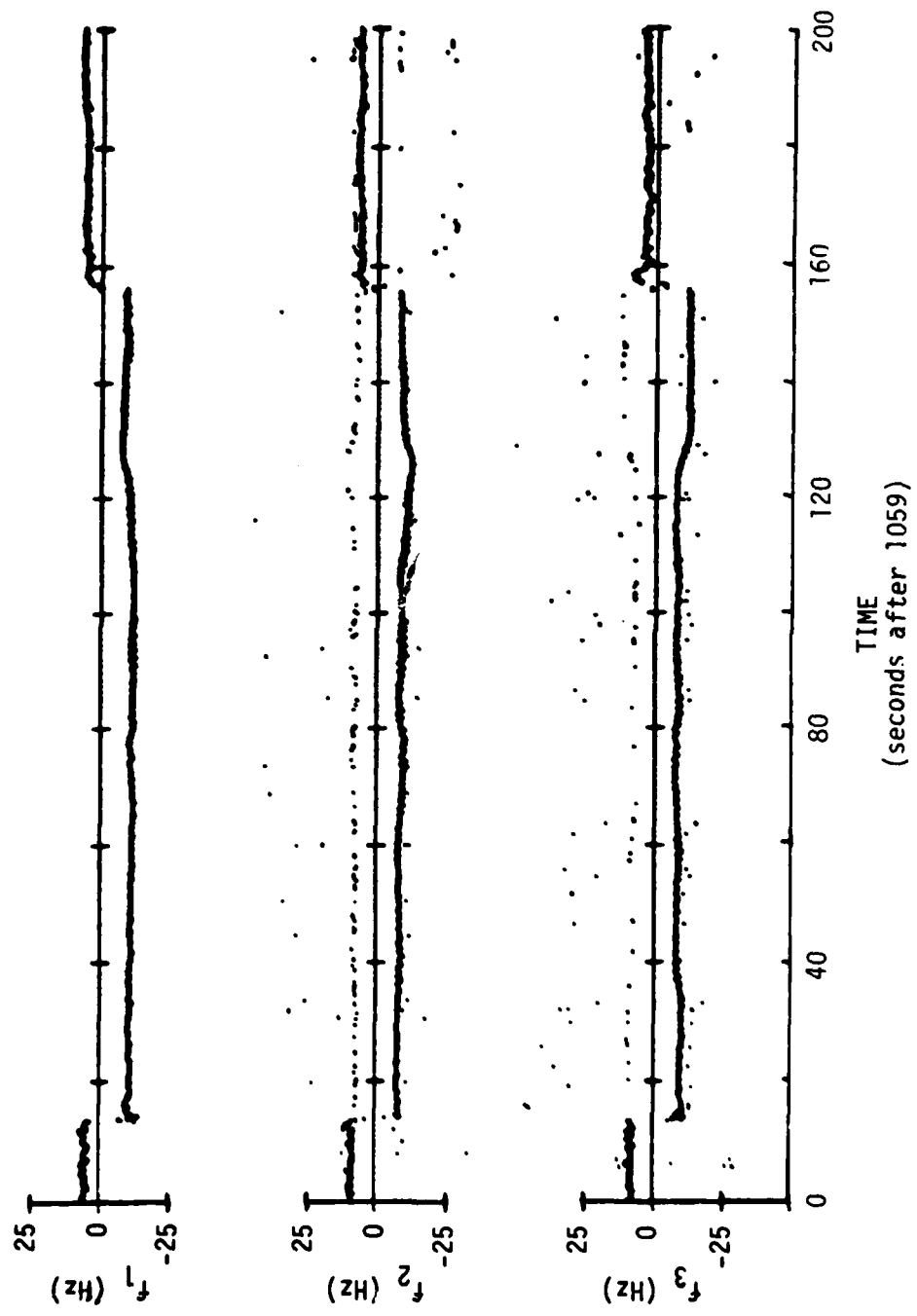


Figure A.11. Raw frequency data from the three APS current meters for 1059-1102 AST 4/8/76. Negative frequency \rightarrow negative velocity.

rotation given every .00512 sec. A change in period indicates a current meter pulse has occurred and the new period is the time between the two previous pulses. Figure A.11 is constructed by taking every new period, inverting it to obtain a frequency and plotting the result as a function of time. Negative frequencies imply negative velocities and the time from 15 seconds to 155 seconds corresponds to a single downcast. The output frequency of all current meters is around 9 Hz which corresponds to component velocities of 34 cm/sec and a lowering speed of 59 cm/sec.

The outputs of the meters are plagued with several types of noise. Due to grounding and shielding errors the compass and rate gyro motors induced noise on all the other analog outputs. (Perversely the compass and rate gyro outputs were fairly clean.) For this reason the rate gyros were used only a couple of times and, in order to obtain good CTD data, the gyrocompass was used only every other hour. The noise in the current meter data is independent of these two sources. Current meters #2 and #3 show occasional scatter and sign errors. Apparently these were caused by faults in the current meter interface system which have subsequently been remedied. The sign errors cause no problems during data reduction because only downcasts are studied and all the velocity signs are assumed to be negative. The points with erroneous magnitudes are edited by comparing each data point with a running average.

All three current meters display a small amplitude, high frequency oscillation in their outputs. This oscillation can also be seen in the accelerometer and rate gyro outputs of Figure A.12. Averages

AD-A091 046

WASHINGTON UNIV SEATTLE DEPT OF OCEANOGRAPHY
FORCED INTERNAL WAVES IN THE ARCTIC OCEAN. (U)

F/6 8/3

MAY 80 J H MORISON

N00014-75-C-0186

UNCLASSIFIED

REF-M80-10

NL

4 4

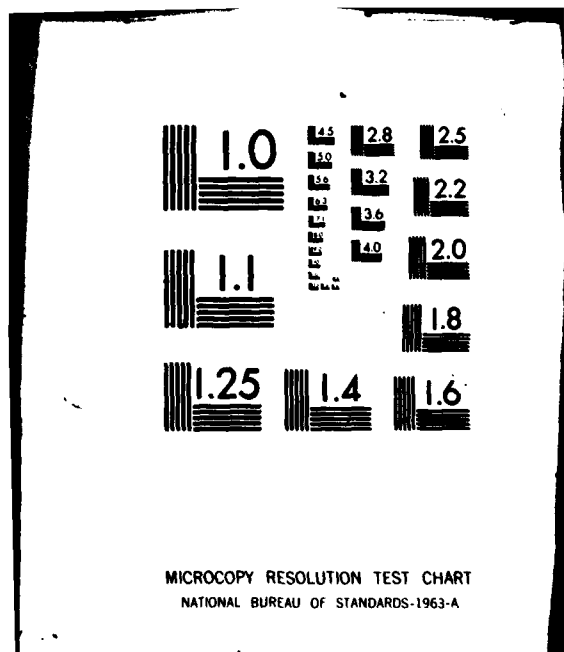
7

END

DATE FILMED

12/30/

DTIC



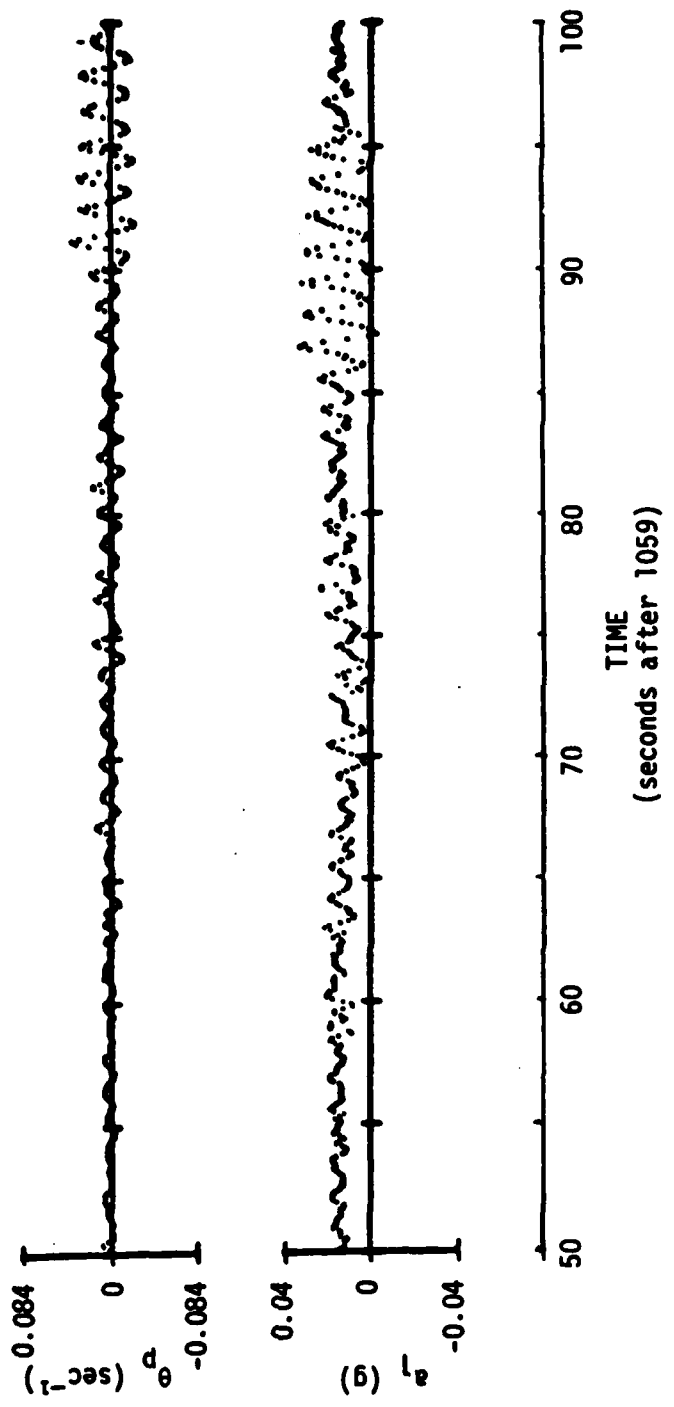


Figure A.12. Data from rate gyro #1 (Positive pitch forward) and accelerometer #1 (positive forward) showing oscillations with 1.26 sec period.

over .1 sec of the outputs of accelerometer #1 and rate gyro #1 are plotted. (Both sense forward tilt.) The period of time covered corresponds to the period 50 to 100 seconds on Figure A.11. Both the rate gyro and accelerometer display oscillations with a period of 1.26 sec. The maximum amplitude of the rate gyro output is about 2.8×10^{-2} rad sec⁻¹ and the amplitude of the accelerometer output is 1.7×10^{-2} g. The rate gyro lags the accelerometer by 90 degrees. Assuming the APS is oscillating about a point below the accelerometers, the values of acceleration and rotation rate can be used to determine the location of the center of rotation and the amplitude of the motion. Doing so, one finds the APS oscillates about a point 80 cm below the accelerometers with an amplitude .0056 radians. Not surprisingly the pivot point is close to the middle of the instrument. It is 128 cm above the current meters so the oscillating motion produces a velocity signal of 2.9 cm sec⁻¹ amplitude. This is on the same order as the oscillation observed in the velocity plots.

In order to filter out the oscillatory motion described above, it was decided to average the current meter frequencies over three current meter records. Each record covers eight interrupts, each 5.12×10^{-2} sec apart, so the total averaging time is 1.23 sec. This is reasonably close to the 1.26 sec oscillation period. The averages are made every record or 0.4096 sec.

There are a number of ways to compute the average frequency. One way is to average the inverse of all the recorded periods. This would be all right if the period were recorded only during the time it was applicable. Unfortunately, during data acquisition, the period

between two pulses is recorded over the subsequent interval between pulses. Simply averaging frequency weights each frequency by the wrong period of time. A way to overcome this problem is to shift the frequency data up in time so that it corresponds to the correct time period. The frequency should then be averaged over two periods because the two magnets on the current meters are not exactly 180 degrees apart. The averaging interval may be shifted one event at a time however. This method is time consuming and is only warranted when the ultimate in frequency response is required. In processing the APS data it is necessary to average the data anyway so the following scheme is used.

While scanning through a record, a change in recorded period is sought. When a change is found the period is compared to the average period from the previous record. If it deviates by more than 20 percent the scanning continues until another change occurs. When the period changes and is not edited out, an event counter is incremented and the new period is added to a total of the good time periods. When the end of a record is reached, the even counter yields the total number of events which occurred during that record and the total period count is the total time required for those events. The number of events from three successive current meter records is added and divided by the sum of periods from the three records to obtain the average pulse frequency. This method averages only "good" events (ones which pass the editing scheme), does not suffer from the time shift problem, and reduces the assymetric magnet problem by averaging over many pulses. There is a small error because the first period in a

record is actually partly in the previous record.

The error associated with each of the two approximate methods has been determined. The squared error for the first method (averaging frequencies as recorded) is found to be

$$\epsilon_0^2 = \overline{\left(\frac{f_a - \bar{f}}{\bar{f}} \right)^2} \leq \frac{18}{N_e} \overline{\left(\frac{\delta T}{T} \right)^2} + \frac{6\sqrt{2} (N_e - 1)}{N_e^2} \left[\overline{\left(\frac{\delta T}{T} \right)^2} \right]^{3/2} + \frac{4(N_e - 1)^2}{N_e^2} \left[\overline{\left(\frac{\delta T}{T} \right)^2} \right]^2 \quad (A.2.1)$$

where f_a represents the frequency approximation, f is the actual frequency, N_e is the number of events in an averaging period and $\overline{\left(\frac{\delta T}{T} \right)^2}$ is the variance in period length. For the method used in analyzing the APS data, the squared error is

$$\epsilon_{APS}^2 = \overline{\left(\frac{f_a - \bar{f}}{\bar{f}} \right)^2} = \frac{\overline{(N_e + 3)^2} \overline{\left(\frac{\delta T}{T} \right)^2}}{\overline{N_e^2 + N_e}} \quad (A.2.2)$$

for typical values of $\overline{\left(\frac{\delta T}{T} \right)^2}$ and $N_e = 12$;

$$\epsilon_0 = 3.03\%$$

and

$$\epsilon_{APS} = 0.67\%$$

The APS method is more than four times as good as the older, frequency average technique.

The analog data, having been synchronized with the current meter data, are also averaged over 1.23 seconds. This filters out the effect of the APS oscillation and the smoothed accelerometer data can then be used to measure tilt. The filtering process also greatly reduces the noise on the CTD channels.

The fourth step in data analysis is the application of current meter calibrations. Once the current meter frequencies are calculated they are converted to velocities with the calibrations described in the previous section. The frequencies are used to determine initial estimates of velocity and C_o and h_o . C_o and h_o are used in (A.1.24) to determine the angle of attack corrections G_1 , G_2 , G_3 and these are multiplied by the original velocity estimates, v_1 , v_2 and v_3 , to obtain the triplet velocities U_1 , U_2 and U_3 .

The fifth step in analyzing the APS velocity data is to rotate the triplet velocities into a body carried coordinate system with x to the north, y to the east, and z vertical down. This is actually done in two rotations. First the triplet velocities are rotated into a coordinate system fixed to the APS but with x forward, y to the left and z positive down the axis of the instrument. This is called the body centered coordinate system. Referring to Figure A.7, the rotation can be expressed in terms of the following matrix transformation.

$$\begin{bmatrix} \bar{U}_B \\ \bar{V}_B \\ \bar{W}_B \end{bmatrix} = \begin{bmatrix} -\cos 35.3^\circ & (\cos 35.3^\circ) \cdot (\sin 30^\circ) & (\cos 35.3^\circ) \cdot (\sin 30^\circ) \\ 0 & -(\cos 35.3^\circ) \cdot (\cos 30^\circ) & (\cos 35.3^\circ) \cdot (\cos 30^\circ) \\ \sin 35.3^\circ & \sin 35.3^\circ & \sin 35.3^\circ \end{bmatrix} \begin{bmatrix} U_1 \\ U_2 \\ U_3 \end{bmatrix}$$

(A.2.3)

where U_B , V_B , W_B are the velocities in the body centered coordinate system.

The rotation from the body centered coordinate system to the body carried, earth centered coordinate system is accomplished with another matrix transformation. From Etkin's (1972) equations (4.5.1), (4.5.3) and (4.4.7) the transformation for small elevation angle, θ , and small bank angle, ϕ , is:

$$\begin{bmatrix} U \\ V \\ W \end{bmatrix} = \begin{bmatrix} (1 - \theta) \cos \psi & -(1 - \phi) \sin \psi & \theta \cos \psi + \phi \sin \psi \\ (1 - \theta) \sin \psi & (1 - \phi) \cos \psi & \theta \sin \psi - \phi \cos \psi \\ -\theta & \phi & 1 - \phi - \theta \end{bmatrix} \begin{bmatrix} U_B \\ V_B \\ W_B \end{bmatrix} \quad (A.2.4)$$

where ψ is the compass bearing, θ is the elevation angle (basically pitch) and ϕ is the bank angle [approximately the roll angle for the small values of (θ)]. U is the velocity north, V is the velocity east and W is the velocity down. Because the rate gyros were not used during most the experiment and because the accelerometer outputs appear to be dominated by tilt after being filtered over 1.23 sec, the accelerometers are used as tiltometers. Thus

$$\theta = \sin^{-1} \frac{a_1}{g} \approx \frac{a_1}{g}$$

and

$$\phi = \left(\sin^{-1} \frac{a_2}{g} \right) / \cos \theta \approx \frac{a_2}{g}$$

These angles are very small (usually on the order of one or two

degrees, occasionally 5 degrees) so the approximation for small angles is appropriate. The compass bearing comes directly from the gyrocompass,

$$\psi = \gamma_{\text{compass}} + 37.05^\circ + 4^\circ$$

where 37.05 degrees is the correction to obtain true north from magnetic north and 4 degrees is the correction for misalignment of the compass.

The steps described above produce running 1.23 sec averages of water velocity, depth, temperature, salinity and σ_t . The averages are made for every .4096 seconds of raw data.

While the processing continues the disposition of the information is controlled by the computer operator. The sixth and final step in data processing is the elimination of the up profiles from the data record. During up profiles the sensors are in the wake of the APS. As such the velocity data is noisy and the density data is rather smeared out in depth. To eliminate the up profiles from the record, the computer operator watches the output of the processing program on a Tektronix display CRT. During up profiles, he selects a program mode which plots σ_t and does not record any results. During a down profile he selects a mode which copies the processed data on tape and plots velocity on the CRT. When finished with a raw tape, the operator has produced a hard copy picture (from the CRT) of velocity from each down profile and σ_t from the succeeding up profile. Data from analyzed down casts is recorded on tape. These profile tapes are the basic data set used in further analysis.

Appendix B

EQUATIONS OF MOTION

The equations of motion for an f-plane ocean with x to the north, y to the east and z down ($\bar{f} = -fk$) are:

$$\rho \left(\frac{d\bar{v}}{dt} + \bar{f} \times \bar{v} \right) = -\nabla p + g\bar{k} \quad (B.1)$$

$$\frac{1}{\rho} \frac{dp}{dt} + \nabla \cdot \bar{v} = 0 \quad (B.2)$$

$$\frac{dp}{dt} = C_s^2 \frac{dp}{dt} + q \quad (B.3)$$

Assuming the flow is adiabatic and incompressible $\frac{dp}{dt} = 0$ and $q = 0$.

Therefore:

$$\frac{dp}{dt} = \nabla \cdot \bar{v} = \frac{dp}{dt} = 0 \quad (B.4)$$

Now we assume:

$$\rho = \rho_0(z) + \rho(x, y, z, t) + \rho'(x, y, z, t) \quad (B.5)$$

$$p = p_0(z) + p(x, y, z, t) + p'(x, y, z, t)$$

$$\bar{v} = \bar{v}(x, y, z, t) + \bar{v}'(x, y, z, t)$$

$\rho_0(z)$ and $p_0(z)$ are the mean density distribution and resulting hydrostatic pressure respectively, i.e.:

$$\frac{\partial p}{\partial z} \Big|_0 = \rho_0 g \quad (B.6)$$

The primed quantities are turbulent perturbations whose ensemble averages (denoted by $\langle \rangle$) are zero. The remaining terms are those portions of the ensemble averages which vary in x , y , and t as well as z .

Substituting these expressions into (B.1), using (B.6), assuming $\rho_0 \gg \rho + \rho'$, and taking an ensemble average of the equation yields:

$$\frac{\partial \bar{v}}{\partial t} + \bar{v} \cdot \nabla \bar{v} + \langle \bar{v}' \cdot \nabla \bar{v}' \rangle + \bar{f} \times \bar{v} = - \frac{1}{\rho_0} \nabla p + \frac{\rho'}{\rho_0} g \bar{k} \quad (B.7)$$

Substitution of the expressions for velocity into the continuity equation and taking ensemble averages yields:

$$\nabla \cdot \bar{v} = \nabla \cdot \bar{v}' = 0 \quad (B.8)$$

It is assumed that the mean motions are of small amplitude and of large horizontal extent so that the non-linear term in (B.7) involving the mean quantities can be neglected. Equation (B.8) can be used to convert $\langle \bar{v}' \cdot \nabla \bar{v}' \rangle$ to $\nabla \cdot \langle \bar{v}' \bar{v}' \rangle$, the divergence of Reynolds stress. It is assumed that the turbulence acts only on thin layers so that the horizontal derivatives of $\langle \bar{v}' \bar{v}' \rangle$, are small relative to the vertical derivatives. Then (B.7) can be written:

$$\rho_0 \left(\frac{\partial \bar{v}}{\partial t} + \bar{f} \times \bar{v} \right) = -\nabla p + \frac{\partial \bar{\tau}}{\partial z} + \rho' g \bar{k} \quad (B.9)$$

where

$$\frac{\partial \bar{\tau}}{\partial z} = -\bar{\tau} \frac{\partial}{\partial z} \langle u' w' \rangle - \bar{j} \frac{\partial}{\partial z} \langle v' w' \rangle - \bar{k} \frac{\partial}{\partial z} \langle w' w' \rangle \quad (B.10)$$

Equation (B.4) states that the total derivatives of ρ is zero.

Using (B.5) and taking the ensemble average of the total derivative yields:

$$\frac{\partial \rho}{\partial t} + w \frac{\partial \rho}{\partial z} \circ + \nabla \cdot \langle v' \rho' \rangle = 0 \quad (B.11)$$

Here it has been assumed that the gradients on ρ are much less than the vertical derivatives of ρ_o . If turbulence only occurs in regions of constant density the turbulent flux of density can be neglected. Then

$$\frac{\partial \rho}{\partial t} + w \frac{\partial \rho}{\partial z} \circ = 0 \quad (B.12)$$

Equations (B.8), (B.9) and (B.12) are the basic equations for the internal wave problem.

Appendix C

LIST OF PHYSICAL VARIABLES IN CHAPTERS 4 AND 5

t	time
x, y, z	linear coordinates north, east, and down
i	$\sqrt{-1}$
$\vec{i}, \vec{j}, \vec{k}$	unit vectors, north, east, and down
\vec{v}	velocity vector, $u\vec{i} + v\vec{j} + w\vec{k}$
f	Coriolis parameter
f_j	current meter pulse frequency [see (2.3.1)]
p	pressure perturbation about hydrostatic due to waves
P_a	atmospheric pressure
$\overline{\tau}$	Reynolds stress
ρ	density
d	mixed layer depth
g	acceleration due to gravity
H	ocean depth, [$H(t) = \text{unit step function}$]
ρ_0	equilibrium density
ρ	density perturbation due to waves
ρ'	turbulent density perturbation
N^2	Brunt Väisälä frequency squared
ζ_w	vertical displacement
t	nondimensional [see (4.2.10)] time
x, y, z	nondimensional [see (4.2.10)] coordinates
u, v, w	nondimensional [see (4.2.10)] velocities
p	nondimensional [see (4.2.10)] perturbation pressure

P_o	nondimensional [see (4.2.10)] atmospheric pressure
\bar{s}	nondimensional [see (4.2.10)] Reynolds stress
r_o	nondimensional [see (4.2.10)] equilibrium density
r	nondimensional [see (4.2.10)] density perturbation
N^2	nondimensional [see (4.2.10)] N^2
w	scale velocity [see (4.2.10)]
u_*	stress velocity [see (4.2.10)]
P_d	pressure scale [see (4.2.10)]
ρ_s	equilibrium density scale [see (4.2.10)]
ρ^s	density perturbation scale [see (4.3.1)]
ζ	nondimensional [see (4.2.14)] vertical displacement
\bar{s}_o	\bar{s} at $z = 0$
$\mathcal{L}[], \mathcal{L}^{-1}[]$	Laplace transform and inverse Laplace transform
$\mathcal{F}[], \mathcal{F}^{-1}[]$	Fourier transform and inverse Fourier transform
σ	Laplace variable
\bar{k}	horizontal wave number vector $\bar{k}_i + \bar{k}_j$
k	magnitude of \bar{k}
λ	$-k^2/(\sigma^2 + 1)$
ϕ	$\mathcal{L}[\mathcal{F}[\zeta]]$
Σ	$\mathcal{L}[\mathcal{F}[\int_0^t \nabla_n \times \bar{s} d \xi - \nabla_n \cdot \bar{s}]]$
Σ_o	Σ at surface
\tilde{P}_o	$\mathcal{L}[\mathcal{F}[P_o]]$
\tilde{p}	$\mathcal{L}[\mathcal{F}[p]]$
Π	see (4.2.20)
ω_B^2	$1 + gk^2/Hf^2$

ψ	baroclinic component of ϕ
n	mode number
ψ_n	eigenvalue of internal wave equations
σ_n	eigenvalue of σ ($\pm i\omega_n$)
λ_n	eigenvalue [see (4.2.34)]
a_n	modal amplitude of transformed displacement response
ψ_Σ	component of ψ due to stress forcing
ψ_p	component of ψ due to pressure forcing
ψ_Σ	$\mathcal{L}^{-1}[\psi_\Sigma] = \mathcal{F}[\text{stress response}]$
ψ_p	$\mathcal{L}^{-1}[\psi_p] = \mathcal{F}[\text{pressure response}]$
τ_o	$\mathcal{L}^{-1}[\tau_o] = \mathcal{F}[\tau_o]$
τ_o	$\int_0^t (\nabla_n \times \bar{s}_o) d\xi - \nabla_n \cdot \bar{s}_o$
P_i	$\mathcal{L}^{-1}[\tilde{P}_o] = \mathcal{F}[P_o]$
E	see equation (4.2.42)
ϕ_o	ϕ at $z = 0$
ϕ_δ	ϕ at $z = \delta = d/H$
u	function satisfying (4.2.19) and (4.2.47)
u_δ	u at $z = \delta$
ϕ_Σ	ϕ due to stress forcing
Φ_Σ	$\mathcal{L}^{-1}[\phi_\Sigma]$
R	see (4.2.53)
R_Σ	see (4.2.60)
R_p	see (4.2.61)
\bar{u}	$\partial \xi / \partial \lambda$
u, v	$\mathcal{L}[\mathcal{F}[u, v]]$

μ_p, v_p	portion of μ_p, v_p due to baroclinic pressure gradients
$\theta_x, \theta_{\bar{x}}$	$\mathcal{L}[\mathcal{F}[x \text{ and } y \text{ components of } \bar{s}]]$
u_p, v_p	portions of u and v due to baroclinic pressure perturbations
u_a, v_a, x_n	see (4.2.74) to (4.2.76)
δ_d	see (4.3.7) (also equals δ)
F_s	buoyancy flux scale
F	for Section 4.2 see (4.2.22), elsewhere F is nondimensional buoyancy flux
F_o	nondimensional buoyancy flux at $z = 0$
u_B, v_B, w_B, p_B	subscripts denote boundary layer component
u_I, v_I, w_I, p_I	subscripts denote internal wave component
$u_B^{(0)}, v_B^{(1)}, p_B^{(2)}, p_B^{(0)}$	superscripts denote order of expansion
ξ	z/δ
P_B	equivalent transformed pressure for buoyancy flux [see (4.3.29)]
B_o	$\mathcal{L}[F_o]$
P_{IB}	$\mathcal{L}^{-1}[P_B]$
ω_G^2	$1 + \delta g k^2 / 2f^2 H$
β_o	$\mathcal{F}[F_o]$
σ_t	$(\rho - 1) \cdot 10^3$ at in situ temperature
α	specific volume in expression for N^2 in Section 4.4, variable of integration elsewhere
T	ocean temperature
Γ	adiabatic lapse rate
S	salinity
h	ice thickness in Section 3.4, step size in Section 4.4
$\tilde{\psi}$	discrete values of ψ for numerical determination of λ_n

λ_n^l	l th estimate of λ_n
ε_n^l	error in estimate λ_n^l
ψ_s	solution of (4.4.1a) and (4.4.2) (typically for $\lambda = \lambda_n$)
\tilde{v}_s	$\partial \psi_s / \partial \lambda$
$ \zeta_{p_{n,\omega,k}} $	wave number frequency response for displacement
$ \mu_{p_{n,\omega,k}} $	wave number frequency response for μ_p
$ \nu_{p_{n,\omega,k}} $	wave number frequency response for ν_p
τ_{oa}	approximation to long wave length components of τ_o
τ_L	short wavelength component of forcing τ_o plus total long wavelength at Big Bear
τ_m	average forcing in Big Bear triangle approximated by total long wavelength forcing τ_{oa}
L	lead spacing with regard to Figure 4.16 and in derivations of Section 4.7, elsewhere it refers to wavelengths
ΔL	lead width
v_i	ice velocity
v_j	velocity of current meter j [see (2.3.1)]
F_{BL}	buoyancy flux at lead surface

UNCLASSIFIED

SECURITY CLASSIFICATION OF THIS PAGE (When Data Entered)

REPORT DOCUMENTATION PAGE		READ INSTRUCTIONS BEFORE COMPLETING FORM
1. REPORT NUMBER	2. GOVT ACCESSION NO.	3. RECIPIENT'S CATALOG NUMBER
	AD-A091	046
4. TITLE (and Subtitle) Forced Internal Waves in the Arctic Ocean	5. TYPE OF REPORT & PERIOD COVERED Final N-00014-75-C-0186 Interim N-00014-79-C-0024	
7. AUTHOR(s) James H. Morison	8. CONTRACT OR GRANT NUMBER(s) N-00014-75-C-0186 N-00014-79-C-0024	
9. PERFORMING ORGANIZATION NAME AND ADDRESS University of Washington Department of Oceanography WB-10 Seattle, Washington 98195	10. PROGRAM ELEMENT, PROJECT, TASK AREA & WORK UNIT NUMBERS	
11. CONTROLLING OFFICE NAME AND ADDRESS ONR Branch Office 1030 East Green Street Pasadena, California 91106	12. REPORT DATE May 1980	
14. MONITORING AGENCY NAME & ADDRESS (if different from Controlling Office)	13. NUMBER OF PAGES 289	
	15. SECURITY CLASS. (of this report) UNCLASSIFIED	
	18a. DECLASSIFICATION/DOWNGRADING SCHEDULE	
16. DISTRIBUTION STATEMENT (of this Report) Approved for public release; distribution unlimited.		
17. DISTRIBUTION STATEMENT (of the abstract entered in Block 20, if different from Report)		
18. SUPPLEMENTARY NOTES		
19. KEY WORDS (Continue on reverse side if necessary and identify by block number) Internal Waves Arctic Ocean Physical Oceanography		
20. ABSTRACT (Continue on reverse side if necessary and identify by block number) When the surface of an ocean is disturbed by the effects of a storm, motions may be excited in the pycnocline by the action of forced internal waves. This dissertation deals with experimental and theoretical studies of such motions. During the Arctic Mixed Layer Experiment in the Spring of 1976, manifestations of forced internal waves were observed with a new profiling current meter-CTD system. The device is unique in that it is capable of producing simultaneous, accurate profiles of density and horizontal velocity, repeatedly and at high frequency. Of particular interest are measurements made with the		

UNCLASSIFIED

SECURITY CLASSIFICATION OF THIS PAGE(When Data Entered)

instrument in the upper 80 m of the ocean during a small storm which occurred April 8, 1976. During the storm the isopycnals deflected downward about 2 m and then rebounded and oscillated with periods on the order of 5 to 10 hours. Horizontal velocity perturbations at about the inertial frequency were also excited by the storm.

In an effort to explain the observed motions, new theories were developed which deal with the forcing of internal waves by surface stress, atmospheric pressure and buoyancy flux. Solutions are derived for the forced motions as sums of internal wave normal modes. Arbitrary stratification is allowed below the surface mixed layer and the kinematic surface boundary condition is used.

The solution for forcing by surface stress is unique in that it combines the use of arbitrary stratification with a body force approximation for surface stress. Two different integral expressions are derived for the response and they give identical results. Using estimates of surface stress based on ice velocity measurements from a large array of AIDJEX navigation buoys, the response of the first 49 modes are combined to predict the response as a function of depth and time at the experimental location. The resultant vertical displacement response resembles qualitatively the observed motions in phase and form but is smaller than the observed response by a factor of three. The predicted velocities display inertial oscillations extending across the top pycnocline just as observed but are also three times smaller than the observed motions.

The response to surface pressure is determined using normal mode decomposition. This produces a result identical to that of A. Leonov and Y. Miropolskiy. The response to atmospheric pressure is found to be negligible but the pressure response is used in the model of internal waves driven by buoyancy flux in leads.

The model of buoyancy flux forced waves is an extension of a model by L. Magaard. It employs a vertical diffusion coefficient which is large in the mixed layer and zero below. Using a buoyancy flux geometry and magnitude representative of conditions during the storm yields predictions of vertical displacement on the order of 1.2 m, nearly twice as large as those predicted for surface stress forcing. This contrasts with Magaard's finding that, for a temperate ocean, the buoyancy flux response should be less than the stress response. The difference is that the buoyancy flux response increases with wave number and the forcing is at shorter wavelengths (lead spacing \approx 10-20 km) in the Arctic than in temperate oceans. Horizontal velocities predicted by the model display shears at the inertial frequency with an amplitude of about 2 cm sec^{-1} which are quite similar to the observed oscillations. Due to the simplifying assumption of no horizontal salt advection, the displacement and velocity predictions become unreasonably large at high wave numbers. This has required the forcing for wavelengths shorter than 5.5 km be neglected and suggests a better model would account for the effects of horizontal spreading.

The conclusion of the dissertation is that internal waves forced by surface stress and buoyancy flux probably accounted for much of the observed response on April 8, 1976 and that, in general, forced motions create vertical displacements on the order of 1 meter at wavelengths down to a few kilometers. The remnants of such motions, which persist after forcing stops, may also appear as significant events when the ice moves over them, thus adding further complexity to observations of the responses of subsequent storms.

UNCLASSIFIED

SECURITY CLASSIFICATION OF THIS PAGE(When Data Entered)

FOR UNCLASSIFIED TECHNICAL REPORTS, REPRINTS & FINAL REPORTS
PUBLISHED BY OCEANOGRAPHIC CONTRACTORS
OF THE OCEAN SCIENCE & TECHNOLOGY DIVISION
OF THE OFFICE OF NAVAL RESEARCH

12 Defense Documentation Center
Cameron Station
Alexandria, Virginia 22314

Office of Naval Research
Department of the Navy
Arlington, Virginia 22217

6 ATTN: Code 102-IP

1 Cognizant ONR Branch Office
1030 East Green Street
Pasadena, California 91106

1 ONR Resident Representative

Director
Naval Research Laboratory
Washington, D.C. 20375

6 ATTN: Library, Code 2627

Scientific Officer
NORDA
Bay St. Louis, Mississippi 39520

1 ATTN: Code 461